DOE/ID/13320-2

Microstructures and Properties of Aluminum Die Casting Alloys

M. M. Makhlouf
D. Apelian
L. Wang

Work Performed Under Contract No. DE-FC07-94ID13320

For
U.S. Department of Energy
Assistant Secretary for
Energy Efficiency and Renewable Energy
Washington, DC

By
North American Die Casting Association
Rosemont, IL

DISCLAIMER

DOE/ID/13320-2

MICROSTRUCTURES AND PROPERTIES OF ALUMINUM DIE CASTING ALLOYS

M. M. Makhlouf
D. Apelian
L. Wang

Work Performed Under Contract No. DE-FC07-94ID13320

Prepared for the
U.S. Department of Energy
Assistant Secretary for
Energy Efficiency and Renewable Energy
Washington, DC

Prepared by
North American Die Casting Association
Rosemont, IL

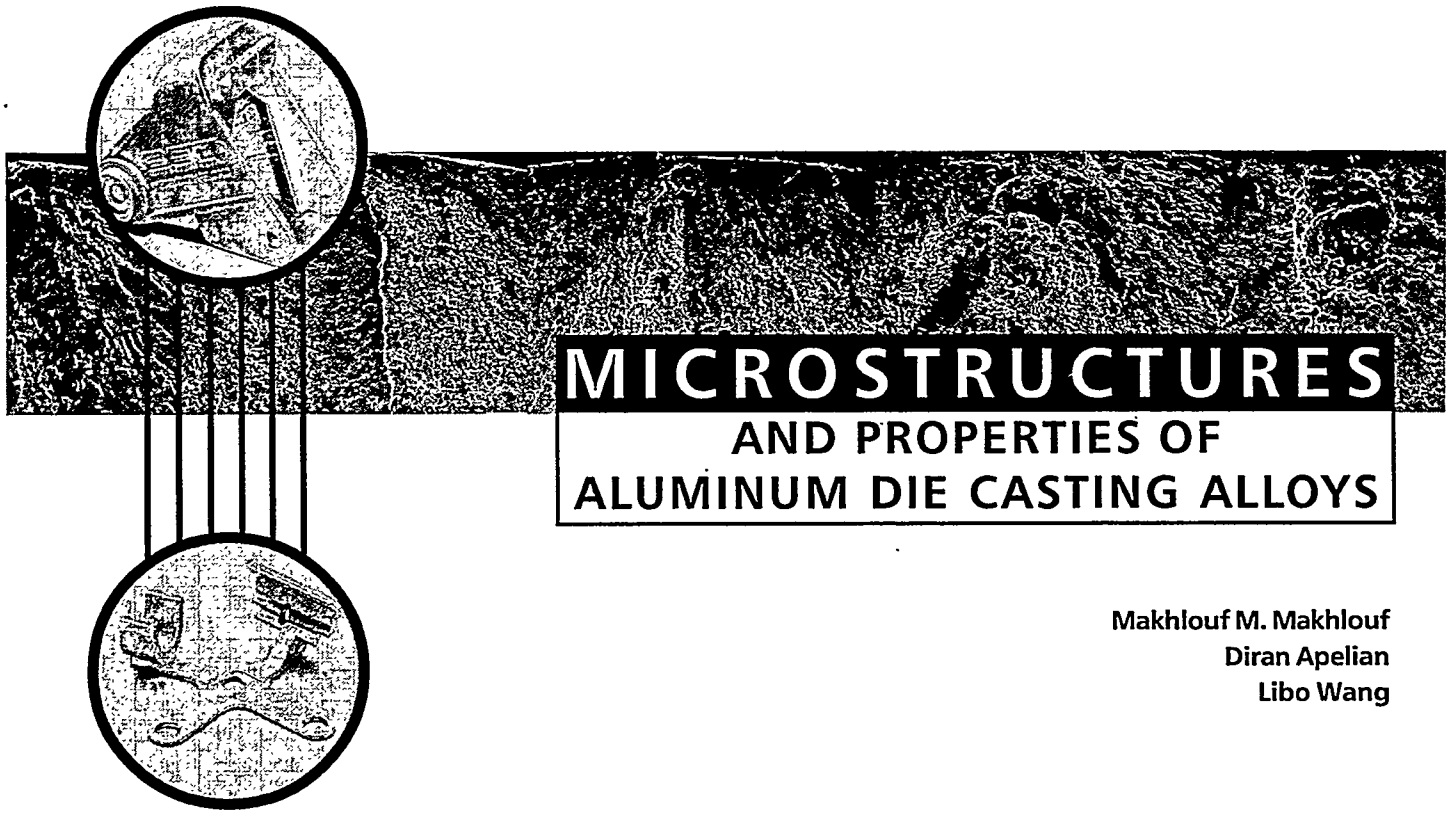

MICROSTRUCTURES AND PROPERTIES OF ALUMINUM DIE CASTING ALLOYS

Makhlouf M. Makhlouf
Diran Apelian
Libo Wang

NADCA®

North American Die Casting Association
Rosemont, Illinois U.S.A.

Contents

This book is written primarily as a reference source for die-casters, alloy designers, as well as for manufacturing engineers and design engineers. It is organized to allow easy access to important alloy data while providing a basic understanding of the relationship between chemistry, microstructure, and properties of aluminum die casting alloys. This book strives to cover the area between theoretical books and practical handbooks and is intended to be a valuable guide to metal casters. Consequently, the main objectives of the book are:

1. To provide descriptions of the microstructure of different aluminum die casting alloys and to relate the various microstructures to the alloy chemistry.
2. To relate the microstructures of the alloys to their main engineering properties such as ultimate tensile strength, yield strength, elongation, fatigue life, impact resistance, wear resistance, hardness, thermal conductivity and electrical conductivity.
3. To be a reference source for aluminum die casting alloys.

The book is organized in four chapters. Chapter 1 begins with a general introduction to aluminum die casting alloys, concentrating on the specific alloys covered in this book. The procedures used in preparing test specimens for property measurements, specifically melt preparation, specimen production and testing, are described in detail in Chapter 2. Chapter 3 is an extensive database of microstructures and properties of aluminum die casting alloys of varying compositions. Also included in Chapter 3 are cooling curves and differential thermal analysis curves for the alloys. The documented properties are room temperature ultimate tensile strength, yield strength, elongation, fatigue life, impact strength, and wear resistance, hardness, thermal conductivity, electrical conductivity, and specific gravity. In addition, data on high temperature ultimate tensile strength yield strength, and elongation are also given. Chapter 4 discusses the evolution of the various microstructures based on alloy chemistry, and relates the alloy performance, through its mechanical and physical properties, to the observed microstructure. Empirical equations for predicting each of the properties from the alloy chemistry are also provided.

The data and knowledge base presented in this book is the result of a research project that was cooperatively sponsored by the North American Die-Casting Association (NADCA) and the US Department of Energy (DOE). We express our gratitude to both organizations. Special thanks go to the corporate sector that contributed towards this major project not only in terms of resources, suppliers and materials, but most importantly they provided guidance, counsel and many years of experience. We would like to acknowledge the following: CMI International, Inc., Doehler-Jarvis Company, General Motors Corporation, Gibbs Die Casting, Kennedy Die Castings, Inc., Reynolds Metals Company, US Reduction, and Wabash Alloys.

Finally, we thank all the research scientists, graduate students, and technicians at the Metal Processing Institute who played an important role helping us perform the measurements and collect the data.

M. MAKHLOUF, D. APELIAN, L. WANG

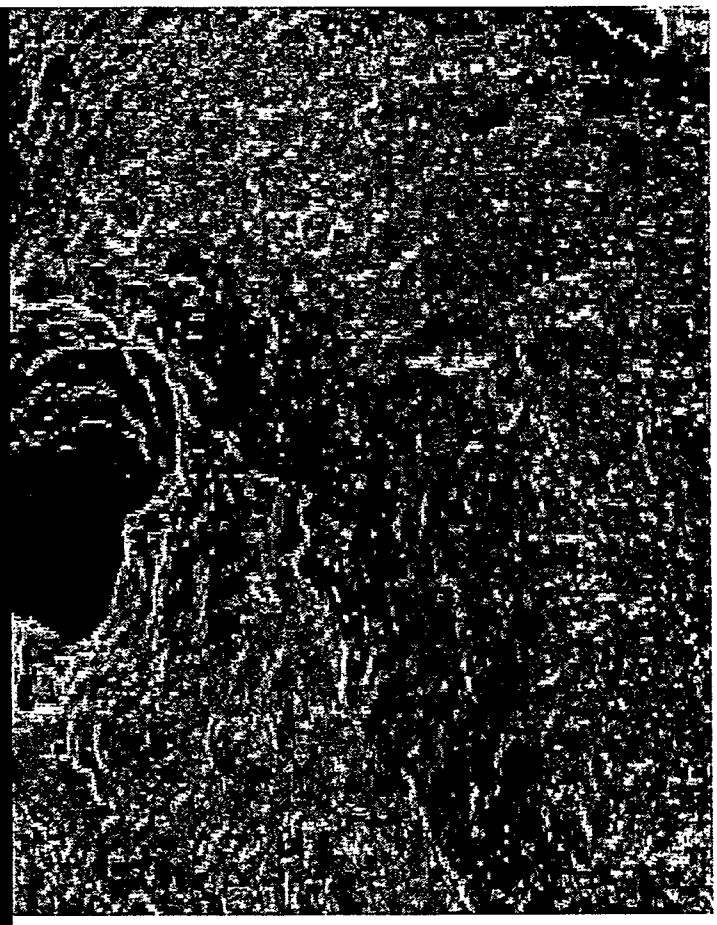

CHAPTER 1:

INTRODUCTION

The casting process has always been a major manufacturing method for aluminum based products. The production of aluminum castings by the thirty-seven major industrial countries in 1996 totaled 6.37 million tons, and of those the USA accounted for 1.64 million tons.[1] Generally speaking, cast aluminum alloy components can be produced by any of the traditional casting processes. However, advances in die casting technology, especially the development of the cold chamber die casting process, and improvements in die materials, have made the die casting process the most commonly used method for producing aluminum castings. The increase in the appeal of the die casting process may also be attributed to the excellent die casting characteristics of aluminum alloys, as well as, to the increased demand for large quantities of identical parts. In the 1980s the die casting process produced about 68% of the total aluminum alloy castings made in the USA.[2] In 1996 Japan produced 64.4% of its total aluminum alloy castings *via* the die casting process[1]. Among all the various different alloys that may be die cast, aluminum alloys are the most predominant. In 1997, 1.66 billion pounds of aluminum were die cast in the USA, in contrast to 439.7 million pounds of zinc and 91 millions pounds of magnesium.[3]

In addition to advances in manufacturing technology and the increased demands of the market, research and development efforts dedicated to aluminum alloys have played an important role in the dramatic growth in the use of these alloys. This is reflected in the number of publications per year dedicated to aluminum alloys. For example, reviewing Metal Abstracts, under the subtitle "*Aluminum Alloys*", shows that the number of papers published annually has increased from about 1,100 in 1970 to over 6,000 in 1992. However, only a small fraction of the published literature is pertinent to die casting alloys. A search for technical papers directly related to aluminum die casting alloys in *World Aluminum Abstracts* from 1968 to 1992 and *Metal Abstracts* from 1982 to 1992 shows that only 200 such papers were published during that time period.

Clearly, recent innovations in die casting technology have significantly expanded the commercial applications of cast aluminum products. However, the development of complementary new alloys, the optimization of existing alloys, and the documentation of reliable mechanical properties data for these alloys, have all categorically lagged behind. In 1995, the North American Die Casting Association (NADCA) and the US Department of Energy cooperatively sponsored a research program at Worcester Polytechnic Institute (WPI) aimed at systematically investigating alloy-microstructure-property interactions in aluminum die casting alloys. Twenty-four aluminum-based alloys containing elements common to aluminum die-casting alloys in the range typical to these alloys were produced. The alloys were die-cast into standard ASTM specimens, and their mechanical and physical properties were determined. The properties measured included: room temperature tensile properties, elevated temperature tensile properties, room temperature fatigue, hardness, wear resistance, impact strength, thermal conductivity, electrical conductivity, and specific weight. In addition, microstructure examination using scanning electron microscopy (SEM) and energy dispersive x-rays (EDX), as well as thermal analysis were performed on each of the alloys in order to correlate the alloy chemistry with its die cast microstructure and properties. The results of this comprehensive study are presented in this book.

References

1. *A modern casting Staff Report, "31st Census of World Casting Production–1996", Modern Casting, Vol. 87, No 12, Dec, 1997, p40-41.*
2. *Aluminum Statistical Review for 1988, The Aluminum Association, 1989.*
3. *"State of the Industry Summary,"* NADCA LINKS, *Feb 1998, p. 1.*

CHAPTER 2:

SPECIMEN PRODUCTION AND TEST PROCEDURES

2.1 Alloy Chemistry

The elements which are commonly found in aluminum die casting alloys and have a substantial effect on the alloy's microstructure and performance are copper, magnesium, manganese, silicon, zinc, chromium, titanium, iron, nickel, and strontium. Copper, magnesium, manganese, silicon, and zinc are usually intentionally added to commercial aluminum alloys to increase strength, particularly when coupled with heat treatment. These elements are all soluble in aluminum, and in all cases the solubility increases with increasing temperature. Of all the elements, zinc has the greatest solubility in aluminum (a maximum of 66.4%). Most of the other alloying elements form second phase microstructural constituents that are usually intermetallic in nature. Iron is always present in commercial aluminum alloys, it is often introduced into the alloy unintentionally through the use of steel tools during melting and casting and the use of scrap that contains iron or iron oxide. For most aluminum foundry alloys, the presence of iron is detrimental, and efforts are made to keep its levels as low as possible and economically feasible. However, in aluminum die casting alloys iron is added purposely to minimize die soldering. Various types of iron bearing phases may form in aluminum alloys, and the effects of iron depend to a large extent on the morphology of the phases that it forms.

The alloys presented in this book are aluminum-based alloys having compositions with the above mentioned elements in quantities that are commonly found in typical die casting alloys. They are experimental alloys intended to illustrate the effects of the various elements on the microstructure and mechanical and physical properties of die casting alloys. In order to illustrate the effects of these ten elements on the microstructure and properties of the alloys selected, the Taguchi method for design of experiments was used. Two Taguchi Orthogonal Arrays were employed: an L_{16} and a modified L_8. The L_{16} orthogonal array called for sixteen alloys where each of the ten elements was used at two specific different levels. In addition, those element interactions that are known to have a significant effect on alloy properties were also included. Since the range of silicon, copper, magnesium, iron and zinc in typical die casting alloys is quite wide, and since the L_{16} Taguchi orthogonal array incorporates only the high and low ends of this range, an L_8 array was needed in order to investigate the effects of these elements at levels that are intermediate to the range used in the L_{16} orthogonal array. In the modified L_8 orthogonal array, silicon is used at four different levels while each of the other four elements is tested at two levels. Table 2.1 shows the layout of the L_{16} Taguchi Orthogonal Array, and Table 2.2 shows the targeted and achieved average compositions in this array. Table 2.3 shows the layout of the modified L_8 Taguchi Orthogonal Array, and Table 2.4 shows the targeted and achieved average compositions in this array. Tables 2.5 and 2.6 list the composition of all twenty-four alloys which are covered in this book.

Table 2.1 Layout of the L_{16} Taguchi Orthogonal Array.

Alloy No.	Column No.														
	1	2	3	4	5	6	7	8	9	10	11	12	13	14	15
1	1	1	1	1	1	1	1	1	1	1	1	1	1	1	1
2	1	1	1	1	1	1	1	2	2	2	2	2	2	2	2
3	1	1	1	2	2	2	2	1	1	1	1	2	2	2	2
4	1	1	1	2	2	2	2	2	2	2	2	1	1	1	1
5	1	2	2	1	1	2	2	1	1	2	2	1	1	2	2
6	1	2	2	1	1	2	2	2	2	1	1	2	2	1	1
7	1	2	2	2	2	1	1	1	1	2	2	2	2	1	1
8	1	2	2	2	2	1	1	2	2	1	1	1	1	2	2
9	2	1	2	1	2	1	2	1	2	1	2	1	2	1	2
10	2	1	2	1	2	1	2	2	1	2	1	2	1	2	1
11	2	1	2	2	1	2	1	1	2	1	2	2	1	2	1
12	2	1	2	2	1	2	1	2	1	2	1	1	2	1	2
13	2	2	1	1	2	2	1	1	2	2	1	1	2	2	1
14	2	2	1	1	2	2	1	2	1	1	2	2	1	1	2
15	2	2	1	2	1	1	2	1	2	2	1	2	1	1	2
16	2	2	1	2	1	1	2	2	1	1	2	1	2	2	1

Table 2.2 Targeted and achieved average compositions in the L_{16} Taguchi Orthogonal Array.

Column No.	Element	Level 1 (%)		Level 2 (%)	
		Targeted	Achieved	Targeted	Achieved
1	Si	7.0	6.96±0.11	13.0	12.85±0.12
2	Mg	0.05	0.04±0.01	0.50	0.46±0.03
3	Si•Mg				
4	Fe	0.7	0.65±0.07	1.6	1.55±0.06
5	Cu	1.25	1.21±0.06	5.0	4.90±0.14
6	Ni	0.05	0.04±0.03	0.50	0.47±0.03
7	Cr	0	0.01±0.00	0.15	0.14±0.01
8	Mn	0	0.01±0.00	0.50	0.45±0.06
9	Ti	0	0.01±0.00	0.20	0.19±0.02
10	Zn	0.50	0.46±0.05	3.0	2.78±0.12
11	(FeMn)Cr				
12	Fe•Mn				
13	Sr	0	0.00±0.00	0.020	0.020±0.003
14	Unused				
15	Cu•Zn	-			

Table 2.3. Layout of the modified L_8 Taguchi Orthogonal Array.

Trial No.	Column No.						
	1	2	3	4	5	6	7
1	1	- - -	- - -	1	1	1	1
2	1	- - -	- - -	2	2	2	2
3	2	- - -	- - -	1	1	2	2
4	2	- - -	- - -	2	2	1	1
5	3	- - -	- - -	1	2	1	2
6	3	- - -	- - -	2	1	2	1
7	4	- - -	- - -	1	2	2	1
8	4	- - -	- - -	2	1	1	2

Table 2.4. Targeted and achieved average compositions in the modified L_8 Taguchi Orthogonal Array.

Column No.	Element	Level 1 (%)		Level 2 (%)		Level 3 (%)		Level 4 (%)	
		Targeted	Achieved	Targeted	Achieved	Targeted	Achieved	Targeted	Achieved
1	Si	8.0	8.29±0.14	9.0	9.50±0.01	10.0	9.68±0.02	11.0	10.91±0.04
2	Unused								
3	Unused								
4	Cu	2.5	2.66±0.05	3.75	4.37±0.55				
5	Fe	1.0	0.96±0.09	1.3	1.21±0.22				
6	Mg	0.10	0.05±0.03	0.30	0.04±0.02				
7	Zn	1.0	1.15±0.06	2.0	2.18±0.05				

Table 2.5. Chemical composition of the alloys in the L_{16} Taguchi Orthogonal Array.

No.	Composition (%)									
		Si	Mg	Fe	Cu	Ni	Cr	Mn	Ti	Zn	Sr
1	Targeted	7.00	0.05	0.70	1.25	0.05	0.00	0.00	0.00	0.50	0.000
	Achieved	**7.15**	**0.03**	**0.68**	**1.24**	**0.01**	**0.01**	**0.01**	**0.01**	**0.44**	**0.000**
2	Targeted	7.00	0.05	0.70	1.25	0.05	0.00	0.50	0.20	3.00	0.020
	Achieved	**6.99**	**0.01**	**0.56**	**1.15**	**0.01**	**0.01**	**0.47**	**0.24**	**2.87**	**0.018**
3	Targeted	7.00	0.05	1.60	5.00	0.50	0.15	0.00	0.00	0.50	0.020
	Achieved	**6.98**	**0.04**	**1.49**	**4.99**	**0.44**	**0.13**	**0.01**	**0.01**	**0.47**	**0.018**
4	Targeted	7.00	0.05	1.60	5.00	0.50	0.15	0.50	0.20	3.00	0.000
	Achieved	**6.94**	**0.04**	**1.48**	**4.74**	**0.47**	**0.15**	**0.45**	**0.16**	**2.69**	**0.000**
5	Targeted	7.00	0.50	0.70	1.25	0.50	0.15	0.00	0.00	3.00	0.000
	Achieved	**7.05**	**0.44**	**0.67**	**1.18**	**0.53**	**0.14**	**0.01**	**0.01**	**2.76**	**0.000**
6	Targeted	7.00	0.50	0.70	1.25	0.50	0.15	0.50	0.20	0.50	0.020
	Achieved	**6.98**	**0.44**	**0.57**	**1.13**	**0.48**	**0.13**	**0.45**	**0.18**	**0.38**	**0.002**
7	Targeted	7.00	0.50	1.60	5.00	0.05	0.00	0.00	0.00	3.00	0.020
	Achieved	**6.92**	**0.50**	**1.63**	**4.94**	**0.03**	**0.01**	**0.02**	**0.01**	**2.73**	**0.022**
8	Targeted	7.00	0.50	1.60	5.00	0.05	0.00	0.50	0.20	0.50	0.000
	Achieved	**6.79**	**0.46**	**1.49**	**4.77**	**0.01**	**0.01**	**0.45**	**0.20**	**0.42**	**0.000**
9	Targeted	13.00	0.05	0.70	5.00	0.05	0.15	0.00	0.20	0.50	0.020
	Achieved	**12.71**	**0.05**	**0.63**	**4.96**	**0.06**	**0.14**	**0.01**	**0.20**	**0.50**	**0.017**
10	Targeted	13.00	0.05	0.70	5.00	0.05	0.15	0.50	0.00	3.00	0.000
	Achieved	**12.69**	**0.03**	**0.73**	**5.09**	**0.07**	**0.11**	**0.37**	**0.01**	**2.73**	**0.000**
11	Targeted	13.00	0.05	1.60	1.25	0.50	0.00	0.00	0.20	0.50	0.000
	Achieved	**12.86**	**0.04**	**1.59**	**1.21**	**0.45**	**0.01**	**0.01**	**0.18**	**0.49**	**0.000**
12	Targeted	13.00	0.05	1.60	1.25	0.50	0.00	0.50	0.00	3.00	0.020
	Achieved	**12.95**	**0.05**	**1.55**	**1.29**	**0.46**	**0.01**	**0.43**	**0.01**	**2.91**	**0.023**
13	Targeted	13.00	0.50	0.70	5.00	0.50	0.00	0.00	0.20	3.00	0.020
	Achieved	**13.03**	**0.46**	**0.58**	**4.70**	**0.44**	**0.01**	**0.01**	**0.17**	**2.61**	**0.021**
14	Targeted	13.00	0.50	0.70	5.00	0.50	0.00	0.50	0.00	0.50	0.000
	Achieved	**12.94**	**0.48**	**0.74**	**4.77**	**0.50**	**0.01**	**0.57**	**0.01**	**0.55**	**0.000**
15	Targeted	13.00	0.50	1.60	1.25	0.05	0.15	0.00	0.20	3.00	0.000
	Achieved	**12.78**	**0.47**	**1.51**	**1.27**	**0.06**	**0.14**	**0.01**	**0.18**	**2.94**	**0.000**
16	Targeted	13.00	0.50	1.60	1.25	0.05	0.15	0.50	0.00	0.50	0.020
	Achieved	**12.86**	**0.41**	**1.63**	**1.21**	**0.06**	**0.14**	**0.44**	**0.01**	**0.46**	**0.024**

Table 2.6. Chemical composition of the alloys in the L_8 Taguchi Orthogonal Array.

Alloy No.		Composition (%)								
		Si	Mg	Fe	Cu	Ni	Cr	Mn	Ti	Zn
17	Targeted	8.00	0.10	1.00	2.50	0.05	0.00	0.00	0.00	1.00
	Achieved	**8.39**	**0.02**	**0.90**	**2.71**	**0.04**	**0.06**	**0.22**	**0.03**	**1.10**
18	Targeted	8.00	0.30	1.30	3.75	0.05	0.00	0.00	0.00	2.00
	Achieved	**8.19**	**0.02**	**0.91**	**3.87**	**0.03**	**0.04**	**0.17**	**0.03**	**2.20**
19	Targeted	9.00	0.30	1.00	2.50	0.05	0.00	0.00	0.00	2.00
	Achieved	**9.49**	**0.02**	**0.87**	**2.61**	**0.03**	**0.05**	**0.23**	**0.03**	**2.20**
20	Targeted	9.00	0.10	1.30	3.75	0.05	0.00	0.00	0.00	1.00
	Achieved	**9.50**	**0.09**	**1.43**	**4.00**	**0.13**	**0.06**	**0.21**	**0.05**	**1.10**
21	Targeted	10.00	0.10	1.30	2.50	0.05	0.00	0.00	0.00	2.00
	Achieved	**9.66**	**0.05**	**1.22**	**2.68**	**0.03**	**0.06**	**0.26**	**0.03**	**2.10**
22	Targeted	10.00	0.30	1.00	3.75	0.05	0.00	0.00	0.00	1.00
	Achieved	**9.69**	**0.05**	**1.05**	**4.54**	**0.04**	**0.06**	**0.27**	**0.03**	**1.20**
23	Targeted	11.00	0.30	1.30	2.50	0.05	0.00	0.00	0.00	1.00
	Achieved	**10.88**	**0.05**	**1.27**	**2.62**	**0.04**	**0.06**	**0.26**	**0.03**	**1.20**
24	Targeted	11.00	0.10	1.00	3.75	0.05	0.00	0.00	0.00	2.00
	Achieved	**10.93**	**0.05**	**1.02**	**5.06**	**0.12**	**0.06**	**0.24**	**0.05**	**2.20**

2.2 Specimen Production

The data that are presented in this book were obtained from specimens produced by the following procedure: one thousand pounds of each of the alloy compositions were melted and held in a clean graphite crucible in a typical melting/holding furnace. The specimens were produced on a 250-ton aluminum die casting machine. Prior to every die casting run, the die was preheated, and the first twenty shots were discarded to ensure specimen consistency. The shot profile was continuously monitored and recorded. A list of typical process parameters is shown in Table 2.7. All the test specimens were x-ray inspected and defective specimens were identified and discarded.

2.3 Material Characterization

Cooling Curves

Cooling curves for the alloys investigated were obtained using a *K*-type thermocouple placed at the center of a graphite mold cavity. The thermocouple was connected to a data acquisition system to record the thermal history. The mold and thermocouple set-up is shown in Figure 2.1. In each test 10 lbs. of alloy were melted in a gas-fired furnace in a 12-lb. capacity silicon carbide crucible. The melt was heated to 795±5°C. At this temperature the melt surface was drossed and the melt was transferred and poured into the mold using a 2 lb. ladle. The time elapsed during melt transfer and pouring was less than 10 seconds. In order to insure repeatability, three measurements were performed for each alloy.

Samples (0.5x0.5x0.25 inch) were sectioned from the area around the thermocouple tip at the center of each casting. The locations of the samples are shown in Figure 2.2. Optical microscopy and scanning electron microscopy (SEM) were used to analyze the morphology, size, and distribution of the various phases in each sample. The different phases and their compositions were also identified using EDX.

Differential Thermal Analysis

The Differential Thermal Analysis (DTA) samples were taken from a location that is next to the microstructure analysis sample, as shown in Figure 2.2. DTA measurements were conducted using a Perkin-Elmer DTA 1700 System equipped with a Thermal Analysis Data Station. The sample weight

Table 2.7. Die casting parameters used to produce the test specimens.

Casting Temperature	650°C (1200°F)
Cycle Time	20 seconds
Slow shot velocity	9.4 inches per second
Fast shot velocity	23.0 inches per second
Peak velocity	48-58 inches per second
Die close pressure	1,100 psi
Shot pressure	1,000 psi
Intensifying pressure	3,100 psi

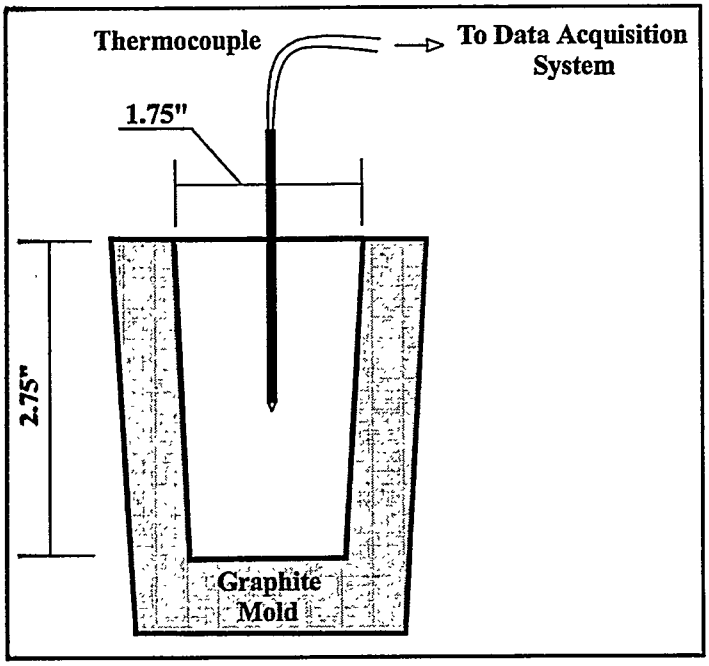

Fig. 2.1. The mold and thermocouple setup for the the thermal history measurement.

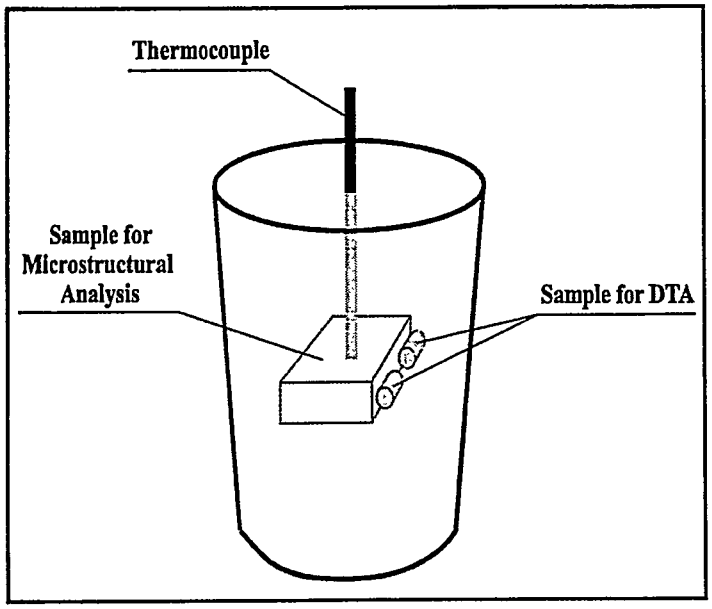

Fig. 2.2. The locations of the samples for microstructure analysis and DTA.

was between 60 and 70 mg, and the purge gas used was nitrogen at a flow rate of 40 cc/min. The sample was rapidly heated to 800°C and then the analysis was conducted at a cooling rate of 10°C/min.

Microstructure Analysis

Specimens cut from the die cast tensile bars were prepared for microstructure analysis using standard metallographic techniques. These techniques included mounting in Bakelite followed by grinding with silicon carbide paper and polishing with silica gel. When needed, specimens were etched with a 5% HF solution for 15 seconds. The specimens were examined using optical microscopy and scanning electron microscopy[1] (SEM). Energy Dispersive X-rays (EDX) was used to identify the various phases present in the structure and their chemical compositions. The fractured surfaces of the fatigue specimens were also examined using optical microscopy and scanning electron microscopy to identify the origins of the fatigue cracks.

2.4 Property Measurement

Mechanical Property Tests

Room Temperature Tensile Test

A minimum of thirty-five specimens from each alloy composition was used to determine the room temperature tensile properties of the alloys. The specimens were tested three months after they were produced. The tensile tests were conducted according to ASTM standard B557 [1] using the ASTM standard tensile specimen shown schematically in Figure 2.3. All tests were performed at room temperature using a Universal Testing[2] machine. Strain was measured using an axial extensometer[3] with a gage length of 2 inches. The extensometer was used until the specimen fractured and the testing machine ramp rate was 0.05 in/min. The data, in the form of load vs. displacement, was monitored using a strip chart plotter, and also stored in a personal computer. The data stored in the computer was analyzed using specially designed software to obtain tensile strength (TS), yield strength (YS), elongation (e), and modulus of elasticity (E).

[1] *JSM840 scanning electron microscope equipped with stage automated digital image analysis, a light element Quantum X-Ray detector with a Kevex Delta system, and a wavelength dispersive x-ray analyzer.*

[2] *Instron Servo-Hydraulic Tension-compression System model 1332 equipped with an 8500 controller and a 5620 pound load cell.*

[3] *MTS extensometer model 634.25.*

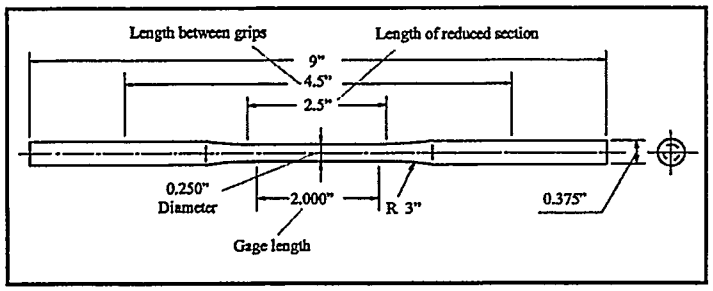

Fig. 2.3. ASTM Standard tensile test bar for die castings [1].

Elevated Temperature Tensile Test

A minimum of five specimens from each alloy composition was used to determine the elevated temperature tensile properties of the alloys at each of the elevated temperatures. The specimens were tested five months after they were produced. The tensile tests were conducted according to ASTM standard E21 [2] using the ASTM standard tensile specimen shown schematically in Figure 2.3. Tests were performed at two temperatures: 100°C and 200°C using a Universal Testing[4] machine. Strain was measured using a high temperature axial extensometer[5] with a gage length of 1 inch. The extensometer was used until the specimen fractured and the testing machine ramp rate was 0.05 in/min. The data, in the form of load vs. displacement, was monitored using a strip chart plotter, and also stored in a personal c/ uter. The data stored in the computer was analyzed using sp..ally designed software to obtain ultimate tensile strength (UTS), yield strength (YS)[6], elongation (e), and modulus of elasticity (E).

Specimens were heated to the test temperature, held at temperature, and tested to fracture in an environment chamber[7]. Three thermocouples were securely attached to the specimen's surface inside the reduced section. In addition, a fourth thermocouple was left in air inside the chamber in close proximity to the specimen. The readings of these four thermocouples were used to monitor the heating schedule. For tests at 100°C, the chamber preheating time was 60 minutes when the chamber was cold-started and then for each specimen the heating time was 20 minutes and the holding time was 20 min. For the tests at 200°C, the chamber preheating time was 90 minutes when the chamber was cold-started and then for each specimen the heating time was 40 minutes and the holding time was 20 min. The chamber temperature did not vary by more than ±3°C, and the temperature at the center of the specimen was within ±1°C of the desired test temperature. The temperature difference along the reduced section of the specimen was within ±1°C during holding and testing.

Fatigue Test

Two to five specimens from each alloy composition were tested at each stress level, and a minimum of six different stress levels was used to generate the fatigue curve for each o' ' alloys. Specimens were prepared according to ASTM st.. .dard E466 [3], which is shown in Figure 2.4. The grip sections of each specimen were machined to fit the fatigue machine and to ensure proper alignment. The reduced section of the specimens was kept in the as-cast condition; however, the parting line flash was removed with a fine file. After removing the parting line flash, the specimens were polished in a longitudinal direction with 800 grit silicon carbide paper followed by 1200 grit silicon carbide paper. Specimen testing was started three months after the specimens were produced and lasted approximately twelve months. All tests were performed at room temperature using R. R. Moore Rotating–Bending Fatigue machines. A schematic representation of the R. R. Moore Rotating–Bending Fatigue machine is shown in Figure 2.5.

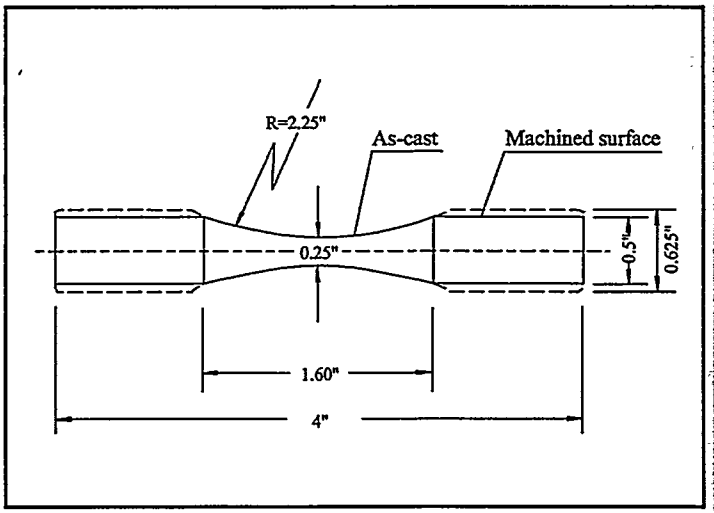

Fig. 2.4. Schematic of fatigue test specimen.

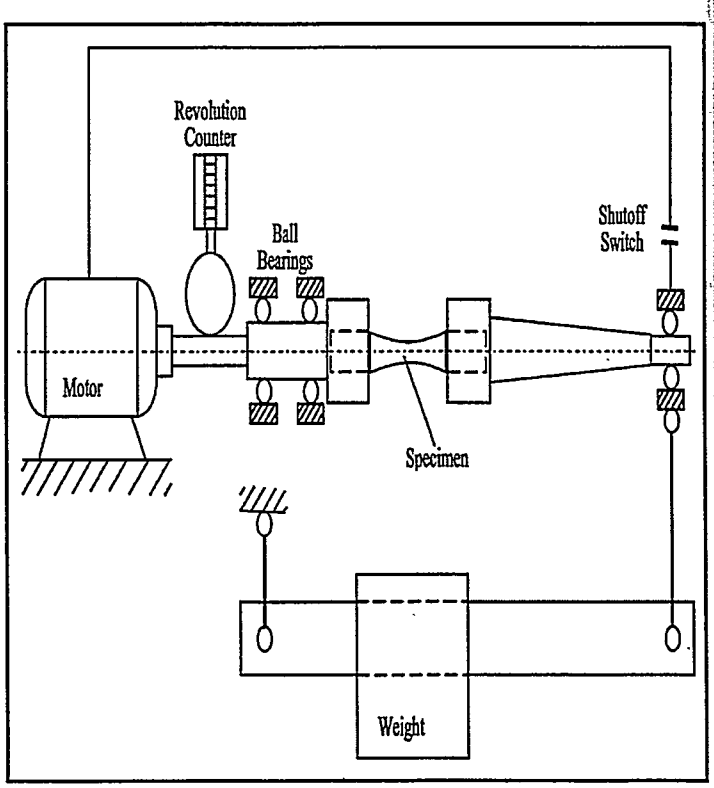

Fig. 2.5. Schematic diagram of a R.R. Moore Rotating Bending Test Machine.

[4] *Instron model 1332 equipped with an 8500 controller and a 5620 pound load cell.*

[5] *MTS high temperature extensometer Model 633.11B-15.*

[6] *Since it is difficult to discern the stress at which yielding occurs in these alloys, the 0.2% offset method was used to determine the yield point.*

[7] *Instron environment chamber Model 3116.*

Four identical machines were used, and specimens were tested randomly on all four machines. The tests were conducted according to established standards and the rotation speed used was approximately 7500 rpm.

Although many analysis procedures are available for describing stress vs. number of Cycles (*S/N*) curves, none of those procedures is universally accepted and applied. The procedure best suited for a particular experiment depends to a large extent on the characteristics of the raw data and on the objectives of the analysis. The general mathematical model used to represent the mean *S/N* curves presented in this book is [4].

$$Log\ N = A_o + A_1 \times Log\ (S_{max} - S_o) \quad (2.1)$$

Where A_0, A_1, and S_o are constants that are calculated using an iterative least square technique. It can be easily seen from Equation 2.1 that when $S_{max} \longrightarrow S_o$, $N \longrightarrow \infty$. Therefore, S_o is the endurance limit, or fatigue life of the alloy for the given test conditions. Nonlinear regression analysis was used to derive the particular curve that best fits the *S/N* data for each alloy. One of the most important issues in performing regression analysis on fatigue data is the treatment of "*runouts*". The term "*runout*" refers to data points where the number of fatigue cycles recorded did not cause failure under the imposed stress level. In this study, the experiment was stopped when the number of cycles exceeded 5×10^7 and the specimen did not fail. For each alloy, three or more such runouts were recorded. At least five procedures have been proposed for treating runouts [4, 5]. In this work the two step process [4, 5] was used to treat the runouts. In this process a trial analysis is performed with all runouts excluded and a mean *S/N* curve is derived. Subsequently, the analysis is repeated with all the runouts which fell above the mean curve obtained from the trial analysis.

Impact Test

The impact test is a dynamic fracture test that measures the alloy's fracture toughness. The data reported in this book were obtained from a Charpy Impact Test, which is the standard test for aluminum die casting alloys. Testing was performed according to ASTM standard E23 [6]. The fracture toughness measured in this test is the energy absorbed by the specimen in fracture under a dynamic load, which is also called absorbed energy, fracture energy, and impact energy. A simple beam, pendulum type, Charpy Impact apparatus was used. The weight of the pendulum was 24 lbs. and the distance from the axis of rotation to the center of strike in the specimen was 1.0253 ft. The impact velocity was about 16 ft/s. and the potential energy of the system was measured and found to be 24.0498 lb.ft. The machine had an analogue scale graduated in degrees, and the reading accuracy was ±0.05°. The geometry and dimensions of the standard specimen used is shown in Figure 2.6. Testing started eight months after the specimens were die cast and lasted for about one month. The tests were conducted at room temperature, which was about 77°F. Forty-five specimens were tested for each alloy composition.

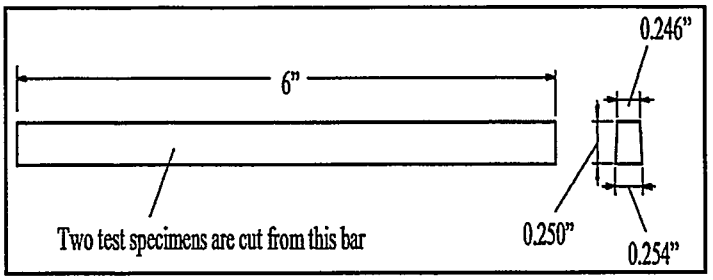

Fig. 2.6. Standard simple beam impact test bar for die casting alloys.

Wear Resistance Test

The standard Dry Sand Abrasive Test described in ASTM standard G65 was used. A schematic of the apparatus is shown in Figure 2.7. The test involves abrading a standard test specimen with silica grit of controlled size and composition. The abrasive is introduced between the test specimen and a rotating wheel with a rubber rim of a specified hardness. The test specimen is pressed against the rotating wheel with a specified force by means of a lever arm while a controlled flow of grit abrades the test surface. The volume loss from the sample is the measure of the wear resistance. The test parameters used are shown in Table 2.8. For each alloy five specimens were tested between 4 to 6 months after they were produced.

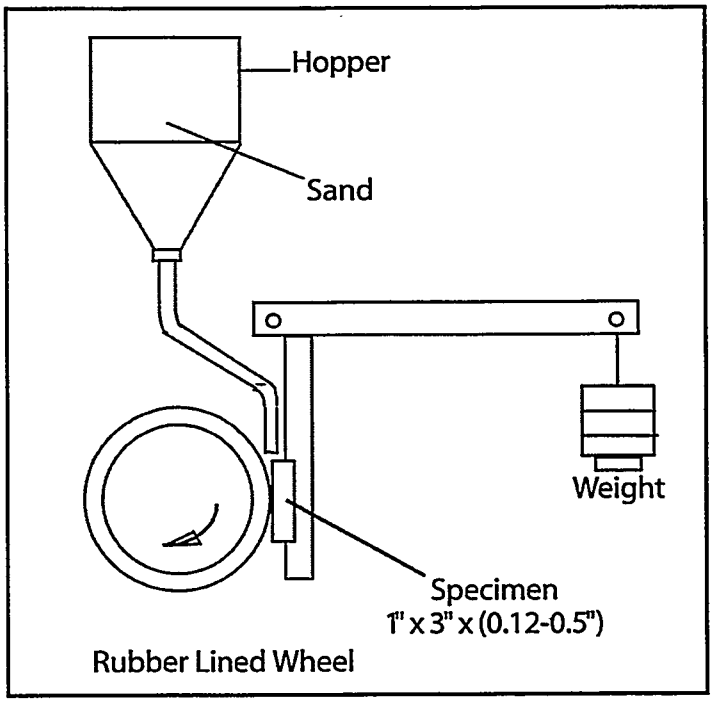

Fig. 2.7. Schematic of the Dry Sand Abrasive Test apparatus.

Hardness Test

Hardness measurements were performed according to ASTM standard E18. The test was performed on a Rockwell Hardness Tester[8], with a 1/16 inch ball and 100 kg load. The Rockwell Hardness Scale B was used. For each alloy, three groups of specimens, each consisting of 10 identical die cast

[8] *Model 3JR.*

Table 2.8. Wear resistance test parameters.

Test Machine	**FALEX Abrasive Tester**
Sample size	**1" x 3" x 0.25"**
Wheel diameter	**9"**
Wheel width	**0.5"**
Wheel hardness	**Durometer A-90**
Wheel speed	**200 rpm**
Test duration	**10 minutes**
Linear abrasive	**4713 ft.**
Test load	**30 lb.**
Abrasive	**AFS 50-70 test sand**
Sand flow rate	**0.74 lb./min.**

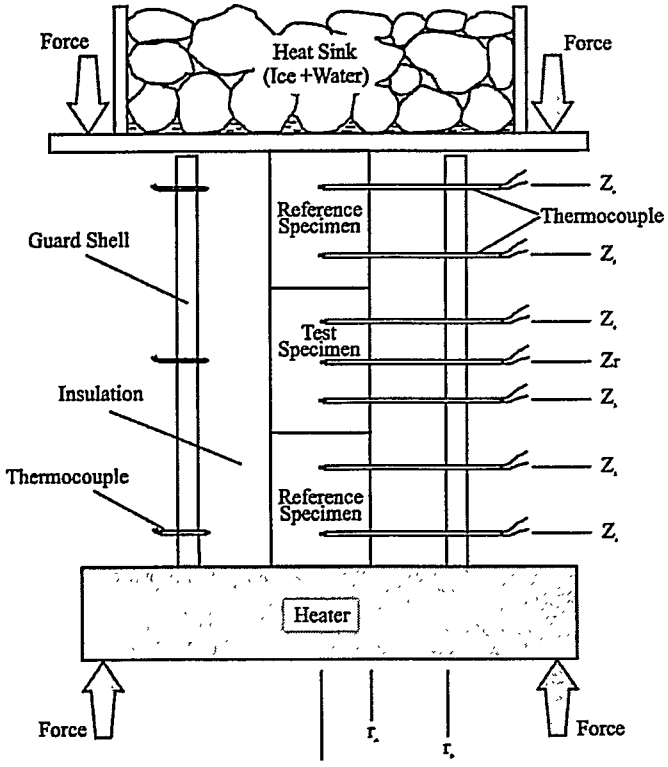

Fig. 2.8. Schematic of apparatus for thermal conductivity measurement using Guarded-Comparative-Longitudinal Heat Flow Technique.

samples, were tested. Each group of specimens represented a different cross sectional area. Group 1 specimens were obtained from the grip sections of the tensile test bars, and the hardness was measured at the location where the diameter is 3/8 inch. Group 2 specimens were obtained from the Charpy impact test bars. These had a square cross section of edge of 1/4 inch. Group 3 specimens were obtained from the grip sections of the fatigue test bars, and the hardness was measured at the location where the diameter is 5/8 inch. Each specimen was tested for hardness 10 times during the first month after it was die cast.

Physical Property Measurements

Specific Gravity Measurements

Archimedes' Principle was used to measure the specific gravity of typical specimens cut from the alloys. The average specific gravity reported for each alloy is obtained from five measurements performed on five different specimens.

Thermal Conductivity Measurements

A minimum of three specimens from each alloy composition were used to determine the room temperature thermal conductivity of the alloys, and each specimen was tested five times. The specimens were tested in the as-cast condition approximately six months after they were produced. Thermal conductivity measurements were conducted according to ASTM standard E1225 [7] using the apparatus shown schematically in Figure 2.8.

The reference material was graphite[9] and had a thermal conductivity of 91.3 W/m.K at 25°C. The thermocouples used were 0.0 inches *K*-type with a closed end stainless steel shield.

Electrical Conductivity Measurements

ASTM standard B109 was used to measure the electrical resistivity of the specimens. The specimens were machined from the tensile test bars to a diameter of 0.200 inch and a length of 8.25 inch[10]. The specimens had a uniform cross section throughout their length and the cross sectional area varied by no more than ±0.75%.

References

1. *ASTM Standard B557 "Standard Methods of Tension Testing Wrought and Cast Aluminum and Magnesium Alloy Products", Annual Book ASTM Standard, Vol. 02.02, 1993.*
2. *ASTM Standard E21 "Elevated Temperature Tensile Test of Metallic Materials", Annual Book of ASTM Standard, Vol. 03.01, 1993.*
3. *ASTM Standard E466 "Standard Practice for Conducting Force Controlled Constant Amplitude Axial Fatigue Test of Metallic Materials", Annual Book of ASTM Standard, Vol. 03.01, 1993.*
4. *J. B. Conway and L. H. Sjodahl, Analysis and Representation of Fatigue Data, ASM International, Materials Park, Ohio, 1991.*
5. *R. C. Rice, "Fatigue Data Analysis", Metals Handbook, Vol. 8, Mechanical Testing, Ninth Edition, 1985, p695-720.*
6. *ASTM Standard E23 "Standard Test Methods for Notched Bar Impact Testing of Metallic Materials", Annual Book of ASTM Standard, Vol. 03.01, 1993.*
7. *ASTM Standard E1225 "Standard Test Method for Thermal Conductivity of Solids by Means of the Guarded-Comparative-Longitudinal Heat Flow Technique", Annual Book of ASTM Standard, Vol. 14.02, 1993.*

[9] *Reference Material SRM8426 purchased from US National Institute for Standards and Technology.*

[10] *ASTM standard B109 suggests a specimen length of at least 12 inches. The standard does not specify what effects the length has on the accuracy of the measurements, but it suggests a 12-inch specimen length to ensure a resistance of more than 0.00001 Ω in the test length between the potentiometer contacts. The specimens that were used were 8.25 inches in length but had a resistance in the range of 0.0003 - 0.0005 Ω, which satisfies the standard's requirement on resistivity.*

CHAPTER 3:

ATLAS OF MICROSTRUCTURES AND PROPERTIES OF ALUMINUM DIE CASTING ALLOYS

Actual (Achieved) *Compositions.*

Alloy No.	Composition (%)									
	Si	Mg	Fe	Cu	Ni	Cr	Mn	Ti	Zn	Sr
1	7.15	0.03	0.68	1.24	0.01	0.01	0.01	0.01	0.44	0.000
2	6.99	0.01	0.56	1.15	0.01	0.01	0.47	0.24	2.87	0.018
3	6.98	0.04	1.49	4.99	0.44	0.13	0.01	0.01	0.47	0.018
4	6.94	0.04	1.48	4.74	0.47	0.15	0.45	0.16	2.69	0.000
5	7.05	0.44	0.67	1.18	0.53	0.14	0.01	0.01	2.76	0.000
6	6.98	0.44	0.57	1.13	0.48	0.13	0.45	0.18	0.38	0.018
7	6.92	0.50	1.63	4.94	0.03	0.01	0.02	0.01	2.73	0.022
8	6.79	0.46	1.49	4.77	0.01	0.01	0.45	0.20	0.42	0.000
9	12.71	0.05	0.63	4.96	0.06	0.14	0.01	0.20	0.50	0.017
10	12.69	0.03	0.73	5.09	0.07	0.11	0.37	0.01	2.73	0.000
11	12.86	0.04	1.59	1.21	0.45	0.01	0.01	0.18	0.49	0.000
12	12.95	0.05	1.55	1.29	0.46	0.01	0.43	0.01	2.91	0.023
13	13.03	0.46	0.58	4.70	0.44	0.01	0.01	0.17	2.61	0.021
14	12.94	0.48	0.74	4.77	0.50	0.01	0.57	0.01	0.55	0.000
15	12.78	0.47	1.51	1.27	0.06	0.14	0.01	0.18	2.94	0.000
16	12.86	0.41	1.63	1.21	0.06	0.14	0.44	0.01	0.46	0.024
17	8.39	0.02	0.90	2.71	0.04	0.06	0.22	0.03	1.10	---
18	8.19	0.02	0.91	3.87	0.03	0.04	0.17	0.03	2.20	---
19	9.49	0.02	0.87	2.61	0.03	0.05	0.23	0.03	2.20	---
20	9.50	0.09	1.43	4.00	0.13	0.06	0.21	0.05	1.10	---
21	9.66	0.05	1.22	2.68	0.03	0.06	0.26	0.03	2.10	---
22	9.69	0.05	1.05	4.54	0.04	0.06	0.27	0.03	1.20	---
23	10.88	0.05	1.27	2.62	0.04	0.06	0.26	0.03	1.20	---
24	10.93	0.05	1.02	5.06	0.12	0.06	0.24	0.05	2.20	---

Alloy #1	Wt.%	Si	Mg	Fe	Cu	Ni	Cr	Mn	Ti	Zn	Sr	Al
		7.15	0.03	0.68	1.24	0.01	0.01	0.01	0.01	0.44	0.00	Balance

Tensile	Strength	Ultimate	25°C	Ksi	39.6±0.9
				MPa	273.0±6.2
			100°C	Ksi	32.9±1.0
				MPa	227.0±6.9
			200°C	Ksi	20.2±0.2
				MPa	139.0±1.1
		Yield	25°C	Ksi	16.6±0.4
				MPa	114.5±2.8
			100°C	Ksi	16.8±0.5
				MPa	115.8±3.2
			200°C	Ksi	14.5±0.3
				MPa	100.0±2.2
	Elongation		25°C	%	5.85±0.97
			100°C	%	10.49±2.03
			200°C	%	19.35±2.71
	Modulus of Elasticity		25°C	10^3 Ksi	10.54±1.02
				10^3 MPa	72.64±7.06
			100°C	10^3 Ksi	7.77±0.88
				10^3 MPa	53.57±6.03
			200°C	10^3 Ksi	7.47±0.68
				10^3 MPa	51.50±4.68
Endurance Limit	100,000,000 cycles		25°C	Ksi	15.40
				MPa	106.18
	500,000,000 cycles		25°C	Ksi	14.96
				MPa	103.15
Impact Resistance	Absorbed Energy		25°C	Joules	6.83±0.58
				lb.ft.	5.04±0.43
Wear Resistance	Volume Loss		25°C	cm^3	0.3883±0.0220
Hardness	¼ × ¼ inch flat die casting		25°C	RHB	29.9±2.1
	3/8 inch diameter die casting		25°C	RHB	16.9±3.7
	5/8 inch diameter die casting		25°C	RHB	19.8±1.6
Thermal Conductivity			25°C	W/m.K	137.1±1.0
Electrical Conductivity			25°C	% IACS	30.71±0.19
Electrical Resistivity			25°C	10^{-8} Ωm	5.614±0.035
Specific Gravity			25°C	g/cm^3	2.720

ALLOY 1

Alloy #1	Wt.%	Si	Mg	Fe	Cu	Ni	Cr	Mn	Ti	Zn	Sr	Al
		7.15	0.03	0.68	1.24	0.01	0.01	0.01	0.01	0.44	0.00	Balance

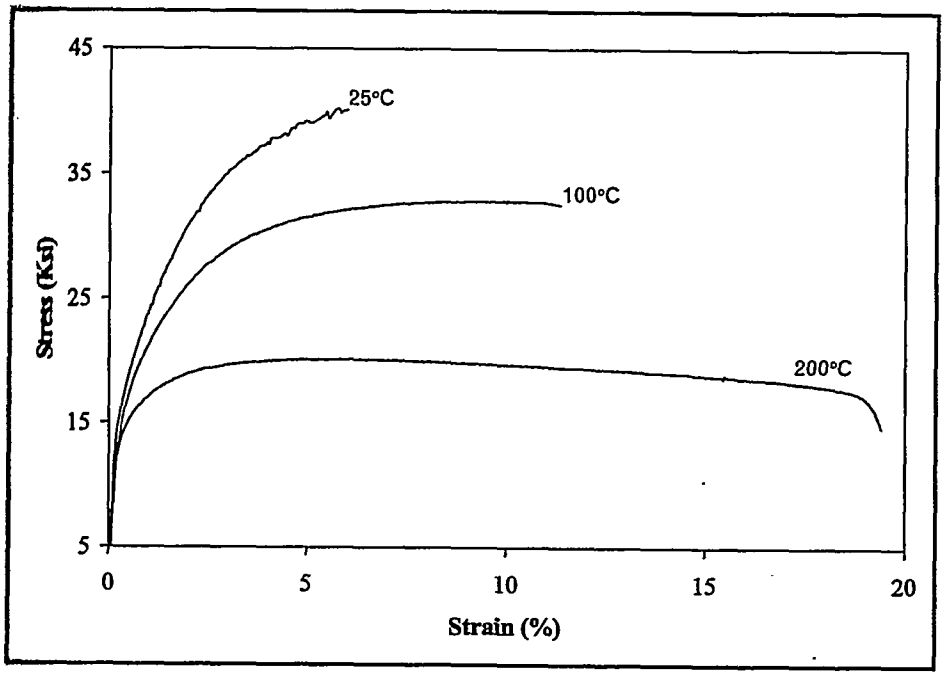

Fig. 3.1.1. Typical stress vs strain curves for Alloy 1 at temperatures of 25°C, 100 °C, and 200 °C.

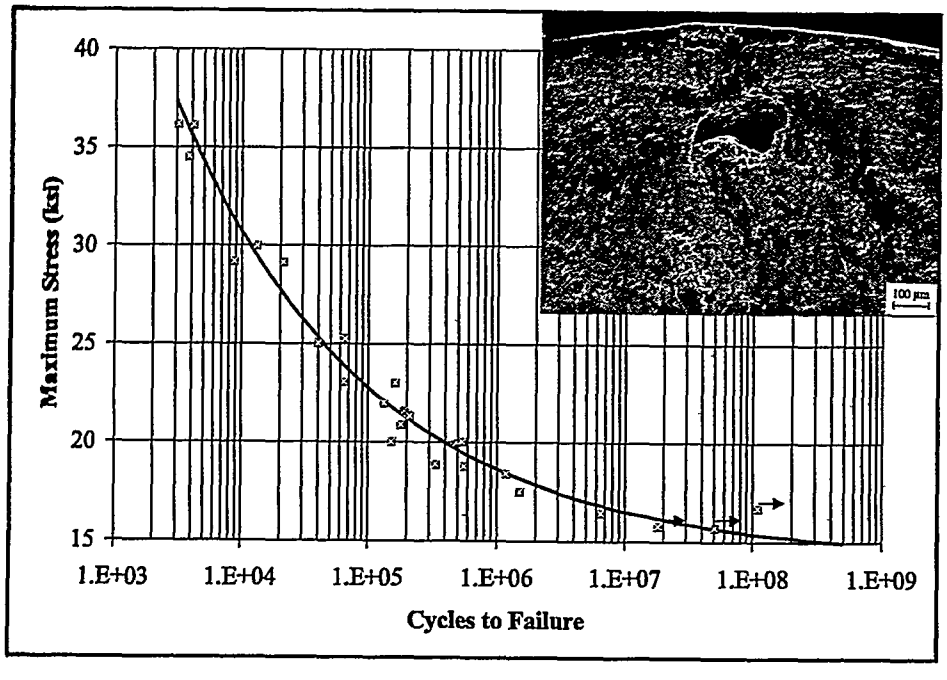

Fig. 3.1.2. S/N curve for Alloy 1; the fracture surface shown is from the specimen which failed at 6.5 x 10^5 cycles under a maximum stress of 16.4 ksi.

ALLOY 1

Alloy #1	Wt.%	Si	Mg	Fe	Cu	Ni	Cr	Mn	Ti	Zn	Sr	Al
		7.15	0.03	0.68	1.24	0.01	0.01	0.01	0.01	0.44	0.00	Balance

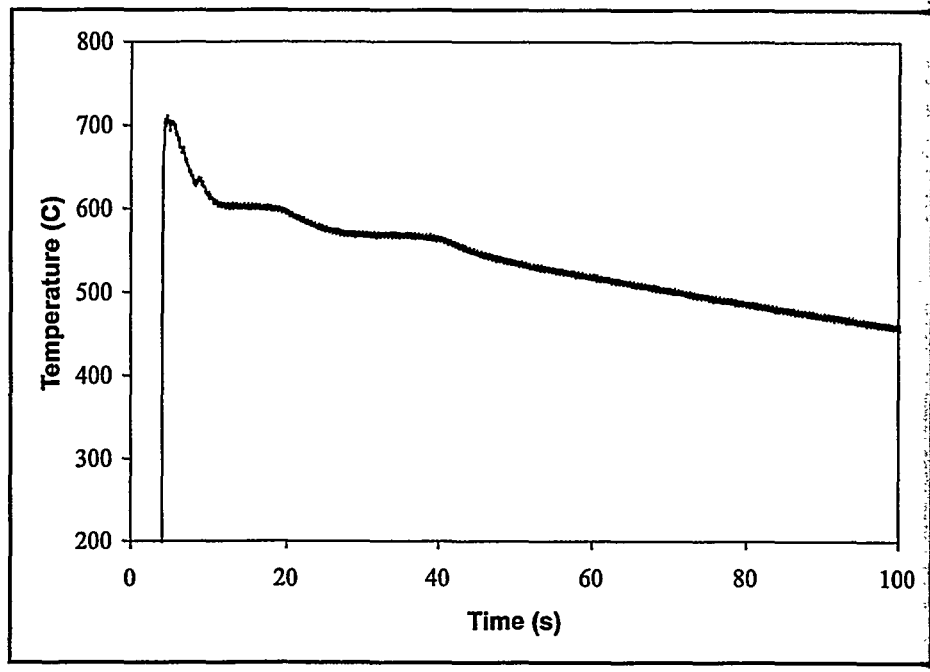

Fi .3. Thermal history of Alloy 1 cast in a graphite ...old.

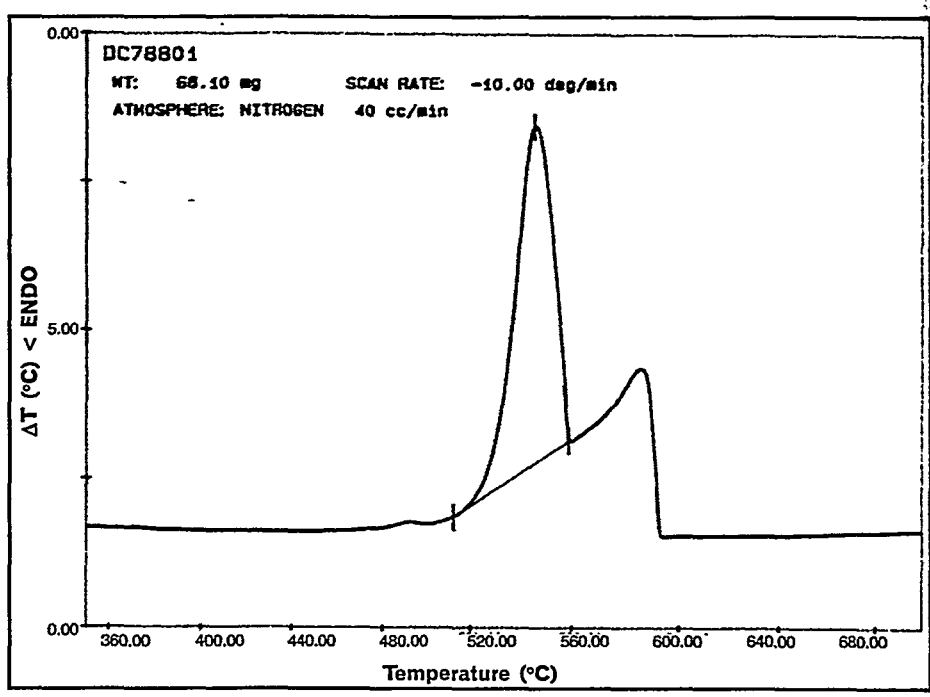

Fig. 3.1.4. DTA curve for Alloy 1 cooled at 10 °C/min.

ALLOY 1

Alloy #2	Wt.%	Si	Mg	Fe	Cu	Ni	Cr	Mn	Ti	Zn	Sr	Al
		6.99	0.01	0.56	1.15	0.01	0.01	0.47	0.24	2.87	0.018	Balance

Tensile	Strength	Ultimate	25°C	Ksi	42.4±0.8
				MPa	292.3±5.5
			100°C	Ksi	36.5±0.4
				MPa	251.4±2.4
			200°C	Ksi	22.1±0.2
				MPa	152.2±1.5
		Yield	25°C	Ksi	20.0±0.4
				MPa	137.9±2.8
			100°C	Ksi	19.7±0.4
				MPa	135.7±2.6
			200°C	Ksi	17.3±0.3
				MPa	119.1±1.9
	Elongation		25°C	%	7.43±1.18
			100°C	%	11.53±2.16
			200°C	%	14.77±0.90
	Modulus of Elasticity		25°C	10^3 Ksi	10.92±0.75
				10^3 MPa	75.26±5.19
			100°C	10^3 Ksi	8.93±0.49
				10^3 MPa	61.54±3.39
			200°C	10^3 Ksi	7.37±0.53
				10^3 MPa	50.80±3.66
Endurance Limit	100,000,000 cycles		25°C	Ksi	19.12
				MPa	131.83
	500,000,000 cycles		25°C	Ksi	19.05
				MPa	131.35
Impact Resistance	Absorbed Energy		25°C	Joules	8.78±0.78
				lb.ft.	6.48±0.57
Wear Resistance	Volume Loss		25°C	cm^3	0.4187±0.0288
Hardness	¼ × ¼ inch flat die casting		25°C	RHB	33.8±2.1
	3/8 inch diameter die casting		25°C	RHB	22.5±2.1
	5/8 inch diameter die casting		25°C	RHB	21.2±2.1
Thermal Conductivity			25°C	W/m.K	115.5±1.1
Electrical Conductivity			25°C	% IACS	26.21±1.53
Electrical Resistivity			25°C	10^{-8} Ωm	6.578±0.384
Specific Gravity			25°C	g/cm^3	2.778

ALLOY 2

Alloy #2	Wt.%	Si	Mg	Fe	Cu	Ni	Cr	Mn	Ti	Zn	Sr	Al
		6.99	0.01	0.56	1.15	0.01	0.01	0.47	0.24	2.87	0.018	Balance

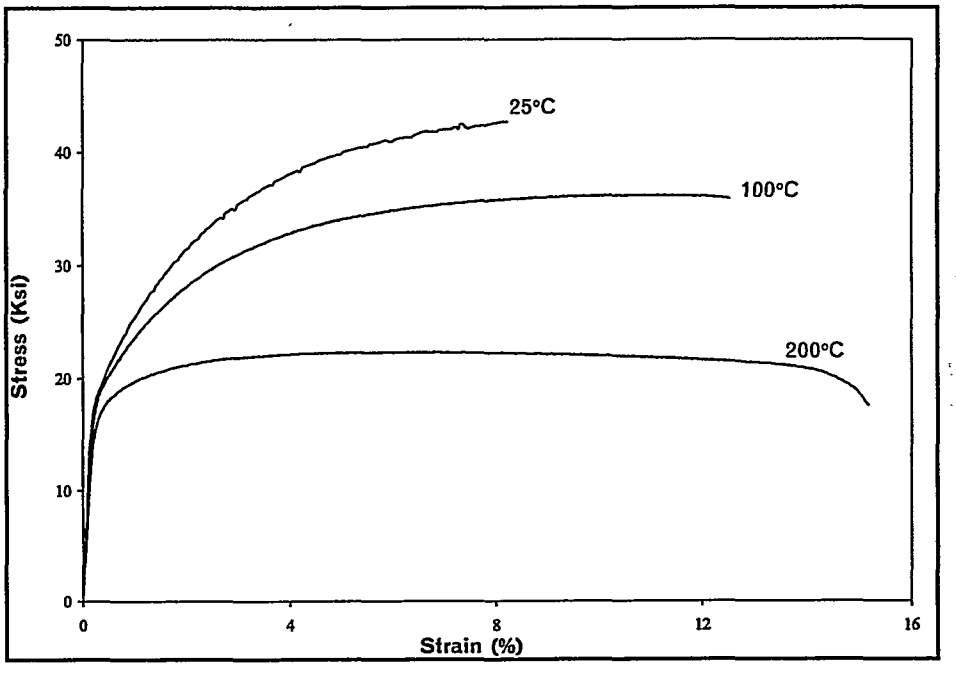

Fig. ___.1. Typical stress vs strain curves for Alloy 2 at temperatures of 25°C, 100 °C, and 200 °C.

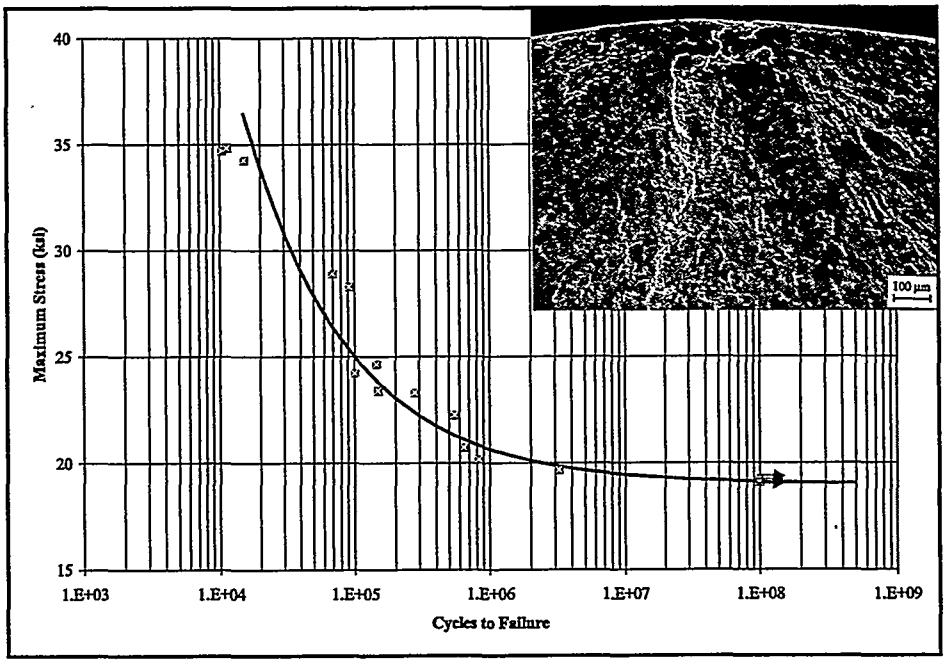

F_ ___2.2. S/N curve for Alloy 2; the fracture surface shown is from the specimen which failed at 2.8 x 10^5 cycles under a maximum stress of 25.3 ksi.

ALLOY 2

Alloy #2	Wt.%	Si	Mg	Fe	Cu	Ni	Cr	Mn	Ti	Zn	Sr	Al
		6.99	0.01	0.56	1.15	0.01	0.01	0.47	0.24	2.87	0.018	Balance

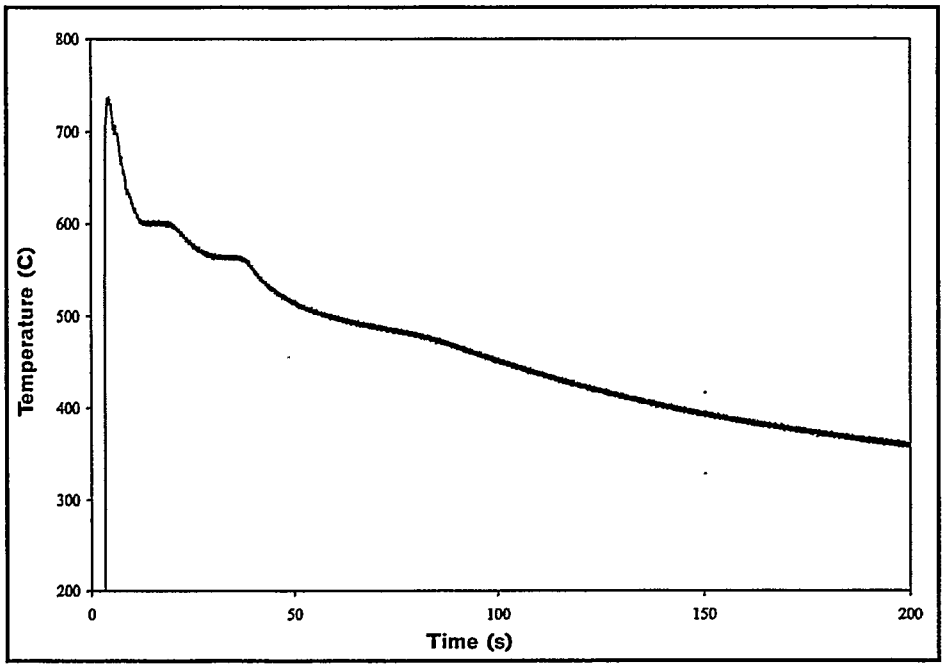

Fig. 3.2.3. Thermal history of Alloy 2 cast in a graphite mold.

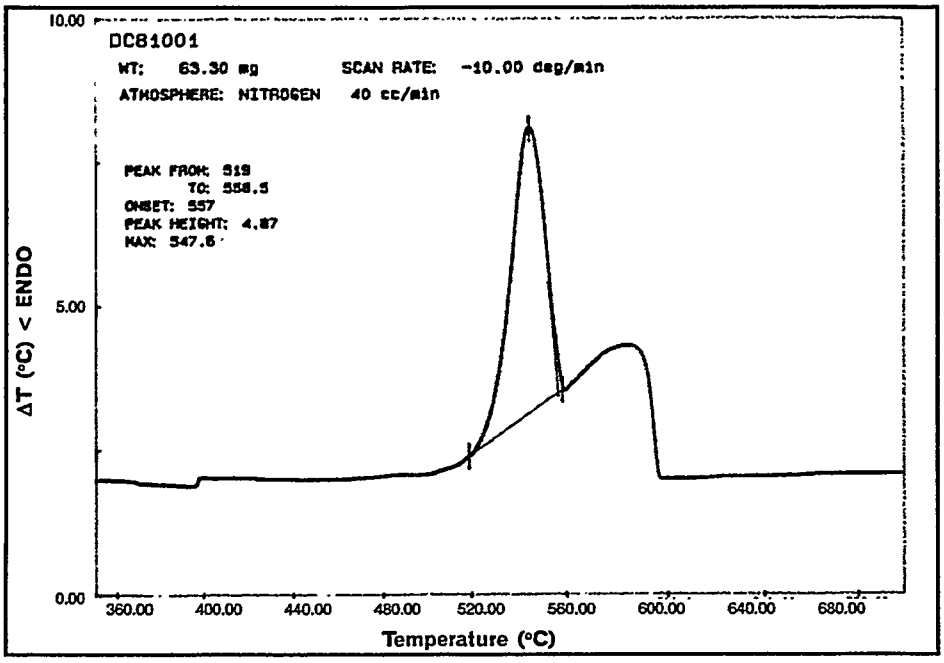

Fig. 3.2.4. DTA curve for Alloy 2 cooled at 10 °C/min.

ALLOY 2

Alloy #3	Wt.%	Si	Mg	Fe	Cu	Ni	Cr	Mn	Ti	Zn	Sr	Al
		6.98	0.04	1.49	4.99	0.44	0.13	0.01	0.01	0.47	0.018	Balance

Tensile	Strength	Ultimate	25°C	Ksi	45.4±1.0
				MPa	313.0±6.9
			100°C	Ksi	42.6±0.4
				MPa	293.5±2.8
			200°C	Ksi	30.2±0.2
				MPa	208.5±1.1
		Yield	25°C	Ksi	24.8±0.3
				MPa	171.0±2.1
			100°C	Ksi	24.8±0.4
				MPa	171.0±2.9
			200°C	Ksi	21.5±0.2
				MPa	148.2±1.3
	Elongation		25°C	%	2.08±0.23
			100°C	%	2.92±0.40
			200°C	%	5.00±0.78
	Modulus of Elasticity		25°C	10^3 Ksi	11.26±0.75
				10^3 MPa	77.65±5.20
			100°C	10^3 Ksi	8.94±0.32
				10^3 MPa	61.60±2.18
			200°C	10^3 Ksi	7.94±0.31
				10^3 MPa	54.74±2.13
Endurance Limit	100,000,000 cycles		25°C	Ksi	16.68
				MPa	115.00
	500,000,000 cycles		25°C	Ksi	16.41
				MPa	113.14
Impact Resistance	Absorbed Energy		25°C	Joules	2.27±0.35
				lb.ft.	1.68±0.26
Wear Resistance	Volume Loss		25°C	cm^3	0.4527±0.0370
Hardness	¼ × ¼ inch flat die casting		25°C	RHB	60.9±1.3
	3/8 inch diameter die casting		25°C	RHB	53.7±2.9
	5/8 inch diameter die casting		25°C	RHB	54.1±1.2
Thermal Conductivity			25°C	W/m.K	117.1±0.6
Electrical Conductivity			25°C	% IACS	26.6±0.21
Electrical Resistivity			25°C	10^{-8} Ωm	6.481±0.051
Specific Gravity			25°C	g/cm^3	2.819

ALLOY 3

Alloy #3	Wt.%	Si	Mg	Fe	Cu	Ni	Cr	Mn	Ti	Zn	Sr	Al
		6.98	0.04	1.49	4.99	0.44	0.13	0.01	0.01	0.47	0.018	Balance

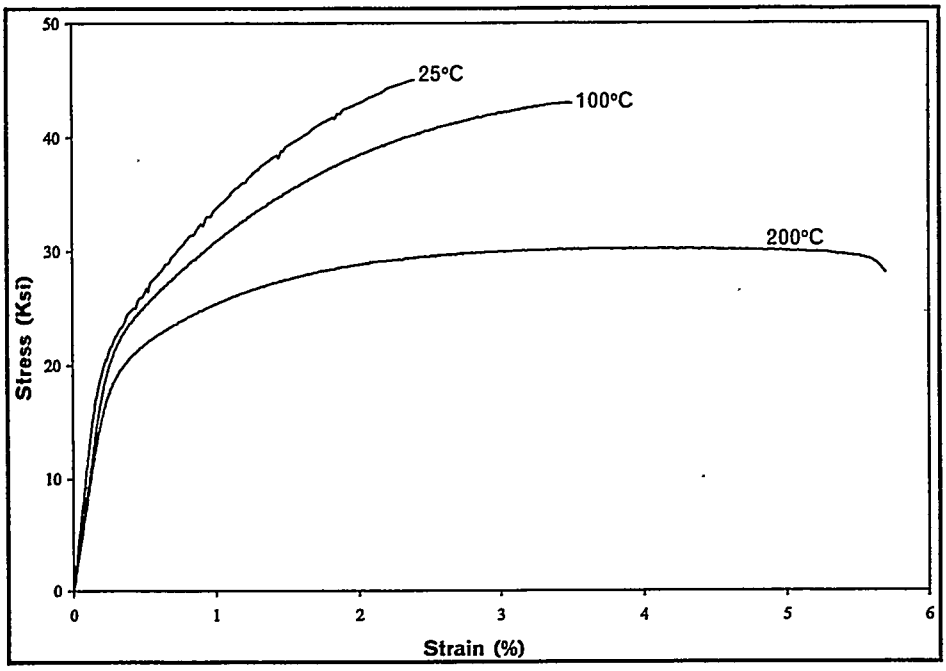

Fig. 3.3.1. Typical stress vs strain curves for Alloy 3 at temperatures of 25°C, 100 °C, and 200 °C.

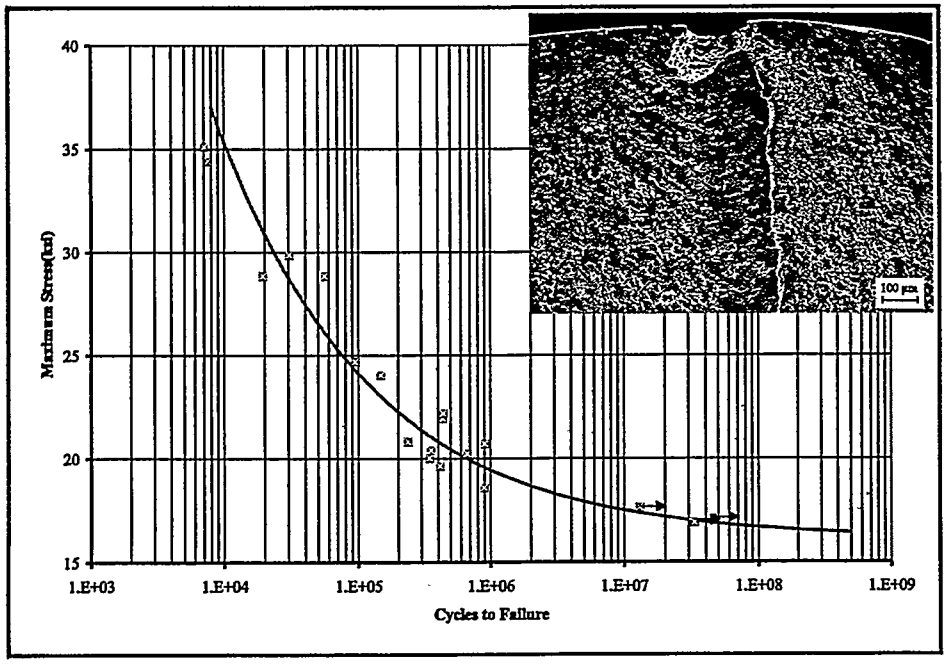

Fig. 3.3.2. S/N curve for Alloy 3; the fracture surface shown is from the specimen which failed at 6.7 x 10⁵ cycles under a maximum stress of 20.3 ksi.

ALLOY 3

Alloy #3	Wt.%	Si	Mg	Fe	Cu	Ni	Cr	Mn	Ti	Zn	Sr	Al
		6.98	0.04	1.49	4.99	0.44	0.13	0.01	0.01	0.47	0.018	Balance

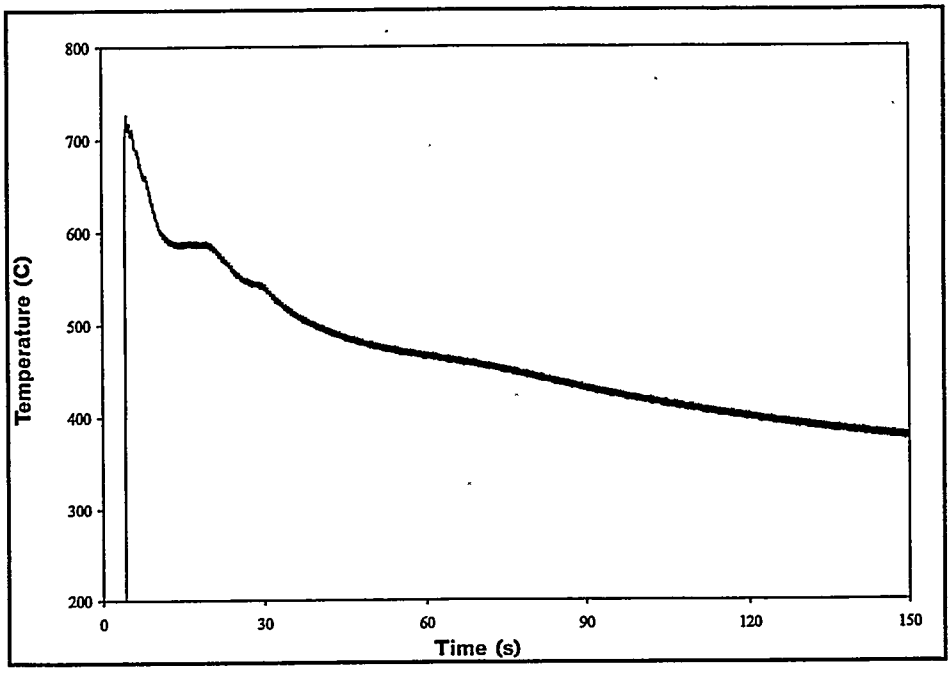

3.3. Thermal history of Alloy 3 cast in a graphite

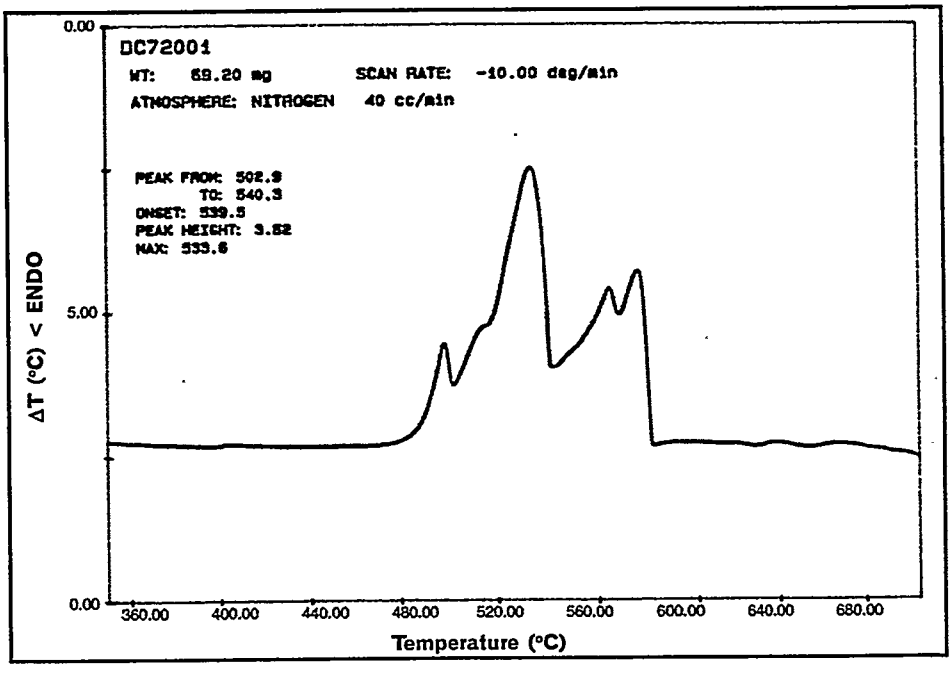

Fig. 3.3.4. DTA curve for Alloy 3 cooled at 10 °C/min.

ALLOY 3

Alloy #4	Wt.%	Si	Mg	Fe	Cu	Ni	Cr	Mn	Ti	Zn	Sr	Al
		6.94	0.04	1.48	4.74	0.47	0.15	0.45	0.16	2.69	0.00	Balance

Tensile	Strength	Ultimate	25°C	Ksi	47.0±0.9
				MPa	324.1±6.2
			100°C	Ksi	42.9±0.5
				MPa	295.9±3.7
			200°C	Ksi	31.2±0.4
				MPa	215.0±2.8
		Yield	25°C	Ksi	25.5±0.4
				MPa	175.8±2.8
			100°C	Ksi	24.9±0.4
				MPa	172.0±2.6
			200°C	Ksi	24.0±0.2
				MPa	165.6±1.1
	Elongation		25°C	%	2.81±0.29
			100°C	%	4.10±0.78
			200°C	%	5.12±0.86
	Modulus of Elasticity		25°C	10^3 Ksi	11.08±0.75
				10^3 MPa	76.39±5.15
			100°C	10^3 Ksi	8.72±0.16
				10^3 MPa	60.10±1.08
			200°C	10^3 Ksi	8.06±0.32
				10^3 MPa	55.60±2.24
Endurance Limit	100,000,000 cycles		25°C	Ksi	20.47
				MPa	141.14
	500,000,000 cycles		25°C	Ksi	20.33
				MPa	140.17
Impact Resistance	Absorbed Energy		25°C	Joules	2.43±0.32
				lb.ft.	1.78±0.24
Wear Resistance	Volume Loss		25°C	cm^3	0.4333±0.0322
Hardness	¼ × ¼ inch flat die casting		25°C	RHB	60.4±1.0
	3/8 inch diameter die casting		25°C	RHB	52.7±1.5
	5/8 inch diameter die casting		25°C	RHB	56.0±0.8
Thermal Conductivity			25°C	W/m.K	108.4±0.8
Electrical Conductivity			25°C	% IACS	22.56±0.22
Electrical Resistivity			25°C	10^{-8} Ωm	7.642±0.075
Specific Gravity			25°C	g/cm^3	2.866

ALLOY 4

Alloy #4	Wt.%	Si	Mg	Fe	Cu	Ni	Cr	Mn	Ti	Zn	Sr	Al
		6.94	0.04	1.48	4.74	0.47	0.15	0.45	0.16	2.69	0.00	Balance

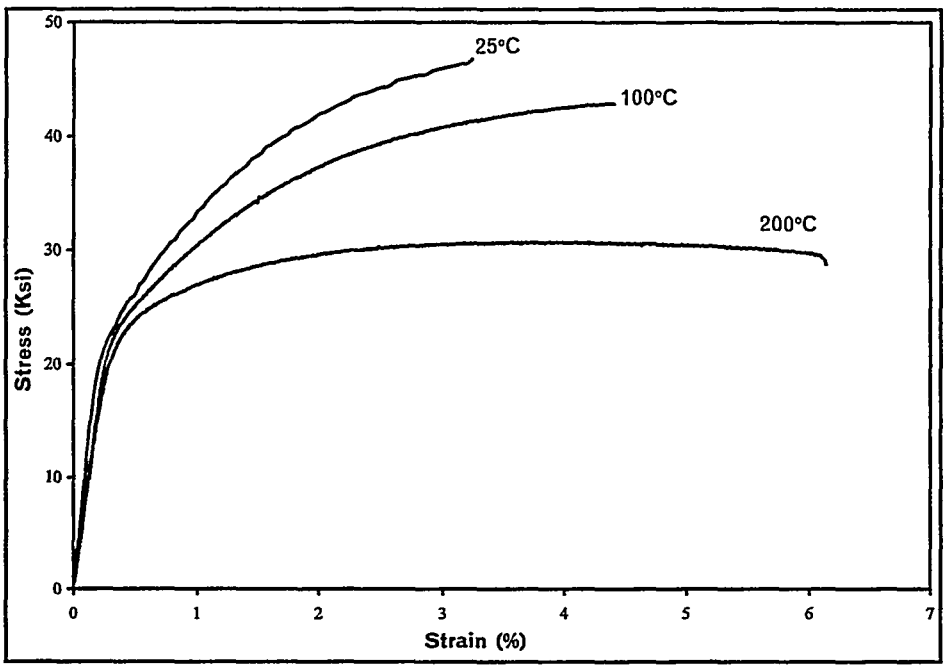

).4.1. Typical stress vs strain curves for Alloy 4 at temperatures of 25°C, 100 °C, and 200 °C.

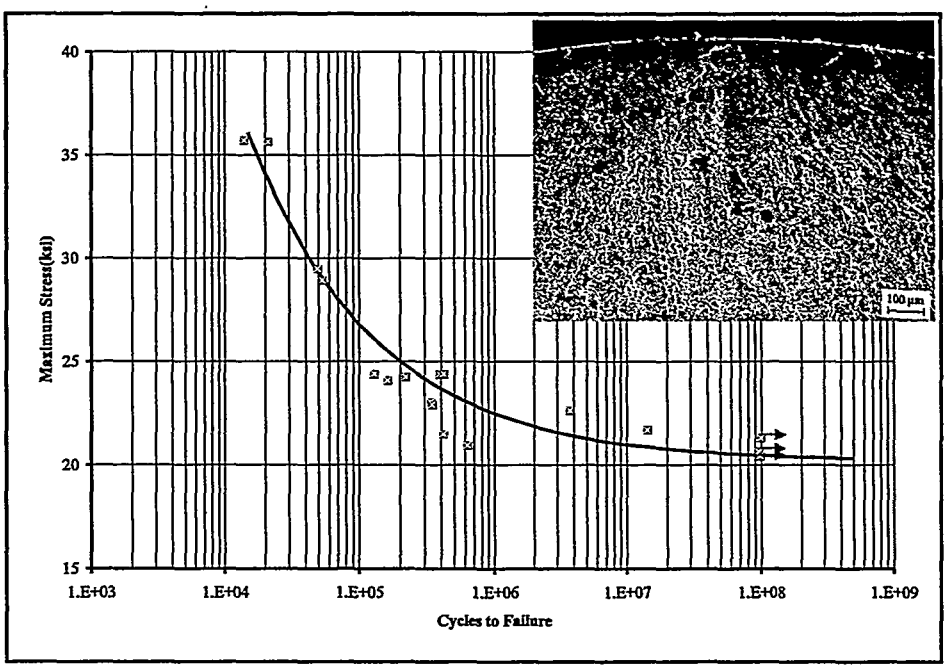

3.4.2. S/N curve for Alloy 4; the fracture surface ..own is from the specimen which failed at 1.4 x 10^7 cycles under a maximum stress of 21.7 ksi.

ALLOY 4

Alloy #4	Wt.%	Si	Mg	Fe	Cu	Ni	Cr	Mn	Ti	Zn	Sr	Al
		6.94	0.04	1.48	4.74	0.47	0.15	0.45	0.16	2.69	0.00	Balance

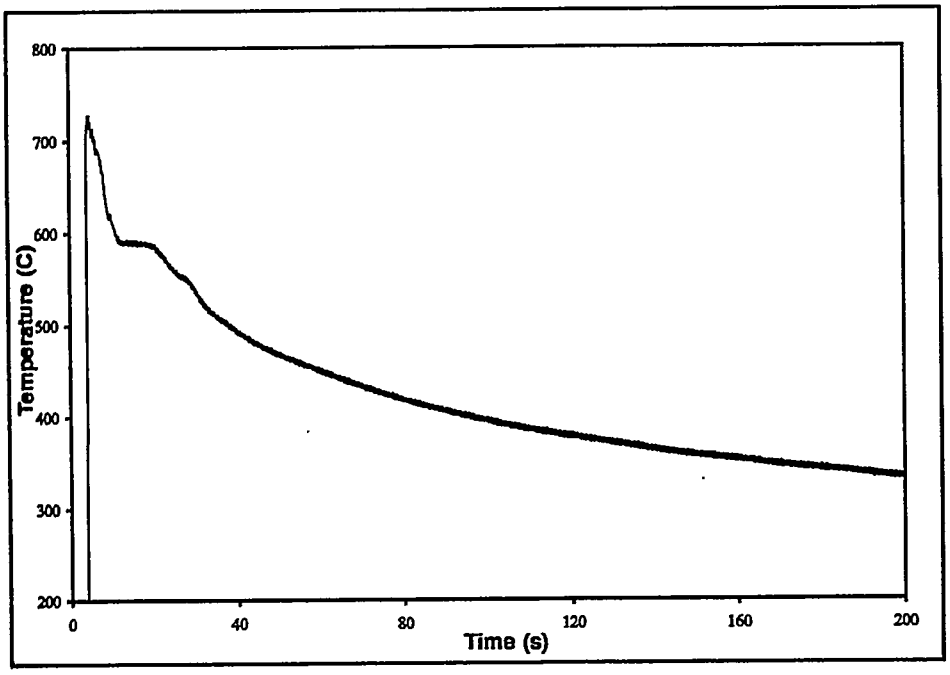

Fig. 3.4.3. Thermal history of Alloy 4 cast in a graphite mold.

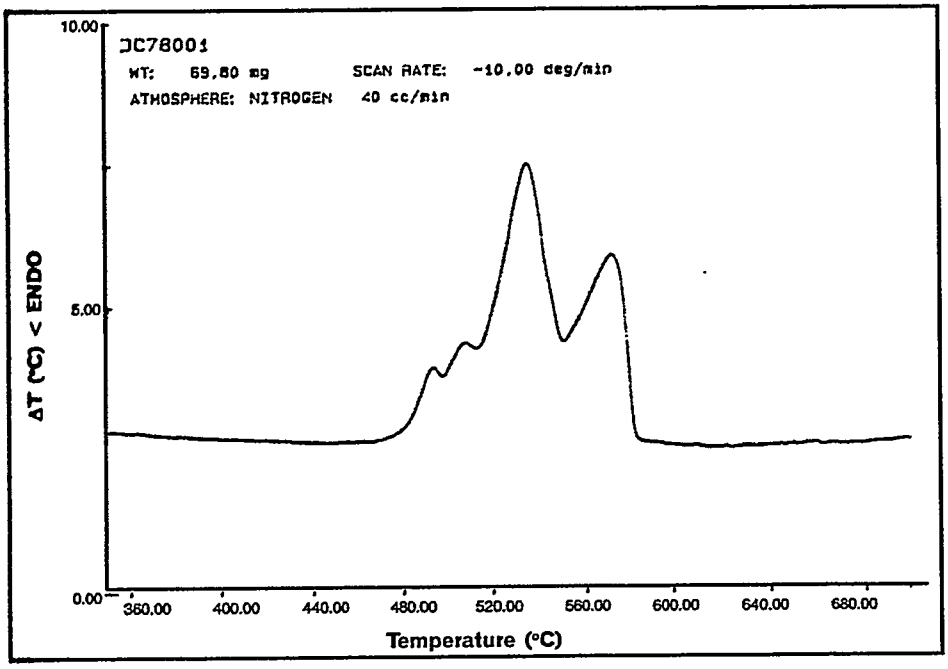

Fig. 3.4.4. DTA curve for Alloy 4 cooled at 10 °C/min.

ALLOY 4

Alloy #5	Wt.%	Si	Mg	Fe	Cu	Ni	Cr	Mn	Ti	Zn	Sr	Al
		7.05	0.44	0.67	1.18	0.53	0.14	0.01	0.01	2.76	0.00	Balance

Tensile	Strength	Ultimate	25°C	Ksi	44.4±0.7
				MPa	306.1±4.8
			100°C	Ksi	40.2±0.5
				MPa	277.4±3.3
			200°C	Ksi	29.6±0.4
				MPa	204.3±2.9
		Yield	25°C	Ksi	24.9±0.3
				MPa	171.7±2.1
			100°C	Ksi	24.5±0.6
				MPa	169.2±3.8
			200°C	Ksi	24.3±0.5
				MPa	167.3±3.6
	Elongation		25°C	%	3.76±0.52
			100°C	%	6.39±1.05
			200°C	%	7.00±1.83
	Modulus of Elasticity		25°C	10^3 Ksi	10.67±0.43
				10^3 MPa	73.57±2.94
			100°C	10^3 Ksi	8.55±0.23
				10^3 MPa	58.94±1.58
			200°C	10^3 Ksi	7.72±0.20
				10^3 MPa	53.25±1.26
Endurance Limit	100,000,000 cycles		25°C	Ksi	17.55
				MPa	121.00
	500,000,000 cycles		25°C	Ksi	17.37
				MPa	119.76
Impact Resistance	Absorbed Energy		25°C	Joules	4.24±0.49
				lb.ft.	3.13±0.36
Wear Resistance	Volume Loss		25°C	cm^3	0.5256±0.0312
Hardness	¼ × ¼ inch flat die casting		25°C	RHB	51.0±1.2
	3/8 inch diameter die casting		25°C	RHB	38.9±1.3
	5/8 inch diameter die casting		25°C	RHB	46.8±1.5
Thermal Conductivity			25°C	W/m.K	126.0±1.0
Electrical Conductivity			25°C	% IACS	26.99±0.09
Electrical Resistivity			25°C	10^{-8} Ωm	6.388±0.021
Specific Gravity			25°C	g/cm^3	2.760

ALLOY 5

Alloy #5	Wt.%	Si	Mg	Fe	Cu	Ni	Cr	Mn	Ti	Zn	Sr	Al
		7.05	0.44	0.67	1.18	0.53	0.14	0.01	0.01	2.76	0.00	Balance

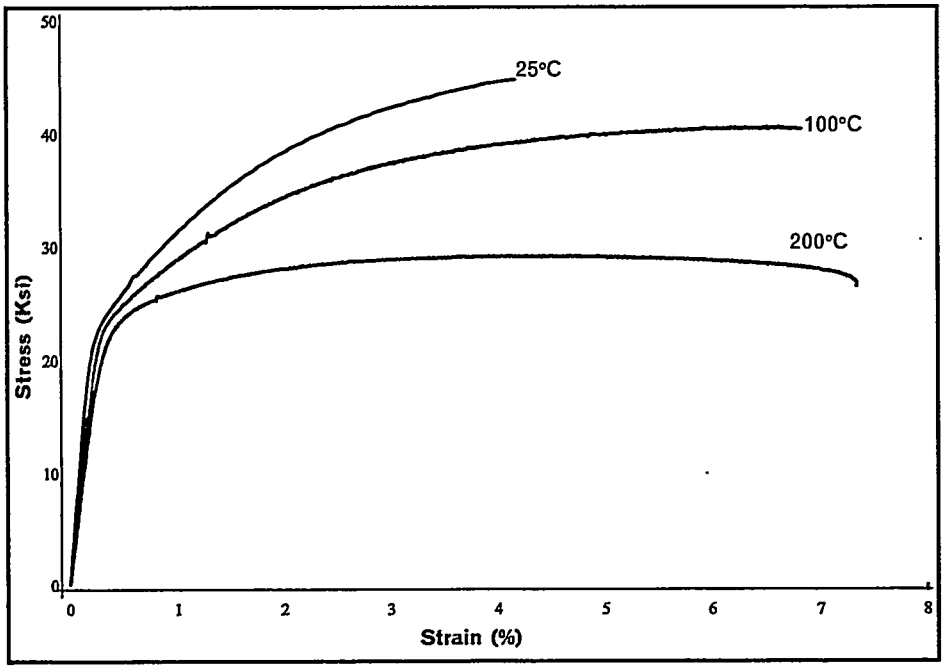

Fig. 3.5.1. Typical stress vs strain curves for Alloy 5 at temperatures of 25°C, 100 °C, and 200 °C.

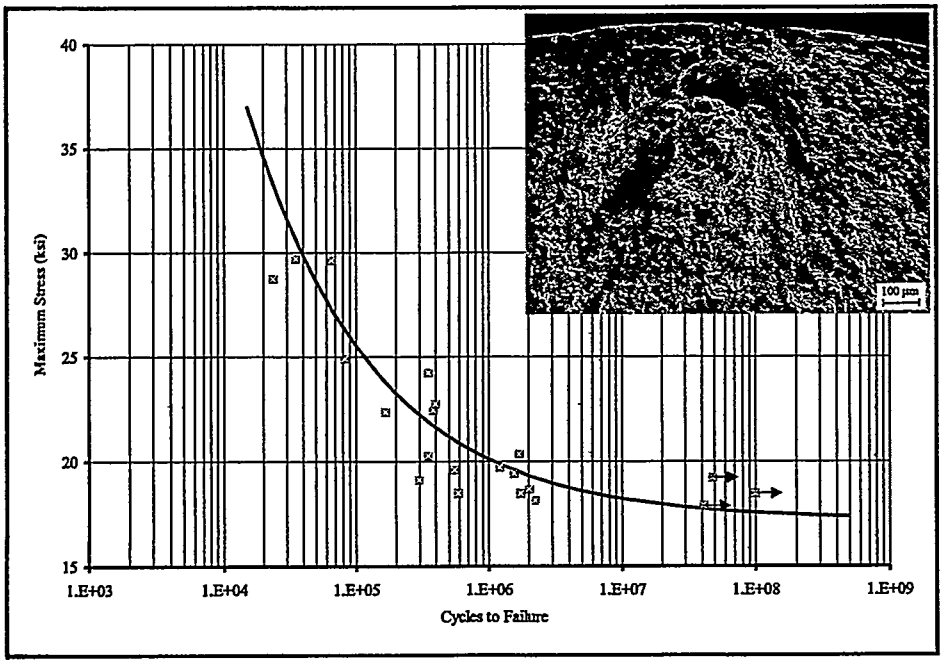

Fig. 3.5.2. S/N curve for Alloy 5; the fracture surface shown is from the specimen which failed at 1.2 x 10^5 cycles under a maximum stress of 19.7 ksi.

ALLOY 5

Alloy	Wt.%	Si	Mg	Fe	Cu	Ni	Cr	Mn	Ti	Zn	Sr	Al
#5		7.05	0.44	0.67	1.18	0.53	0.14	0.01	0.01	2.76	0.00	Balance

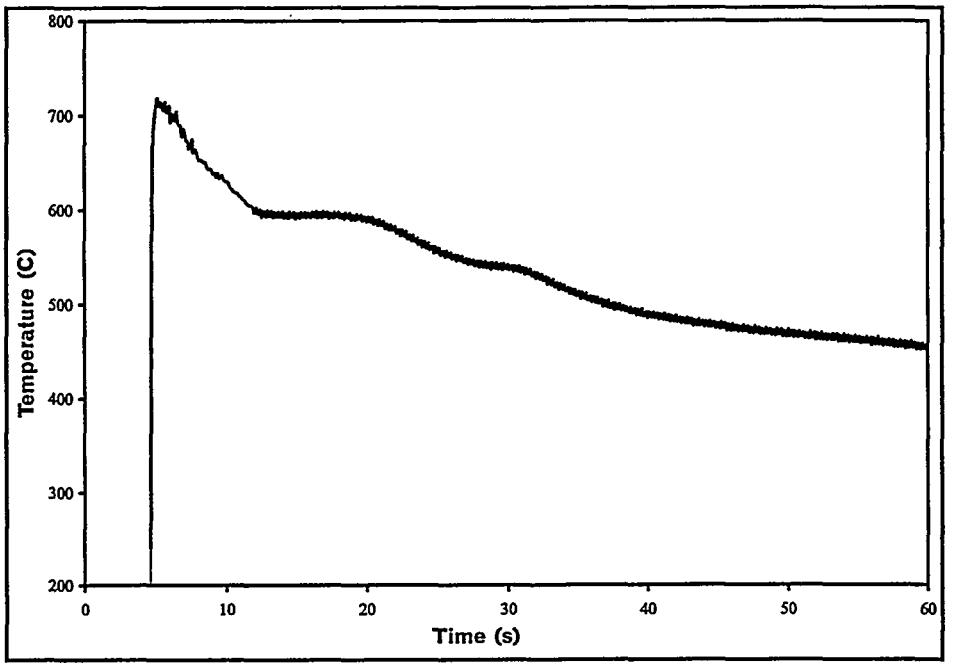

Fig. 3.5.3. Thermal history of Alloy 5 cast in a graphite mold.

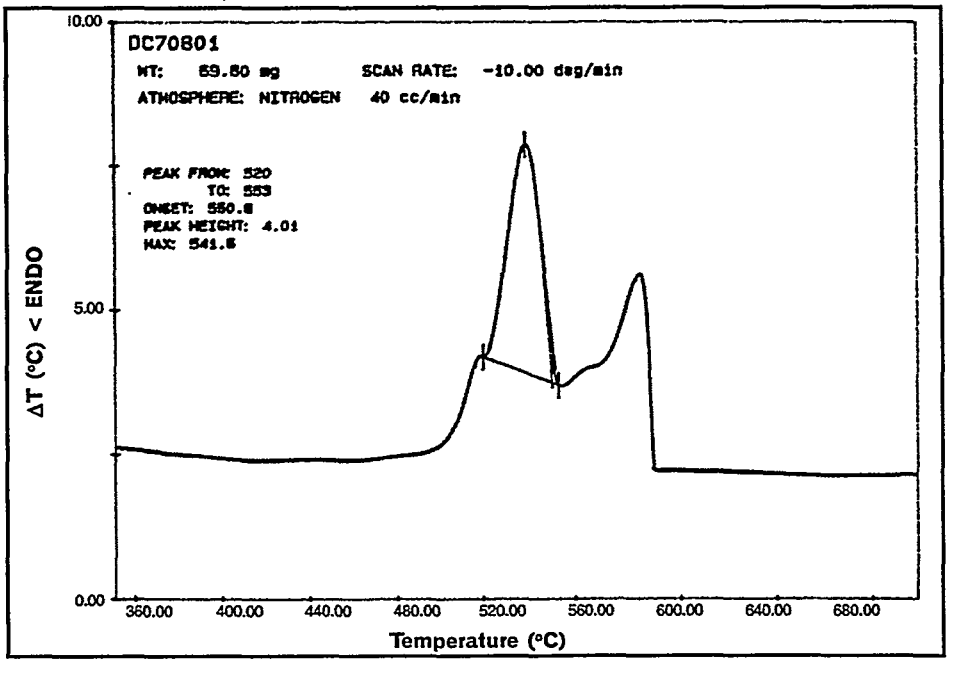

Fig. 3.5.4. DTA curve for Alloy 5 cooled at 10 °C/min.

ALLOY 5

Alloy #6	Wt.%	Si	Mg	Fe	Cu	Ni	Cr	Mn	Ti	Zn	Sr	Al
		6.98	0.44	0.57	1.13	0.48	0.13	0.45	0.18	0.38	0.018	Balance

Tensile	Strength	Ultimate	25°C	Ksi	46.2±1.5
				MPa	318.5±10.3
			100°C	Ksi	42.3±0.9
				MPa	292.0±6.0
			200°C	Ksi	33.6±0.8
				MPa	231.7±5.8
		Yield	25°C	Ksi	24.9±0.5
				MPa	171.7±3.4
			100°C	Ksi	25.0±0.7
				MPa	172.5±4.8
			200°C	Ksi	27.6±0.5
				MPa	190.5±3.6
	Elongation		25°C	%	3.78±0.75
			100°C	%	5.29±1.23
			200°C	%	4.98±1.70
	Modulus of Elasticity		25°C	10^3 Ksi	11.01±0.75
				10^3 MPa	75.90±5.16
			100°C	10^3 Ksi	9.01±0.34
				10^3 MPa	62.12±2.32
			200°C	10^3 Ksi	8.18±0.43
				10^3 MPa	56.38±2.98
Endurance Limit	100,000,000 cycles		25°C	Ksi	17.52
				MPa	120.80
	500,000,000 cycles		25°C	Ksi	17.32
				MPa	119.42
Impact Resistance	Absorbed Energy		25°C	Joules	3.28±0.39
				lb.ft.	2.42±0.29
Wear Resistance	Volume Loss		25°C	cm^3	0.4730±0.0171
Hardness	¼ × ¼ inch flat die casting		25°C	RHB	58.2±1.3
	3/8 inch diameter die casting		25°C	RHB	47.9±1.9
	5/8 inch diameter die casting		25°C	RHB	46.6±2.2
Thermal Conductivity			25°C	W/m.K	119.9±2.4
Electrical Conductivity			25°C	% IACS	25.41±0.15
Electrical Resistivity			25°C	10^{-8} Ωm	6.786±0.041
Specific Gravity			25°C	g/cm^3	2.736

ALLOY 6

Alloy #6	Wt.%	Si	Mg	Fe	Cu	Ni	Cr	Mn	Ti	Zn	Sr	Al
		6.98	0.44	0.57	1.13	0.48	0.13	0.45	0.18	0.38	0.018	Balance

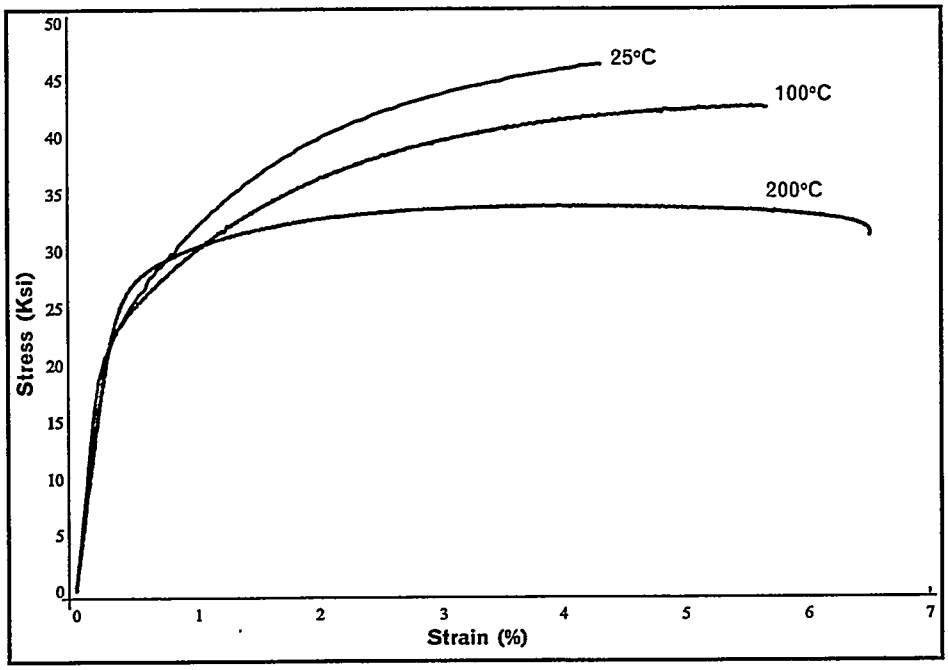

F. 6.1. Typical stress vs strain curves for Alloy 6 at temperatures of 25°C, 100 °C, and 200 °C.

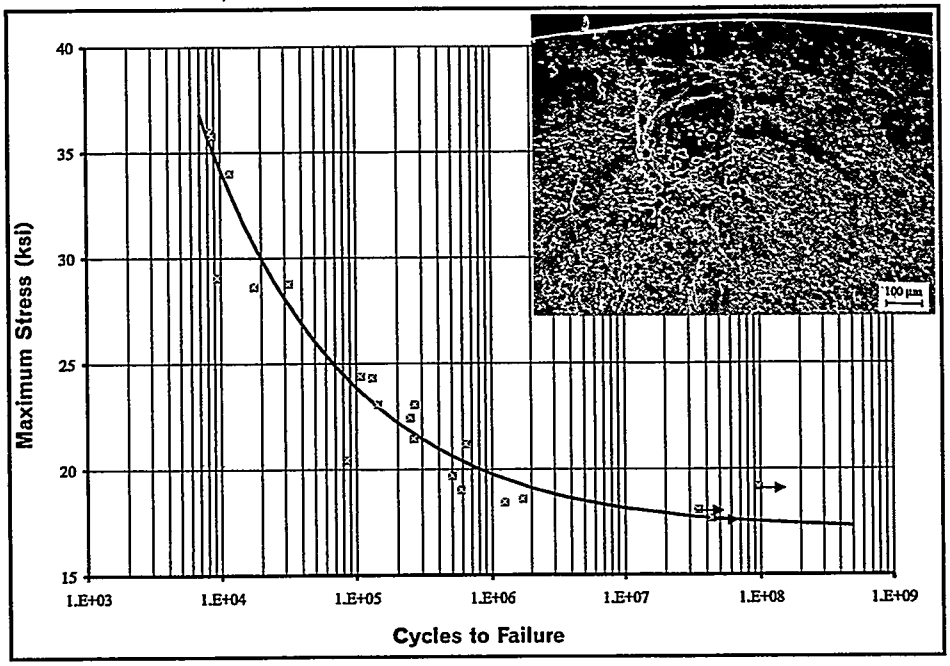

F. 6.2. S/N curve for Alloy 6; the fracture surface shown is from the specimen which failed at 6.7 x 10^5 cycles under a maximum stress of 20.3 ksi.

ALLOY 6

Alloy #6	Wt.%	Si	Mg	Fe	Cu	Ni	Cr	Mn	Ti	Zn	Sr	Al
		6.98	0.44	0.57	1.13	0.48	0.13	0.45	0.18	0.38	0.018	Balance

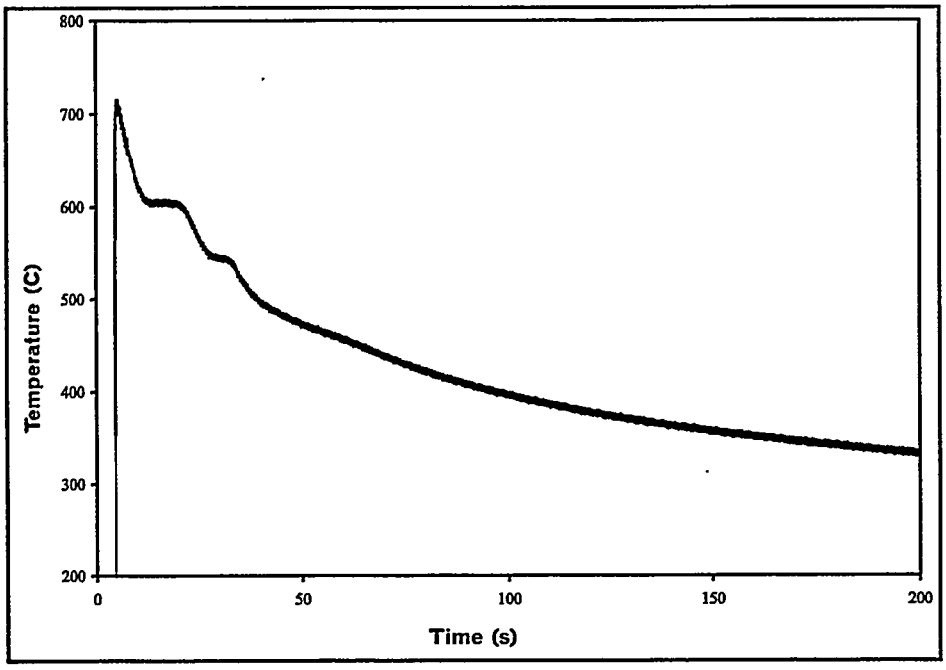

Fig. 3.6.3. Thermal history of Alloy 6 cast in a graphite mold.

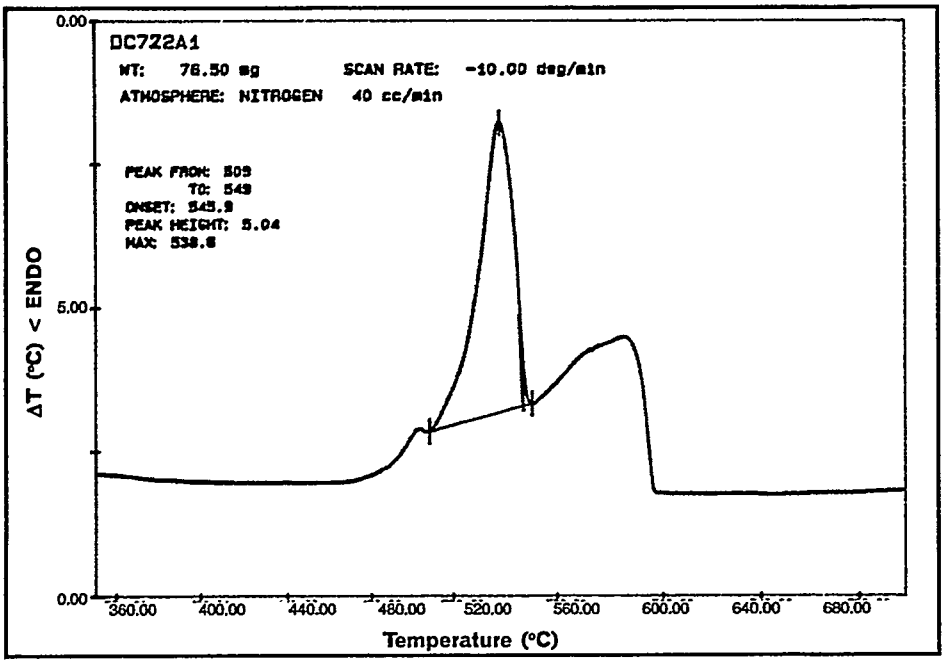

Fig. 3.6.4. DTA curve for Alloy 6 cooled at 10 °C/min.

ALLOY 6

Alloy #7	Wt.%	Si	Mg	Fe	Cu	Ni	Cr	Mn	Ti	Zn	Sr	Al
		6.92	0.50	1.63	4.94	0.03	0.01	0.02	0.01	2.73	0.022	Balance

Tensile	Strength	Ultimate	25°C	Ksi	49.1±0.6
				MPa	338.5±4.1
			100°C	Ksi	45.2±1.1
				MPa	311.8±7.6
			200°C	Ksi	36.6±0.7
				MPa	252.2±4.6
		Yield	25°C	Ksi	32.2±0.6
				MPa	222.0±4.1
			100°C	Ksi	30.4±0.6
				MPa	209.6±4.5
			200°C	Ksi	30.5±0.5
				MPa	210.1±3.2
	Elongation		25°C	%	1.42±0.08
			100°C	%	1.86±0.14
			200°C	%	2.40±0.09
	Modulus of Elasticity		25°C	10^3 Ksi	11.44±0.69
				10^3 MPa	78.84±4.74
			100°C	10^3 Ksi	9.37±1.20
				10^3 MPa	64.60±8.24
			200°C	10^3 Ksi	8.44±0.32
				10^3 MPa	58.16±2.23
Endurance Limit	100,000,000 cycles		25°C	Ksi	19.50
				MPa	134.45
	500,000,000 cycles		25°C	Ksi	19.25
				MPa	132.72
Impact Resistance	Absorbed Energy		25°C	Joules	1.75±0.27
				lb.ft.	1.29±0.20
Wear Resistance	Volume Loss		25°C	cm^3	0.5289±0.0204
Hardness	¼ × ¼ inch flat die casting		25°C	RHB	71.9±0.8
	3/8 inch diameter die casting		25°C	RHB	64.9±3.19
	5/8 inch diameter die casting		25°C	RHB	64.3±2.1
Thermal Conductivity			25°C	W/m.K	105.6±0.4
Electrical Conductivity			25°C	% IACS	22.16±0.72
Electrical Resistivity			25°C	10^{-8} Ωm	7.782±0.251
Specific Gravity			25°C	g/cm^3	2.854

ALLOY 7

Alloy #7	Wt.%	Si	Mg	Fe	Cu	Ni	Cr	Mn	Ti	Zn	Sr	Al
		6.92	0.50	1.63	4.94	0.03	0.01	0.02	0.01	2.73	0.022	Balance

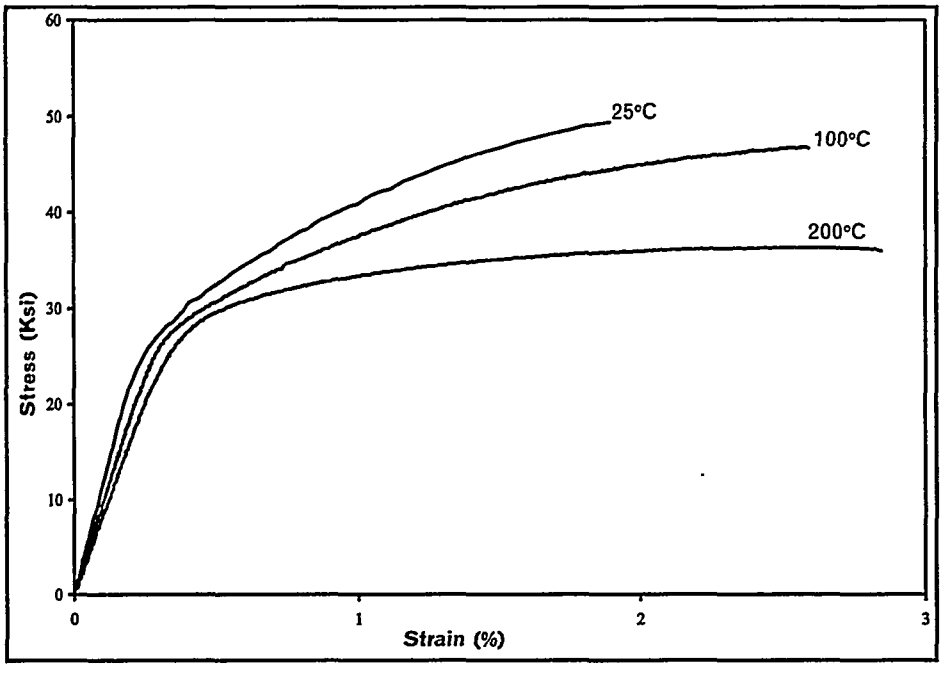

Fig. 3.7.1. Typical stress vs strain curves for Alloy 7 at temperatures of 25°C, 100 °C, and 200 °C.

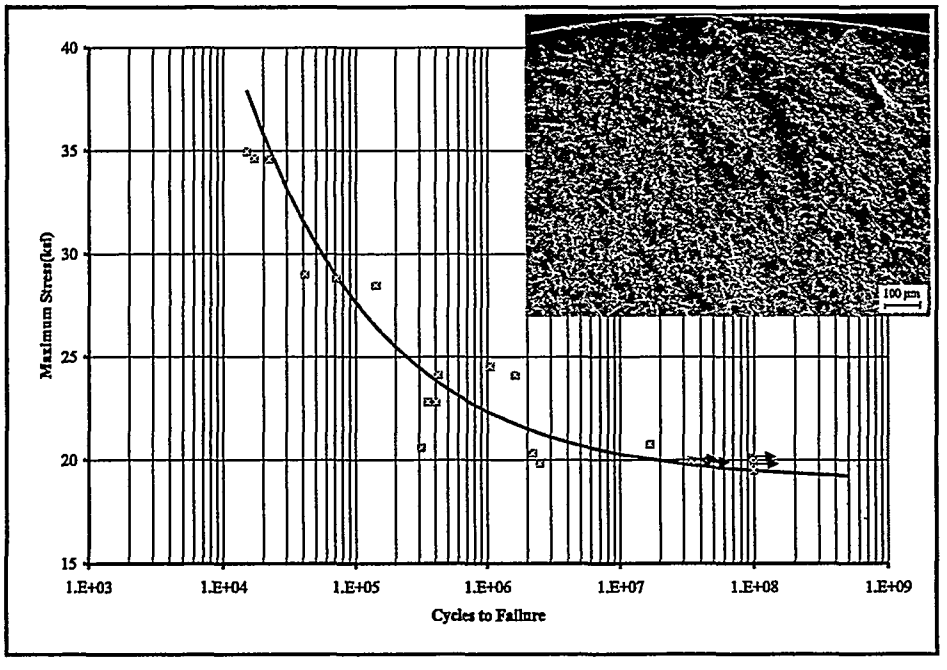

Fig. 3.7.2. S/N curve for Alloy 7; the fracture surface shown is from the specimen which failed at 2.2 x 10^6 cycles under a maximum stress of 20.3 ksi.

ALLOY 7

Alloy	Wt.%	Si	Mg	Fe	Cu	Ni	Cr	Mn	Ti	Zn	Sr	Al
117		6.92	0.50	1.63	4.94	0.03	0.01	0.02	0.01	2.73	0.022	Balance

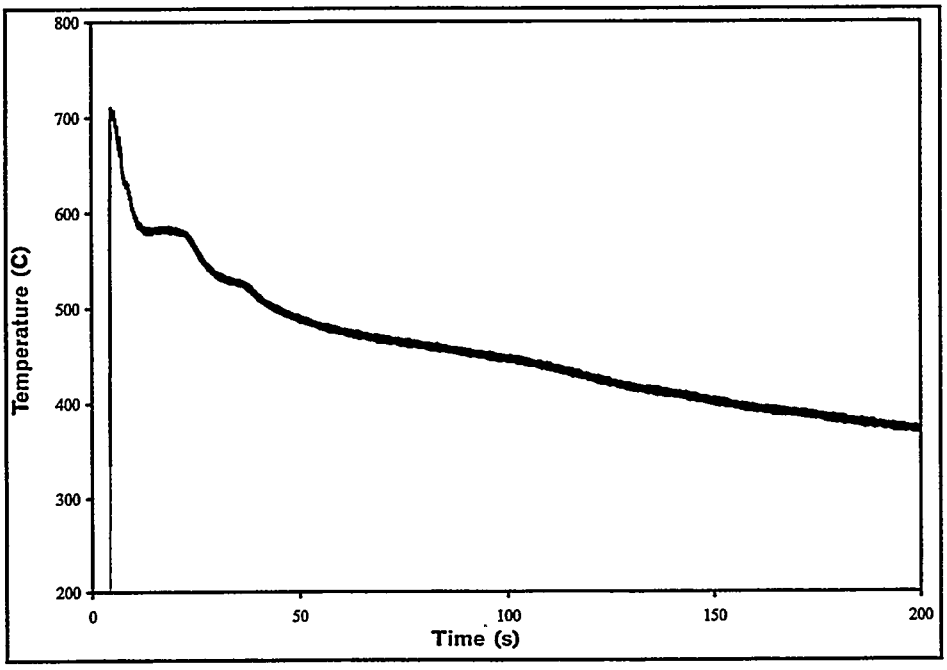

Fig. 3.7.3. Thermal history of Alloy 7 cast in a graphite mold.

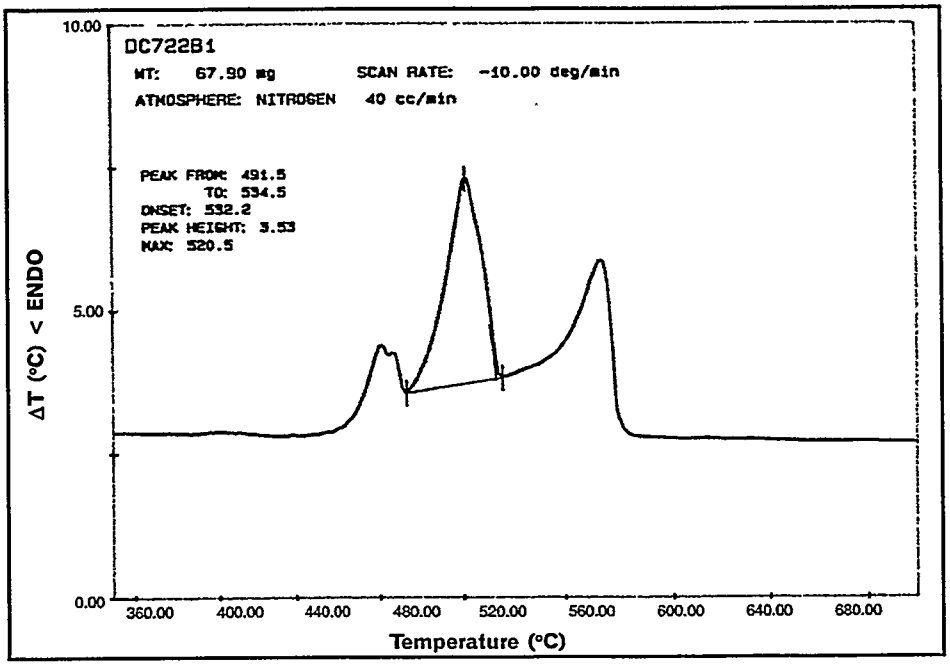

Fig. 3.7.4. DTA curve for Alloy 7 cooled at 10 °C/min.

ALLOY 7

Alloy #8	Wt.%	Si	Mg	Fe	Cu	Ni	Cr	Mn	Ti	Zn	Sr	Al
		6.79	0.46	1.49	4.77	0.01	0.01	0.45	0.20	0.42	0.00	Balance

Tensile	Strength	Ultimate	25°C	Ksi	48.9±0.9
				MPa	337.2±6.2
			100°C	Ksi	46.8±1.3
				MPa	322.4±9.3
			200°C	Ksi	37.0±0.5
				MPa	254.8±3.5
		Yield	25°C	Ksi	30.0±0.3
				MPa	206.8±2.1
			100°C	Ksi	29.5±0.4
				MPa	203.2±3.1
			200°C	Ksi	29.9±0.3
				MPa	206.1±2.4
	Elongation		25°C	%	1.93±0.19
			100°C	%	2.66±0.49
			200°C	%	3.22±0.30
	Modulus of Elasticity		25°C	10^3 Ksi	11.11±0.39
				10^3 MPa	76.61±2.65
			100°C	10^3 Ksi	8.78±0.24
				10^3 MPa	60.51±1.66
			200°C	10^3 Ksi	8.27±0.29
				10^3 MPa	57.05±1.97
Endurance Limit	100,000,000 cycles		25°C	Ksi	19.18
				MPa	132.24
	500,000,000 cycles		25°C	Ksi	19.08
				MPa	131.55
Impact Resistance	Absorbed Energy		25°C	Joules	2.23±0.26
				lb.ft.	1.65±0.19
Wear Resistance	Volume Loss		25°C	cm^3	0.5067±0.0373
Hardness	¼ × ¼ inch flat die casting		25°C	RHB	67.0±0.7
	3/8 inch diameter die casting		25°C	RHB	58.9±1.8
	5/8 inch diameter die casting		25°C	RHB	57.8±1.4
Thermal Conductivity			25°C	W/m.K	108.6±1.4
Electrical Conductivity			25°C	% IACS	23.51±0.02
Electrical Resistivity			25°C	10^{-8} Ωm	7.334±0.006
Specific Gravity			25°C	g/cm^3	2.800

ALLOY 8

Alloy #8	Wt.%	Si	Mg	Fe	Cu	Ni	Cr	Mn	Ti	Zn	Sr	Al
		6.79	0.46	1.49	4.77	0.01	0.01	0.45	0.20	0.42	0.00	Balance

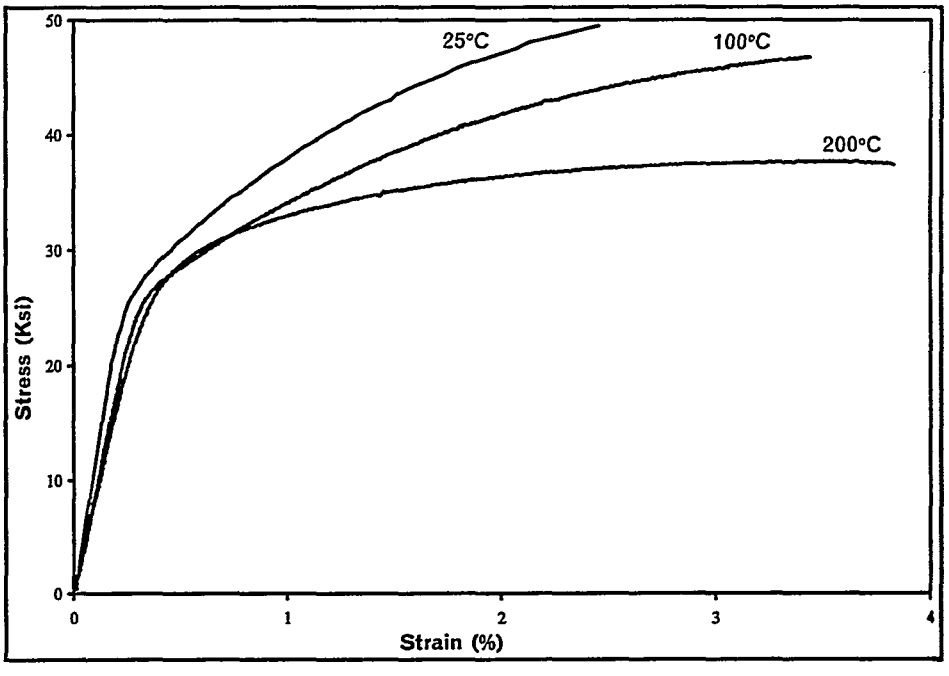

8.1. Typical stress vs strain curves for Alloy 8 at temperatures of 25°C, 100 °C, and 200 °C.

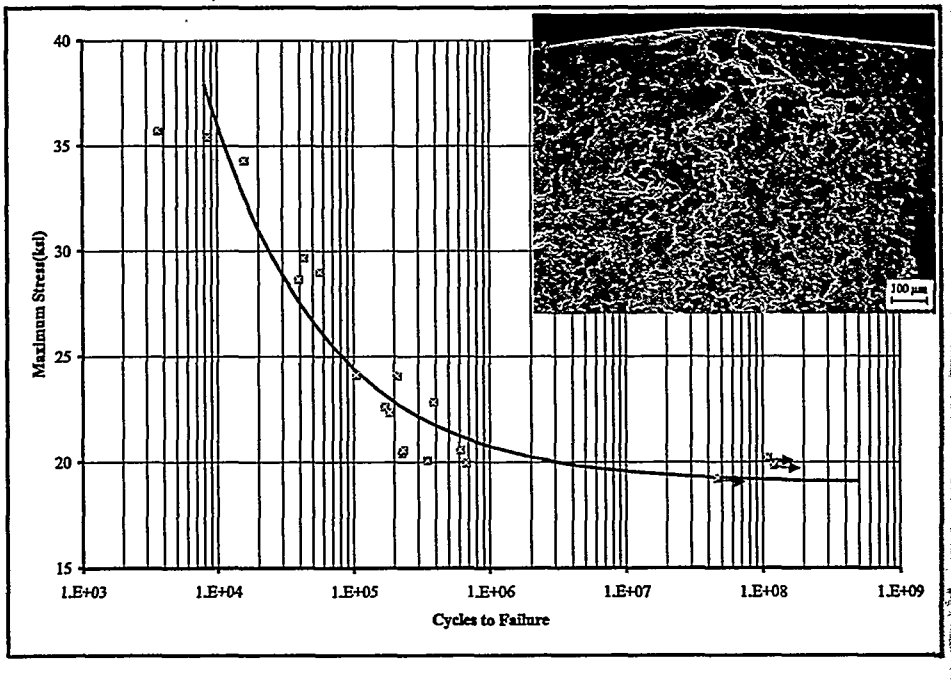

8.2. S/N curve for Alloy 8; the fracture surface shown is from the specimen which failed at 6.8 x 10^5 cycles under a maximum stress of 20.0 ksi.

ALLOY 8

Alloy #8	Wt.%	Si	Mg	Fe	Cu	Ni	Cr	Mn	Ti	Zn	Sr	Al
		6.79	0.46	1.49	4.77	0.01	0.01	0.45	0.20	0.42	0.00	Balance

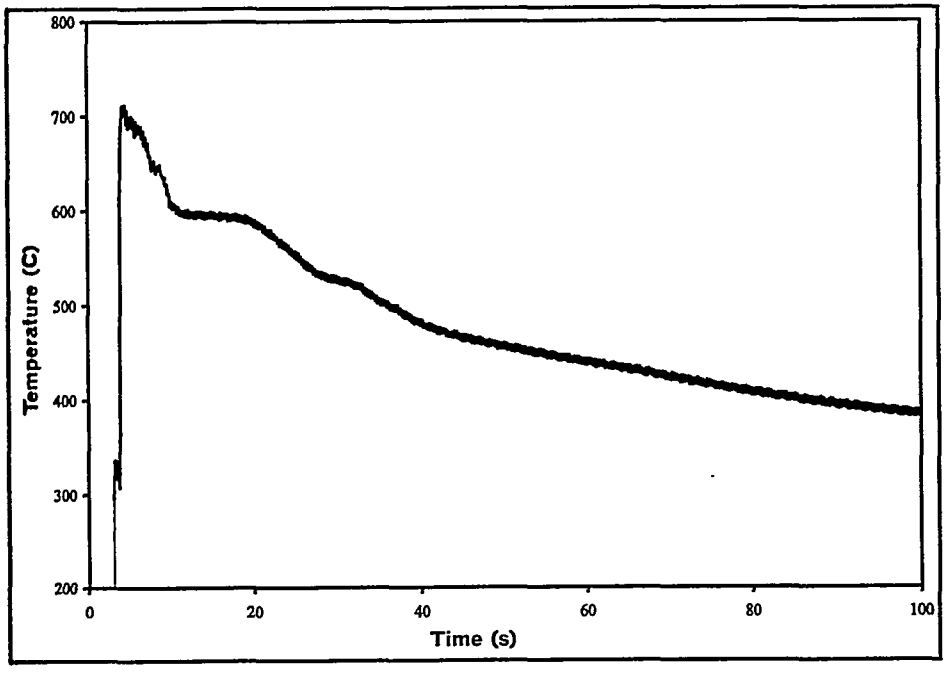

Fig. 3.8.3. Thermal history of Alloy 8 cast in a graphite mold.

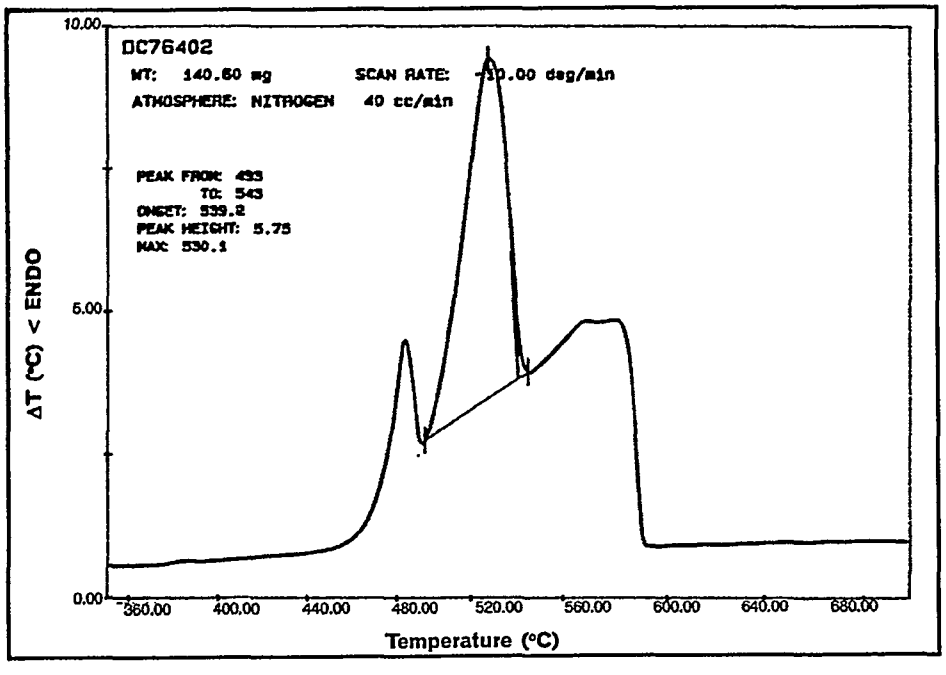

Fig. 3.8.4. DTA curve for Alloy 8 cooled at 10 °C/min.

ALLOY 8

Alloy #9	Wt.%	Si	Mg	Fe	Cu	Ni	Cr	Mn	Ti	Zn	Sr	Al
		12.71	0.05	0.63	4.96	0.06	0.14	0.01	0.20	0.50	0.017	Balance

Tensile	Strength	Ultimate	25°C	Ksi	46.8±1.8
				MPa	322.7±12.4
			100°C	Ksi	44.0±1.8
				MPa	303.4±12.7
			200°C	Ksi	31.2±0.7
				MPa	215.1±4.8
		Yield	25°C	Ksi	27.5±0.4
				MPa	189.6±2.8
			100°C	Ksi	27.3±0.6
				MPa	188.0±4.1
			200°C	Ksi	23.0±0.4
				MPa	158.7±2.5
	Elongation		25°C	%	1.69±0.29
			100°C	%	2.35±0.68
			200°C	%	4.25±1.33
	Modulus of Elasticity		25°C	10^3 Ksi	11.58±0.69
				10^3 MPa	79.86±4.72
			100°C	10^3 Ksi	8.98±0.23
				10^3 MPa	61.88±1.56
			200°C	10^3 Ksi	8.45±0.64
				10^3 MPa	58.23±4.44
Endurance Limit	100,000,000 cycles		25°C	Ksi	22.97
				MPa	158.37
	500,000,000 cycles		25°C	Ksi	21.97
				MPa	151.48
Impact Resistance	Absorbed Energy		25°C	Joules	2.65±0.18
				lb.ft.	1.95±0.13
Wear Resistance	Volume Loss		25°C	cm^3	0.3974±0.0079
Hardness	¼ × ¼ inch flat die casting		25°C	RHB	70.8±2.0
	3/8 inch diameter die casting		25°C	RHB	60.9±2.8
	5/8 inch diameter die casting		25°C	RHB	60.3±1.8
Thermal Conductivity			25°C	W/m.K	111.7±0.4
Electrical Conductivity			25°C	% IACS	21.28±0.30
Electrical Resistivity			25°C	10^{-8} Ωm	8.101±0.115
Specific Gravity			25°C	g/cm^3	2.755

ALLOY 9

Alloy #9	Wt.%	Si	Mg	Fe	Cu	Ni	Cr	Mn	Ti	Zn	Sr	Al
		12.71	0.05	0.63	4.96	0.06	0.14	0.01	0.20	0.50	0.017	Balance

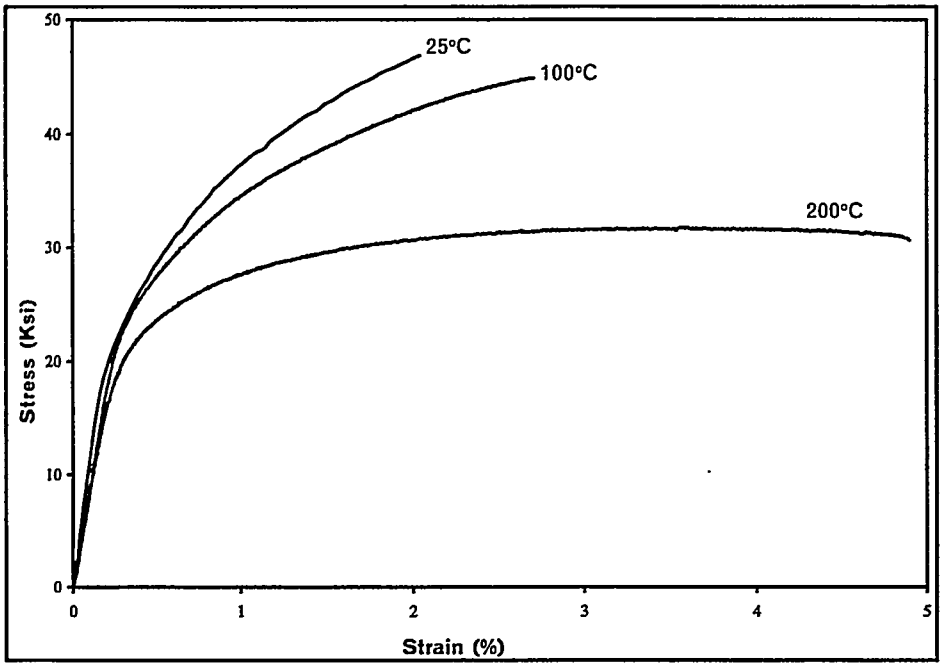

Fig. 3.9.1. Typical stress vs strain curves for Alloy 9 at temperatures of 25°C, 100 °C, and 200 °C.

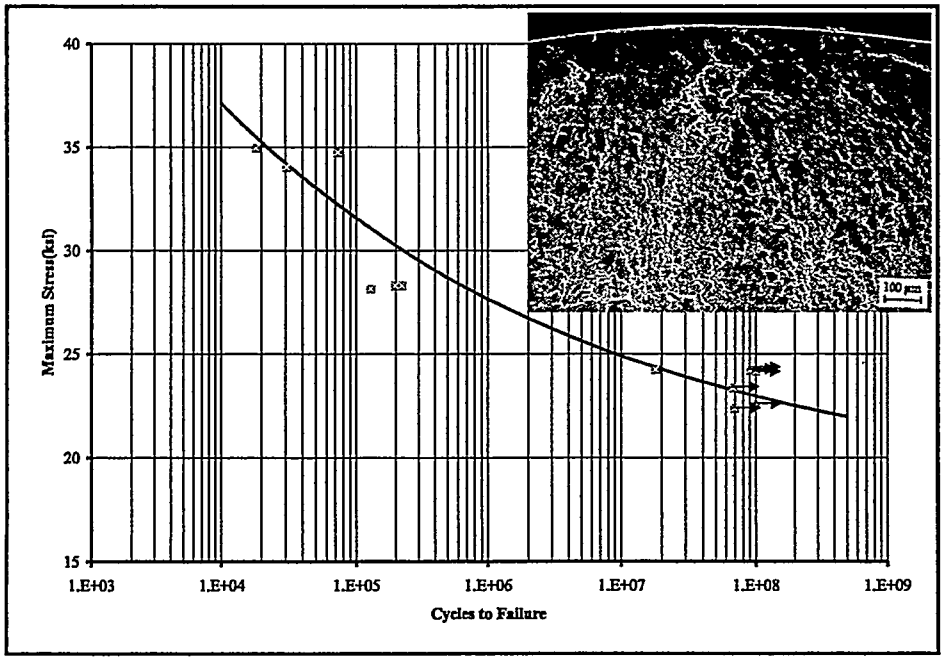

Fig. 3.9.2. S/N curve for Alloy 9; the fracture surface shown is from the specimen which failed at 1.3 x 10^5 cycles under a maximum stress of 28.2 ksi.

ALLOY 9

Alloy #9	Wt.%	Si	Mg	Fe	Cu	Ni	Cr	Mn	Ti	Zn	Sr	Al
		12.71	0.05	0.63	4.96	0.06	0.14	0.01	0.20	0.50	0.017	Balance

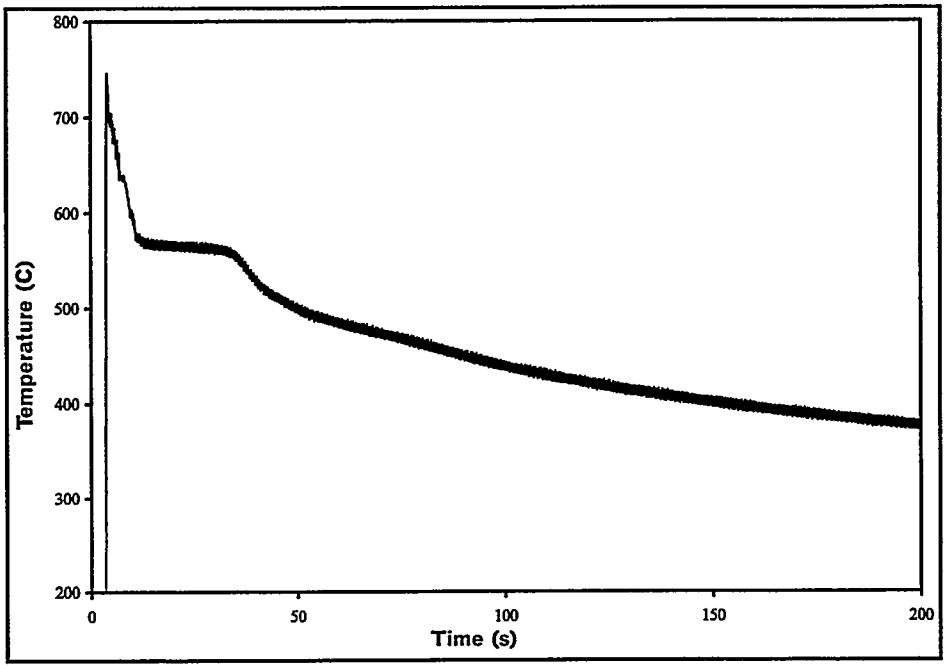

Fig. 3.9.3. Thermal history of Alloy 9 cast in a graphite mold.

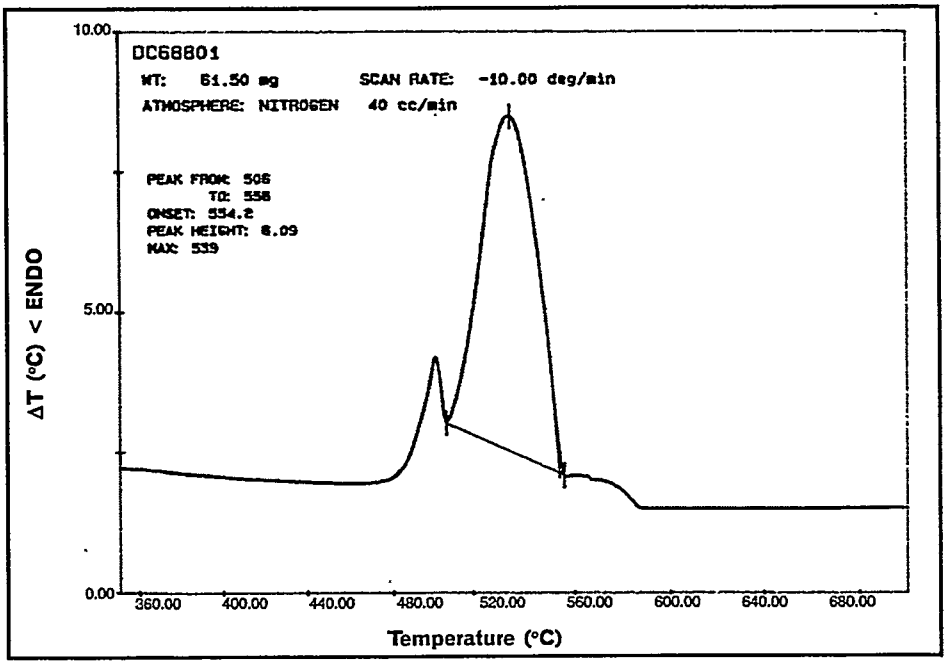

Fig. 3.9.4. DTA curve for Alloy 9 cooled at 10 °C/min.

ALLOY 9

Alloy #10	Wt.%	Si	Mg	Fe	Cu	Ni	Cr	Mn	Ti	Zn	Sr	Al
		12.69	0.03	0.73	5.09	0.07	0.11	0.37	0.01	2.73	0.00	Balance

Tensile	Strength	Ultimate	25°C	Ksi	44.3±2.4
				MPa	305.4±16.5
			100°C	Ksi	39.2±3.8
				MPa	270.5±25.9
			200°C	Ksi	29.7±0.5
				MPa	204.4±3.2
		Yield	25°C	Ksi	28.2±0.4
				MPa	194.4±2.8
			100°C	Ksi	27.9±0.4
				MPa	192.1±2.8
			200°C	Ksi	23.2±0.3
				MPa	159.8±2.1
	Elongation		25°C	%	1.40±0.37
			100°C	%	1.38±0.61
			200°C	%	4.46±1.62
	Modulus of Elasticity		25°C	10^3 Ksi	11.42±0.54
				10^3 MPa	78.74±3.72
			100°C	10^3 Ksi	9.30±0.23
				10^3 MPa	64.10±1.57
			200°C	10^3 Ksi	8.36±0.27
				10^3 MPa	57.62±1.87
Endurance Limit	100,000,000 cycles		25°C	Ksi	23.46
				MPa	161.75
	500,000,000 cycles		25°C	Ksi	23.14
				MPa	159.54
Impact Resistance	Absorbed Energy		25°C	Joules	2.48±0.32
				lb.ft.	1.83±0.24
Wear Resistance	Volume Loss		25°C	cm^3	0.3979±0.0159
Hardness	¼ × ¼ inch flat die casting		25°C	RHB	69.5±1.7
	3/8 inch diameter die casting		25°C	RHB	63.2±1.4
	5/8 inch diameter die casting		25°C	RHB	61.3±1.7
Thermal Conductivity			25°C	W/m.K	110.6±1.3
Electrical Conductivity			25°C	% IACS	20.31±0.06
Electrical Resistivity			25°C	10^{-8} Ωm	8.489±0.027
Specific Gravity			25°C	g/cm^3	2.797

ALLOY 10

Alloy #10	Wt.%	Si	Mg	Fe	Cu	Ni	Cr	Mn	Ti	Zn	Sr	Al
		12.69	0.03	0.73	5.09	0.07	0.11	0.37	0.01	2.73	0.00	Balance

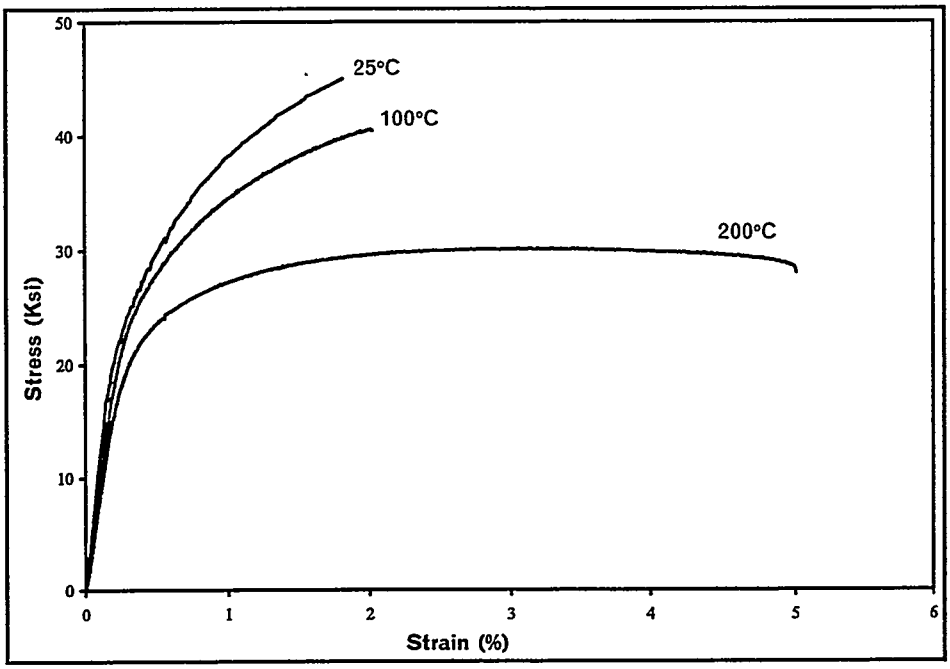

10.1. Typical stress vs strain curves for Alloy 10 at temperatures of 25°C, 100 °C, and 200 °C.

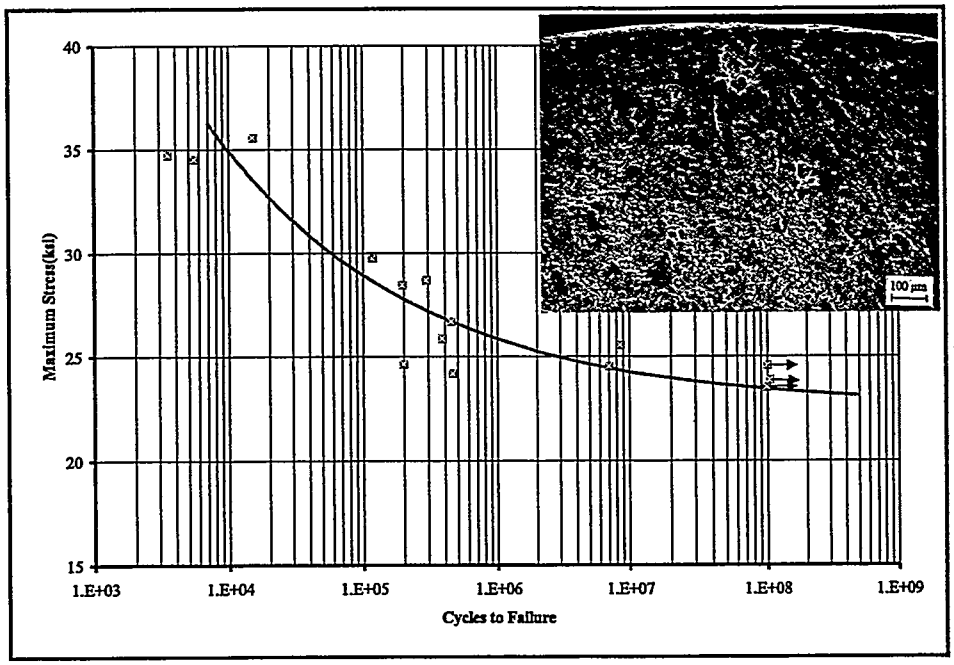

3.10.2. S/N curve for Alloy 10; the fracture surface shown is from the specimen which failed at 6.7 x 10^5 cycles under a maximum stress of 20.3 ksi.

ALLOY 10

Alloy #10	Wt.%	Si	Mg	Fe	Cu	Ni	Cr	Mn	Ti	Zn	Sr	Al
		12.69	0.03	0.73	5.09	0.07	0.11	0.37	0.01	2.73	0.00	Balance

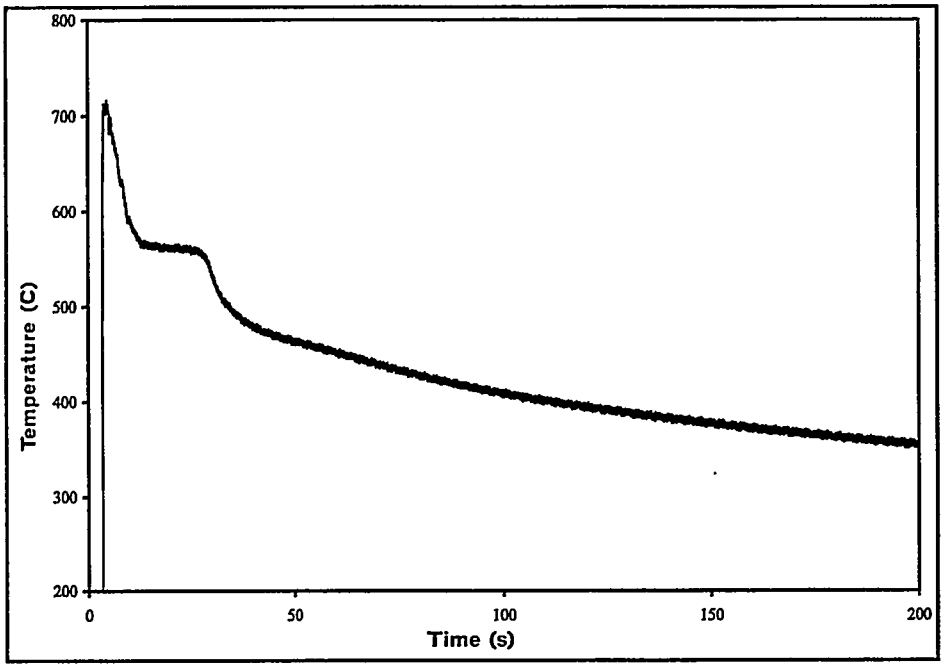

Fig. 3.10.3. Thermal history of Alloy 10 cast in a graphite mold.

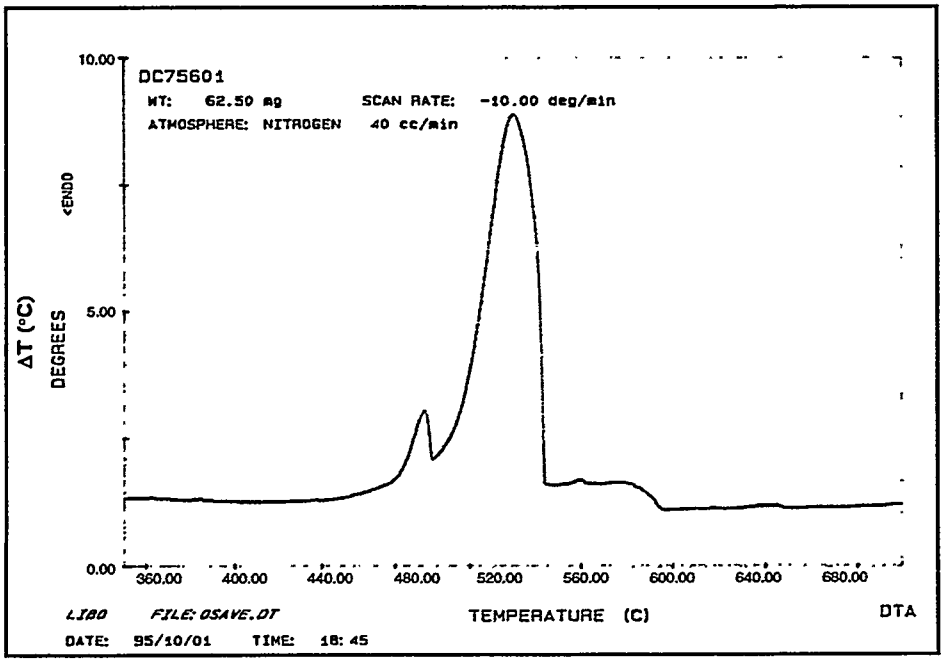

Fig. 3.10.4. DTA curve for Alloy 10 cooled at 10 °C/min.

ALLOY 10

Alloy #11	Wt.%	Si	Mg	Fe	Cu	Ni	Cr	Mn	Ti	Zn	Sr	Al
		12.86	0.04	1.59	1.21	0.45	0.01	0.01	0.18	0.49	0.00	Balance

Tensile	Strength	Ultimate	25°C	Ksi	35.1±2.0
				MPa	242.0±13.8
			100°C	Ksi	34.9±0.7
				MPa	240.4±4.8
			200°C	Ksi	29.5±1.1
				MPa	203.4±7.3
		Yield	25°C	Ksi	23.8±0.5
				MPa	164.1±3.4
			100°C	Ksi	24.2±0.2
				MPa	166.8±1.3
			200°C	Ksi	21.9±0.2
				MPa	151.2±1.4
	Elongation		25°C	%	0.75±0.13
			100°C	%	1.00±0.09
			200°C	%	1.57±0.46
	Modulus of Elasticity		25°C	10^3 Ksi	11.62±0.60
				10^3 MPa	80.12±4.10
			100°C	10^3 Ksi	9.32±0.37
				10^3 MPa	64.28±2.52
			200°C	10^3 Ksi	8.64±0.44
				10^3 MPa	59.60±3.00
Endurance Limit	100,000,000 cycles		25°C	Ksi	20.97
				MPa	144.58
	500,000,000 cycles		25°C	Ksi	20.28
				MPa	139.83
Impact Resistance	Absorbed Energy		25°C	Joules	2.22±0.21
				lb.ft.	1.64±0.16
Wear Resistance	Volume Loss		25°C	cm^3	0.4190±0.0252
Hardness	¼ × ¼ inch flat die casting		25°C	RHB	63.7±1.2
	3/8 inch diameter die casting		25°C	RHB	55.1±2.3
	5/8 inch diameter die casting		25°C	RHB	53.7±2.1
Thermal Conductivity			25°C	W/m.K	103.2±4.3
Electrical Conductivity			25°C	% IACS	19.42±0.19
Electrical Resistivity			25°C	10^{-8} Ωm	8.880±0.088
Specific Gravity			25°C	g/cm^3	2.732

ALLOY 11

Alloy #11	Wt.%	Si	Mg	Fe	Cu	Ni	Cr	Mn	Ti	Zn	Sr	Al
		12.86	0.04	1.59	1.21	0.45	0.01	0.01	0.18	0.49	0.00	Balance

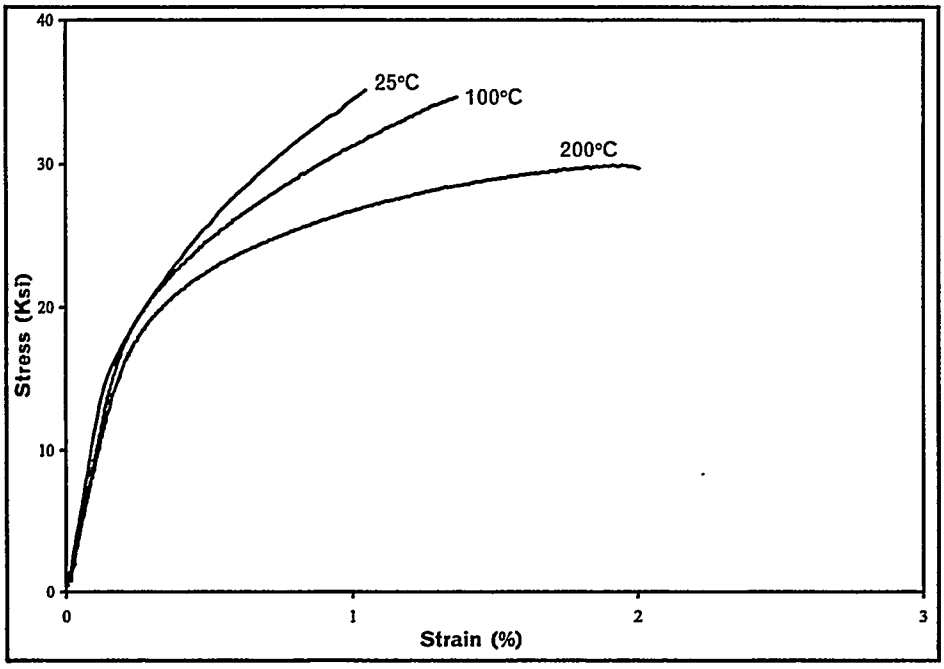

Fig. 3.11.1. Typical stress vs strain curves for Alloy 11 at temperatures of 25°C, 100 °C, and 200 °C.

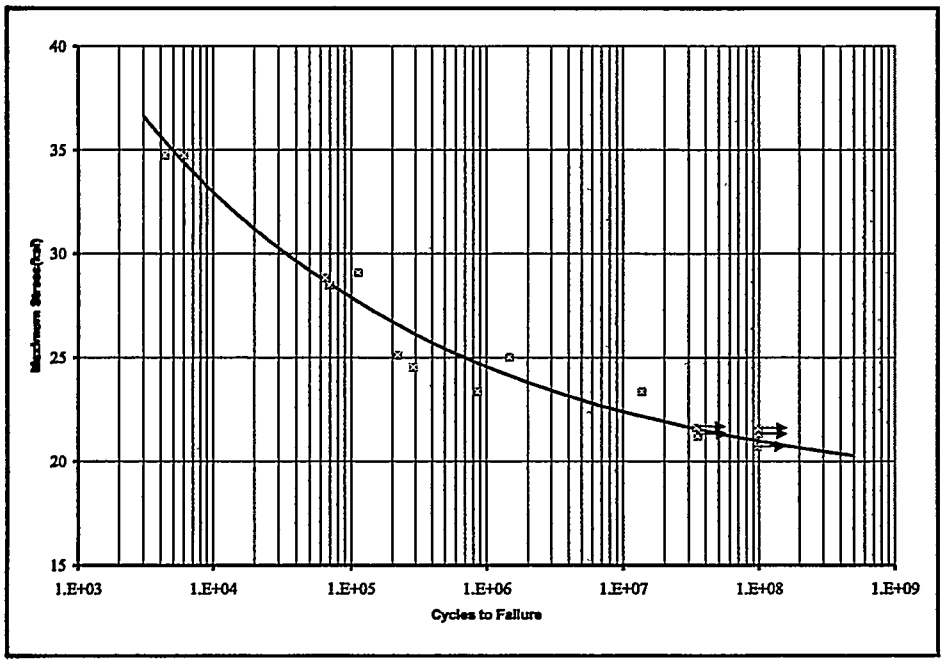

Fig. 3.11.2. S/N curve for Alloy 11.

ALLOY 11

Alloy #11	Wt.%	Si	Mg	Fe	Cu	Ni	Cr	Mn	Ti	Zn	Sr	Al
		12.86	0.04	1.59	1.21	0.45	0.01	0.01	0.18	0.49	0.00	Balance

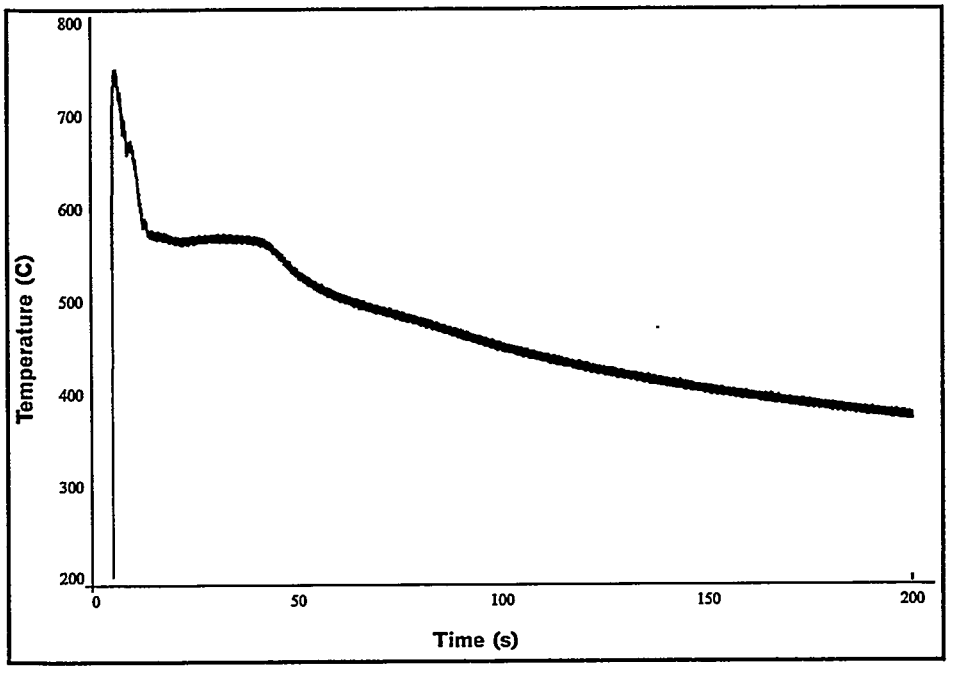

. ,11.3. Thermal history of Alloy 11 cast in a graphite mold.

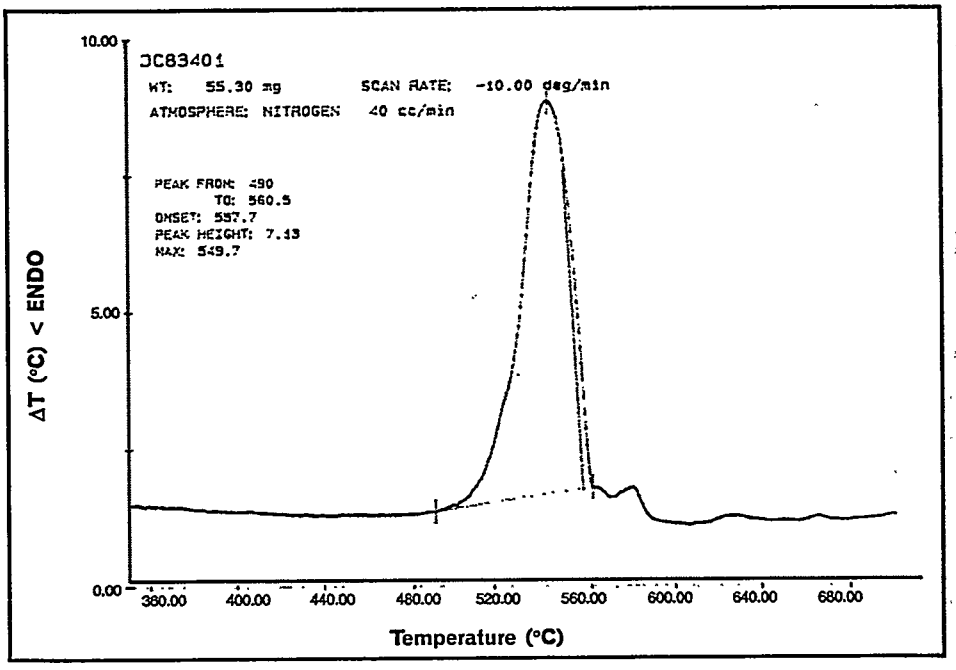

Fig. 3.11.4. DTA curve for Alloy 11 cooled at 10 °C/min.

ALLOY 11

Alloy #12	Wt.%	Si	Mg	Fe	Cu	Ni	Cr	Mn	Ti	Zn	Sr	Al
		12.95	0.05	1.55	1.29	0.46	0.01	0.43	0.01	2.91	0.023	Balance

Tensile	Strength	Ultimate	25°C	Ksi	40.4±2.2
				MPa	278.5±15.2
			100°C	Ksi	38.3±1.2
				MPa	264.1±8.3
			200°C	Ksi	27.8±0.6
				MPa	191.8±4.2
		Yield	25°C	Ksi	23.3±0.4
				MPa	160.6±2.8
			100°C	Ksi	23.3±0.3
				MPa	160.5±2.2
			200°C	Ksi	20.4±0.2
				MPa	140.6±1.7
	Elongation		25°C	%	1.42±0.32
			100°C	%	2.24±0.57
			200°C	%	5.32±1.02
	Modulus of Elasticity		25°C	10^3 Ksi	11.42±0.83
				10^3 MPa	78.72±5.70
			100°C	10^3 Ksi	8.95±0.46
				10^3 MPa	6.17±3.14
			200°C	10^3 Ksi	8.39±0.39
				10^3 MPa	57.86±2.65
Endurance Limit	100,000,000 cycles		25°C	Ksi	20.61
				MPa	142.10
	500,000,000 cycles		25°C	Ksi	20.33
				MPa	140.17
Impact Resistance	Absorbed Energy		25°C	Joules	2.75±0.26
				lb.ft.	2.03±0.19
Wear Resistance	Volume Loss		25°C	cm^3	0.3833±0.0119
Hardness	¼ × ¼ inch flat die casting		25°C	RHB	58.8±1.7
	3/8 inch diameter die casting		25°C	RHB	50.0±1.1
	5/8 inch diameter die casting		25°C	RHB	47.6±1.6
Thermal Conductivity			25°C	W/m.K	115.5±1.4
Electrical Conductivity			25°C	% IACS	23.55±0.11
Electrical Resistivity			25°C	10^{-8} Ωm	7.320±0.035
Specific Gravity			25°C	g/cm^3	2.770

ALLOY 12

Alloy #12	Wt.%	Si	Mg	Fe	Cu	Ni	Cr	Mn	Ti	Zn	Sr	Al
		12.95	0.05	1.55	1.29	0.46	0.01	0.43	0.01	2.91	0.023	Balance

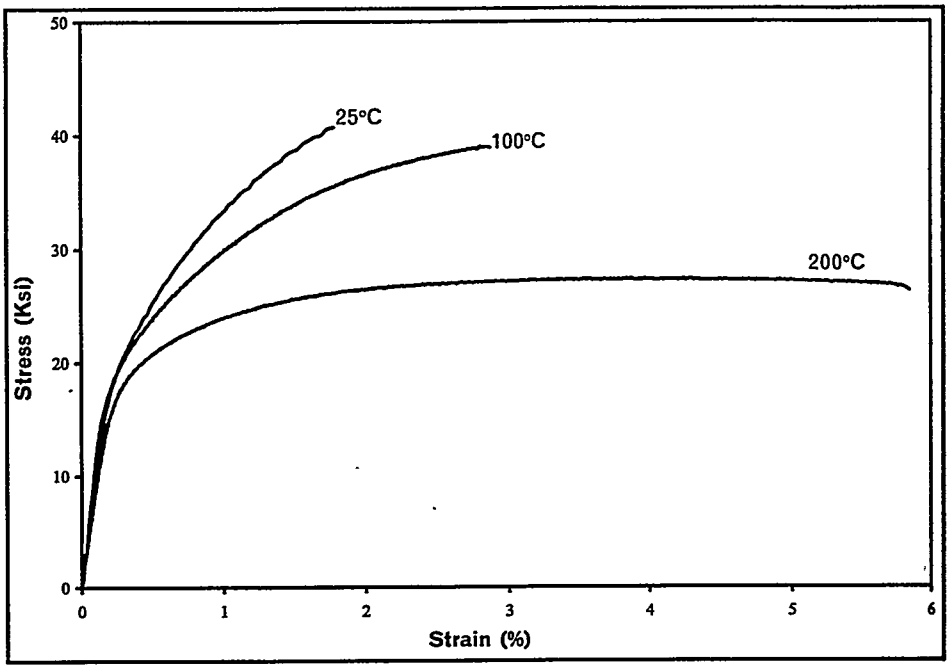

.12.1. Typical stress vs strain curves for Alloy 12 at temperatures of 25°C, 100 °C, and 200 °C.

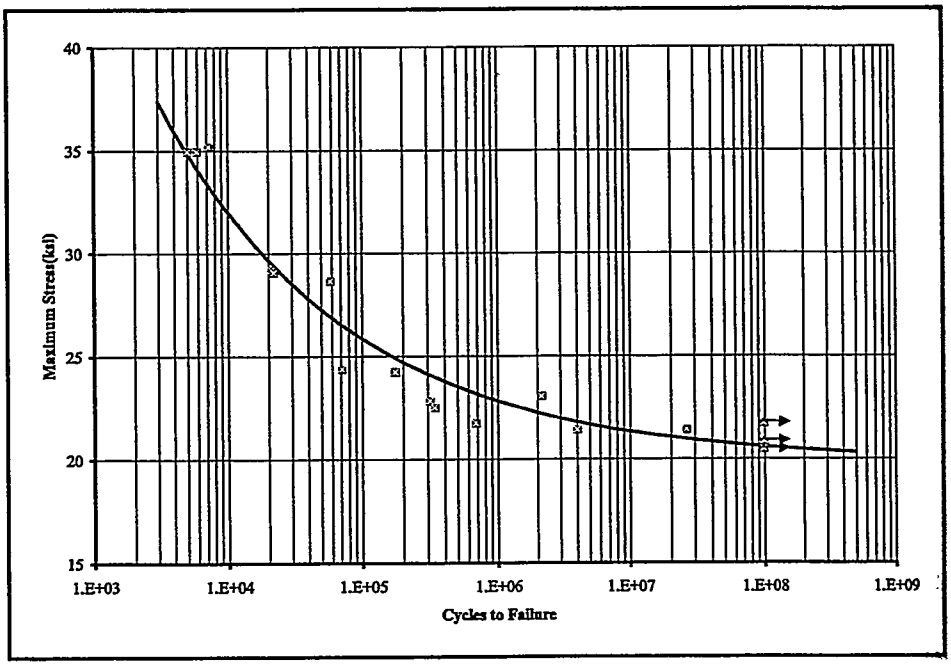

Fig. 3.12.2. S/N curve for Alloy 12.

ALLOY 12

Alloy #12	Wt.%	Si	Mg	Fe	Cu	Ni	Cr	Mn	Ti	Zn	Sr	Al
		12.95	0.05	1.55	1.29	0.46	0.01	0.43	0.01	2.91	0.023	Balance

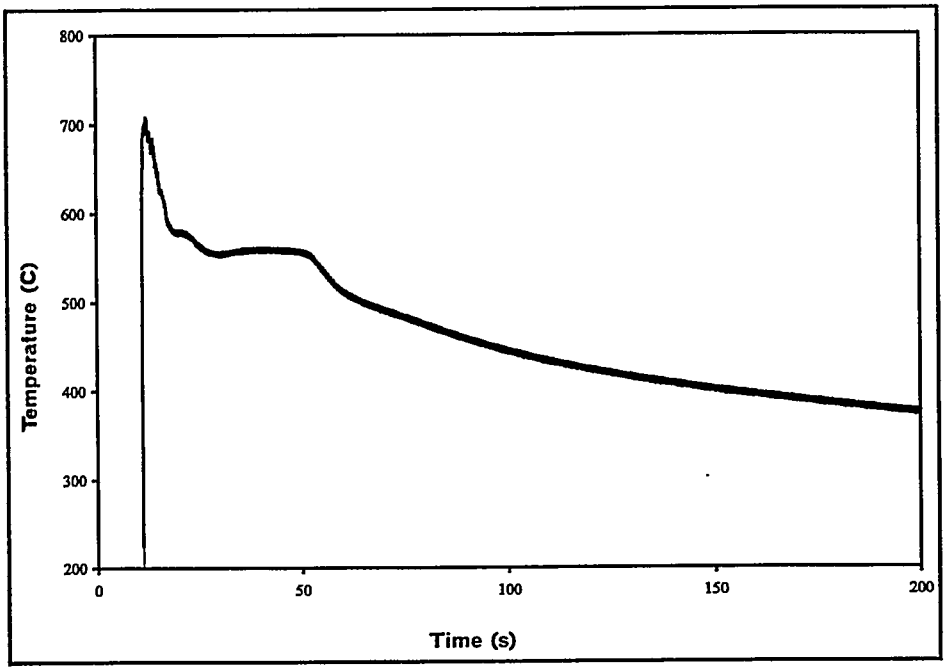

Fig. 3.12.3. Thermal history of Alloy 12 cast in a graphite mold.

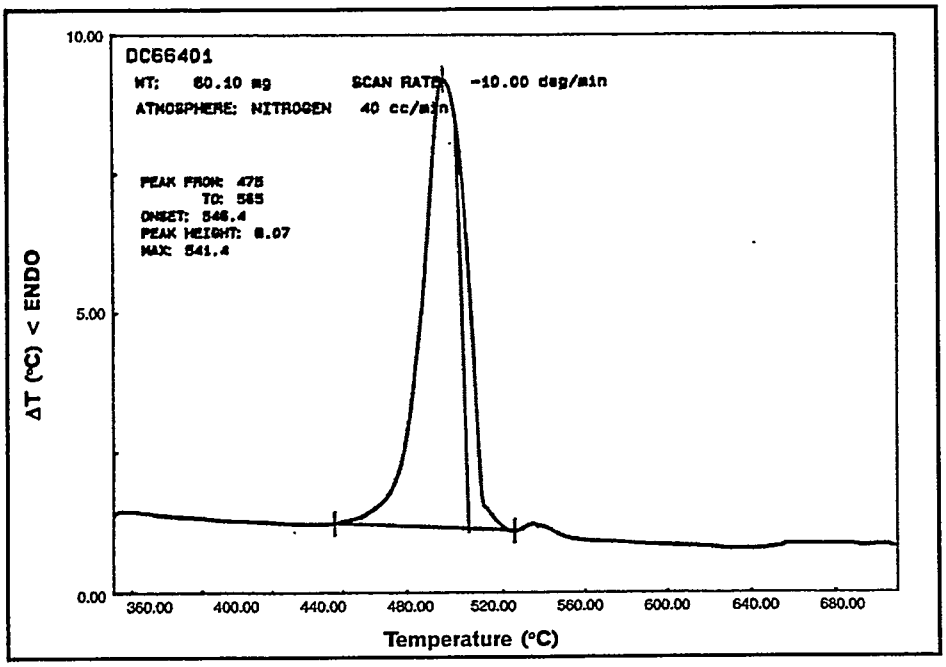

Fig. 3.12.4. DTA curve for Alloy 12 cooled at 10 °C/min.

ALLOY 12

Alloy #13	Wt.%	Si	Mg	Fe	Cu	Ni	Cr	Mn	Ti	Zn	Sr	Al
		13.03	0.46	0.58	4.70	0.44	0.01	0.01	0.17	2.61	0.021	Balance

Tensile	Strength	Ultimate	25°C	Ksi	47.2±1.6
				MPa	325.4±11.0
			100°C	Ksi	44.8±1.4
				MPa	309.0±9.8
			200°C	Ksi	35.4±0.3
				MPa	244.1±1.8
		Yield	25°C	Ksi	31.0±0.5
				MPa	213.7±3.4
			100°C	Ksi	30.3±0.4
				MPa	208.7±2.7
			200°C	Ksi	29.7±0.2
				MPa	204.7±1.6
	Elongation		25°C	%	1.39±0.24
			100°C	%	1.87±0.42
			200°C	%	2.31±0.52
	Modulus of Elasticity		25°C	10^3 Ksi	11.55±0.39
				10^3 MPa	79.65±2.70
			100°C	10^3 Ksi	9.17±0.28
				10^3 MPa	63.20±1.90
			200°C	10^3 Ksi	8.40±0.31
				10^3 MPa	57.91±2.12
Endurance Limit	100,000,000 cycles		25°C	Ksi	21.56
				MPa	148.65
	500,000,000 cycles		25°C	Ksi	20.77
				MPa	143.20
Impact Resistance	Absorbed Energy		25°C	Joules	1.99±0.24
				lb.ft.	1.47±0.18
Wear Resistance	Volume Loss		25°C	cm^3	0.4291±0.0313
Hardness	¼ × ¼ inch flat die casting		25°C	RHB	72.3±0.7
	3/8 inch diameter die casting		25°C	RHB	63.5±1.3
	5/8 inch diameter die casting		25°C	RHB	64.3±1.7
Thermal Conductivity			25°C	W/m.K	102.2±0.8
Electrical Conductivity			25°C	% IACS	20.44±0.04
Electrical Resistivity			25°C	10^{-8} Ωm	8.434±0.018
Specific Gravity			25°C	g/cm^3	2.787

ALLOY 13

Alloy #13	Wt.%	Si	Mg	Fe	Cu	Ni	Cr	Mn	Ti	Zn	Sr	Al
		13.03	0.46	0.58	4.70	0.44	0.01	0.01	0.17	2.61	0.021	Balance

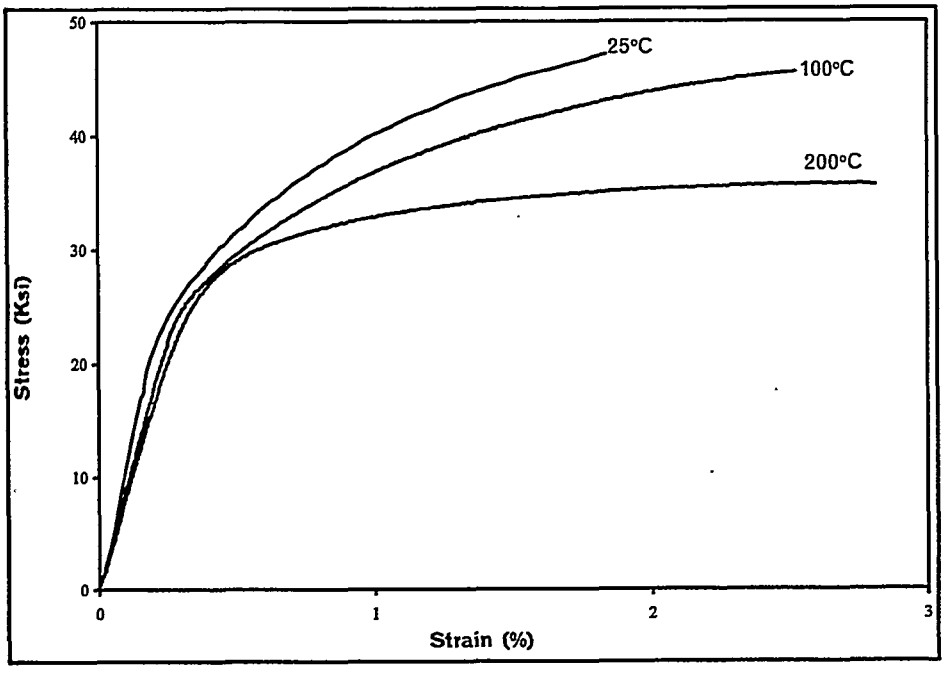

Fig. 3.13.1. Typical stress vs strain curves for Alloy 13 at temperatures of 25°C, 100 °C, and 200 °C.

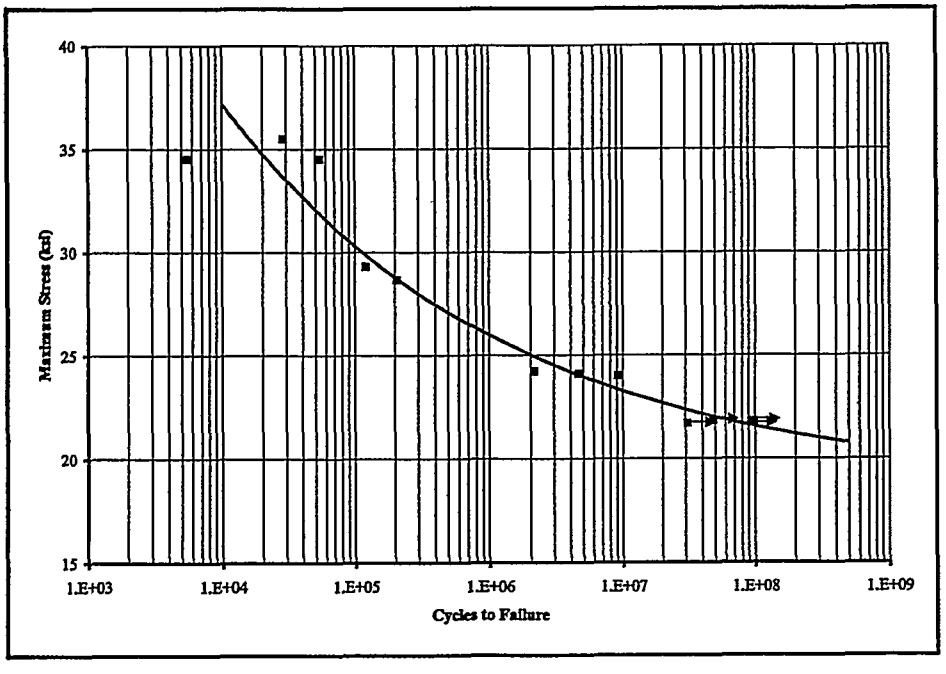

Fig. 3.13.2. S/N curve for Alloy 13.

ALLOY 13

Alloy #13	Wt.%	Si	Mg	Fe	Cu	Ni	Cr	Mn	Ti	Zn	Sr	Al
		13.03	0.46	0.58	4.70	0.44	0.01	0.01	0.17	2.61	0.021	Balance

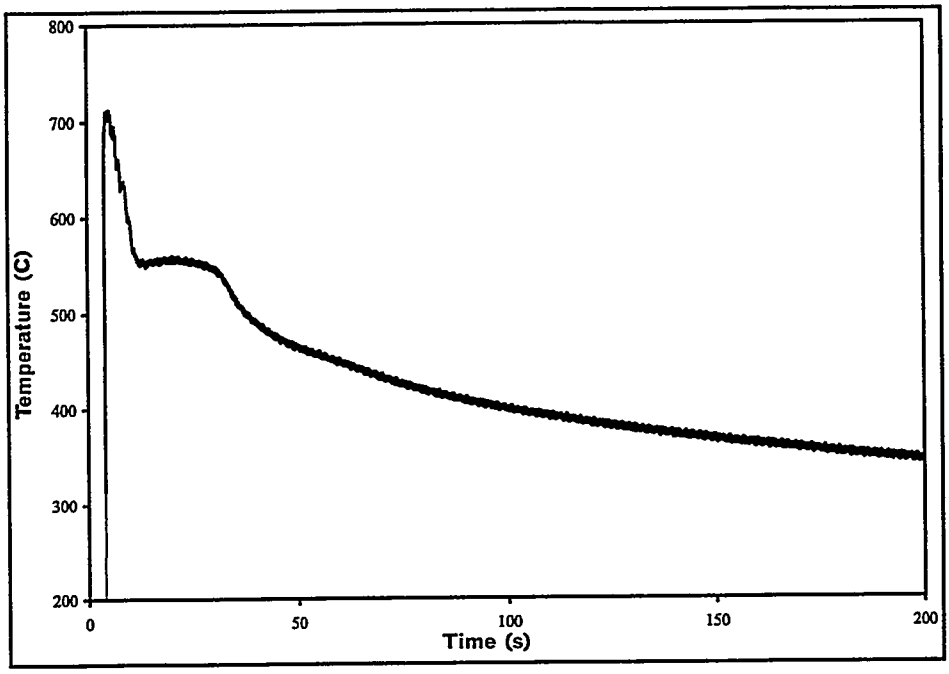

).13.3. Thermal history of Alloy 13 cast in a graphite mold.

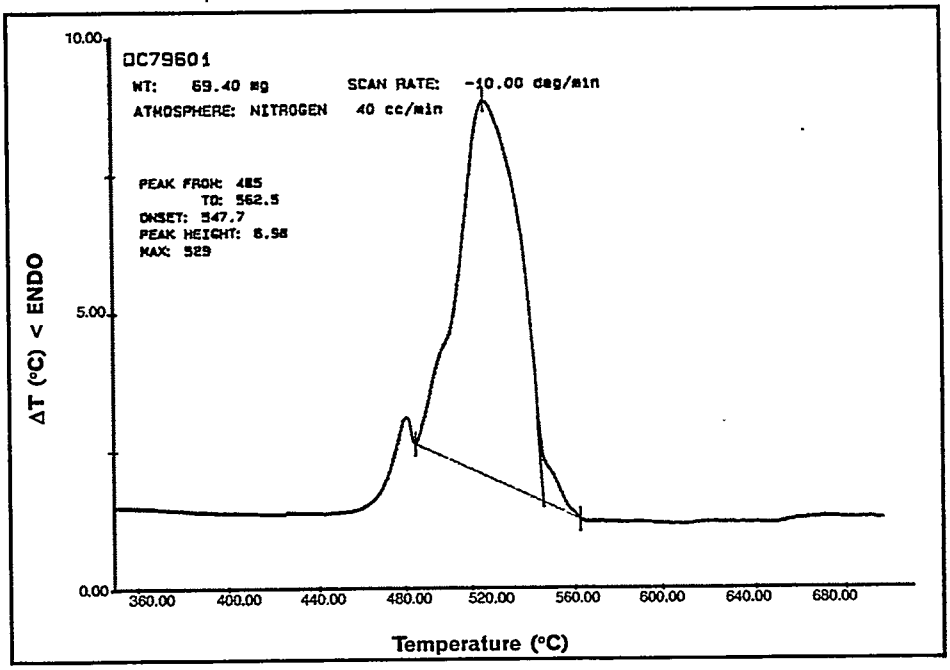

Fig. 3.13.4. DTA curve for Alloy 13 cooled at 10 °C/min.

ALLOY 13

Alloy #14	Wt.%	Si	Mg	Fe	Cu	Ni	Cr	Mn	Ti	Zn	Sr	Al
		12.94	0.48	0.74	4.77	0.50	0.01	0.57	0.01	0.55	0.00	Balance

Tensile	Strength	Ultimate	25°C	Ksi	41.9±4.0
				MPa	288.9±27.6
			100°C	Ksi	44.0±2.8
				MPa	303.2±19.1
			200°C	Ksi	34.5±2.2
				MPa	238.2±14.9
		Yield	25°C	Ksi	32.9±0.7
				MPa	226.8±4.8
			100°C	Ksi	32.7±0.4
				MPa	225.1±3.0
			200°C	Ksi	31.5±0.8
				MPa	217.4±5.3
	Elongation		25°C	%	0.67±0.32
			100°C	%	1.08±0.57
			200°C	%	0.74±0.54
	Modulus of Elasticity		25°C	10^3 Ksi	11.65±0.39
				10^3 MPa	80.28±2.68
			100°C	10^3 Ksi	9.14±0.09
				10^3 MPa	63.04±0.64
			200°C	10^3 Ksi	8.52±0.33
				10^3 MPa	58.74±2.27
Endurance Limit	100,000,000 cycles		25°C	Ksi	22.26
				MPa	153.48
	500,000,000 cycles		25°C	Ksi	22.08
				MPa	152.24
Impact Resistance	Absorbed Energy		25°C	Joules	1.71±0.17
				lb.ft.	1.26±0.13
Wear Resistance	Volume Loss		25°C	cm^3	0.4383±0.0263
Hardness	¼ × ¼ inch flat die casting		25°C	RHB	74.6±1.5
	3/8 inch diameter die casting		25°C	RHB	66.9±1.7
	5/8 inch diameter die casting		25°C	RHB	66.5±2.3
Thermal Conductivity			25°C	W/m.K	113.0±0.2
Electrical Conductivity			25°C	% IACS	21.65±0.11
Electrical Resistivity			25°C	10^{-8} Ωm	7.963±0.042
Specific Gravity			25°C	g/cm^3	2.749

ALLOY 14

Alloy #14	Wt.%	Si	Mg	Fe	Cu	Ni	Cr	Mn	Ti	Zn	Sr	Al
		12.94	0.48	0.74	4.77	0.50	0.01	0.57	0.01	0.55	0.00	Balance

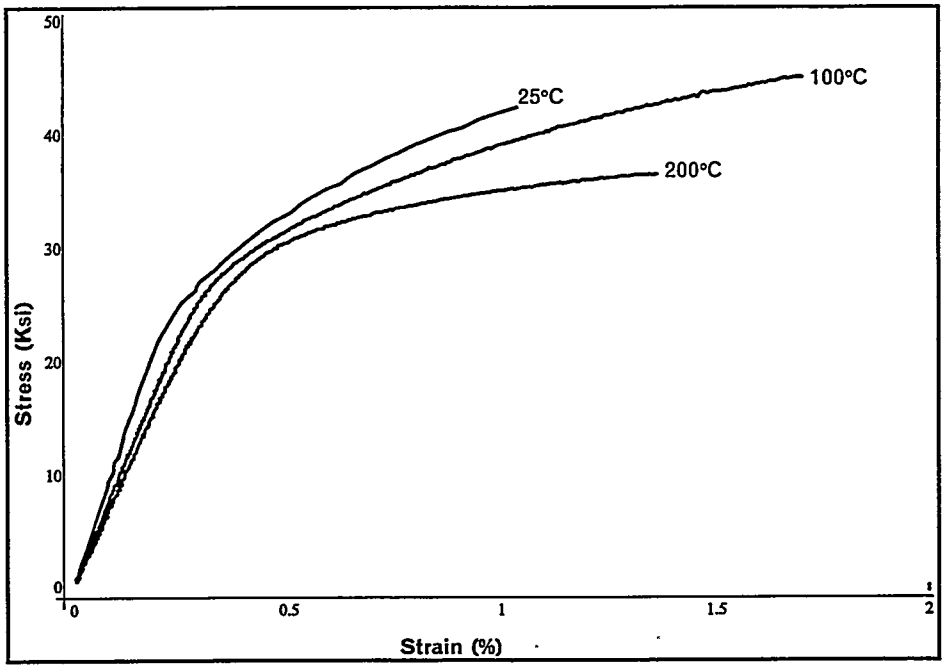

14.1. Typical stress vs strain curves for Alloy 14 at temperatures of 25°C, 100 °C, and 200 °C.

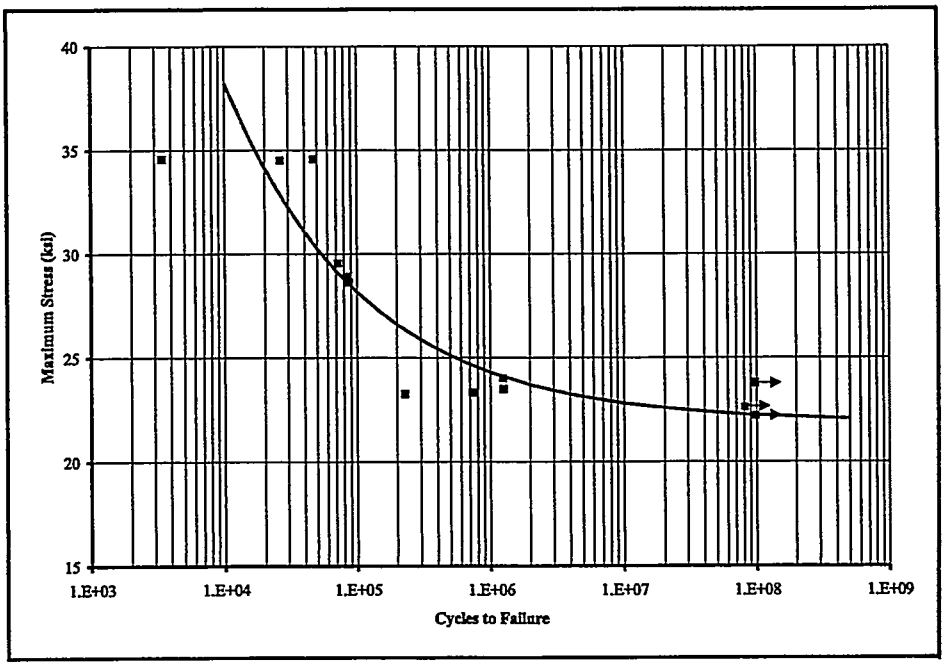

Fig. 3.14.2. S/N curve for Alloy 14.

ALLOY 14

Alloy #14	Wt.%	Si	Mg	Fe	Cu	Ni	Cr	Mn	Ti	Zn	Sr	Al
		12.94	0.48	0.74	4.77	0.50	0.01	0.57	0.01	0.55	0.00	Balance

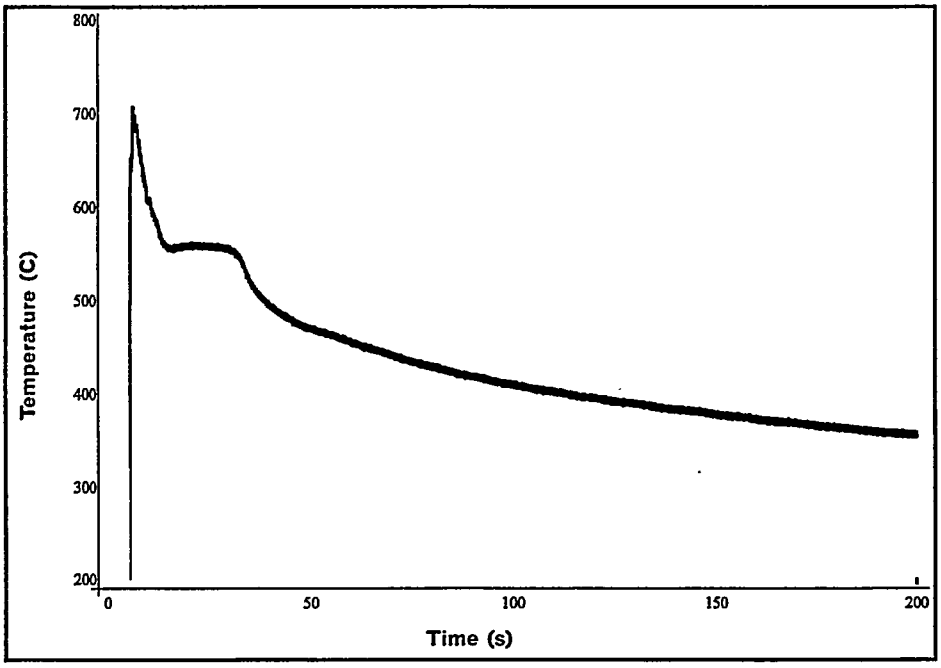

Fig. 3.14.3. Thermal history of Alloy 14 cast in a graphite mold.

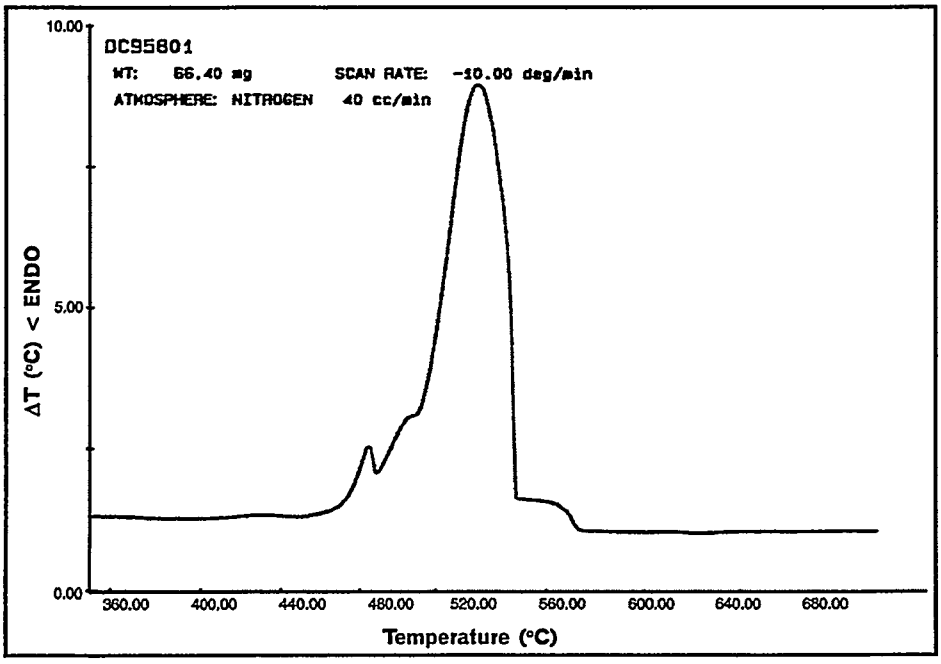

Fig. 3.14.4. DTA curve for Alloy 14 cooled at 10 °C/min.

ALLOY 14

Alloy #15	Wt.%	Si	Mg	Fe	Cu	Ni	Cr	Mn	Ti	Zn	Sr	Al
		12.78	0.47	1.51	1.27	0.06	0.14	0.01	0.18	2.94	0.00	Balance

Tensile	Strength	Ultimate	25°C	Ksi	42.6±2.1
				MPa	293.7±14.5
			100°C	Ksi	39.4±2.9
				MPa	271.8±19.9
			200°C	Ksi	34.6±0.6
				MPa	238.5±4.4
		Yield	25°C	Ksi	29.2±0.4
				MPa	201.3±2.8
			100°C	Ksi	29.1±0.8
				MPa	200.5±5.2
			200°C	Ksi	28.5±0.2
				MPa	196.6±1.3
	Elongation		25°C	%	0.97±0.17
			100°C	%	1.10±0.41
			200°C	%	1.66±0.29
	Modulus of Elasticity		25°C	10^3 Ksi	11.64±0.56
				10^3 MPa	80.25±3.88
			100°C	10^3 Ksi	9.44±0.38
				10^3 MPa	65.05±2.61
			200°C	10^3 Ksi	8.28±0.17
				10^3 MPa	57.05±1.22
Endurance Limit	100,000,000 cycles		25°C	Ksi	19.15
				MPa	132.03
	500,000,000 cycles		25°C	Ksi	18.51
				MPa	127.62
Impact Resistance	Absorbed Energy		25°C	Joules	2.24±0.35
				lb.ft.	1.65±0.26
Wear Resistance	Volume Loss		25°C	cm^3	0.4683±0.0185
Hardness	¼ × ¼ inch flat die casting		25°C	RHB	70.4±1.6
	3/8 inch diameter die casting		25°C	RHB	61.4±2.6
	5/8 inch diameter die casting		25°C	RHB	60.7±1.5
Thermal Conductivity			25°C	W/m.K	99.9±2.2
Electrical Conductivity			25°C	% IACS	20.19±0.58
Electrical Resistivity			25°C	10^{-8} Ωm	8.541±0.246
Specific Gravity			25°C	g/cm^3	2.755

ALLOY 15

Alloy #15	Wt.%	Si	Mg	Fe	Cu	Ni	Cr	Mn	Ti	Zn	Sr	Al
		12.78	0.47	1.51	1.27	0.06	0.14	0.01	0.18	2.94	0.00	Balance

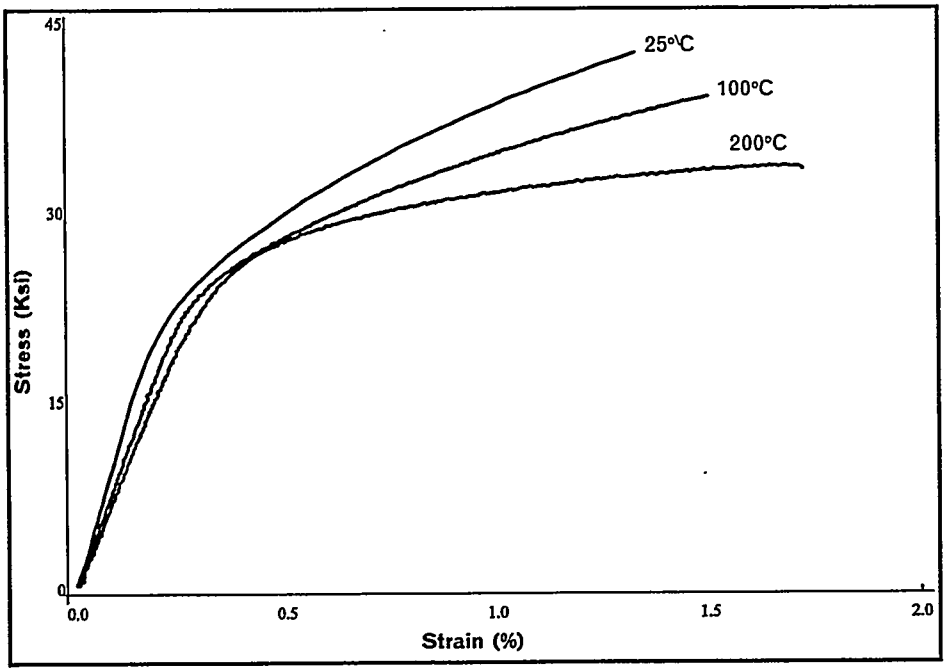

Fig. 3.15.1. Typical stress vs strain curves for Alloy 15 at temperatures of 25°C, 100 °C, and 200 °C.

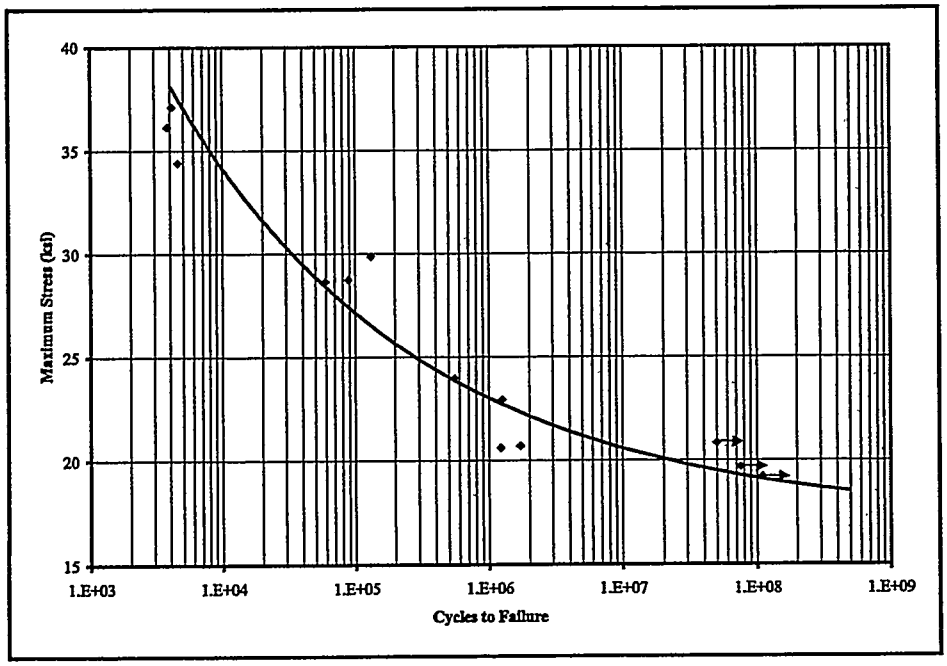

Fig. 3.15.2. S/N curve for Alloy 15.

ALLOY 15

Alloy #15	Wt.%	Si	Mg	Fe	Cu	Ni	Cr	Mn	Ti	Zn	Sr	Al
		12.78	0.47	1.51	1.27	0.06	0.14	0.01	0.18	2.94	0.00	Balance

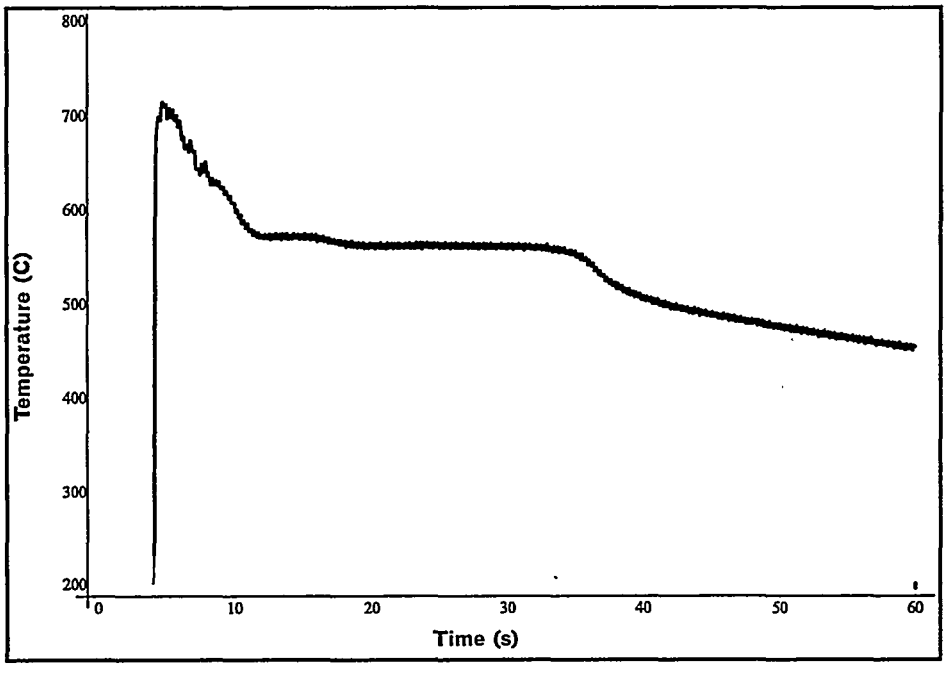

J.15.3. Thermal history of Alloy 15 cast in a graphite mold.

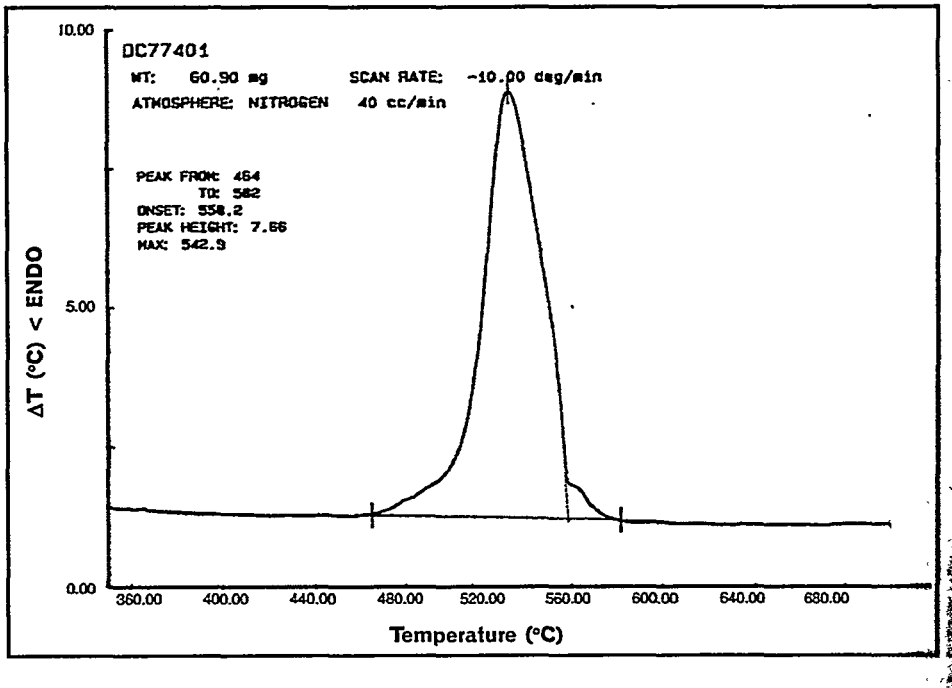

Fig. 3.15.4. DTA curve for Alloy 15 cooled at 10 °C/min.

ALLOY 15

Alloy #16	Wt.%	Si	Mg	Fe	Cu	Ni	Cr	Mn	Ti	Zn	Sr	Al
		12.86	0.41	1.63	1.21	0.06	0.14	0.44	0.01	0.46	0.024	Balance

Tensile	Strength	Ultimate	25°C	Ksi	43.0±2.5
				MPa	296.5±17.2
			100°C	Ksi	41.5±2.0
				MPa	286.4±13.5
			200°C	Ksi	32.7±2.2
				MPa	225.4±15.2
		Yield	25°C	Ksi	26.9±0.4
				MPa	185.5±2.8
			100°C	Ksi	27.2±0.3
				MPa	187.3±1.9
			200°C	Ksi	26.4±2.5
				MPa	182.2±17.5
	Elongation		25°C	%	1.41±0.39
			100°C	%	1.92±0.44
			200°C	%	1.81±0.64
	Modulus of Elasticity		25°C	10^3 Ksi	11.62±0.70
				10^3 MPa	80.12±4.83
			100°C	10^3 Ksi	8.92±0.26
				10^3 MPa	61.52±1.80
			200°C	10^3 Ksi	7.93±1.06
				10^3 MPa	54.70±7.28
Endurance Limit	100,000,000 cycles		25°C	Ksi	20.30
				MPa	139.96
	500,000,000 cycles		25°C	Ksi	20.12
				MPa	138.72
Impact Resistance	Absorbed Energy		25°C	Joules	2.67±0.22
				lb.ft.	1.97±0.16
Wear Resistance	Volume Loss		25°C	cm^3	0.4871±0.0210
Hardness	¼ × ¼ inch flat die casting		25°C	RHB	63.1±1.0
	3/8 inch diameter die casting		25°C	RHB	52.8±1.1
	5/8 inch diameter die casting		25°C	RHB	50.7±1.1
Thermal Conductivity			25°C	W/m.K	116.1±1.1
Electrical Conductivity			25°C	% IACS	24.53±0.49
Electrical Resistivity			25°C	10^{-8} Ωm	7.029±0.141
Specific Gravity			25°C	g/cm^3	2.719

ALLOY 16

Alloy #16	Wt.%	Si	Mg	Fe	Cu	Ni	Cr	Mn	Ti	Zn	Sr	Al
		12.86	0.41	1.63	1.21	0.06	0.14	0.44	0.01	0.46	0.024	Balance

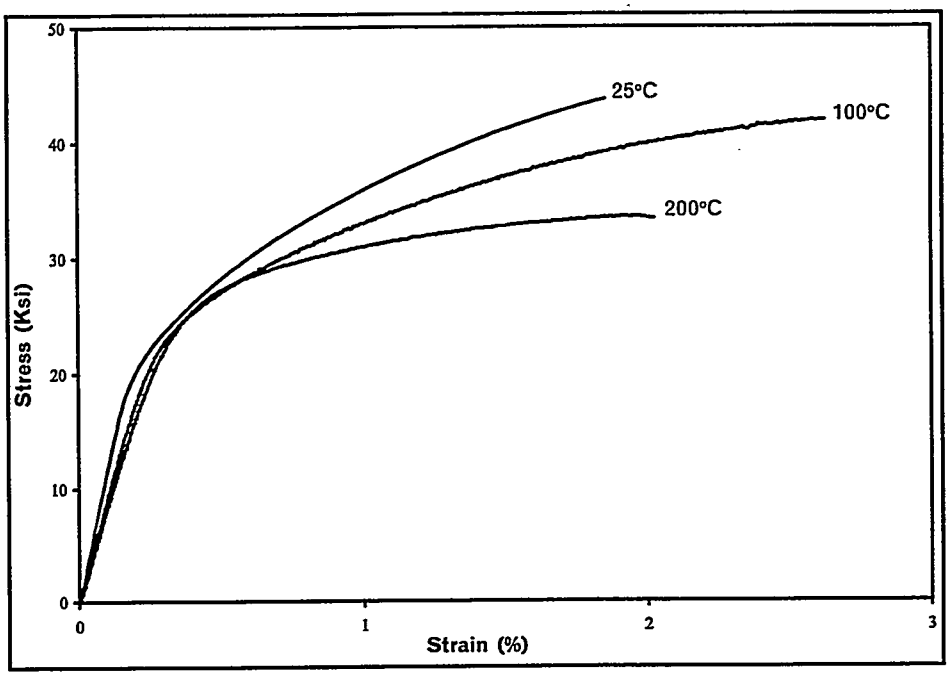

Fig. 3.16.1. Typical stress vs strain curves for Alloy 16 at temperatures of 25°C, 100 °C, and 200 °C.

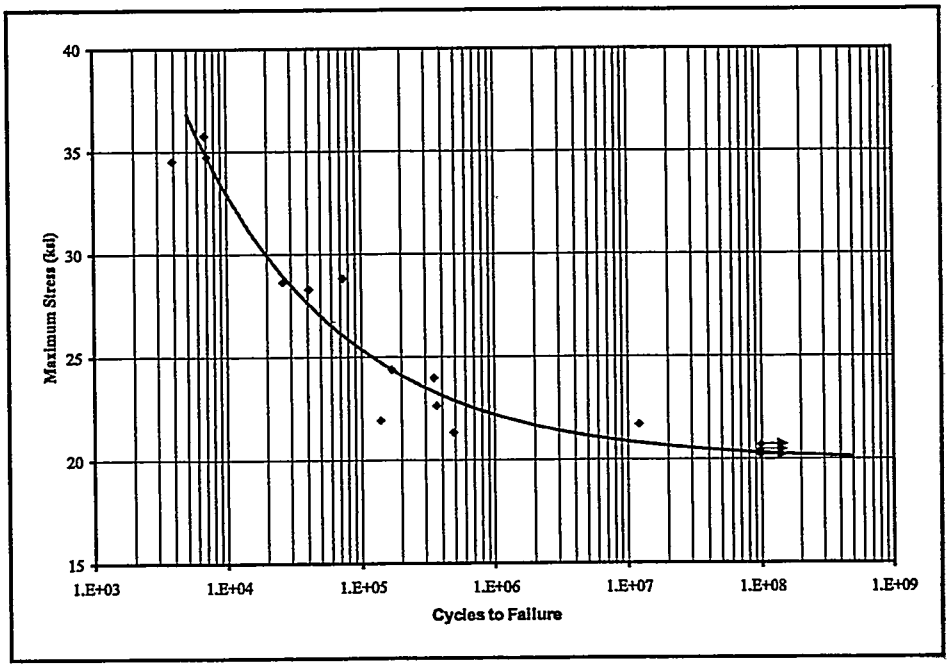

Fig. 3.16.2. S/N curve for Alloy 16.

ALLOY 16

Alloy #16	Wt.%	Si	Mg	Fe	Cu	Ni	Cr	Mn	Ti	Zn	Sr	Al
		12.86	0.41	1.63	1.21	0.06	0.14	0.44	0.01	0.46	0.024	Balance

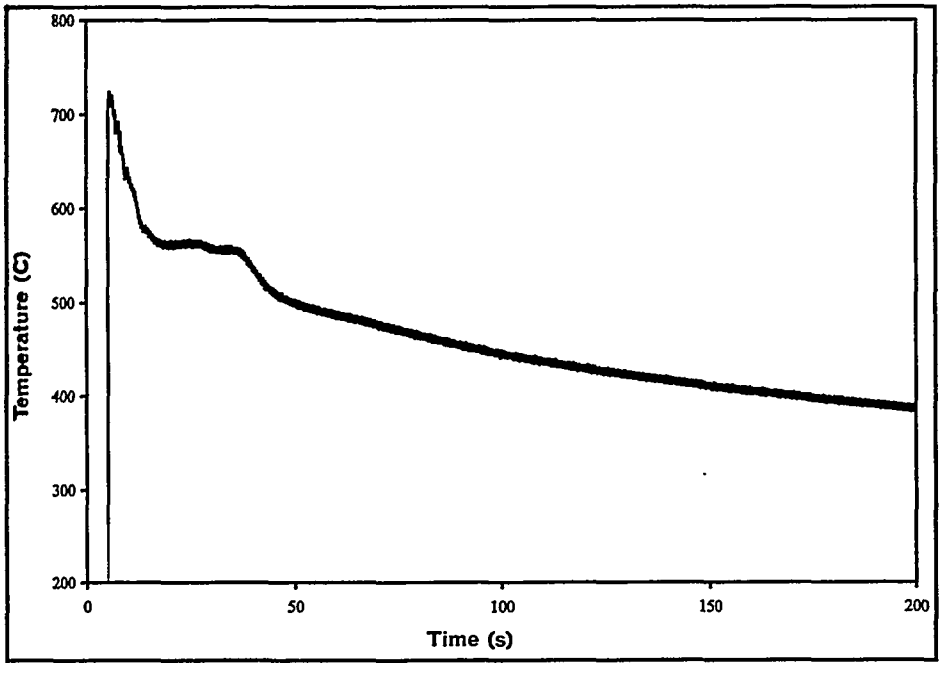

Fig. 3.16.3. Thermal history of Alloy 16 cast in a graphite mold.

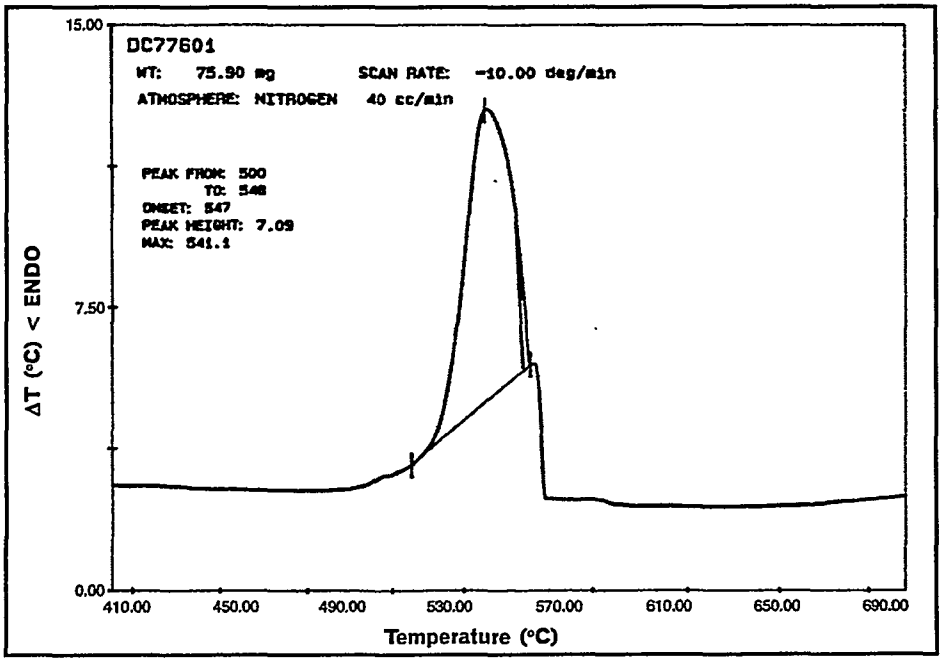

Fig. 3.16.4. DTA curve for Alloy 16 cooled at 10 °C/min.

ALLOY 16

Alloy #17	Wt.%	Si	Mg	Fe	Cu	Ni	Cr	Mn	Ti	Zn	Sr	Al
		8.39	0.02	0.90	2.71	0.04	0.06	0.22	0.03	1.10	—	balance

Tensile	Strength	Ultimate	25°C	Ksi	45.0±0.7
				MPa	310.3±4.8
			100°C	Ksi	38.2±0.9
				MPa	263.4±6.2
			200°C	Ksi	24.3±0.4
				MPa	167.5±2.8
		Yield	25°C	Ksi	19.6±0.3
				MPa	135.1±2.1
			100°C	Ksi	20.1±0.3
				MPa	138.6±2.1
			200°C	Ksi	17.6±0.3
				MPa	121.3±2.1
	Elongation		25°C	%	5.34±0.59
			100°C	%	7.27±2.39
			200°C	%	12.57±1.73
	Modulus of Elasticity		25°C	10^3 Ksi	10.91±0.68
				10^3 MPa	75.24±4.68
			100°C	10^3 Ksi	8.04±0.74
				10^3 MPa	55.41±5.09
			200°C	10^3 Ksi	7.88±0.26
				10^3 MPa	54.36±1.81
Endurance Limit	100,000,000 cycles		25°C	Ksi	18.48
				MPa	127.42
	500,000,000 cycles		25°C	Ksi	18.24
				MPa	125.76
Impact Resistance	Absorbed Energy		25°C	Joules	5.02±0.39
				lb.ft.	3.70±0.29
Wear Resistance	Volume Loss		25°C	cm^3	0.4150±0.0330
Hardness	¼ × ¼ inch flat die casting		25°C	RHB	47.4±1.0
	3/8 inch diameter die casting		25°C	RHB	39.9±1.4
	5/8 inch diameter die casting		25°C	RHB	37.3±2.1
Thermal Conductivity			25°C	W/m.K	122.1±1.0
Electrical Conductivity			25°C	% IACS	26.12±0.38
Electrical Resistivity			25°C	10^{-8} Ωm	6.601±0.096
Specific Gravity			25°C	g/cm^3	2.770

ALLOY 17

Alloy #17	Wt.%	Si	Mg	Fe	Cu	Ni	Cr	Mn	Ti	Zn	Sr	Al
		8.39	0.02	0.90	2.71	0.04	0.06	0.22	0.03	1.10	–	balance

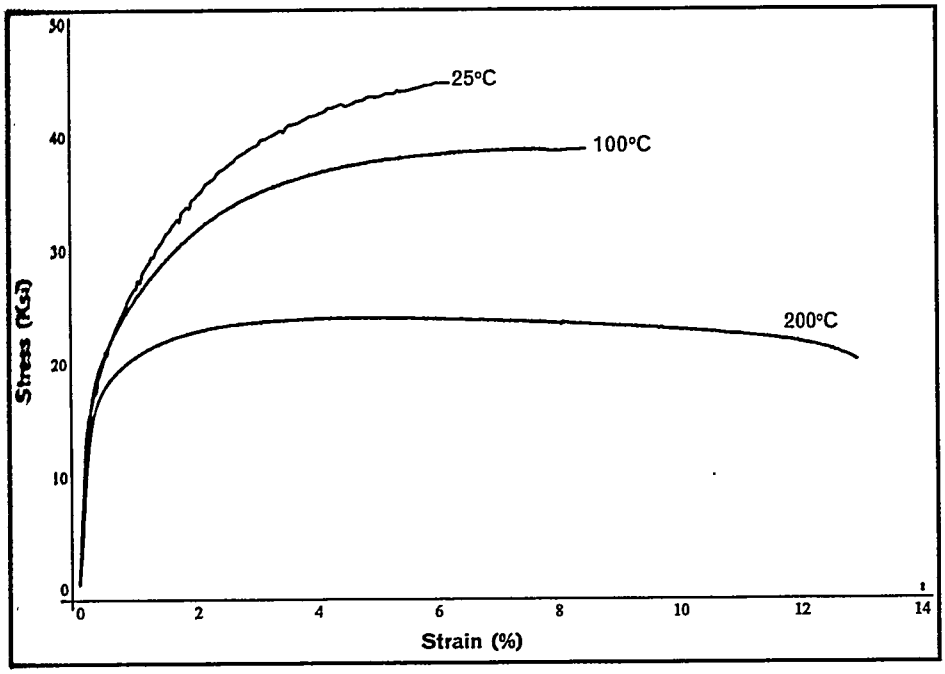

Fig. 3.17.1. Typical stress vs strain curves for Alloy 17 at temperatures of 25°C, 100 °C, and 200 °C.

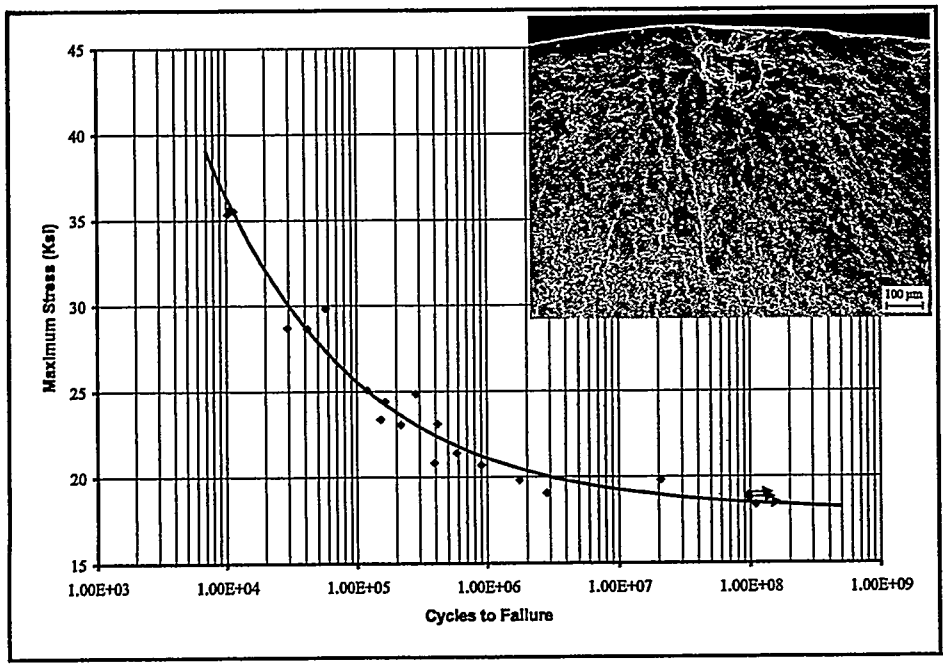

Fig. 3.17.2. S/N curve for Alloy 17; the fracture surface shown is from the specimen which failed at 9.1 x 10^5 cycles under a maximum stress of 20.7 ksi.

ALLOY 17

Alloy #17	Wt.%	Si	Mg	Fe	Cu	Ni	Cr	Mn	Ti	Zn	Sr	Al
		8.39	0.02	0.90	2.71	0.04	0.06	0.22	0.03	1.10	–	balance

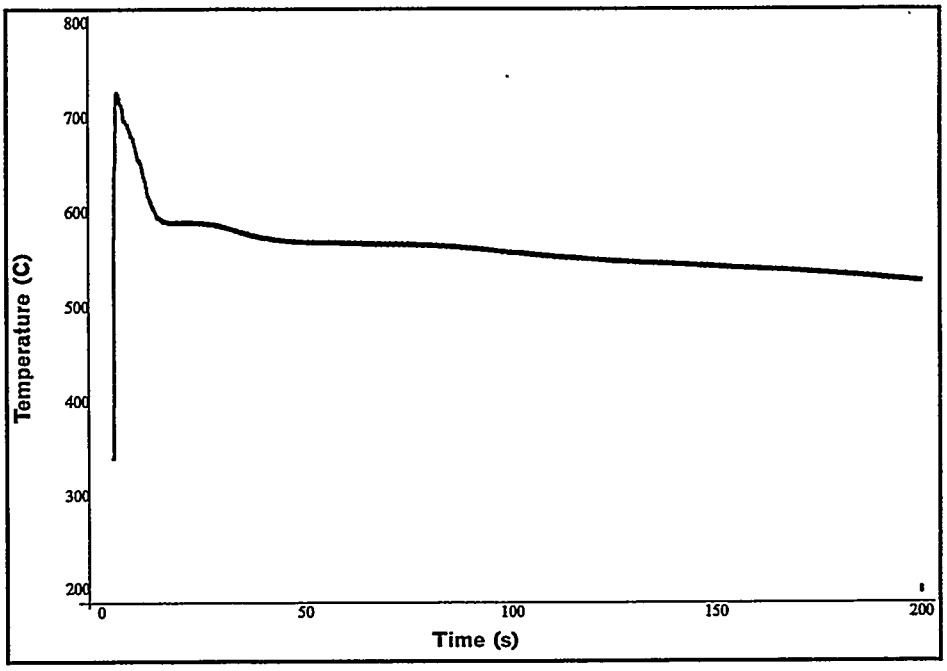

17.3. Thermal history of Alloy 17 cast in a graphite mold.

ALLOY 17

Alloy #18	Wt.%	Si	Mg	Fe	Cu	Ni	Cr	Mn	Ti	Zn	Sr	Al
		8.19	0.02	0.91	3.87	0.03	0.04	0.17	0.03	2.20	—	balance

Tensile	Strength	Ultimate	25°C	Ksi	46.2±0.8
				MPa	318.5±5.5
			100°C	Ksi	41.4±0.1
				MPa	285.4±0.7
			200°C	Ksi	25.6±0.4
				MPa	176.5±2.8
		Yield	25°C	Ksi	21.8±0.7
				MPa	150.3±4.8
			100°C	Ksi	22.2±0.5
				MPa	153.1±3.4
			200°C	Ksi	18.9±0.3
				MPa	130.3±2.1
	Elongation		25°C	%	3.68±0.49
			100°C	%	5.79±1.16
			200°C	%	7.16±3.14
	Modulus of Elasticity		25°C	10^3 Ksi	10.92±0.80
				10^3 MPa	75.28±5.54
			100°C	10^3 Ksi	8.30±0.47
				10^3 MPa	57.21±3.25
			200°C	10^3 Ksi	7.98±0.13
				10^3 MPa	55.01±0.90
Endurance Limit	100,000,000 cycles		25°C	Ksi	17.53
				MPa	120.87
	500,000,000 cycles		25°C	Ksi	17.03
				MPa	117.42
Impact Resistance	Absorbed Energy		25°C	Joules	3.35±0.50
				lb.ft.	2.47±0.37
Wear Resistance	Volume Loss		25°C	cm^3	0.4375±0.0274
Hardness	¼ × ¼ inch flat die casting		25°C	RHB	54.9±0.9
	3/8 inch diameter die casting		25°C	RHB	45.4±1.5
	5/8 inch diameter die casting		25°C	RHB	45.3±1.3
Thermal Conductivity			25°C	W/m.K	119.1±1.8
Electrical Conductivity			25°C	% IACS	24.00±0.14
Electrical Resistivity			25°C	10^{-8} Ωm	7.184±0.042
Specific Gravity			25°C	g/cm^3	2.816

ALLOY 18

Alloy #18	Wt.%	Si	Mg	Fe	Cu	Ni	Cr	Mn	Ti	Zn	Sr	Al
		8.19	0.02	0.91	3.87	0.03	0.04	0.17	0.03	2.20	–	balance

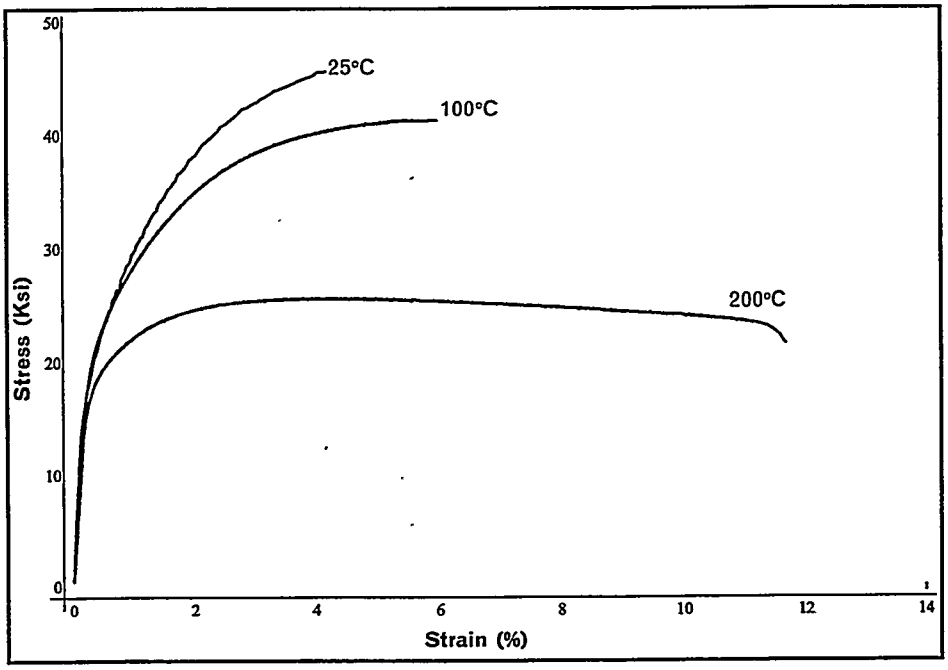

18.1. Typical stress vs strain curves for Alloy 18 at temperatures of 25°C, 100 °C, and 200 °C.

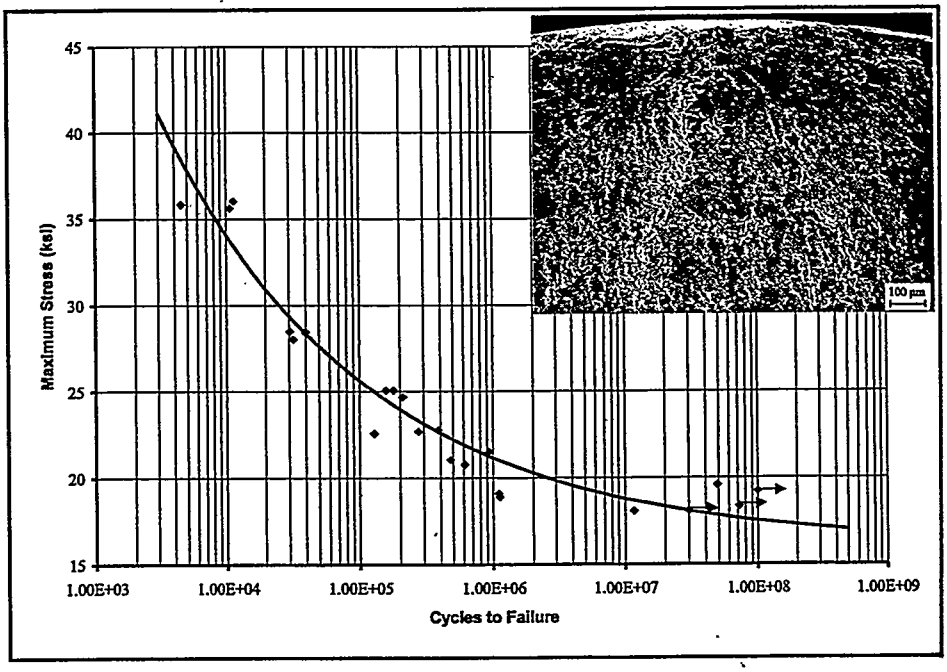

18.2. S/N curve for Alloy 18; the fracture surface shown is from the specimen which failed at 9.4 x 10^5 cycles under a maximum stress of 21.5 ksi.

ALLOY 18

Alloy #18	Wt.%	Si	Mg	Fe	Cu	Ni	Cr	Mn	Ti	Zn	Sr	Al
		8.19	0.02	0.91	3.87	0.03	0.04	0.17	0.03	2.20	–	balance

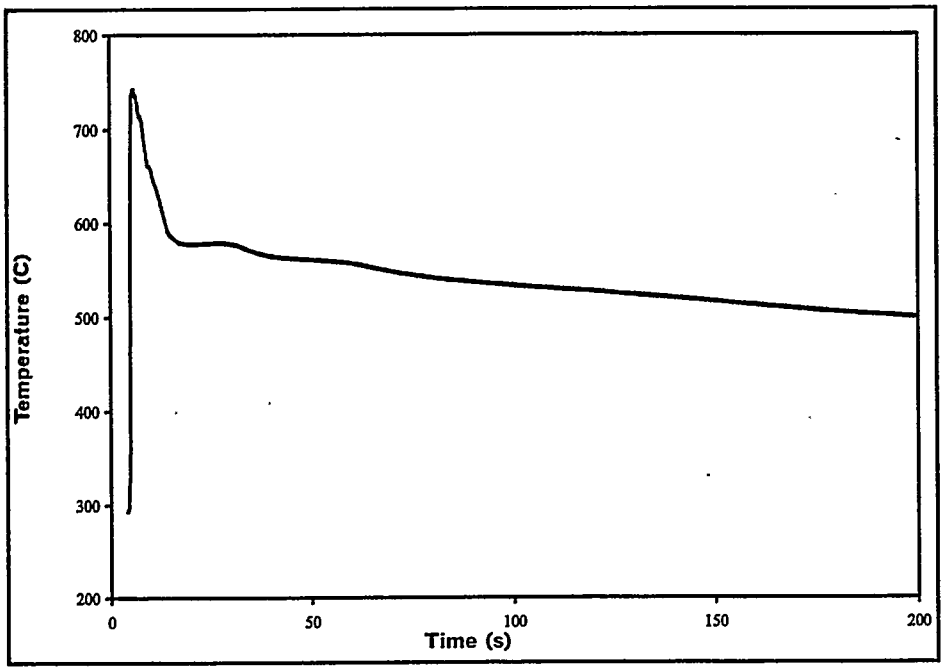

Fig. 3.18.3. Thermal history of Alloy 18 cast in a graphite mold.

ALLOY 18

Alloy #19	Wt.%	Si	Mg	Fe	Cu	Ni	Cr	Mn	Ti	Zn	Sr	Al
		9.49	0.02	0.87	2.61	0.03	0.05	0.23	0.03	2.20	—	balance

Tensile	Strength	Ultimate	25°C	Ksi	45.4±1.6
				MPa	313.0±11.0
			100°C	Ksi	38.8±1.8
				MPa	267.5±12.4
			200°C	Ksi	23.8±0.4
				MPa	164.1±2.8
		Yield	25°C	Ksi	20.3±0.3
				MPa	140.0±2.1
			100°C	Ksi	20.5±0.3
				MPa	141.3±2.1
			200°C	Ksi	17.4±0.3
				MPa	120.0±2.1
	Elongation		25°C	%	4.62±1.00
			100°C	%	6.50±2.49
			200°C	%	13.17±2.36
	Modulus of Elasticity		25°C	10^3 Ksi	11.03±0.77
				10^3 MPa	76.06±5.32
			100°C	10^3 Ksi	8.60±0.91
				10^3 MPa	59.26±6.24
			200°C	10^3 Ksi	8.43±0.23
				10^3 MPa	58.11±1.55
Endurance Limit	100,000,000 cycles		25°C	Ksi	18.42
				MPa	127.00
	500,000,000 cycles		25°C	Ksi	18.20
				MPa	125.48
Impact Resistance	Absorbed Energy		25°C	Joules	4.31±0.26
				lb.ft.	3.18±0.19
Wear Resistance	Volume Loss		25°C	cm^3	0.4213±0.0253
Hardness	¼ × ¼ inch flat die casting		25°C	RHB	50.9±1.3
	3/8 inch diameter die casting		25°C	RHB	43.0±1.3
	5/8 inch diameter die casting		25°C	RHB	41.0±1.7
Thermal Conductivity			25°C	W/m.K	121.0±0.4
Electrical Conductivity			25°C	% IACS	24.34±0.25
Electrical Resistivity			25°C	10^{-8} Ωm	7.083±0.074
Specific Gravity			25°C	g/cm^3	2.780

ALLOY 19

Alloy #19	Wt.%	Si	Mg	Fe	Cu	Ni	Cr	Mn	Ti	Zn	Sr	Al
		9.49	0.02	0.87	2.61	0.03	0.05	0.23	0.03	2.20	–	balance

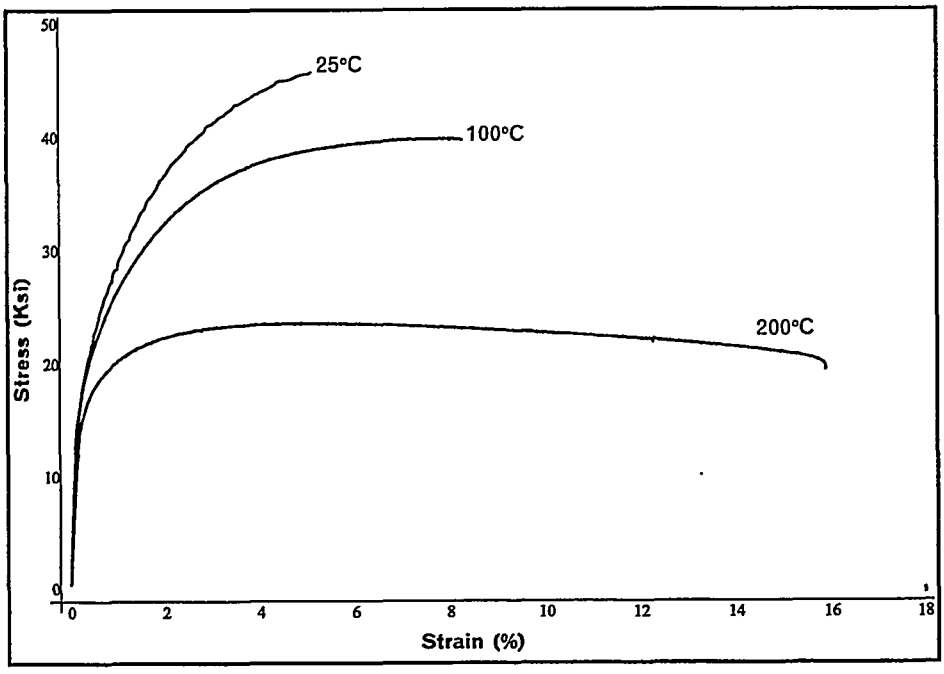

Fig. 3.19.1. Typical stress vs strain curves for Alloy 19 at temperatures of 25°C, 100 °C, and 200 °C.

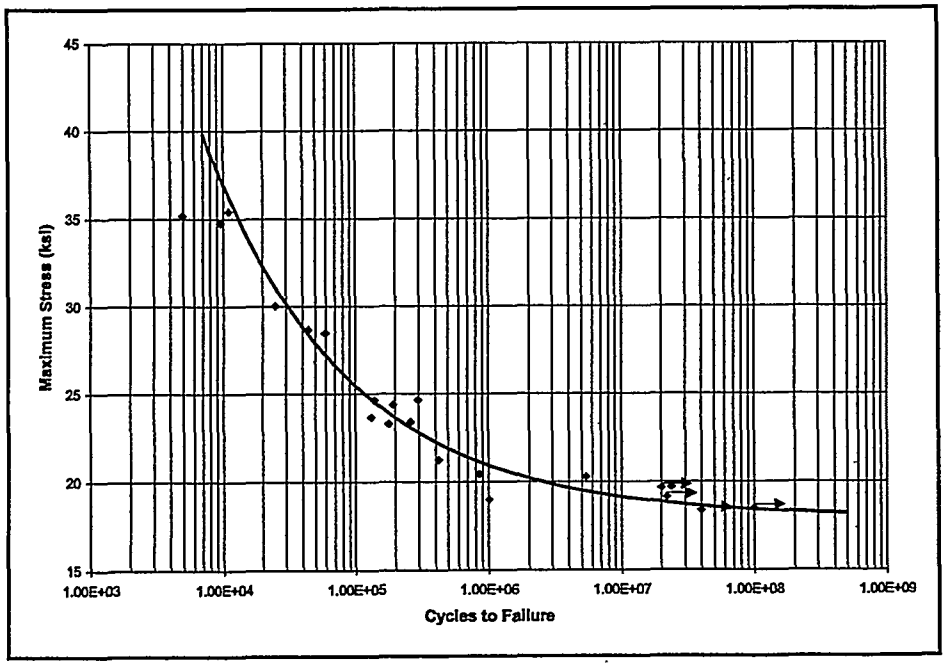

Fig. 3.19.2. S/N curve for Alloy 19; the fracture surface shown is from the specimen which failed at 8.5 x 10^5 cycles under a maximum stress of 20.4 ksi.

ALLOY 19

Alloy #19	Wt.%	Si	Mg	Fe	Cu	Ni	Cr	Mn	Ti	Zn	Sr	Al
		9.49	0.02	0.87	2.61	0.03	0.05	0.23	0.03	2.20	–	balance

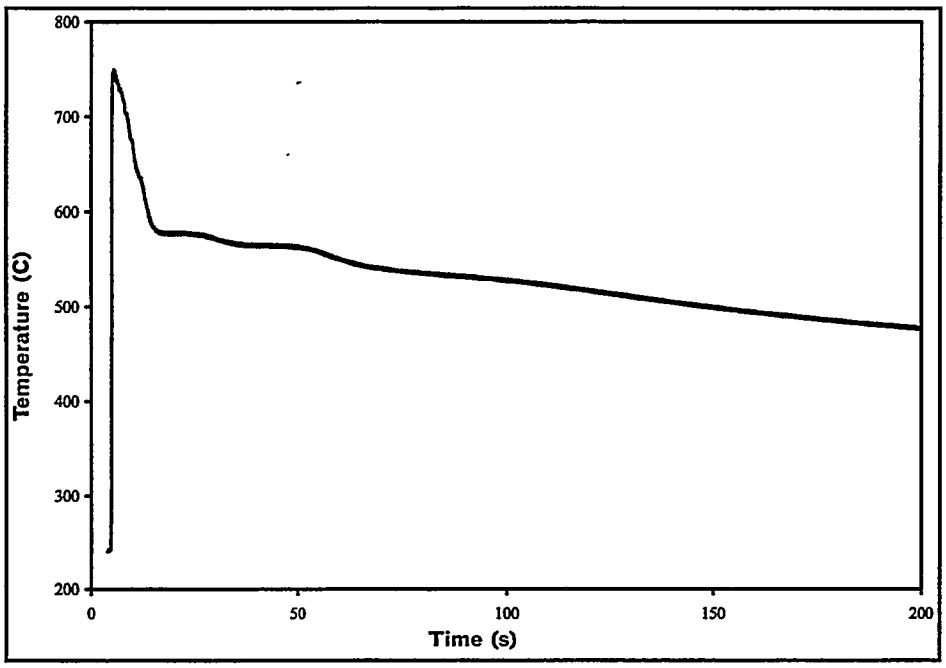

19.3. Thermal history of Alloy 19 cast in a graph-
old.

ALLOY 19

Alloy #20	Wt.%	Si	Mg	Fe	Cu	Ni	Cr	Mn	Ti	Zn	Sr	Al
		9.50	0.09	1.43	4.00	0.13	0.06	0.21	0.05	1.10	–	balance

Tensile	Strength	Ultimate	25°C	Ksi	45.4±2.6
				MPa	313.0±17.9
			100°C	Ksi	43.4±0.7
				MPa	299.2±4.8
			200°C	Ksi	31.0±0.5
				MPa	213.7±3.4
		Yield	25°C	Ksi	25.1±0.2
				MPa	173.1±1.4
			100°C	Ksi	25.3±0.3
				MPa	174.4±2.1
			200°C	Ksi	23.3±0.2
				MPa	160.6±1.4
	Elongation		25°C	%	1.93±0.44
			100°C	%	3.12±0.49
			200°C	%	3.65±1.24
	Modulus of Elasticity		25°C	10^3 Ksi	11.32±0.36
				10^3 MPa	78.03±2.46
			100°C	10^3 Ksi	8.78±0.43
				10^3 MPa	60.52±2.97
			200°C	10^3 Ksi	8.33±0.21
				10^3 MPa	57.41±1.48
Endurance Limit	100,000,000 cycles		25°C	Ksi	17.94
				MPa	123.69
	500,000,000 cycles		25°C	Ksi	17.07
				MPa	117.69
Impact Resistance	Absorbed Energy		25°C	Joules	2.43±0.30
				lb.ft.	1.79±0.22
Wear Resistance	Volume Loss		25°C	cm^3	0.4516±0.0298
Hardness	¼ × ¼ inch flat die casting		25°C	RHB	64.4±1.0
	3/8 inch diameter die casting		25°C	RHB	57.6±1.4
	5/8 inch diameter die casting		25°C	RHB	57.0±1.3
Thermal Conductivity			25°C	W/m.K	111.0±0.4
Electrical Conductivity			25°C	% IACS	22.13±0.09
Electrical Resistivity			25°C	10^{-8} Ωm	7.791±0.031
Specific Gravity			25°C	g/cm^3	2.802

ALLOY 20

Alloy #20	Wt.%	Si	Mg	Fe	Cu	Ni	Cr	Mn	Ti	Zn	Sr	Al
		9.50	0.09	1.43	4.00	0.13	0.06	0.21	0.05	1.10	–	balance

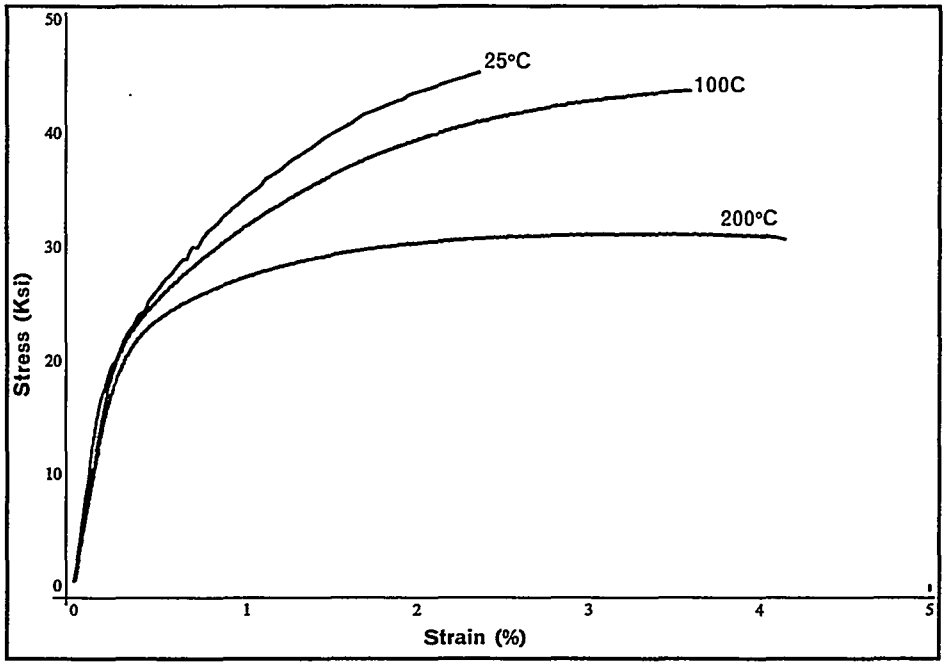

Fig. 3.20.1. Typical stress vs strain curves for Alloy 20 at temperatures of 25°C, 100 °C, and 200 °C.

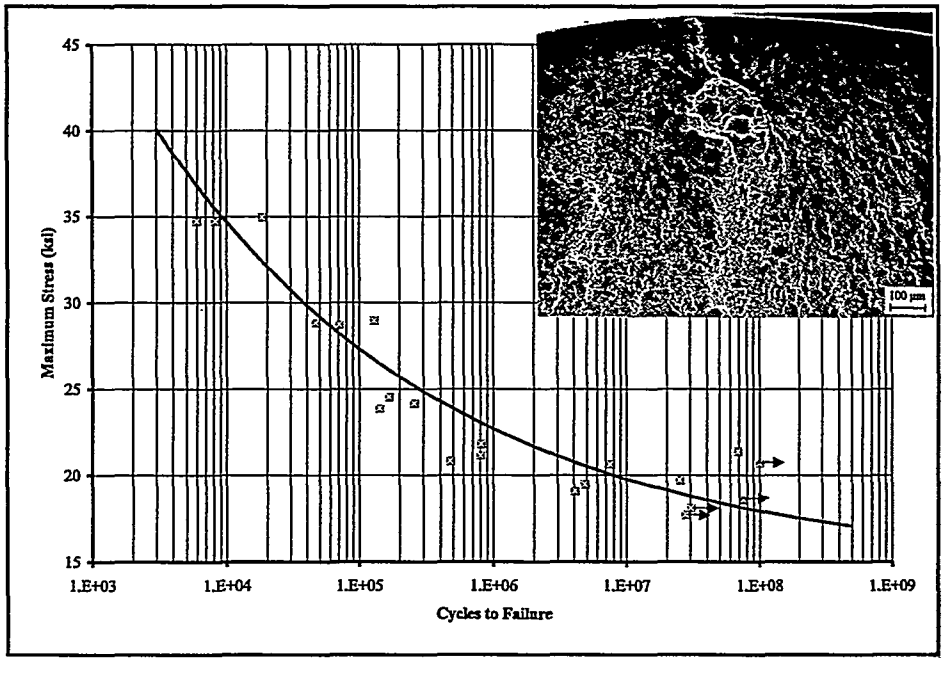

Fig. 3.20.2. S/N curve for Alloy 20; the fracture surface shown is from the specimen which failed at 8.1 x 10⁴ cycles under a maximum stress of 21.8 ksi.

ALLOY 20

Alloy	Wt.%	Si	Mg	Fe	Cu	Ni	Cr	Mn	Ti	Zn	Sr	Al
#20		9.50	0.09	1.43	4.00	0.13	0.06	0.21	0.05	1.10	–	balance

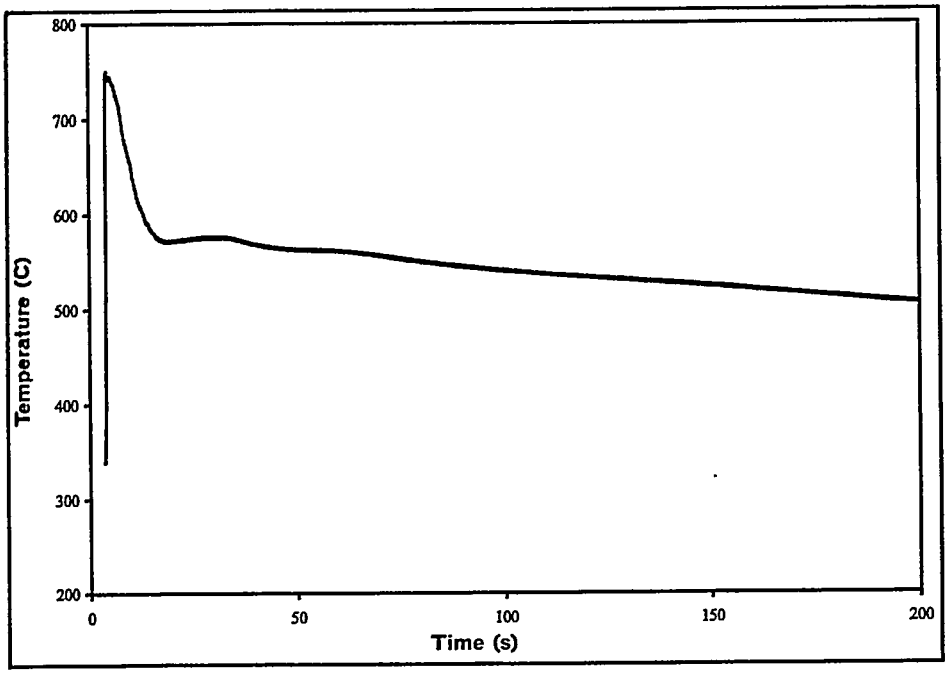

Fig. 3.20.3. Thermal history of Alloy 20 cast in a graphite mold.

ALLOY 20

Alloy #21	Wt.%	Si	Mg	Fe	Cu	Ni	Cr	Mn	Ti	Zn	Sr	Al
		9.66	0.05	1.22	2.68	0.03	0.06	0.26	0.03	2.10	–	balance

Tensile	Strength	Ultimate	25°C	Ksi	44.0±4.6
				MPa	303.4±31.7
			100°C	Ksi	40.0±1.6
				MPa	275.8±11.0
			200°C	Ksi	26.8±0.2
				MPa	184.8±1.4
		Yield	25°C	Ksi	21.8±0.7
				MPa	150.3±4.8
			100°C	Ksi	21.8±0.1
				MPa	150.3±0.7
			200°C	Ksi	19.4±0.3
				MPa	133.8±2.1
	Elongation		25°C	%	2.73±0.73
			100°C	%	4.73±1.83
			200°C	%	7.44±1.90
	Modulus of Elasticity		25°C	10^3 Ksi	10.96±0.68
				10^3 MPa	75.55±4.71
			100°C	10^3 Ksi	8.80±0.25
				10^3 MPa	60.67±1.69
			200°C	10^3 Ksi	8.35±0.13
				10^3 MPa	57.58±0.90
Endurance Limit	100,000,000 cycles		25°C	Ksi	20.42
				MPa	140.79
	500,000,000 cycles		25°C	Ksi	20.07
				MPa	138.38
Impact Resistance	Absorbed Energy		25°C	Joules	3.63±0.27
				lb.ft.	2.68±0.20
Wear Resistance	Volume Loss		25°C	cm^3	0.4457±0.0301
Hardness	¼ × ¼ inch flat die casting		25°C	RHB	56.5±0.9
	3/8 inch diameter die casting		25°C	RHB	49.1±1.1
	5/8 inch diameter die casting		25°C	RHB	48.0±1.4
Thermal Conductivity			25°C	W/m.K	113.8±2.6
Electrical Conductivity			25°C	% IACS	21.56±0.24
Electrical Resistivity			25°C	10^{-8} Ωm	7.999±0.088
Specific Gravity			25°C	g/cm^3	2.789

ALLOY 21

Alloy #21	Wt.%	Si	Mg	Fe	Cu	Ni	Cr	Mn	Ti	Zn	Sr	Al
		9.66	0.05	1.22	2.68	0.03	0.06	0.26	0.03	2.10	–	balance

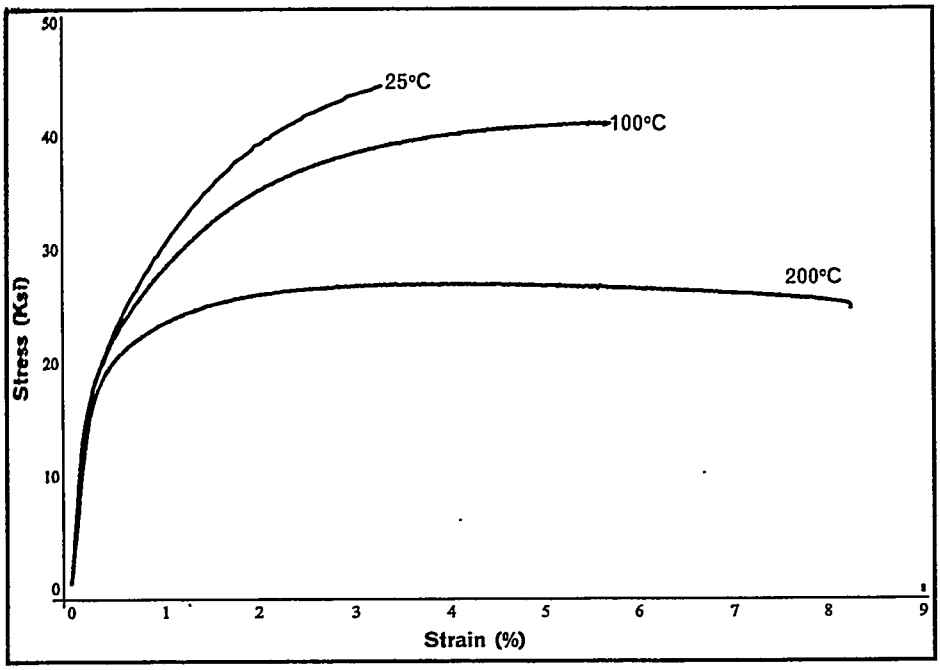

Fig. 3.21.1. Typical stress vs strain curves for Alloy 21 at temperatures of 25°C, 100 °C, and 200 °C.

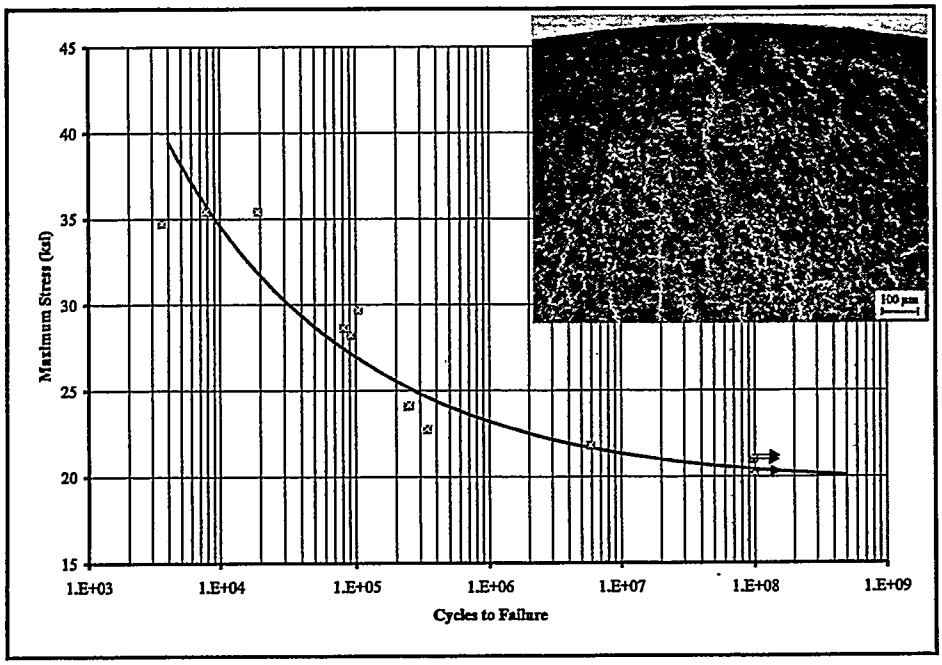

Fig. 3.21.2. S/N curve for Alloy 21; the fracture surface shown is from the specimen which failed at 3.4 x 10^5 cycles under a maximum stress of 22.8 ksi.

ALLOY 21

Alloy #21	Wt.%	Si	Mg	Fe	Cu	Ni	Cr	Mn	Ti	Zn	Sr	Al
		9.66	0.05	1.22	2.68	0.03	0.06	0.26	0.03	2.10	–	balance

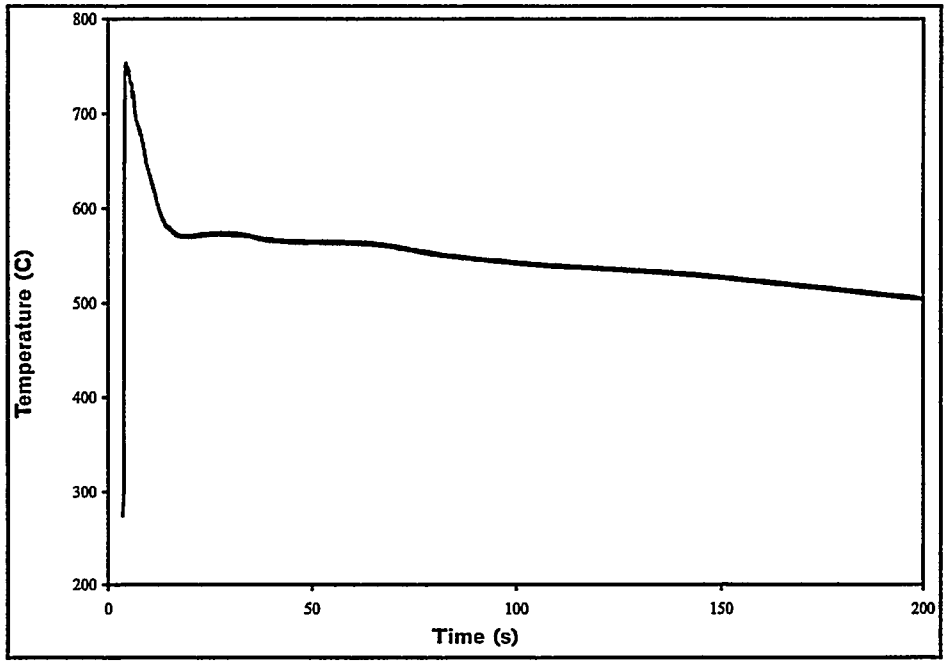

21.3. Thermal history of Alloy 21 cast in a graphite mold.

ALLOY 21

Alloy #22	Wt.%	Si	Mg	Fe	Cu	Ni	Cr	Mn	Ti	Zn	Sr	Al
		9.69	0.05	1.05	4.54	0.04	0.06	0.27	0.03	1.20	–	balance

Tensile	Strength	Ultimate	25°C	Ksi	45.6±3.2
				MPa	314.4±22.1
			100°C	Ksi	41.9±2.4
				MPa	288.9±16.5
			200°C	Ksi	28.9±0.4
				MPa	199.3±2.8
		Yield	25°C	Ksi	24.5±0.4
				MPa	168.9±2.8
			100°C	Ksi	25.2±0.3
				MPa	173.7±2.1
			200°C	Ksi	21.3±0.3
				MPa	146.9±2.1
	Elongation		25°C	%	2.3±0.74
			100°C	%	3.05±1.43
			200°C	%	7.06±2.97
	Modulus of Elasticity		25°C	10^3 Ksi	10.92±0.62
				10^3 MPa	75.27±4.30
			100°C	10^3 Ksi	8.75±0.17
				10^3 MPa	60.34±1.15
			200°C	10^3 Ksi	8.28±0.16
				10^3 MPa	57.06±1.12
Endurance Limit	100,000,000 cycles		25°C	Ksi	22.41
				MPa	154.51
	500,000,000 cycles		25°C	Ksi	22.10
				MPa	152.37
Impact Resistance	Absorbed Energy		25°C	Joules	3.35±0.37
				lb.ft.	2.47±0.27
Wear Resistance	Volume Loss		25°C	cm^3	0.4307±0.0285
Hardness	¼ × ¼ inch flat die casting		25°C	RHB	60.8±1.2
	3/8 inch diameter die casting		25°C	RHB	55.0±1.2
	5/8 inch diameter die casting		25°C	RHB	52.8±1.4
Thermal Conductivity			25°C	W/m.K	119.2±0.7
Electrical Conductivity			25°C	% IACS	23.21±0.45
Electrical Resistivity			25°C	10^{-8} Ωm	7.428±0.145
Specific Gravity			25°C	g/cm^3	2.799

ALLOY 22

Alloy #22	Wt.%	Si	Mg	Fe	Cu	Ni	Cr	Mn	Ti	Zn	Sr	Al
		9.69	0.05	1.05	4.54	0.04	0.06	0.27	0.03	1.20	–	balance

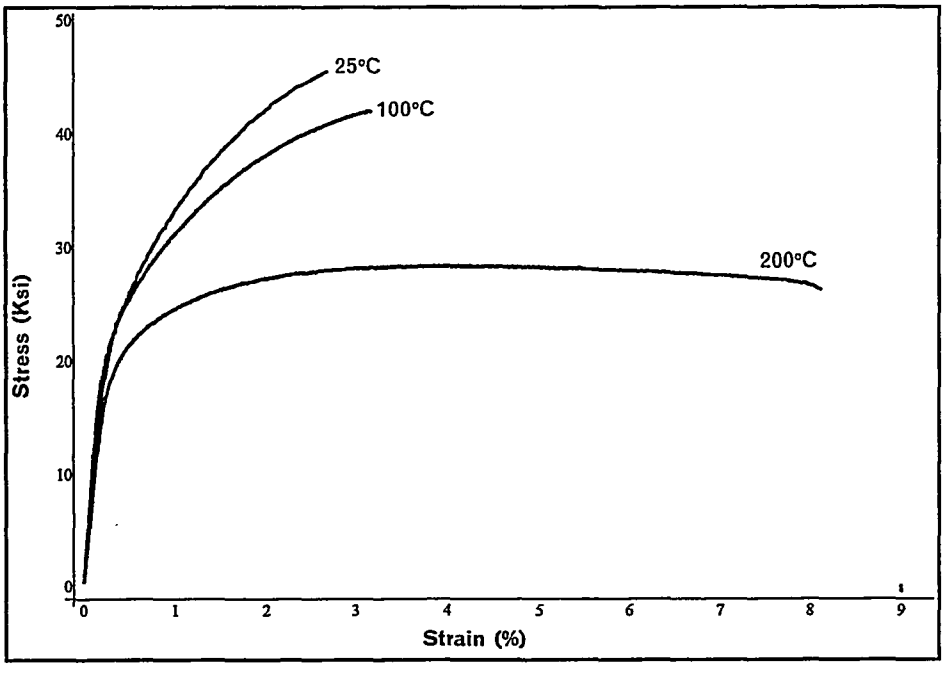

Fig. 22.1. Typical stress vs strain curves for Alloy 22 at temperatures of 25°C, 100 °C, and 200 °C.

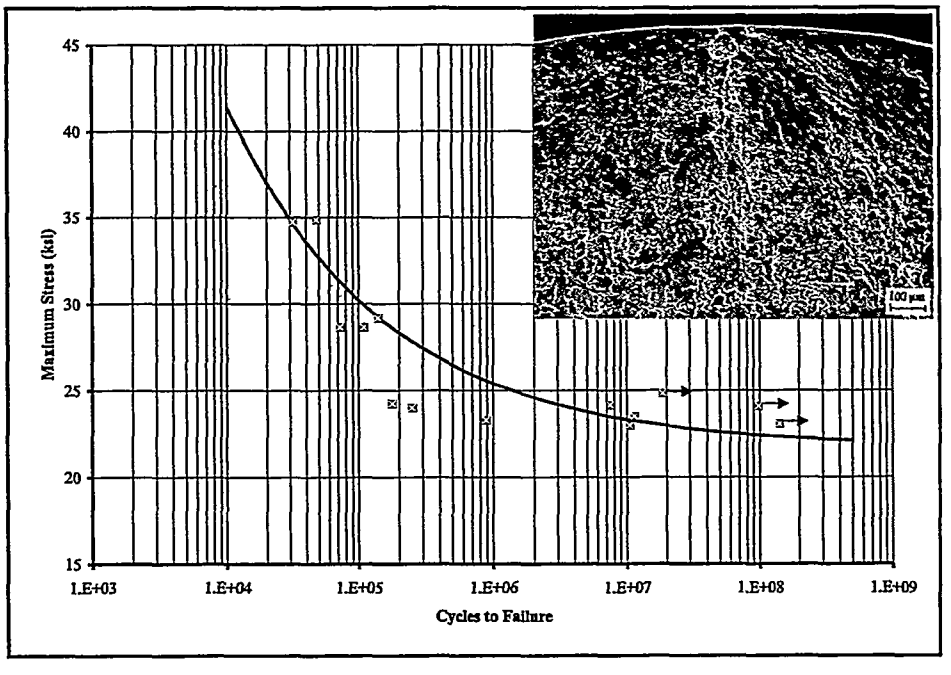

Fig. 22.2. S/N curve for Alloy 22; the fracture surface shown is from the specimen which failed at 1.8 x 10^5 cycles under a maximum stress of 24.2 ksi.

ALLOY 22

Alloy #22	Wt.%	Si	Mg	Fe	Cu	Ni	Cr	Mn	Ti	Zn	Sr	Al
		9.69	0.05	1.05	4.54	0.04	0.06	0.27	0.03	1.20	–	balance

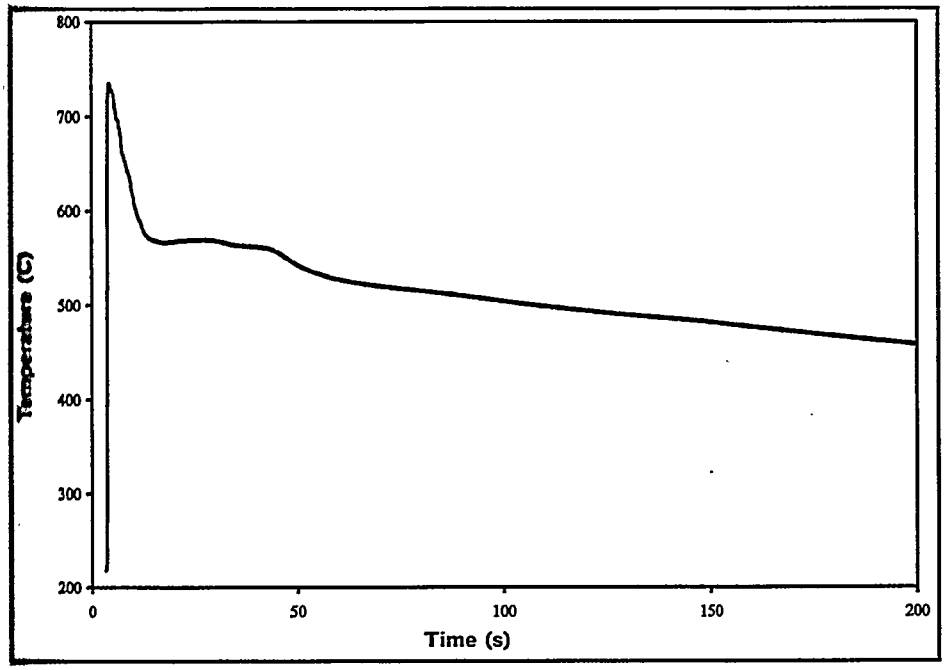

Fig. 3.22.3. Thermal history of Alloy 22 cast in a graphite mold.

Alloy #23	Wt.%	Si	Mg	Fe	Cu	Ni	Cr	Mn	Ti	Zn	Sr	Al
		10.88	0.05	1.27	2.62	0.04	0.06	0.26	0.03	1.20	—	balance

Tensile	Strength	Ultimate	25°C	Ksi	41.3±3.0
				MPa	284.8±20.7
			100°C	Ksi	37.9±2.6
				MPa	261.3±17.9
			200°C	Ksi	27.7±1.4
				MPa	191.0±9.7
		Yield	25°C	Ksi	22.1±0.5
				MPa	152.4±3.4
			100°C	Ksi	22.2±0.5
				MPa	153.1±3.4
			200°C	Ksi	20.3±0.4
				MPa	140.0±2.8
	Elongation		25°C	%	1.79±0.51
			100°C	%	2.39±1.06
			200°C	%	5.43±2.50
	Modulus of Elasticity		25°C	10^3 Ksi	11.19±0.48
				10^3 MPa	77.17±3.32
			100°C	10^3 Ksi	8.72±0.33
				10^3 MPa	60.13±2.28
			200°C	10^3 Ksi	8.65±1.12
				10^3 MPa	59.65±7.75
Endurance Limit	100,000,000 cycles		25°C	Ksi	20.05
				MPa	138.24
	500,000,000 cycles		25°C	Ksi	19.77
				MPa	136.31
Impact Resistance	Absorbed Energy		25°C	Joules	3.43±0.41
				lb.ft.	2.53±0.30
Wear Resistance	Volume Loss		25°C	cm^3	0.4086±0.0326
Hardness	¼ × ¼ inch flat die casting		25°C	RHB	58.8±1.2
	3/8 inch diameter die casting		25°C	RHB	50.6±1.7
	5/8 inch diameter die casting		25°C	RHB	49.9±1.9
Thermal Conductivity			25°C	W/m.K	113.8±2.5
Electrical Conductivity			25°C	% IACS	22.70±0.62
Electrical Resistivity			25°C	10^{-8} Ωm	7.595±0.207
Specific Gravity			25°C	g/cm^3	2.767

ALLOY 23

Alloy	Wt.%	Si	Mg	Fe	Cu	Ni	Cr	Mn	Ti	Zn	Sr	Al
#23		10.88	0.05	1.27	2.62	0.04	0.06	0.26	0.03	1.20	–	balance

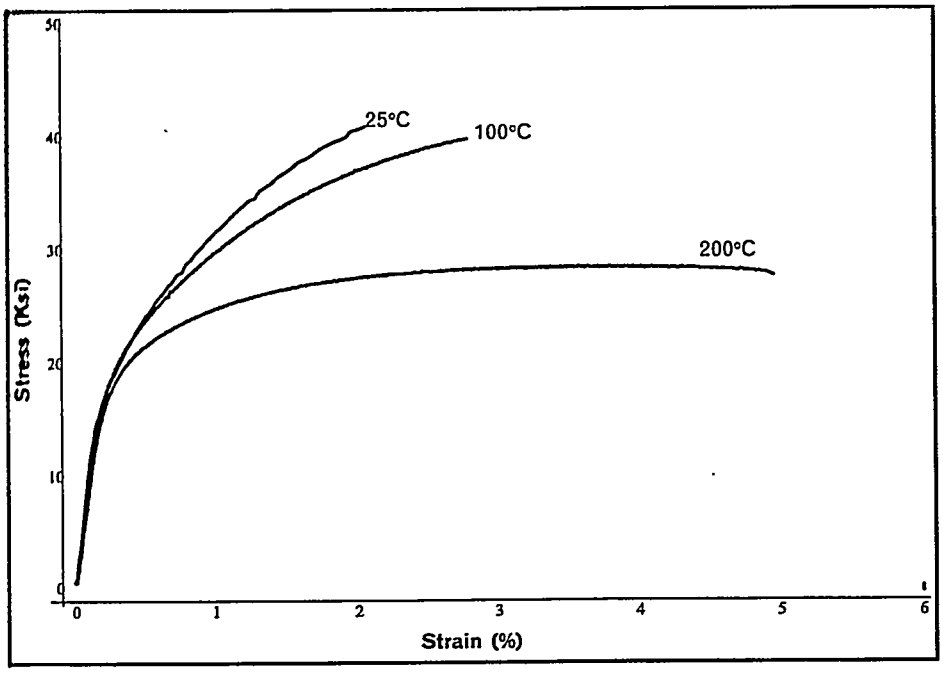

Fig. 3.23.1. Typical stress vs strain curves for Alloy 23 at temperatures of 25°C, 100 °C, and 200 °C.

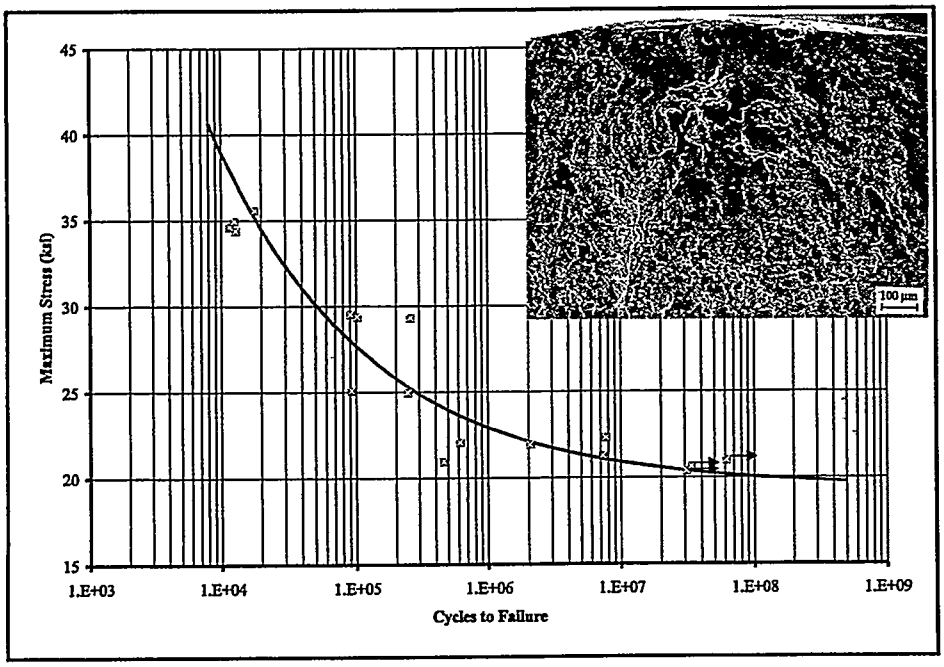

Fig. 3.23.2. S/N curve for Alloy 23; the fracture surface shown is from the specimen which failed at 4.6 x 10^5 cycles under a maximum stress of 21.0 ksi.

ALLOY 23

Alloy #23	Wt.%	Si	Mg	Fe	Cu	Ni	Cr	Mn	Ti	Zn	Sr	Al
		10.88	0.05	1.27	2.62	0.04	0.06	0.26	0.03	1.20	–	balance

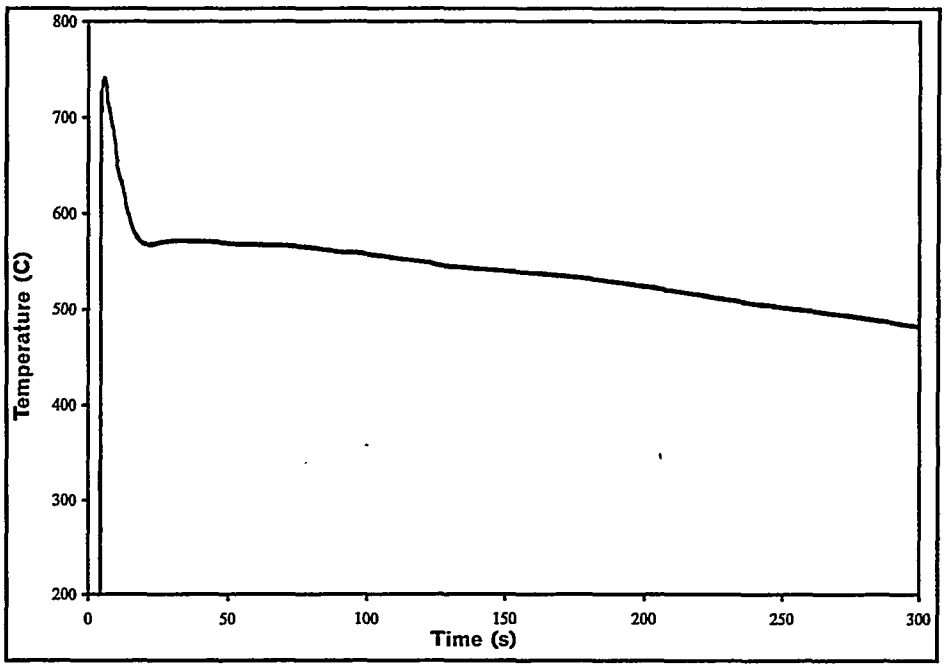

F. 3.3. Thermal history of Alloy 23 cast in a graphite mold.

ALLOY 23

Alloy #24	Wt.%	Si	Mg	Fe	Cu	Ni	Cr	Mn	Ti	Zn	Sr	Al
		10.93	0.05	1.02	5.06	0.12	0.06	0.24	0.05	2.20	–	balance

Tensile	Strength	Ultimate	25°C	Ksi	45.0±2.1
				MPa	310.3±14.5
			100°C	Ksi	41.9±2.7
				MPa	288.9±18.6
			200°C	Ksi	29.6±0.5
				MPa	204.1±3.4
		Yield	25°C	Ksi	26.6±0.4
				MPa	183.4±2.8
			100°C	Ksi	26.9±0.6
				MPa	185.5±4.1
			200°C	Ksi	22.4±0.2
				MPa	154.4±1.4
	Elongation		25°C	%	1.51±0.31
			100°C	%	2.04±0.74
			200°C	%	4.18±2.07
	Modulus of Elasticity		25°C	10^3 Ksi	11.66±0.73
				10^3 MPa	80.37±5.02
			100°C	10^3 Ksi	8.71±0.29
				10^3 MPa	60.07±2.03
			200°C	10^3 Ksi	7.96±0.32
				10^3 MPa	54.87±2.23
Endurance Limit	100,000,000 cycles		25°C	Ksi	21.51
				MPa	148.31
	500,000,000 cycles		25°C	Ksi	21.09
				MPa	145.41
Impact Resistance	Absorbed Energy		25°C	Joules	2.75±0.31
				lb.ft.	2.03±0.23
Wear Resistance	Volume Loss		25°C	cm^3	0.3992±0.0323
Hardness	¼ × ¼ inch flat die casting		25°C	RHB	67.7±0.9
	3/8 inch diameter die casting		25°C	RHB	61.1±1.1
	5/8 inch diameter die casting		25°C	RHB	59.1±1.8
Thermal Conductivity			25°C	W/m.K	111.6±1.5
Electrical Conductivity			25°C	% IACS	21.64±0.09
Electrical Resistivity			25°C	10^{-8} Ωm	7.967±0.032
Specific Gravity			25°C	g/cm^3	2.819

ALLOY 24

Alloy #24	Wt.%	Si	Mg	Fe	Cu	Ni	Cr	Mn	Ti	Zn	Sr	Al
		10.93	0.05	1.02	5.06	0.12	0.06	0.24	0.05	2.20	–	balance

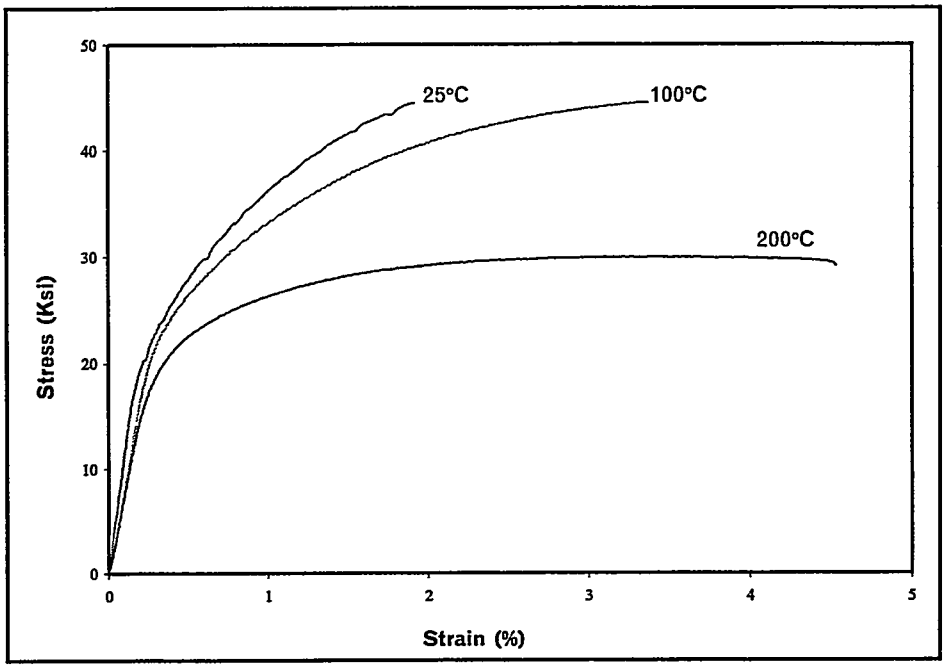

F.. 24.1. Typical stress vs strain curves for Alloy 24 at temperatures of 25°C, 100 °C, and 200 °C.

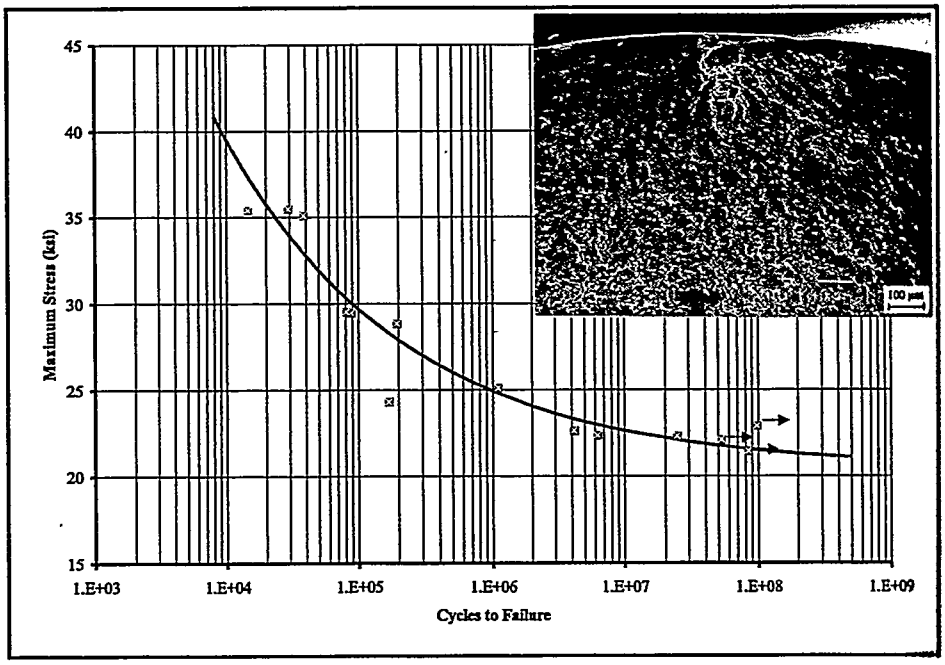

I 24.2. S/N curve for Alloy 24; the fracture surface shown is from the specimen which failed at 6.3 x 10^5 cycles under a maximum stress of 21.3 ksi.

ALLOY 24

Alloy #24	Wt.%	Si	Mg	Fe	Cu	Ni	Cr	Mn	Ti	Zn	Sr	Al
		10.93	0.05	1.02	5.06	0.12	0.06	0.24	0.05	2.20	–	balance

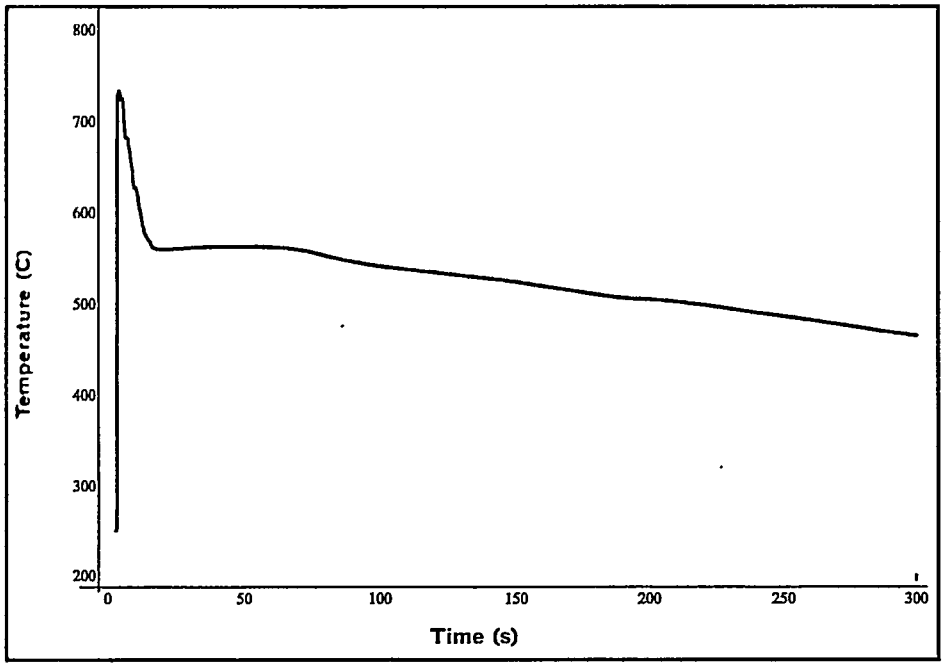

Fig. 3.24.3. Thermal history of Alloy 24 cast in a graphite mold.

ALLOY 24

Alloy #1	Wt.%	Si	Mg	Fe	Cu	Ni	Cr	Mn	Ti	Zn	Sr	Al
		7.15	0.03	0.68	1.24	0.01	0.01	0.01	0.01	0.44	0.00	Balance

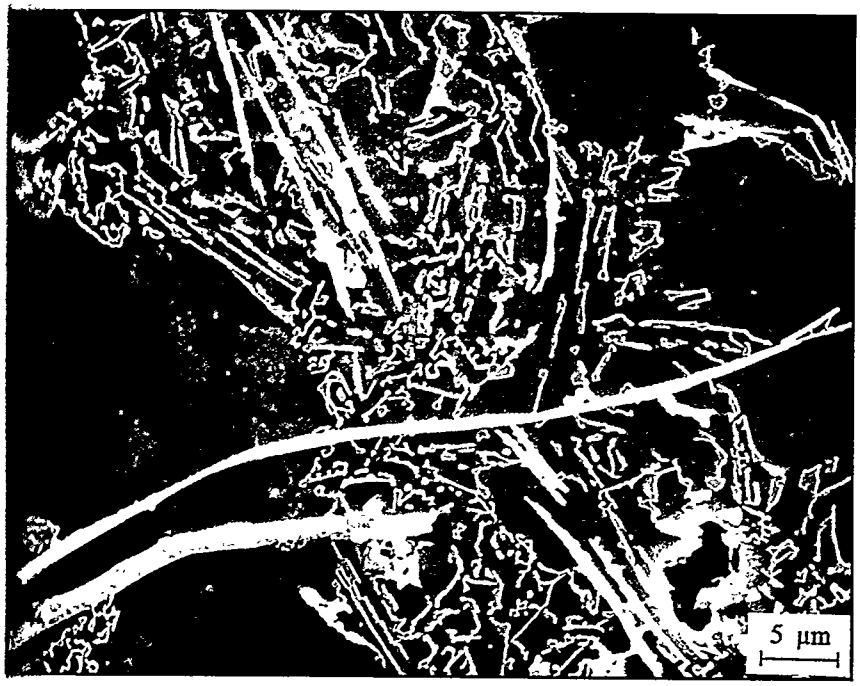

Fig. 3.1.7. SEM micrograph of Alloy 1 in the die cast condition, showing Fe bearing needles and the Al-Si eutectic structure (2000X).

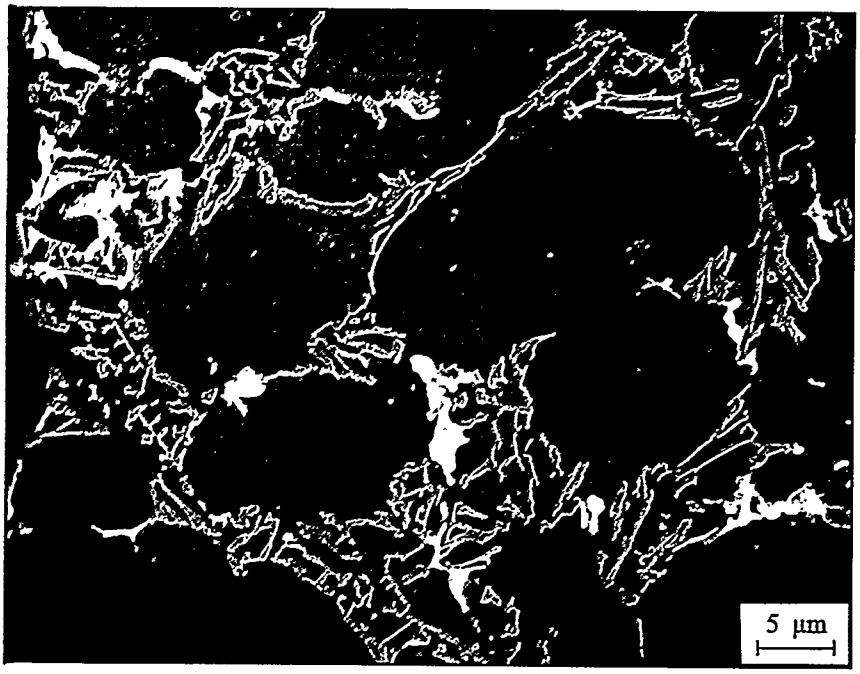

Fig. 3.1.8. SEM micrograph of Alloy 1 in the die cast condition, showing Cu-rich particles (bright phase) *within the Al-Si eutectic (2000X).*

ALLOY 1

Alloy #1	Wt.%	Si	Mg	Fe	Cu	Ni	Cr	Mn	Ti	Zn	Sr	Al
		7.15	0.03	0.68	1.24	0.01	0.01	0.01	0.01	0.44	0.00	Balance

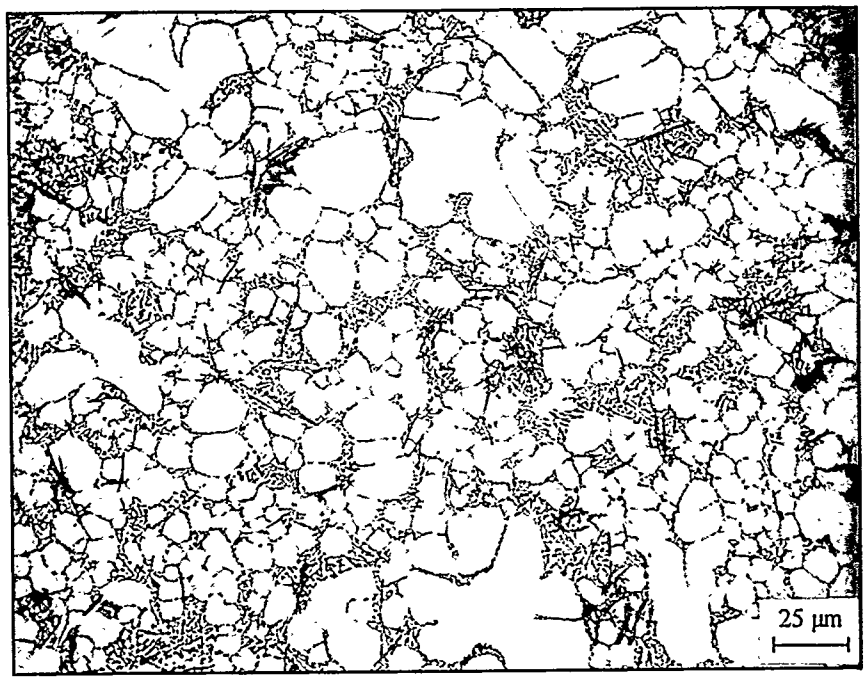

Fig. 3.1.5. Representative optical micrograph of Alloy 1, as die cast condition (400X).

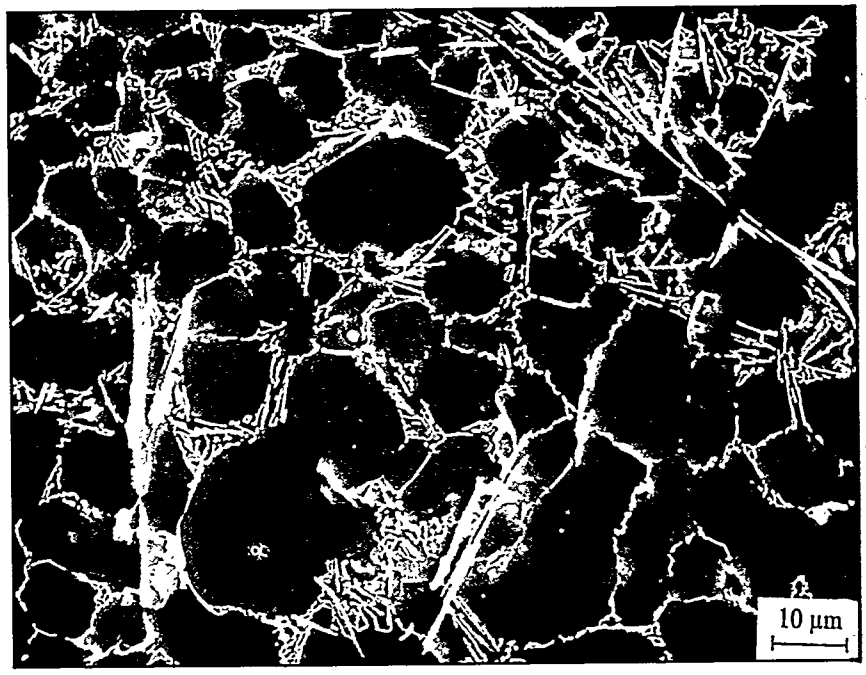

Fig. 3.1.6. Representative SEM micrograph of Alloy 1, as die cast condition (1000X).

ALLOY 1

Alloy #2	Wt.%	Si	Mg	Fe	Cu	Ni	Cr	Mn	Ti	Zn	Sr	Al
		6.99	0.01	0.56	1.15	0.01	0.01	0.47	0.24	2.87	0.018	Balance

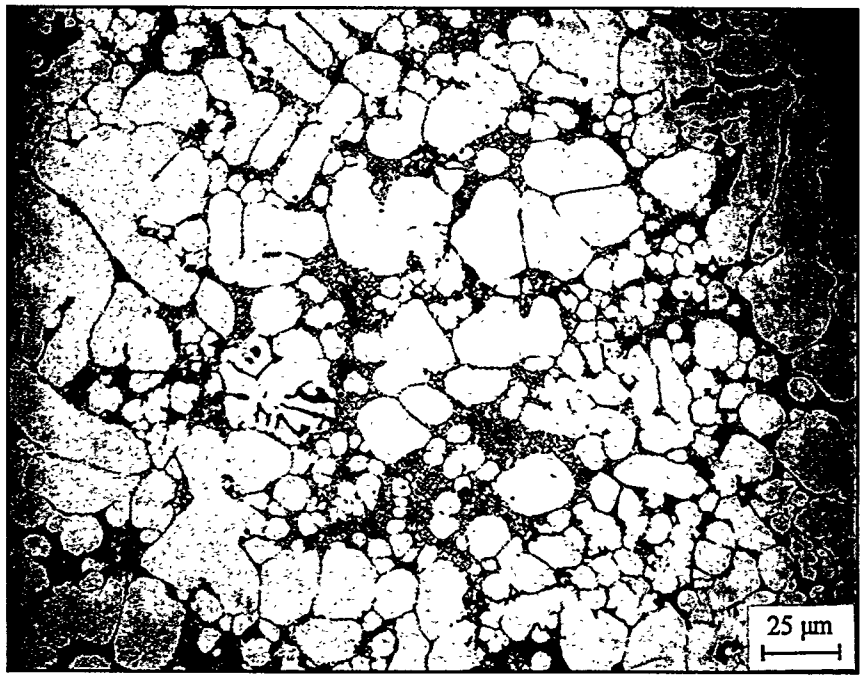

Fig. 3.2.5. Representative optical micrograph of Alloy 2, in the as die cast condition.

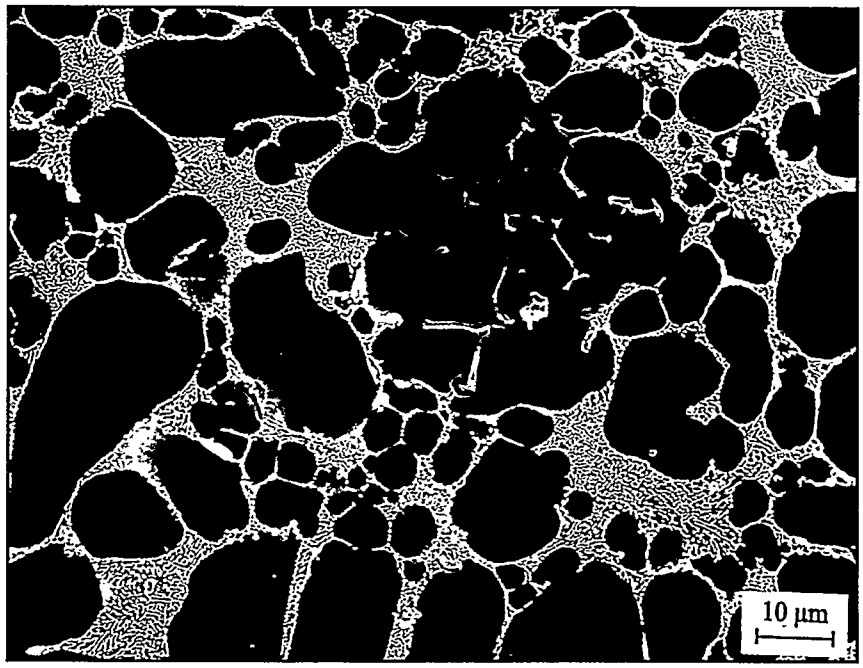

Fig. 3.2.6. Representative SEM micrograph of Alloy 2, in the as die cast condition (1000X).

ALLOY 2

Alloy #2	Wt.%	Si	Mg	Fe	Cu	Ni	Cr	Mn	Ti	Zn	Sr	Al
		6.99	0.01	0.56	1.15	0.01	0.01	0.47	0.24	2.87	0.018	Balance

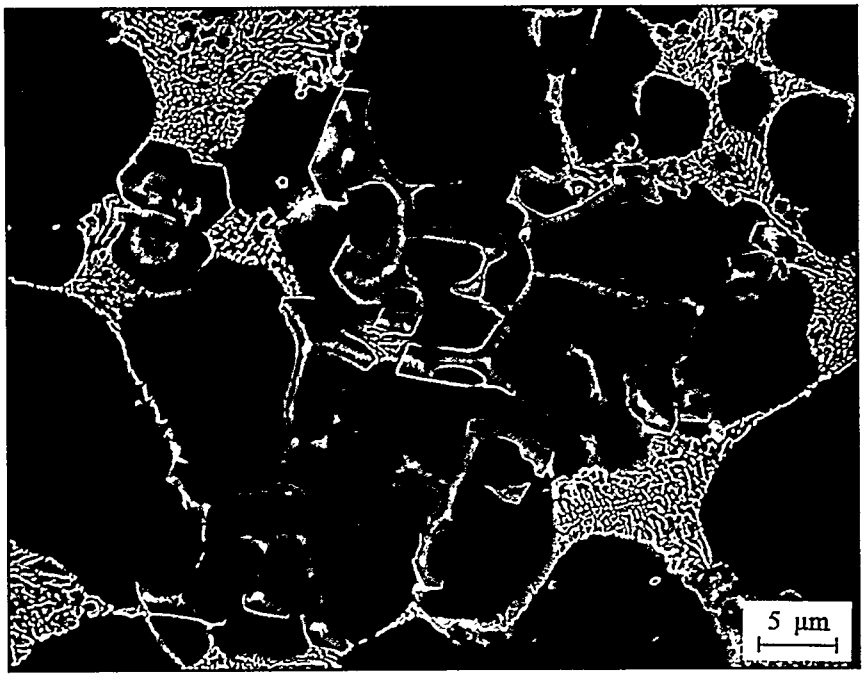

Fig. 3.2.7. SEM micrograph of Alloy 2 in the die cast condition, showing Fe bearing Chinese script and polyhedral crystals, and the Al-Si eutectic structure (2000X).

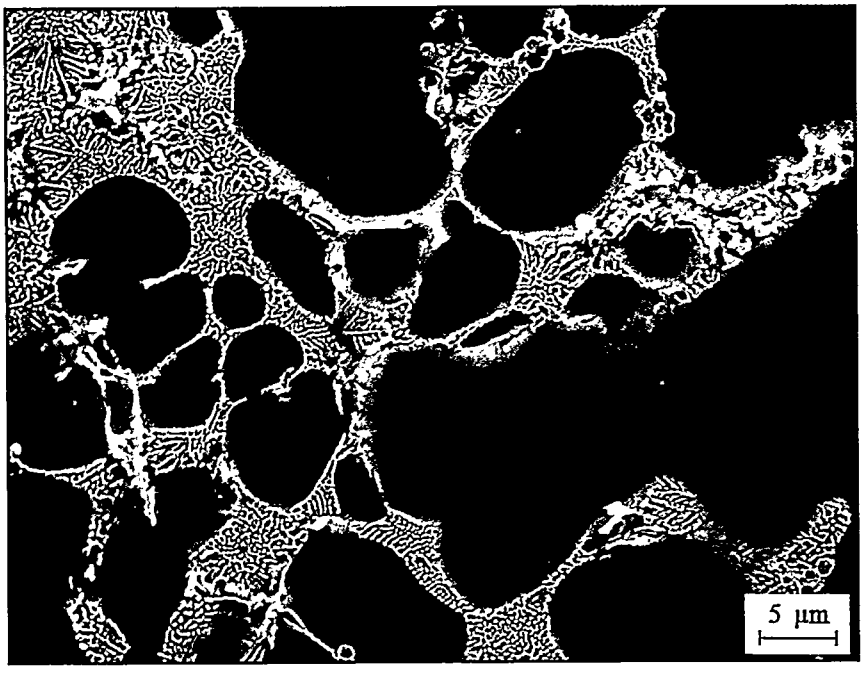

Fig. 3.2.8. SEM micrograph of Alloy 2 in the die cast condition, showing Cu bearing particles (bright phase) *within the Al-Si eutectic and in the interdendritic regions (2000X).*

ALLOY 2

Alloy #3	Wt.%	Si	Mg	Fe	Cu	Ni	Cr	Mn	Ti	Zn	Sr	Al
		6.98	0.04	1.49	4.99	0.44	0.13	0.01	0.01	0.47	0.018	Balance

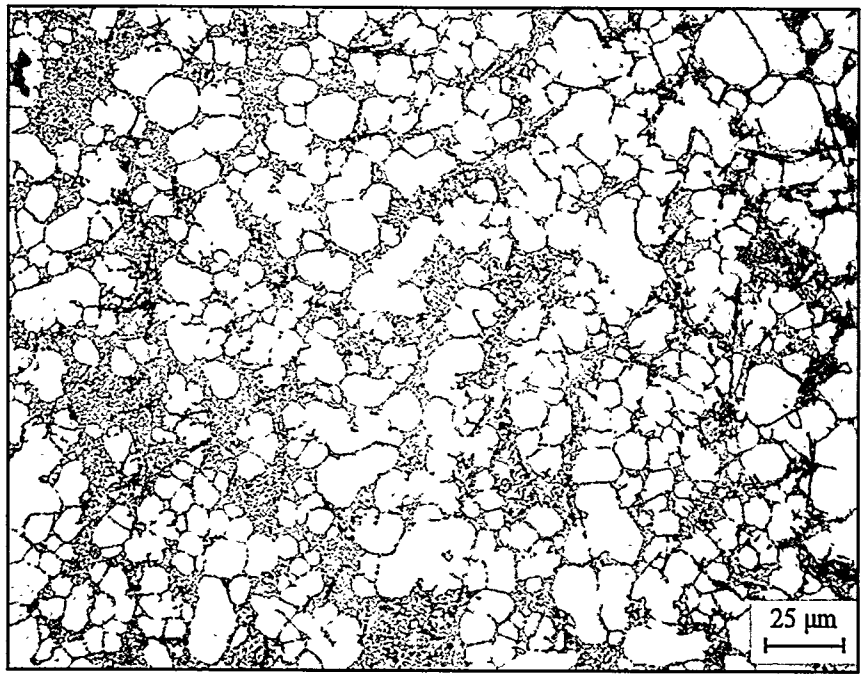

Fig. 3.3.5. Representative optical micrograph of Alloy 3, as die cast condition (400X).

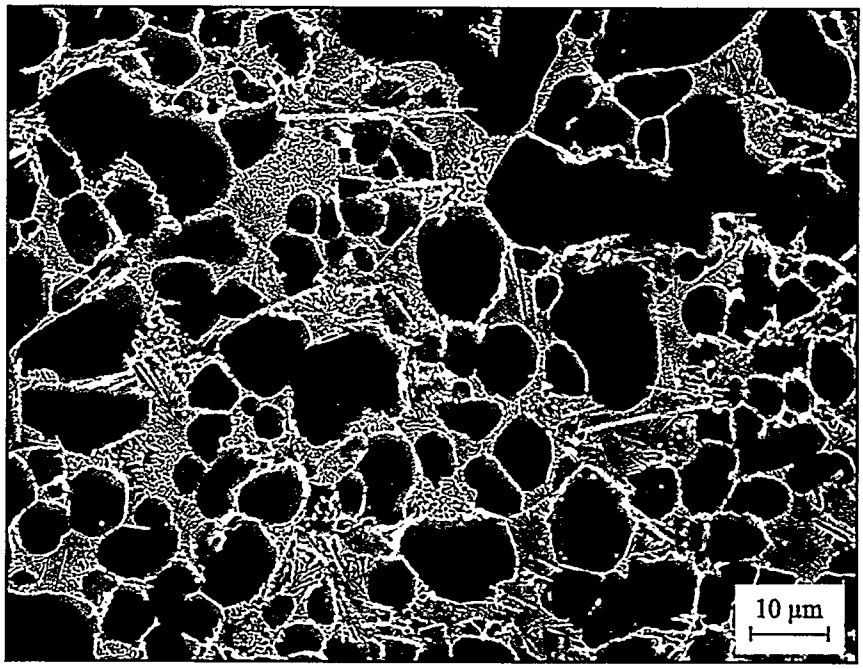

Fig. 3.3.6. Representative SEM micrograph of Alloy 3, as die cast condition (1000X).

ALLOY 3

Alloy #3	Wt.%	Si	Mg	Fe	Cu	Ni	Cr	Mn	Ti	Zn	Sr	Al
		6.98	0.04	1.49	4.99	0.44	0.13	0.01	0.01	0.47	0.018	Balance

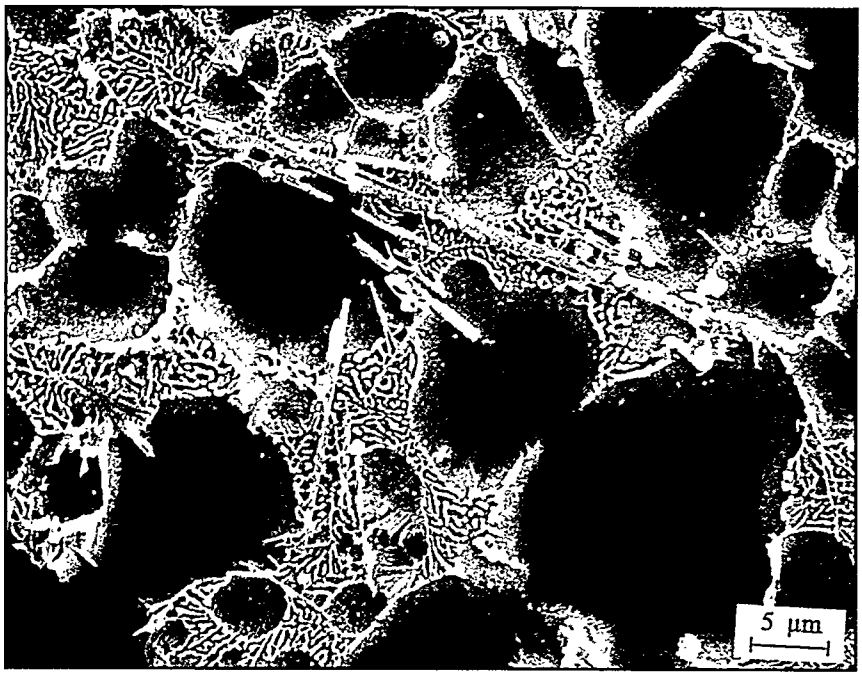

Fig. 3.3.7. SEM micrograph of Alloy 3 in the die cast condition, showing Fe bearing needles and the Al-Si eutectic structure (2000X).

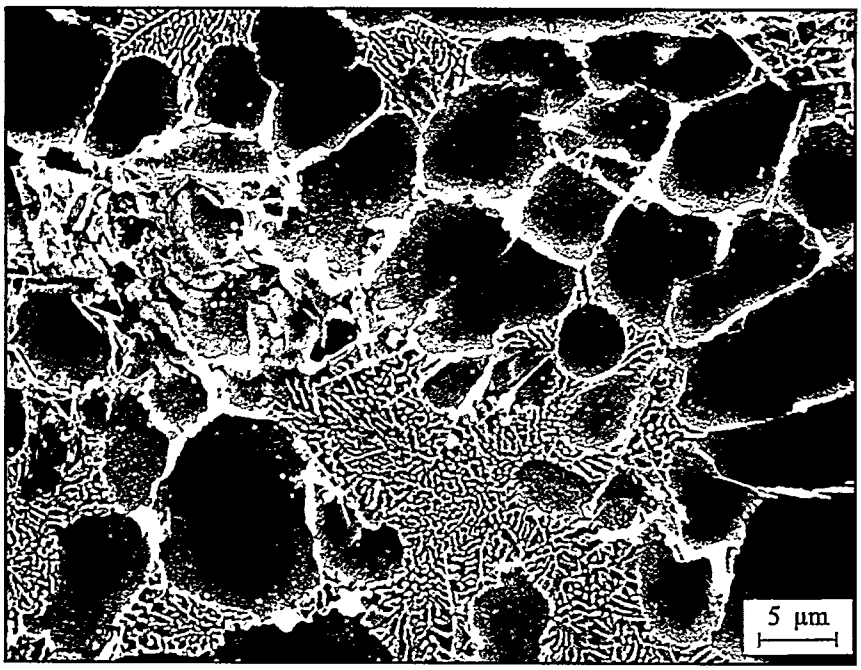

Fig. 3.3.8. SEM micrograph of Alloy 3 in the die cast condition, showing Cu bearing particles (bright phase) *in the interdendritic regions and within the Al-Si eutectic (2000X).*

ALLOY 3

Alloy #4	Wt.%	Si	Mg	Fe	Cu	Ni	Cr	Mn	Ti	Zn	Sr	Al
		6.94	0.04	1.48	4.74	0.47	0.15	0.45	0.16	2.69	0.00	Balance

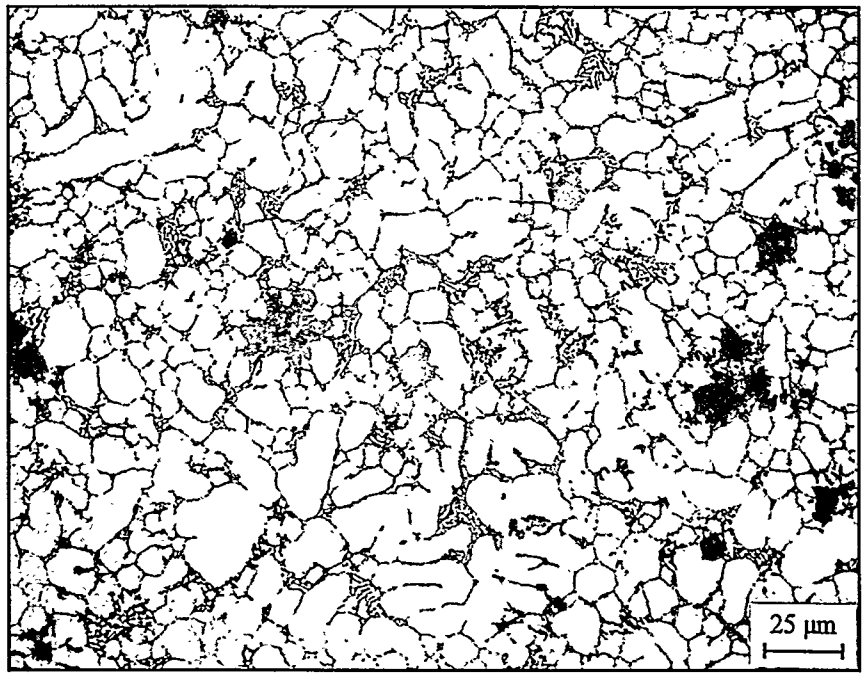

Fig. 3.4.5. Representative optical micrograph of Alloy 4, as die cast condition (400X).

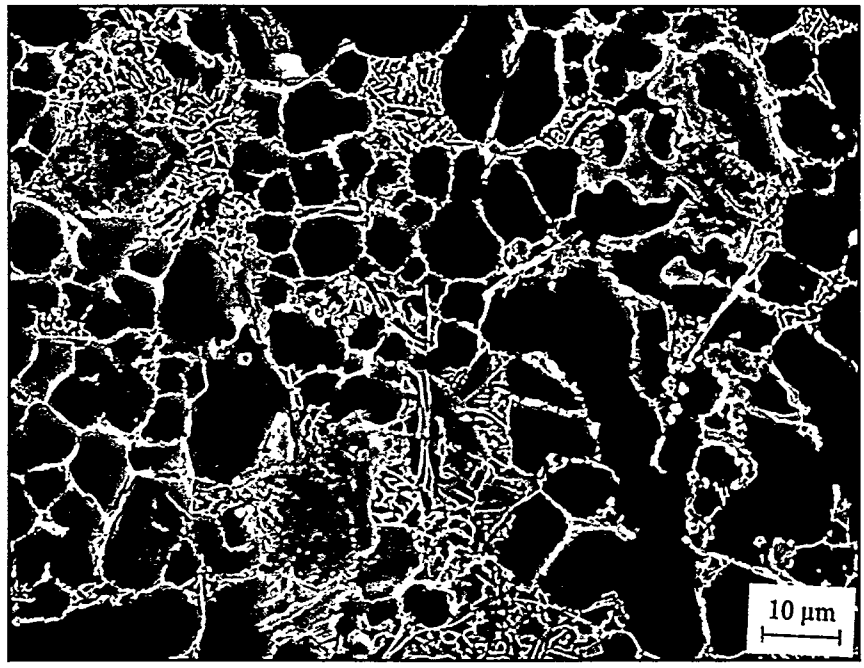

Fig. 3.4.6. Representative SEM micrograph of Alloy 4, as die cast condition (1000X).

ALLOY 4

Alloy #4	Wt.%	Si	Mg	Fe	Cu	Ni	Cr	Mn	Ti	Zn	Sr	Al
		6.94	0.04	1.48	4.74	0.47	0.15	0.45	0.16	2.69	0.00	Balance

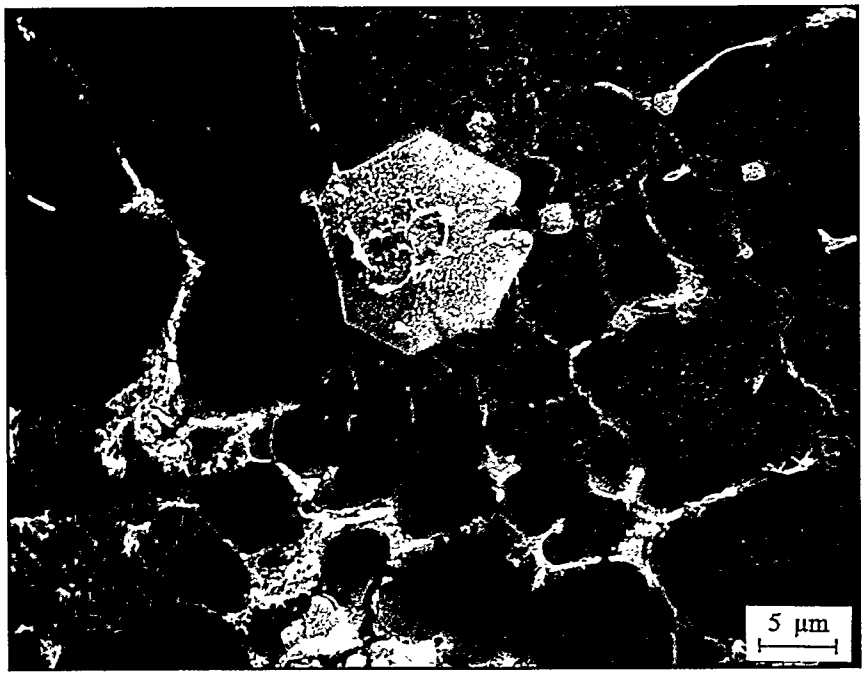

Fig. 3.4.7. SEM micrograph of Ally 4 in the die cast condition, showing an Fe bearing large polyhedral crystal, some small Fe bearing particles, and Cu bearing phase within the Al-Si eutectic structure and in the interdendritic regions (2000X).

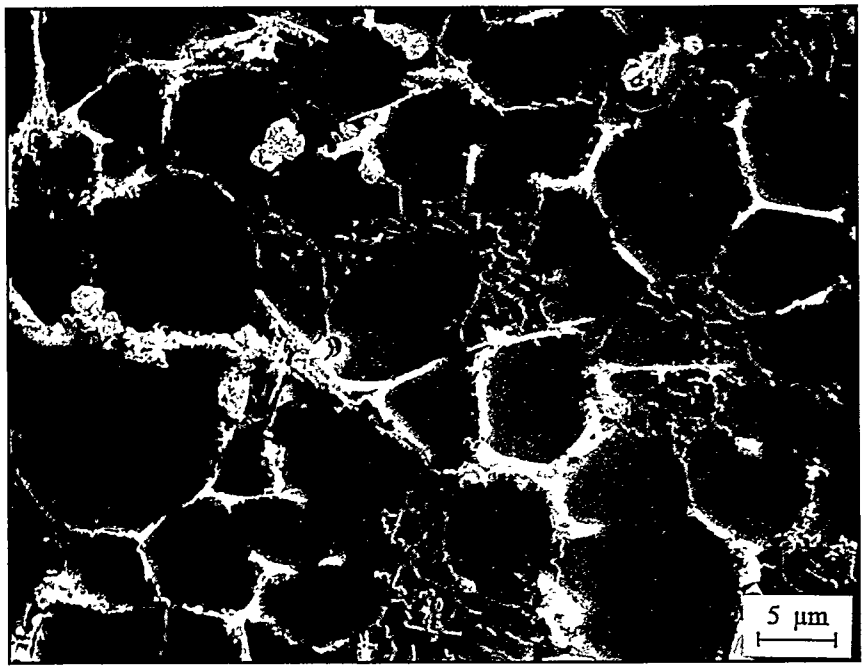

Fig. 3.4.8. SEM micrograph of Alloy 4 in the die cast condition, showing Cu bearing particles (bright phase) *within the Al-Si eutectic and in the interdendritic regions (2000X).*

ALLOY 4

Alloy #5	Wt.%	Si	Mg	Fe	Cu	Ni	Cr	Mn	Ti	Zn	Sr	Al
		7.05	0.44	0.67	1.18	0.53	0.14	0.01	0.01	2.76	0.00	Balance

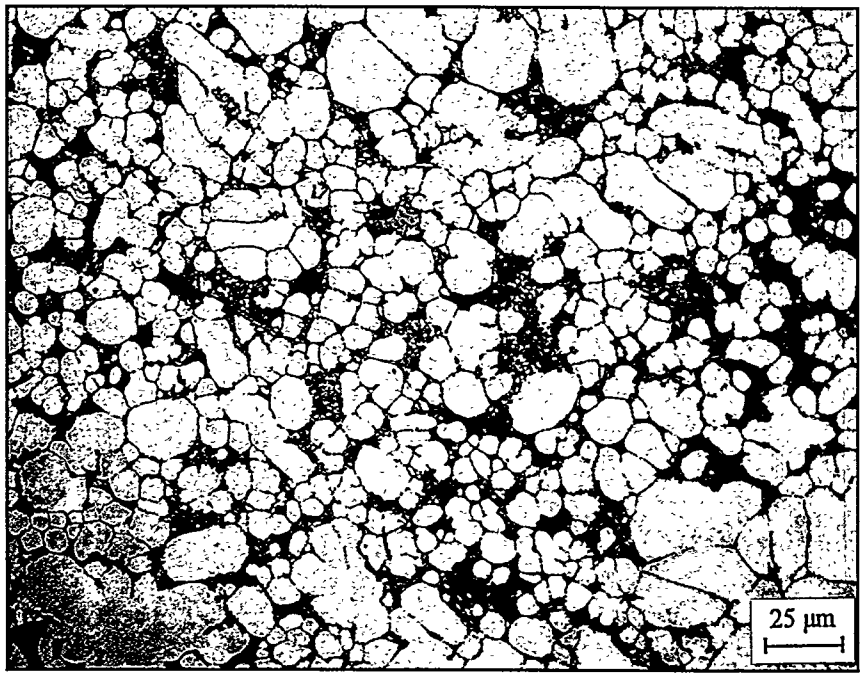

Fig. 3.5.5. Representative optical micrograph of Alloy 5, as die cast condition (400X).

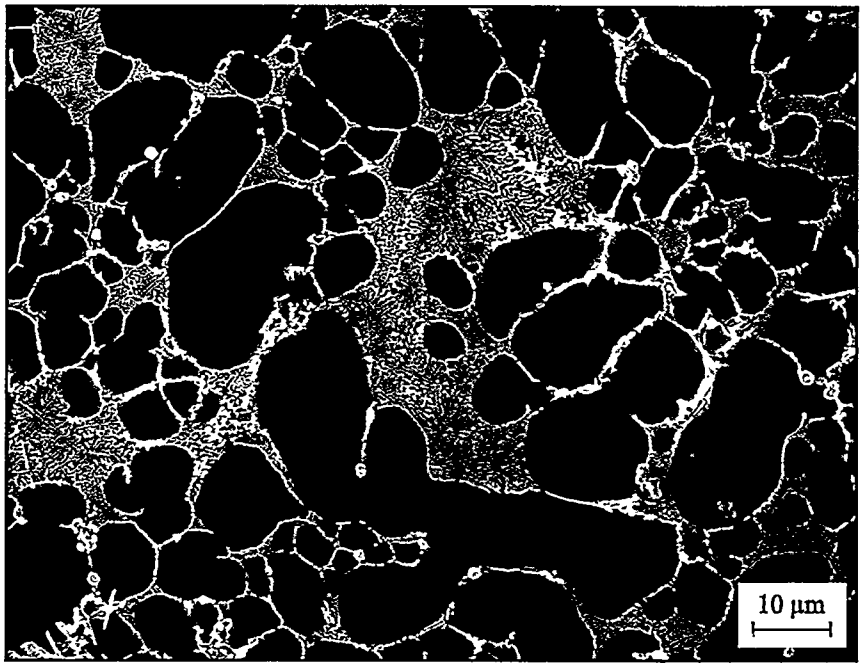

Fig. 3.5.6. Representative SEM micrograph of Alloy 5, as die cast condition (1000X).

ALLOY 5

Alloy #5	Wt.%	Si	Mg	Fe	Cu	Ni	Cr	Mn	Ti	Zn	Sr	Al
		7.05	0.44	0.67	1.18	0.53	0.14	0.01	0.01	2.76	0.00	Balance

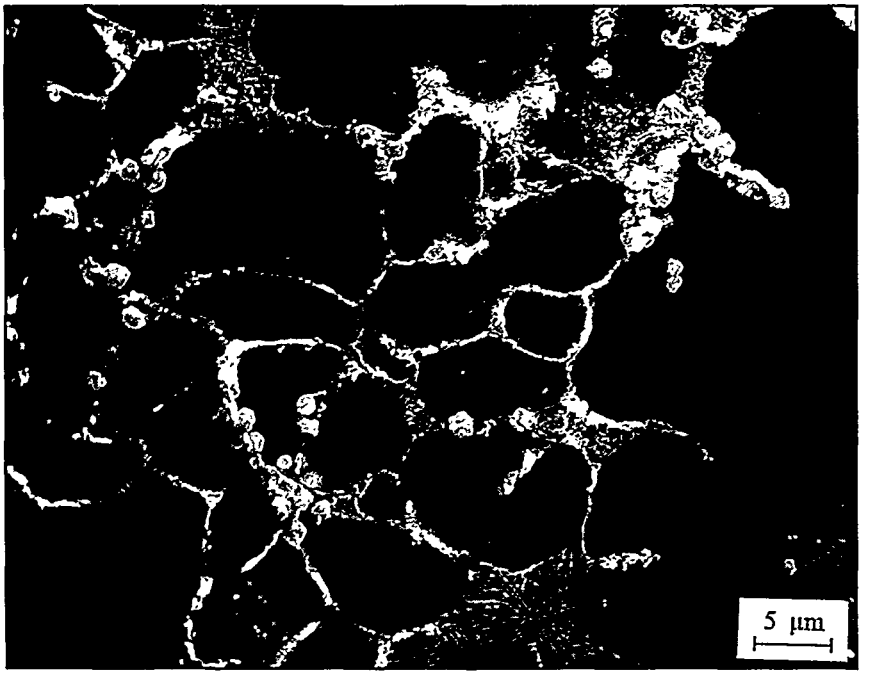

Fig. 3.5.7. SEM micrograph of Alloy 5 in the die cast condition, showing Fe bearing small particles around the inter dendritic regions and the Al-Si eutectic structure (2000X).

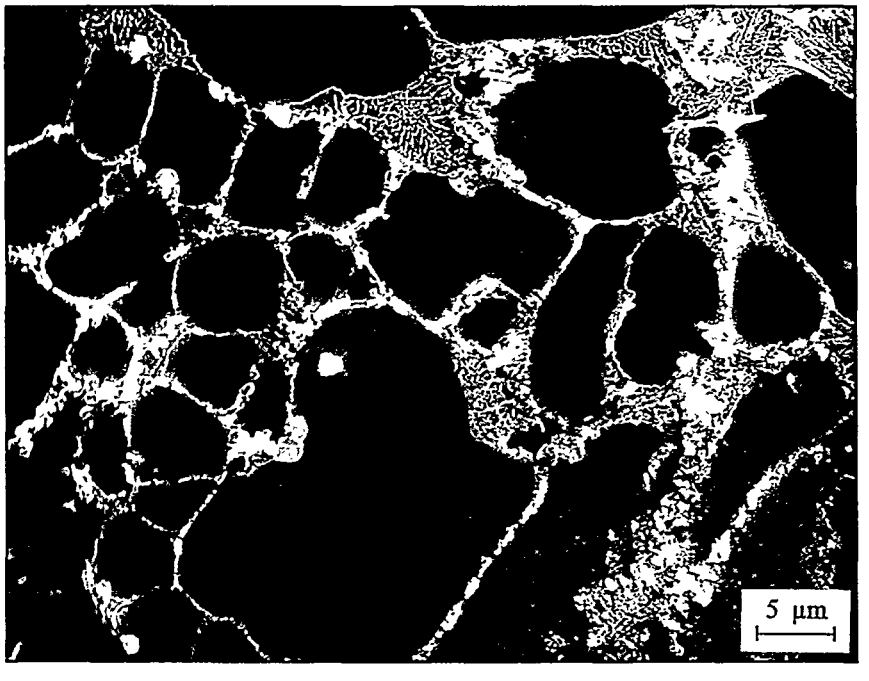

Fig. 3.5.8. SEM micrograph of Alloy 5 in the die cast condition, showing Cu bearing particles (bright phase) *within the Al-Si eutectic and in the interdendritic regions (2000X).*

ALLOY 5

Alloy #6	Wt.%	Si	Mg	Fe	Cu	Ni	Cr	Mn	Ti	Zn	Sr	Al
		6.98	0.44	0.57	1.13	0.48	0.13	0.45	0.18	0.38	0.018	Balance

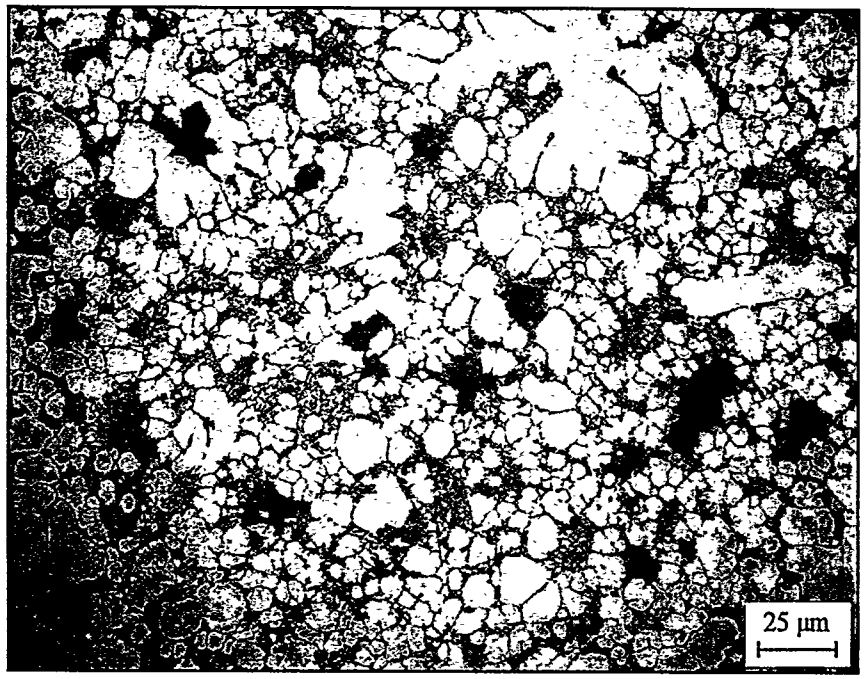

Fig. 3.6.5. Representative optical micrograph of Alloy 6, as die cast condition (400X).

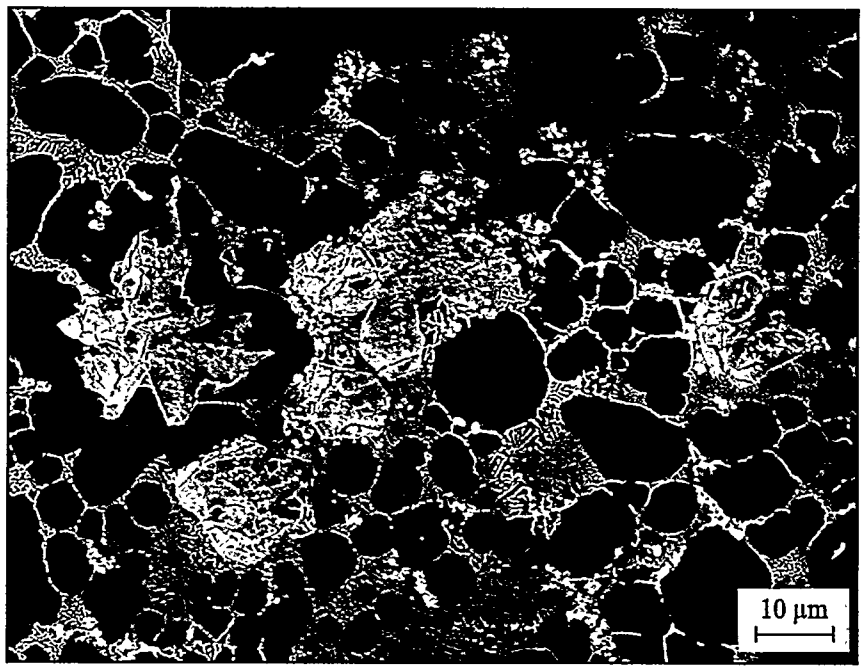

Fig. 3.6.6. Representative SEM micrograph of Alloy 6, as die cast condition (1000X).

ALLOY 6

Alloy #	Wt.%	Si	Mg	Fe	Cu	Ni	Cr	Mn	Ti	Zn	Sr	Al
6		6.98	0.44	0.57	1.13	0.48	0.13	0.45	0.18	0.38	0.018	Balance

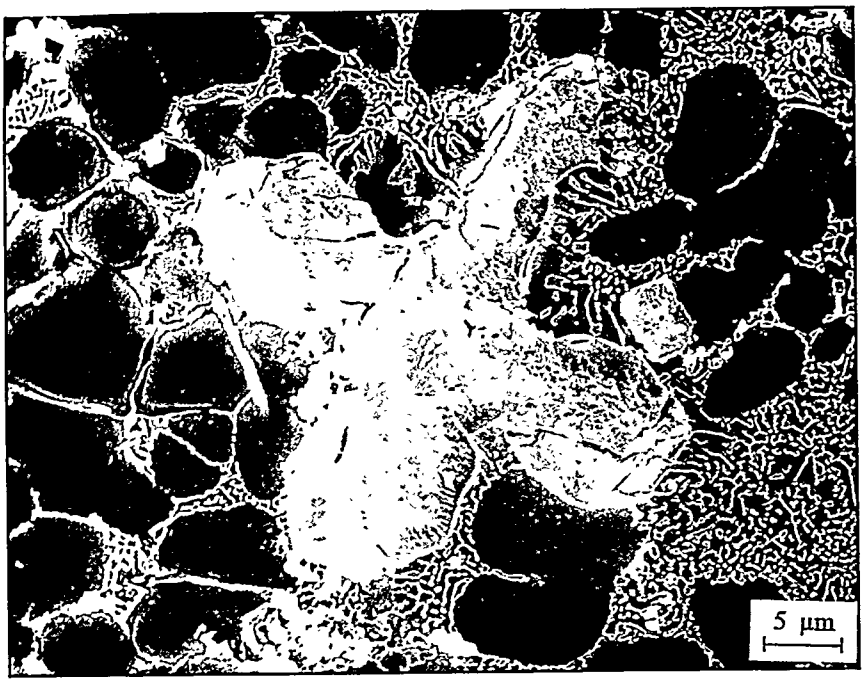

Fig. 3.6.7. SEM micrograph of Alloy 6 in the die cast condition, showing a starlike Fe bearing phase and the Al-Si eutectic structure (2000X).

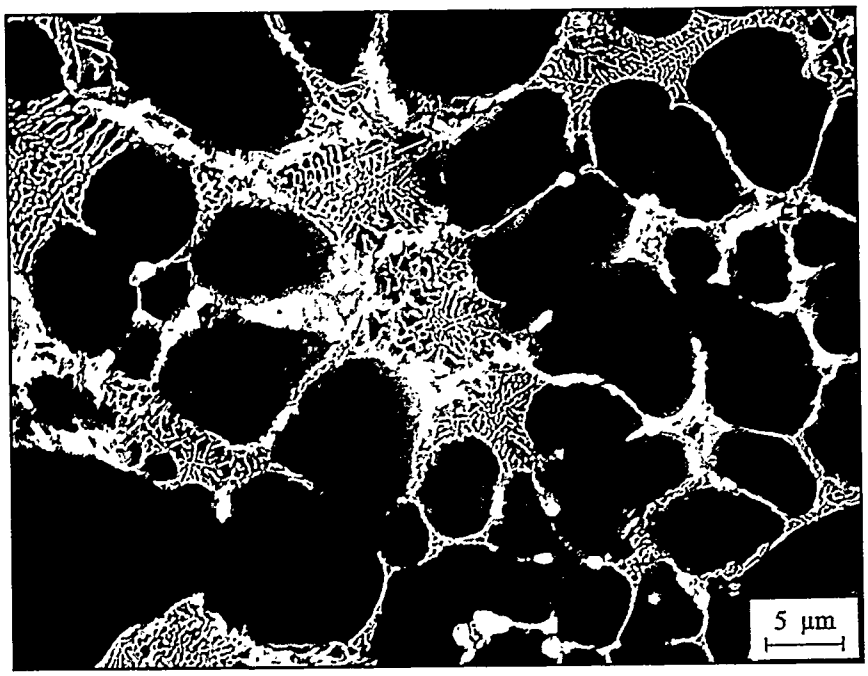

Fig. 3.6.8. SEM micrograph of Alloy 6 in the die cast condition, showing Cu bearing particles (bright phase) *within the Al-Si eutectic and in the interdendritic regions (2000X)*

ALLOY 6

Alloy #7	Wt.%	Si	Mg	Fe	Cu	Ni	Cr	Mn	Ti	Zn	Sr	Al
		6.92	0.50	1.63	4.94	0.03	0.01	0.02	0.01	2.73	0.022	Balance

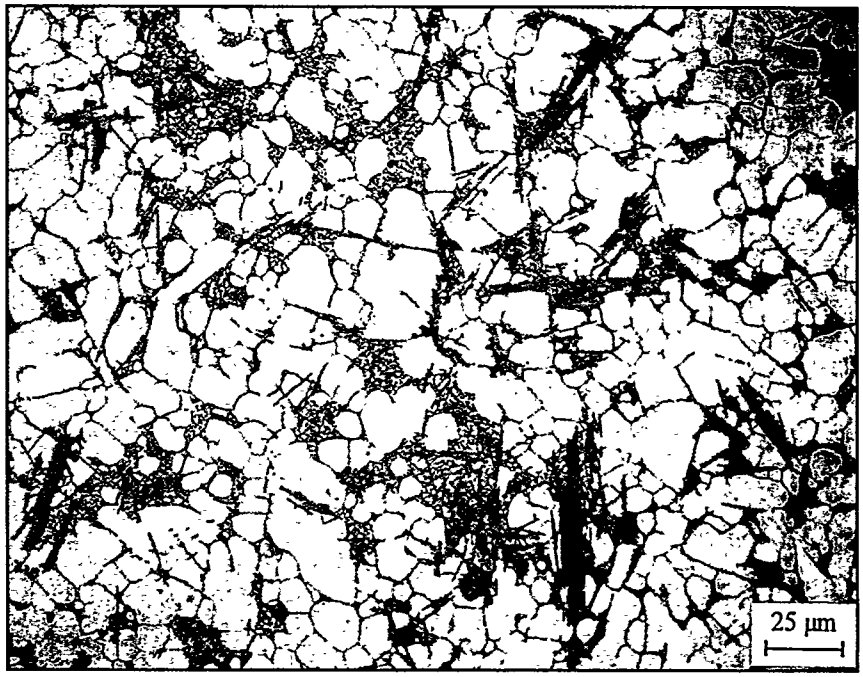

Fig. 3.7.5. Representative optical micrograph of Alloy 7, as die cast condition (400X).

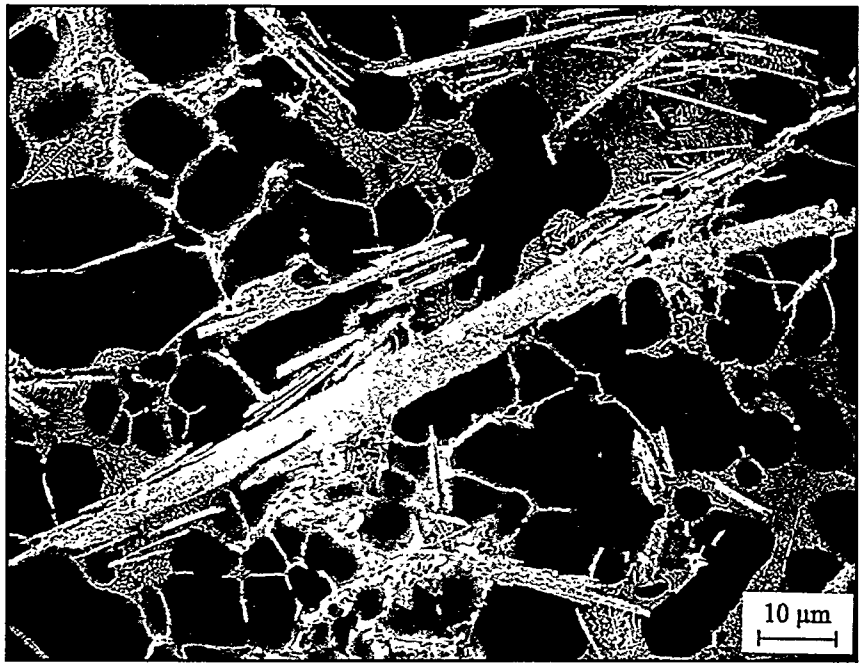

Fig. 3.7.6. Representative SEM micrograph of Alloy 7, as die cast condition (1000X).

ALLOY 7

Alloy #7	Wt.%	Si	Mg	Fe	Cu	Ni	Cr	Mn	Ti	Zn	Sr	Al
		6.92	0.50	1.63	4.94	0.03	0.01	0.02	0.01	2.73	0.022	Balance

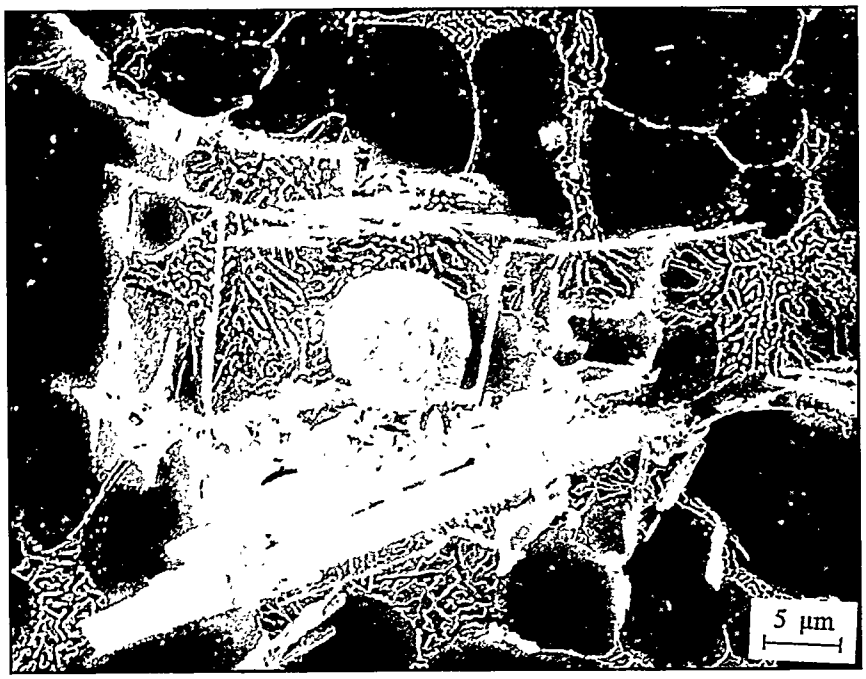

Fig. 3.7.7. SEM micrograph of Alloy 7 in the die cast condition, showing large Fe bearing needles, Cu bearing particles, and the Al-Si eutectic structure (2000X).

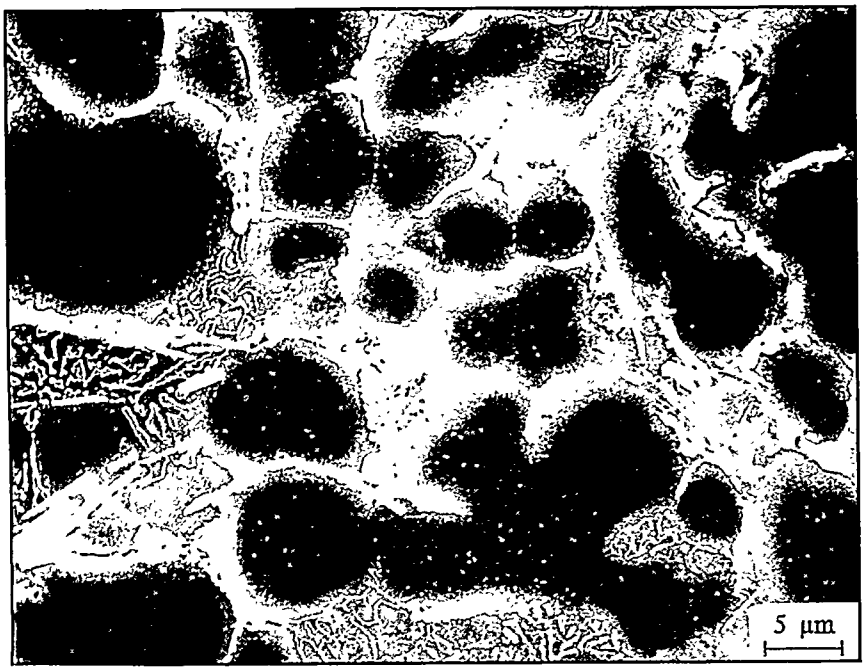

Fig. 3.7.8. SEM micrograph of Alloy 7 in the die cast condition, showing Cu bearing particles (bright phase) in the interdendritic regions and within the Al-Si eutectic (2000X).

ALLOY 7

Alloy #8	Wt.%	Si	Mg	Fe	Cu	Ni	Cr	Mn	Ti	Zn	Sr	Al
		6.79	0.46	1.49	4.77	0.01	0.01	0.45	0.20	0.42	0.00	Balance

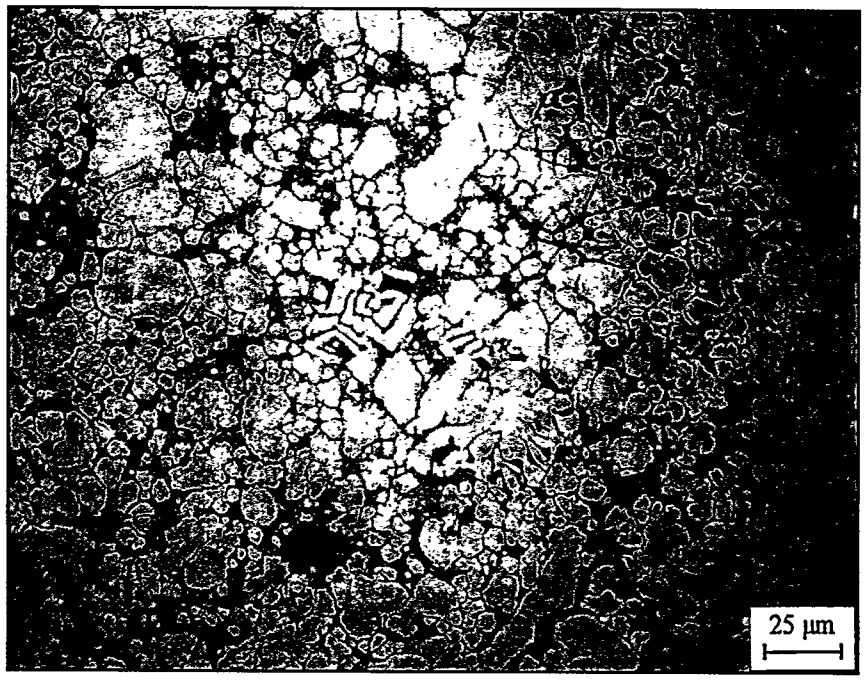

Fig. 3.8.5. Representative optical micrograph of Alloy 8, as die cast condition (400X).

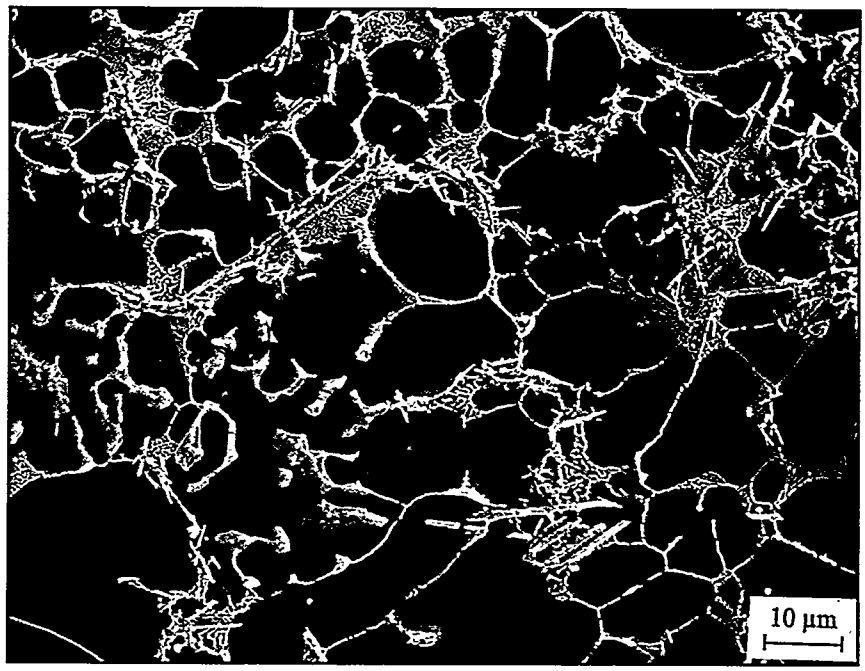

Fig. 3.8.6. Representative SEM micrograph of Alloy 8, as die cast condition (1000X).

ALLOY 8

Alloy #8	Wt.%	Si	Mg	Fe	Cu	Ni	Cr	Mn	Ti	Zn	Sr	Al
		6.79	0.46	1.49	4.77	0.01	0.01	0.45	0.20	0.42	0.00	Balance

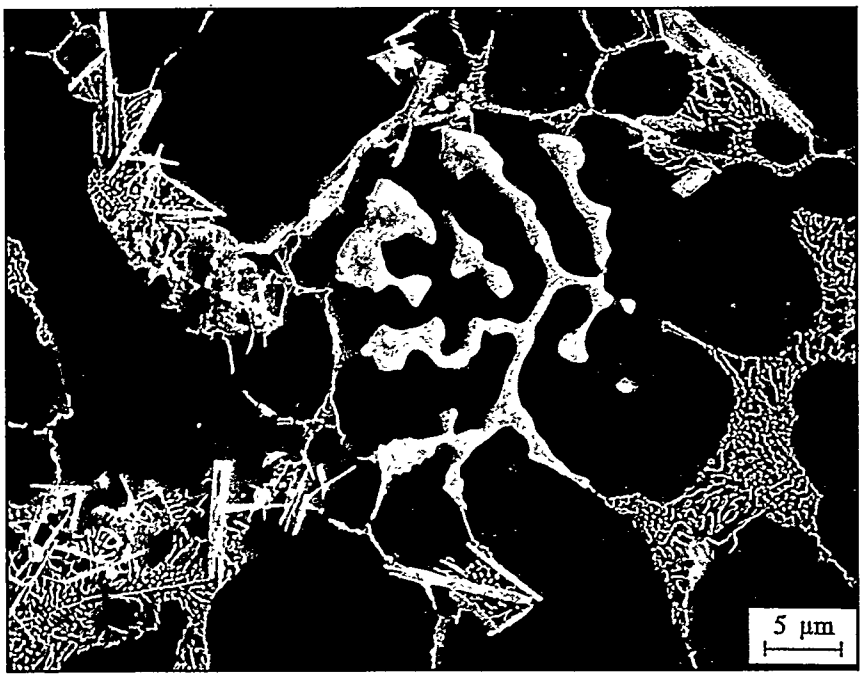

Fig. 3.8.7. SEM micrograph of Alloy 8 in the die cast condition, showing Fe bearing Chinese script and needles, and the Al-Si eutectic structure (2000X).

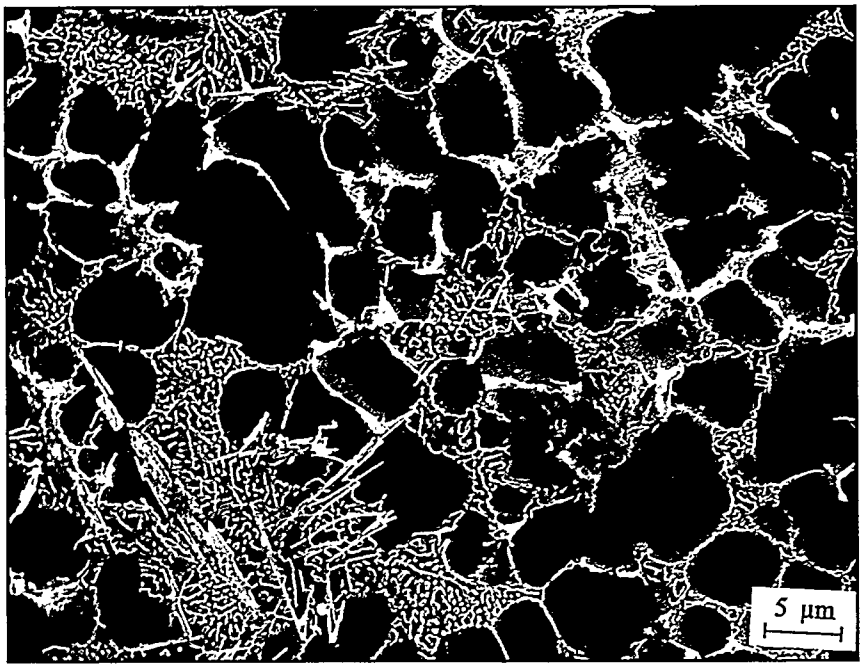

Fig. 3.8.8. SEM micrograph of Alloy 8 in the die cast condition, showing Cu bearing particles (bright phase) *in the interdendritic regions and within the Al-Si (2000X).*

ALLOY 8

Alloy #9	Wt.%	Si	Mg	Fe	Cu	Ni	Cr	Mn	Ti	Zn	Sr	Al
		12.71	0.05	0.63	4.96	0.06	0.14	0.01	0.20	0.50	0.017	Balance

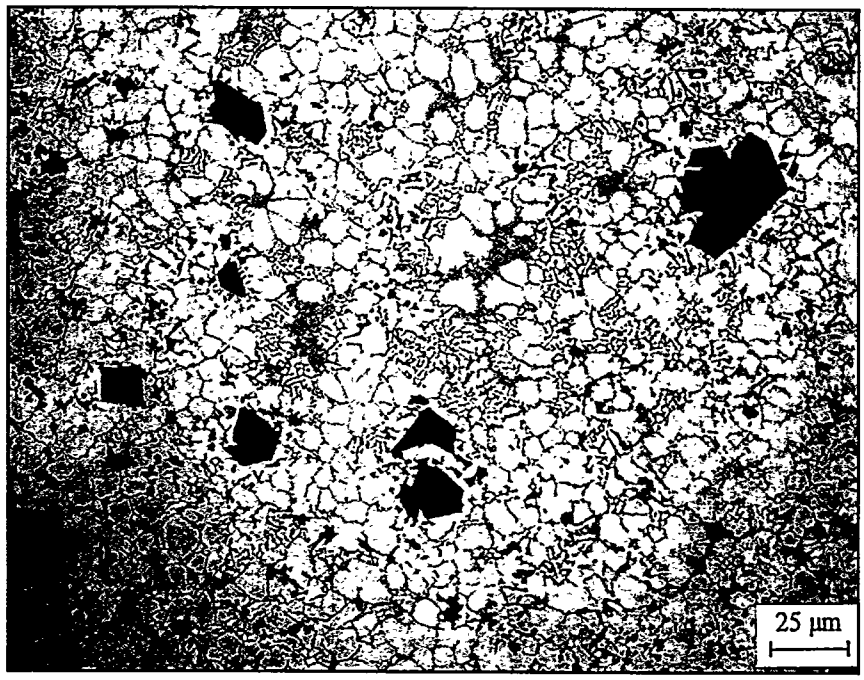

Fig. 3.9.5. Representative optical micrograph of Alloy 9, as die cast condition (400X).

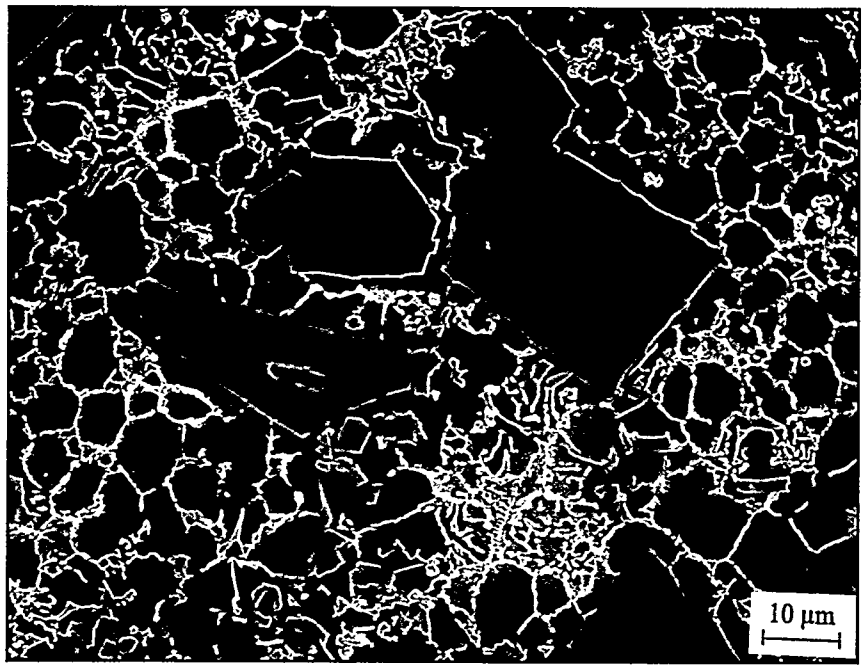

Fig. 3.9.6. Representative SEM micrograph of Alloy 9, as die cast condition (1000X).

ALLOY 9

Alloy #9	Wt.%	Si	Mg	Fe	Cu	Ni	Cr	Mn	Ti	Zn	Sr	Al
		12.71	0.05	0.63	4.96	0.06	0.14	0.01	0.20	0.50	0.017	Balance

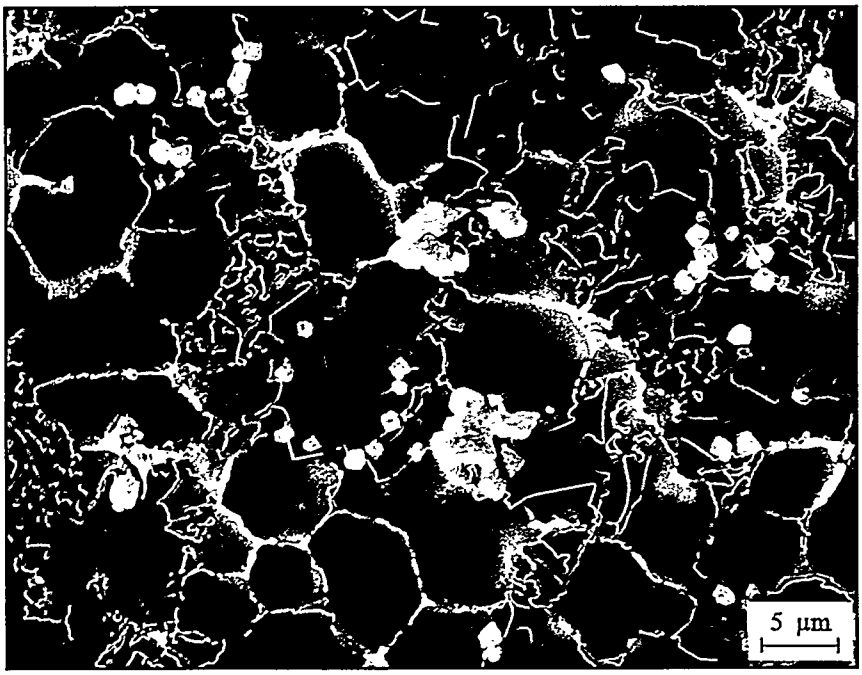

Fig. 3.9.7. SEM micrograph of Alloy 9 in the die cast condition, showing Fe bearing small particles and the Al-Si eutectic structure (2000X).

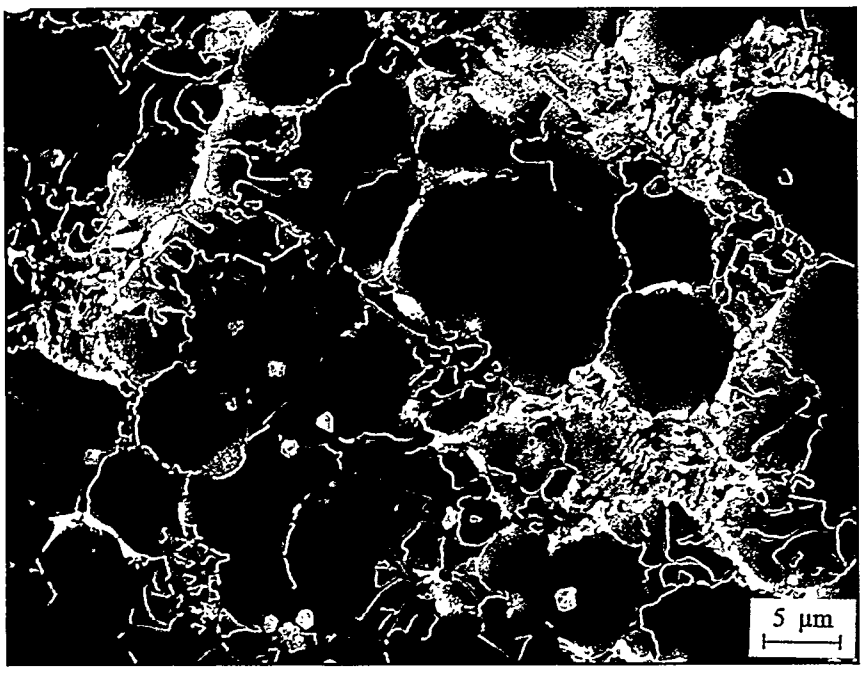

Fig. 3.9.8. SEM micrograph of Alloy 9 in the die cast condition, showing Cu bearing particles (bright phase) *within the Al-Si eutectic and the interdendritic regions (2000X).*

ALLOY 9

Alloy #10	Wt.%	Si	Mg	Fe	Cu	Ni	Cr	Mn	Ti	Zn	Sr	Al
		12.69	0.03	0.73	5.09	0.07	0.11	0.37	0.01	2.73	0.00	Balance

Fig. 3.10.5. Representative optical micrograph of Alloy 10, as die cast condition (400X).

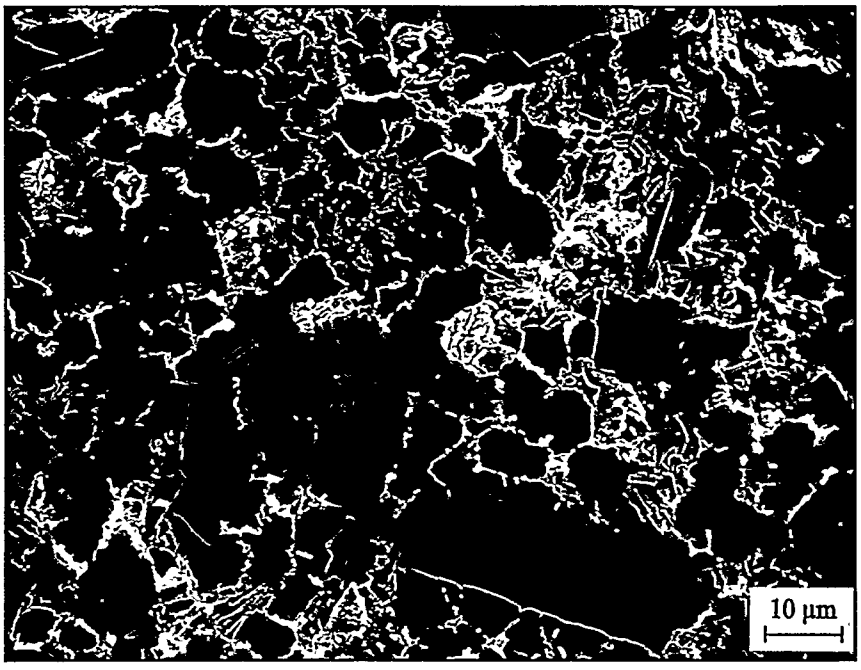

Fig. 3.10.6. Representative SEM micrograph of Alloy 10, as die cast condition (1000X).

ALLOY 10

Alloy #10	Wt.%	Si	Mg	Fe	Cu	Ni	Cr	Mn	Ti	Zn	Sr	Al
		12.69	0.03	0.73	5.09	0.07	0.11	0.37	0.01	2.73	0.00	Balance

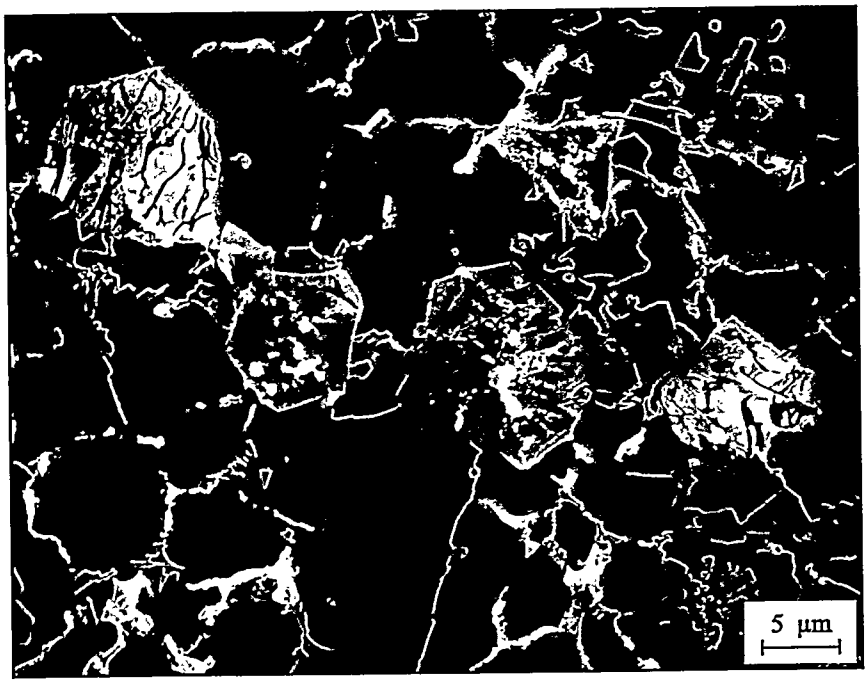

Fig. 3.10.7. SEM micrograph of Alloy 10 in the die cast condition, showing Fe bearing polyhedral crystals, the primary and eutectic Si particles, and the Cu bearing particles in the interdendritic regions (2000X).

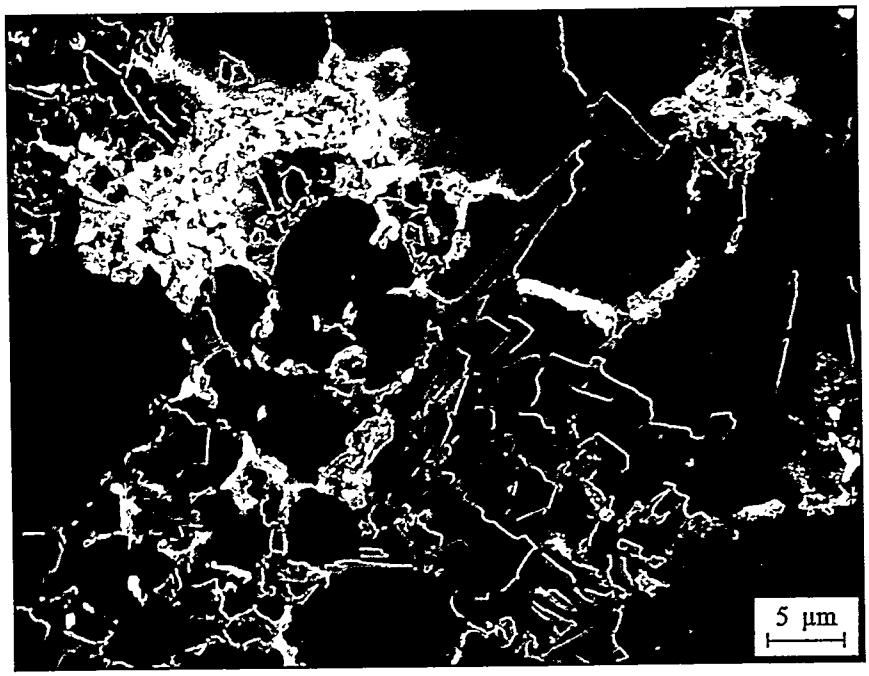

Fig. 3.10.8. SEM micrograph of Alloy 10 in the die cast condition, showing Cu bearing particles (bright phase) *within the Al-Si eutectic (2000X).*

ALLOY 10

Alloy #11	Wt.%	Si	Mg	Fe	Cu	Ni	Cr	Mn	Ti	Zn	Sr	Al
		12.86	0.04	1.59	1.21	0.45	0.01	0.01	0.18	0.49	0.00	Balance

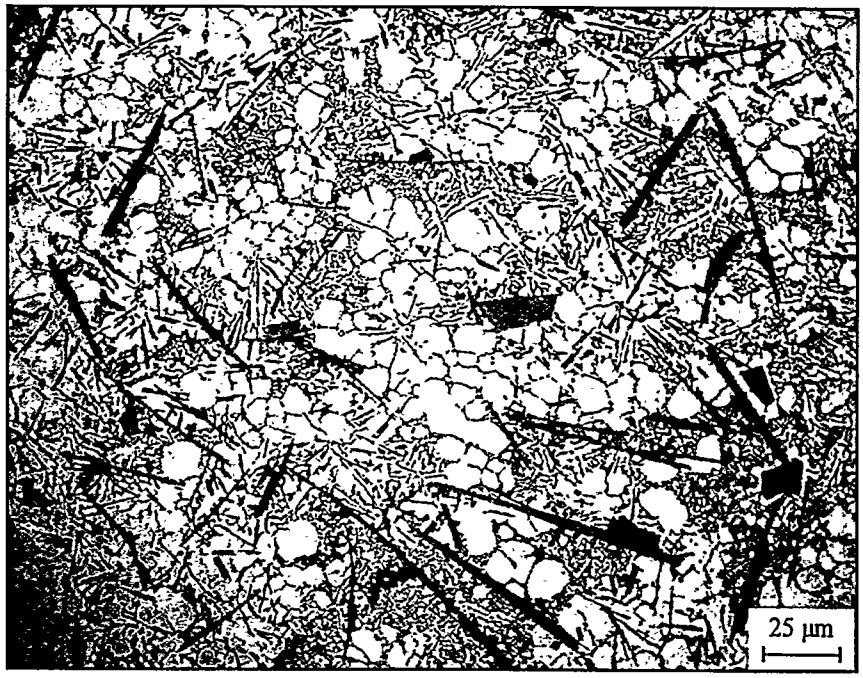

Fig. 3.11.5. Representative optical micrograph of Alloy 11 in the die cast condition, showing Fe bearing needles and the Al-Si eutectic structure (2000X).

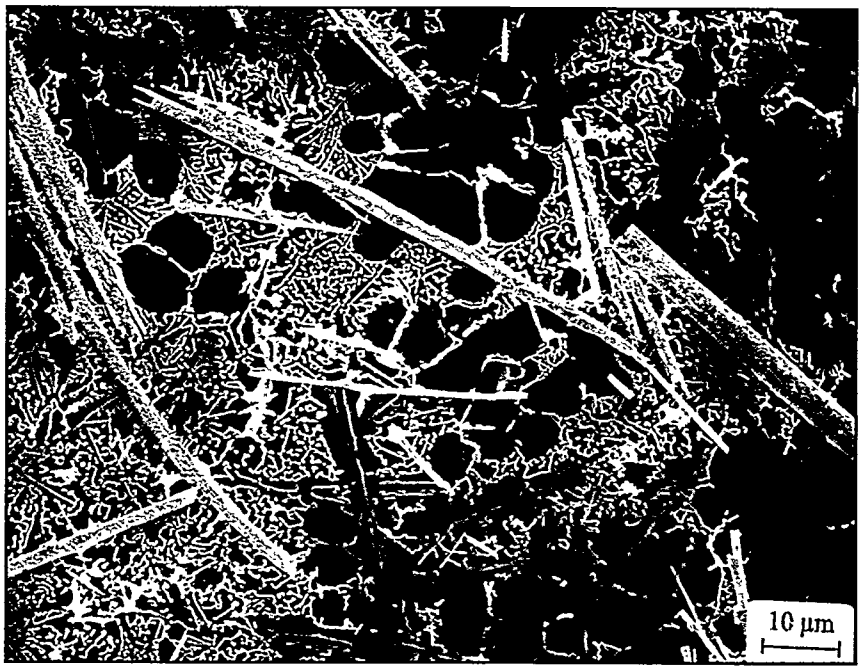

Fig. 3.11.6. Representative SEM micrograph of Alloy 11 in the die cast condition, showing Fe bearing needles and the Al-Si eutectic structure (2000X).

ALLOY 11

Alloy #11	Wt.%	Si	Mg	Fe	Cu	Ni	Cr	Mn	Ti	Zn	Sr	Al
		12.86	0.04	1.59	1.21	0.45	0.01	0.01	0.18	0.49	0.00	Balance

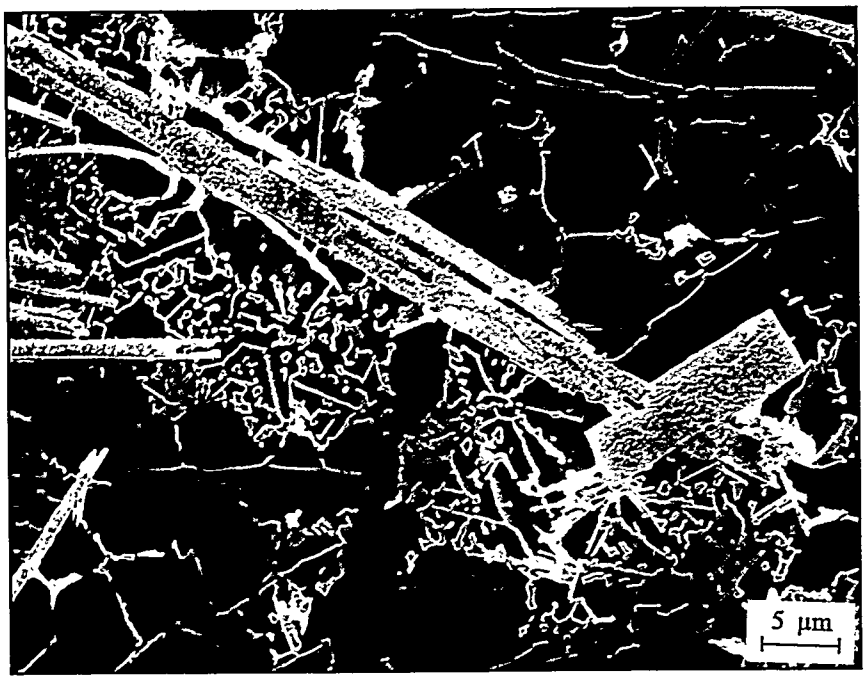

Fig. 3.11.7. SEM micrograph of Alloy 11 in the die cast condition, showing Fe bearing needles and the Al-Si eutectic structure (2000X).

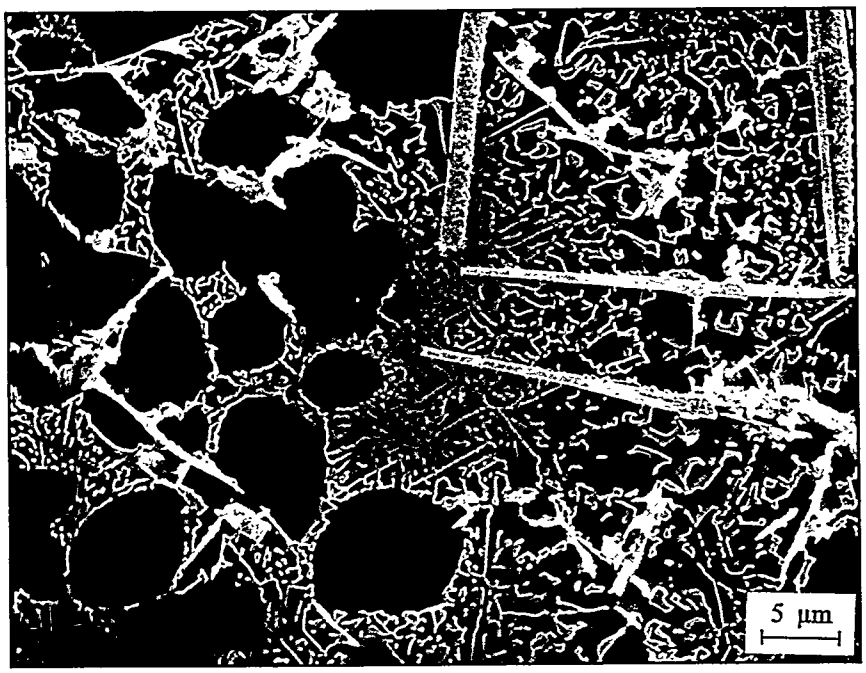

Fig. 3.11.8. SEM micrograph of Alloy 11 in the die cast condition, showing Cu bearing particles (bright phase) *within the Al-Si eutectic and in the interdendritic regions (2000X).*

ALLOY 11

Alloy #12	Wt.%	Si	Mg	Fe	Cu	Ni	Cr	Mn	Ti	Zn	Sr	Al
		12.95	0.05	1.55	1.29	0.46	0.01	0.43	0.01	2.91	0.023	Balance

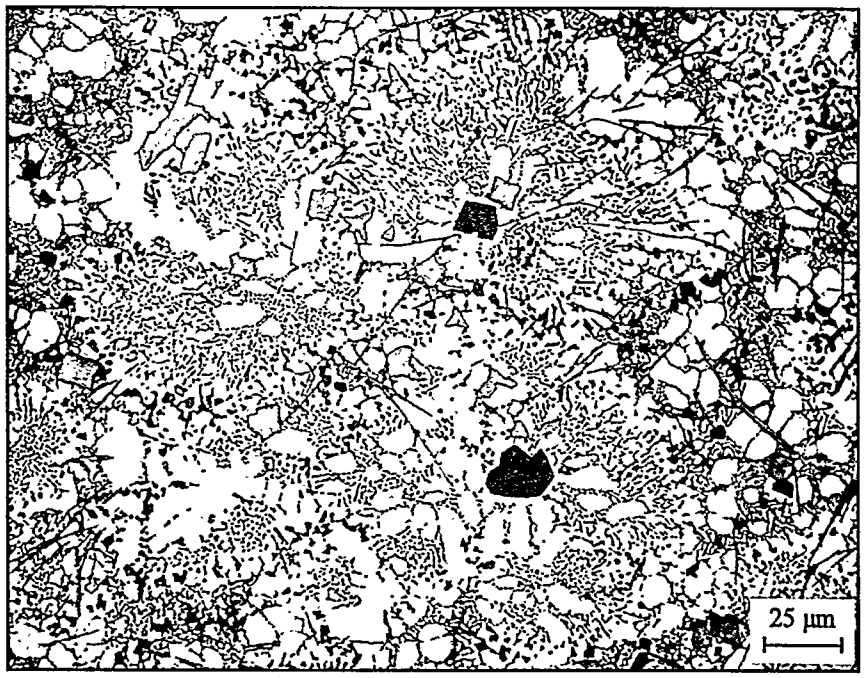

Fig. 3.12.5. Representative optical micrograph of Alloy 12, as die cast condition (400X).

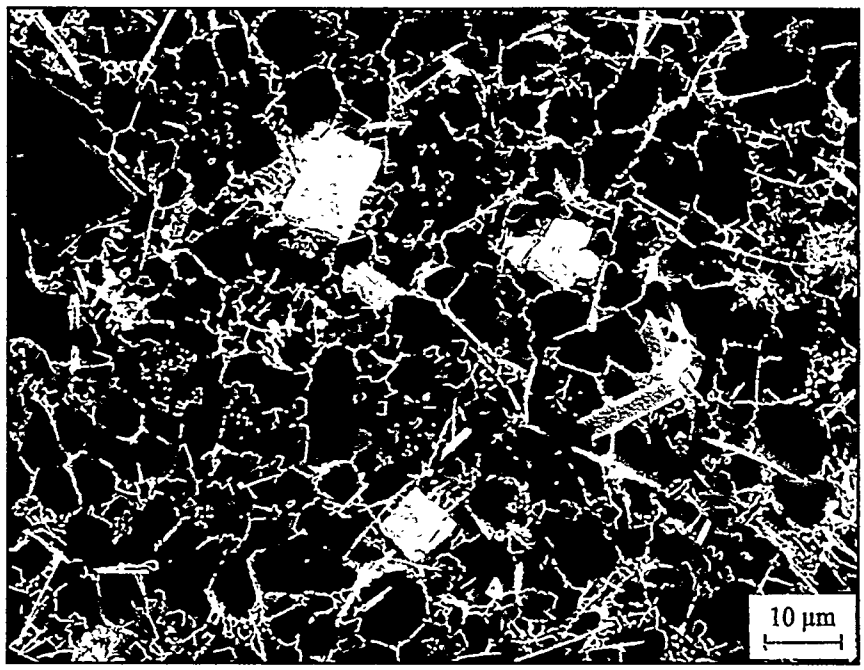

Fig. 3.12.6. Representative SEM micrograph of Alloy 12, as die cast condition.

ALLOY 12

Alloy #12	Wt.%	Si	Mg	Fe	Cu	Ni	Cr	Mn	Ti	Zn	Sr	Al
		12.95	0.05	1.55	1.29	0.46	0.01	0.43	0.01	2.91	0.023	Balance

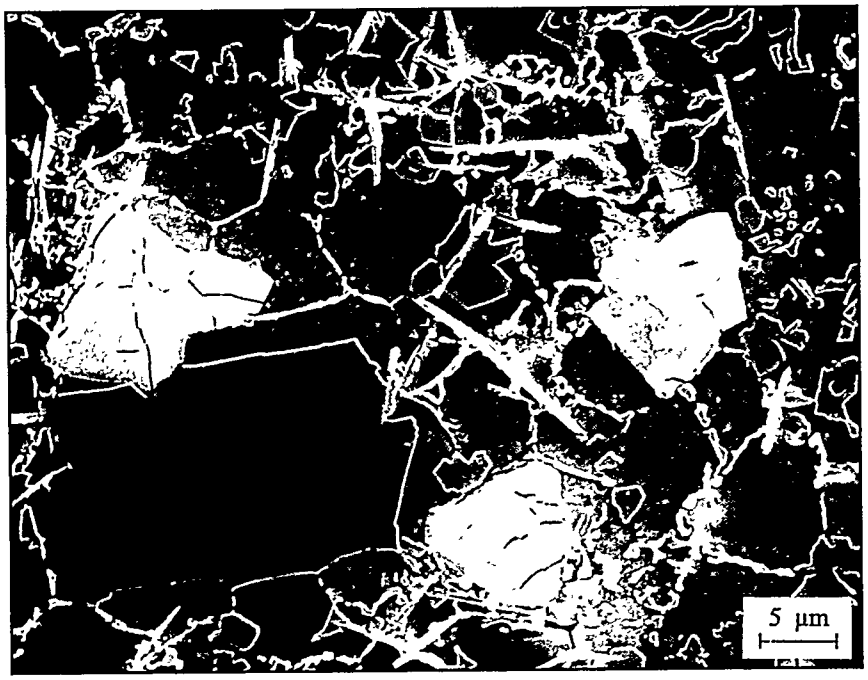

Fig. 3.12.7. SEM micrograph of Alloy 12 in the die cast condition, showing Fe bearing polyhedral crystals and needles, and the primary and eutectic Si particles (2000X).

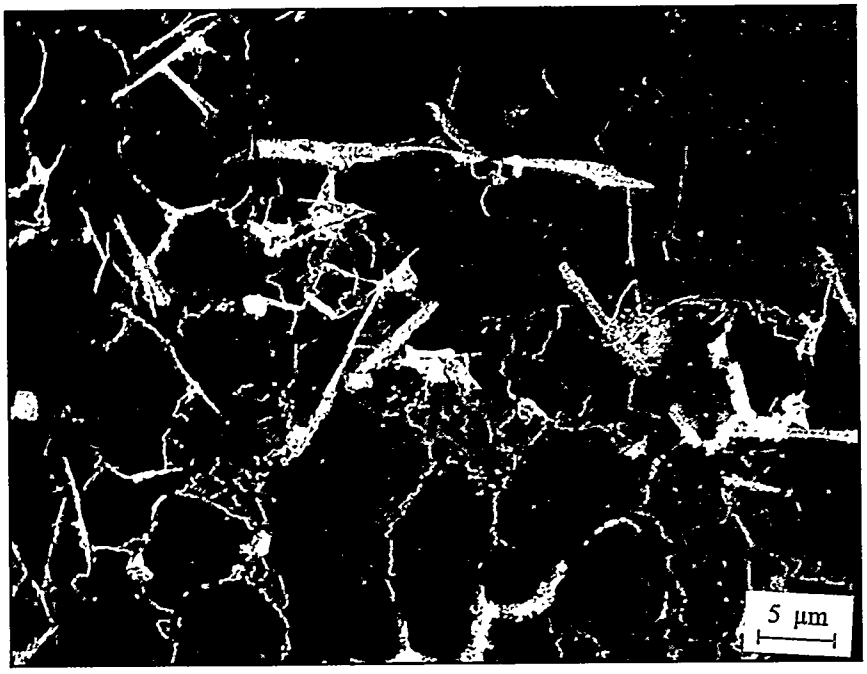

Fig. 3.12.8 SEM micrograph of Alloy 12 in the die cast condition, showing Cu bearing particles (bright phase) *in the interdendritic regions and within the Al-Si eutectic (2000X).*

ALLOY 12

Alloy #13	Wt.%	Si	Mg	Fe	Cu	Ni	Cr	Mn	Ti	Zn	Sr	Al
		13.03	0.46	0.58	4.70	0.44	0.01	0.01	0.17	2.61	0.021	Balance

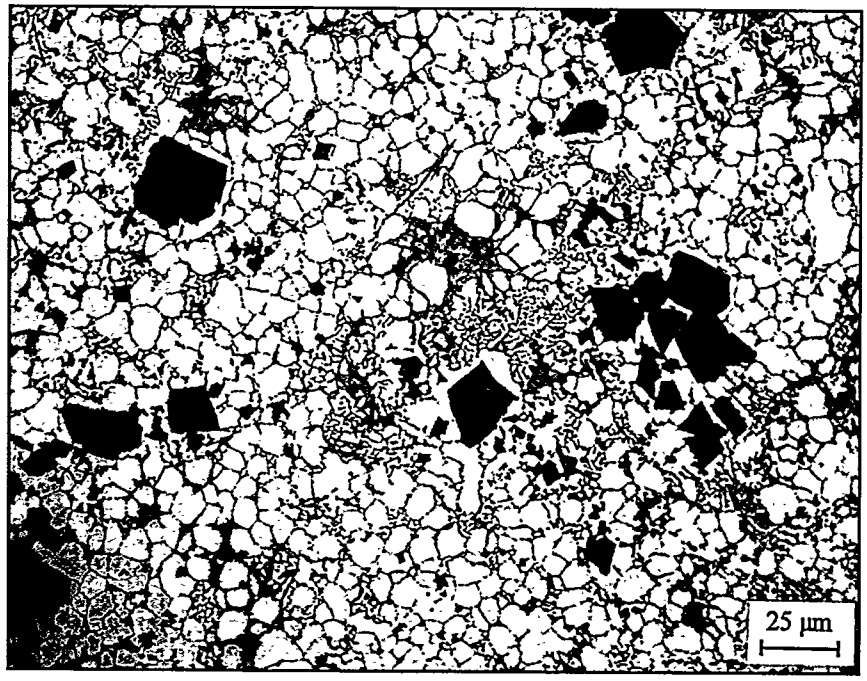

Fig. 3.13.5. Representative optical micrograph of Alloy 13, as die cast condition (400X).

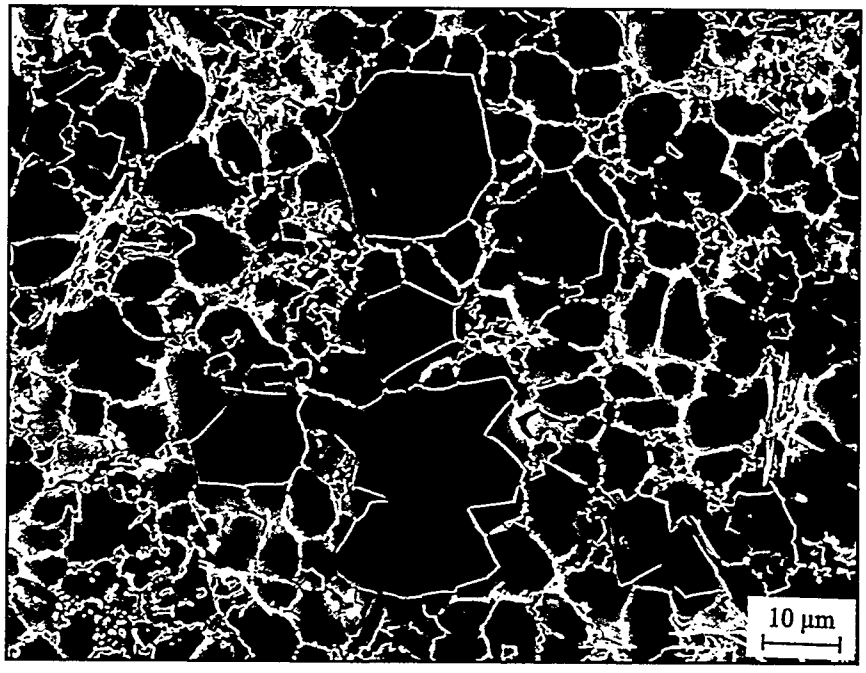

Fig. 3.13.6. Representative SEM micrograph of Alloy 13, as die cast condition (1000X).

ALLOY 13

Alloy #13	Wt.%	Si	Mg	Fe	Cu	Ni	Cr	Mn	Ti	Zn	Sr	Al
		13.03	0.46	0.58	4.70	0.44	0.01	0.01	0.17	2.61	0.021	Balance

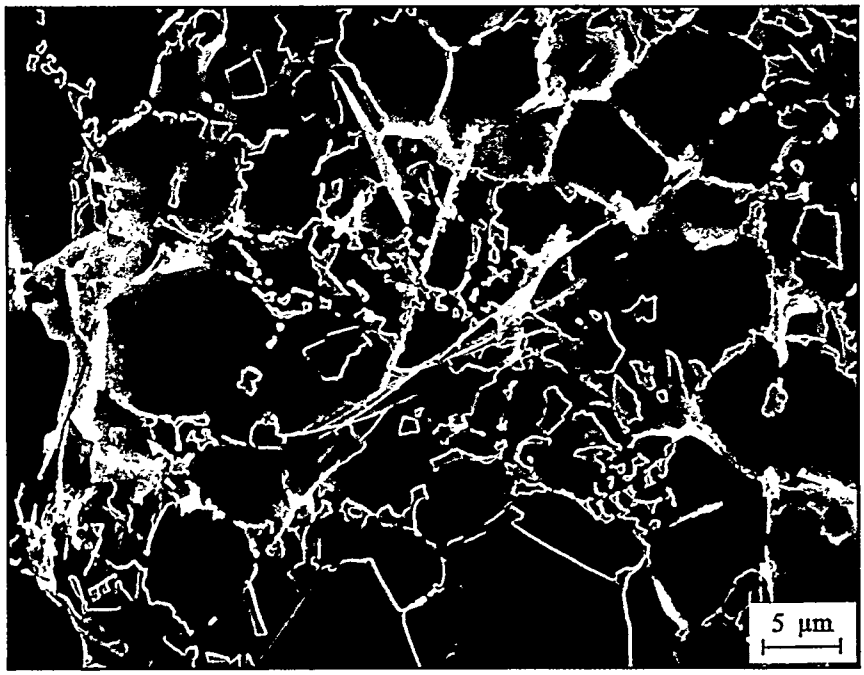

Fig. 3.13.7. SEM micrograph of Alloy 13 in the die cast condition, showing Fe bearing needles, and the primary and eutecttc Si particles (2000X).

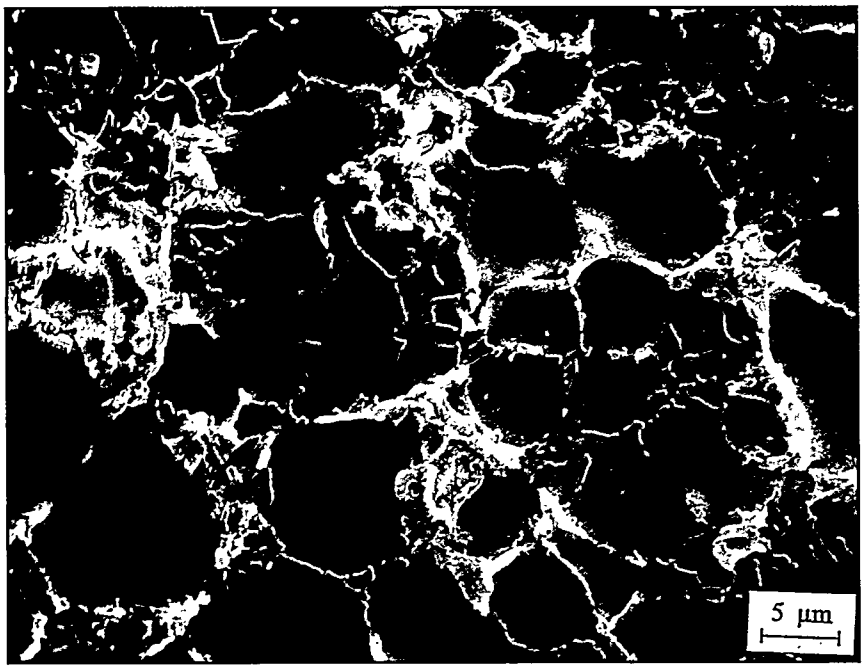

Fig. 3.13.8. SEM micrograph of Alloy 13 in the die cast condition, showing Cu bearing particles (bright phase) *in the interdendritic regions and within the Al-Si eutectic (2000X).*

ALLOY 13

Alloy #14	Wt.%	Si	Mg	Fe	Cu	Ni	Cr	Mn	Ti	Zn	Sr	Al
		12.94	0.48	0.74	4.77	0.50	0.01	0.57	0.01	0.55	0.00	Balance

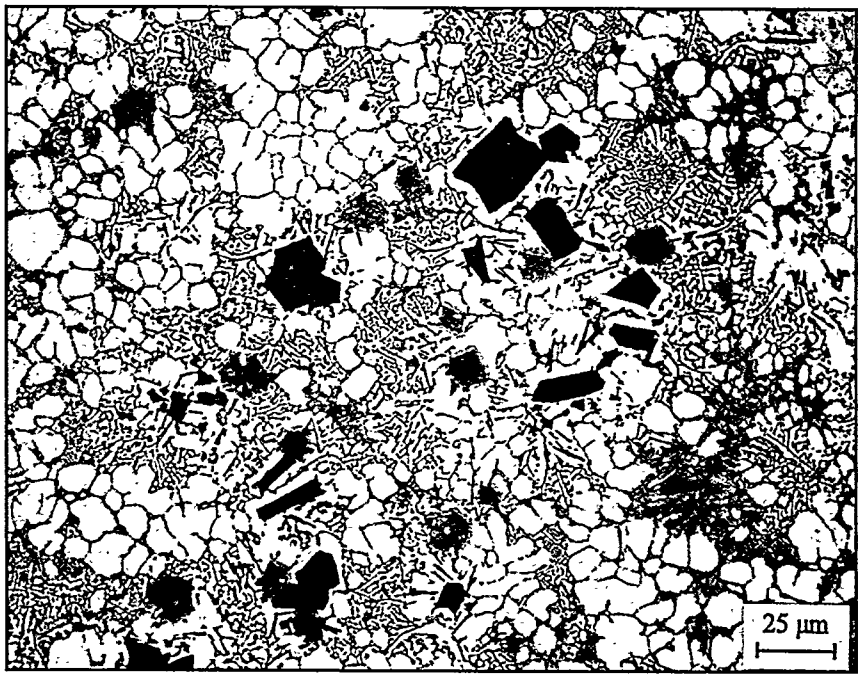

Fig. 3.14.5. Representative optical micrograph of Alloy 14, as die cast condition (400X).

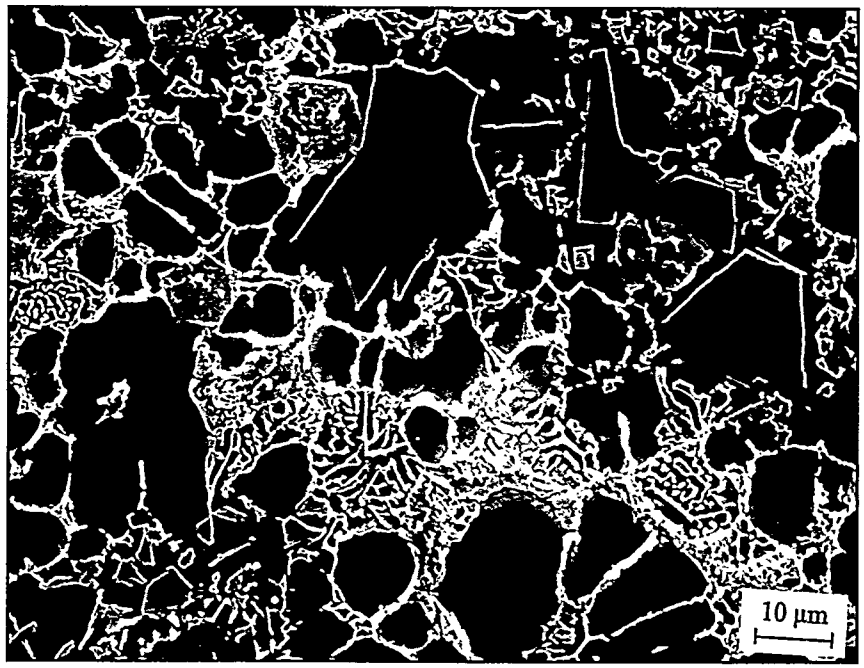

Fig. 3.14.6. Representative SEM micrograph of Alloy 14, as die cast condition (1000X).

ALLOY 14

Alloy #14	Wt.%	Si	Mg	Fe	Cu	Ni	Cr	Mn	Ti	Zn	Sr	Al
		12.94	0.48	0.74	4.77	0.50	0.01	0.57	0.01	0.55	0.00	Balance

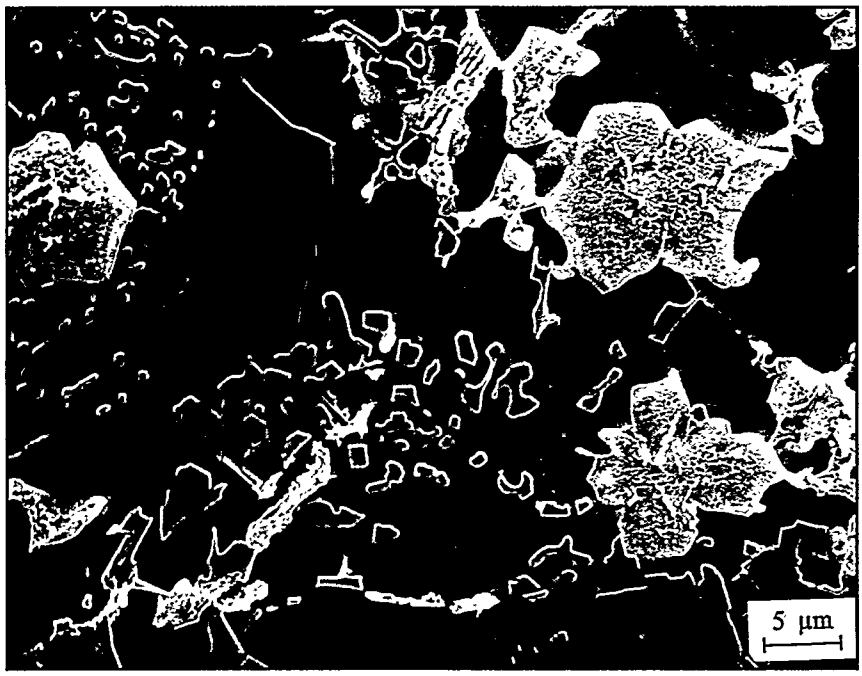

Fig. 3.14.7. SEM micrograph of Alloy 14 in the die cast condition, showing Fe bearing polyhedral and starlike crystals, and the primary and eutectic Si particles (2000X).

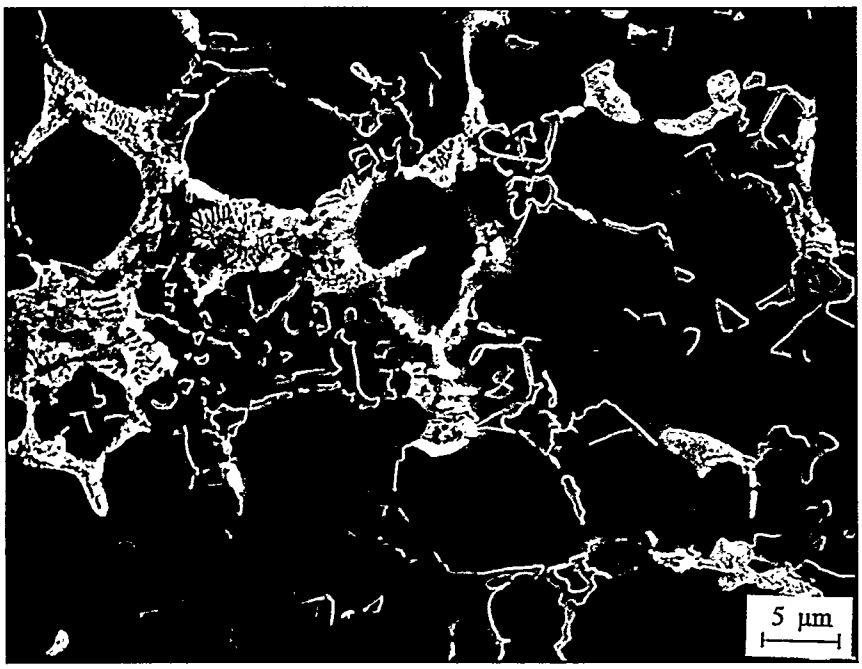

Fig. 3.14.8. SEM micrograph of Alloy 12 in the die cast condition, showing Cu bearing particles (bright phase) *in the interdendritic regions and within the Al-Si eutectic (2000X).*

ALLOY 14

Alloy #15	Wt.%	Si	Mg	Fe	Cu	Ni	Cr	Mn	Ti	Zn	Sr	Al
		12.78	0.47	1.51	1.27	0.06	0.14	0.01	0.18	2.94	0.00	Balance

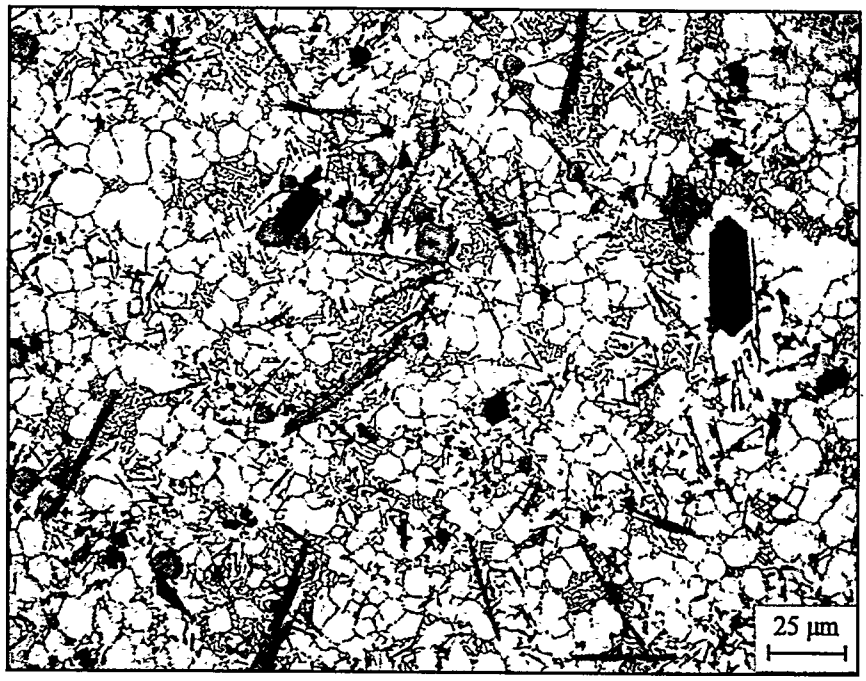

Fig. 3.15.5. Representative optical micrograph of Alloy 15, as die cast condition (400X).

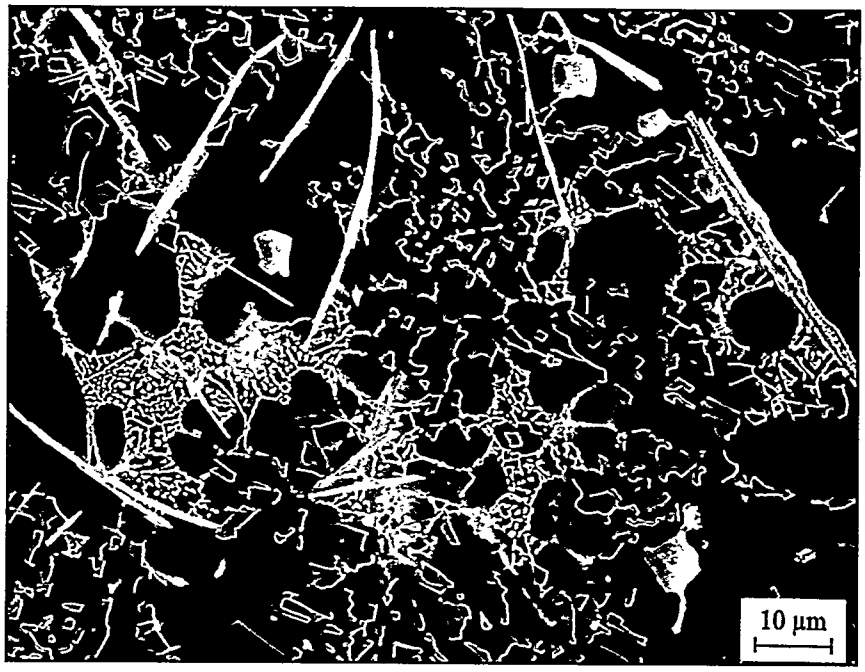

Fig. 3.15.6. Representative SEM micrograph of Alloy 15, as die cast condition (1000X).

ALLOY 15

Alloy #15	Wt.%	Si	Mg	Fe	Cu	Ni	Cr	Mn	Ti	Zn	Sr	Al
		12.78	0.47	1.51	1.27	0.06	0.14	0.01	0.18	2.94	0.00	Balance

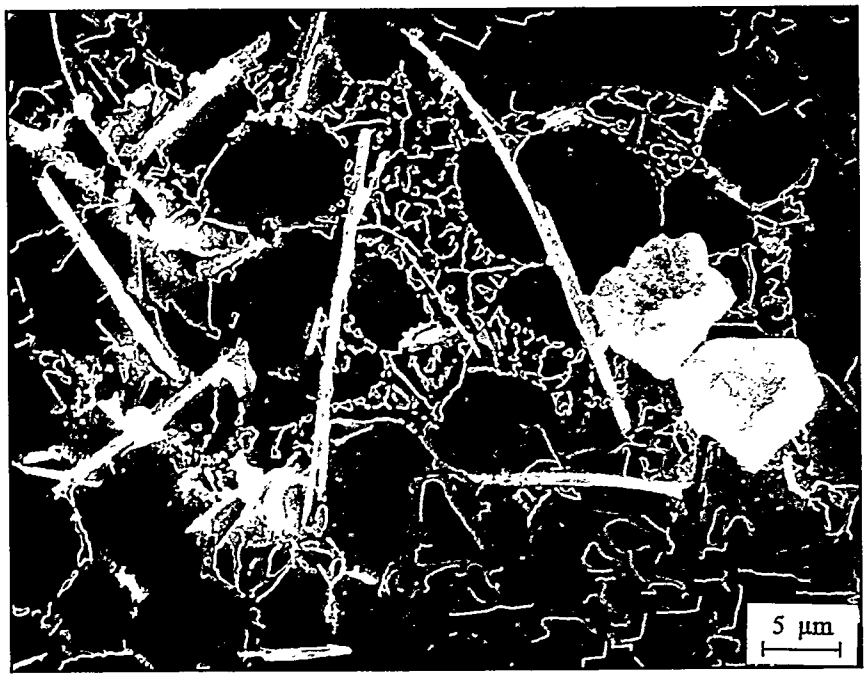

Fig. 3.15.7. SEM micrograph of Alloy 15 in the die cast condition, showing Fe bearing polyhedral crystals, and needles and the Al-Si eutectic structure (2000X).

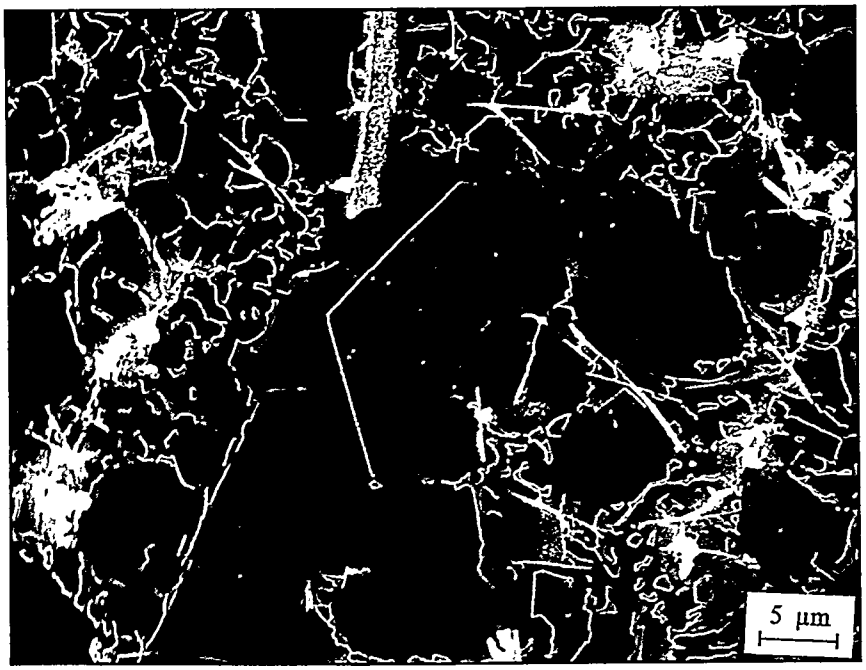

Fig. 3.15.8. SEM micrograph of Alloy 15 in the die cast condition, showing Cu bearing particles (bright phase) *within the Al-Si eutectic and the primary Si particles (2000X).*

ALLOY 15

Alloy #16	Wt.%	Si	Mg	Fe	Cu	Ni	Cr	Mn	Ti	Zn	Sr	Al
		12.86	0.41	1.63	1.21	0.06	0.14	0.44	0.01	0.46	0.024	Balance

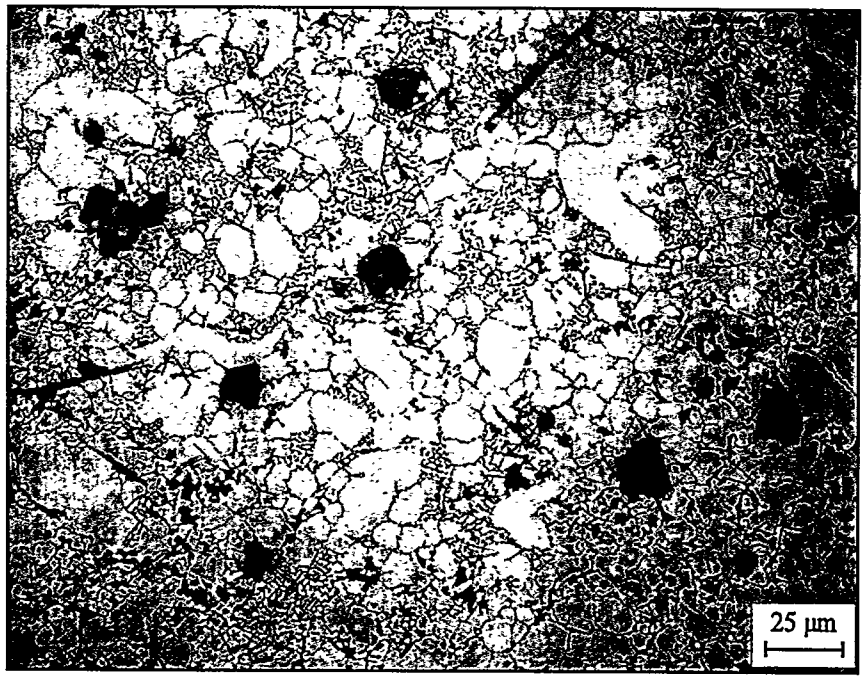

Fig. 3.16.5. Representative optical micrograph of Alloy 16, as die cast condition (400X).

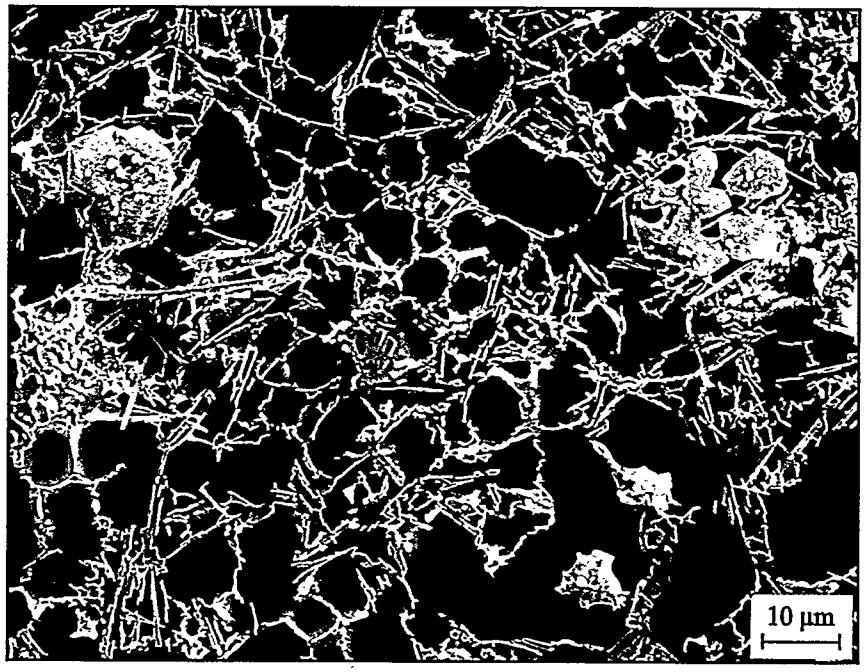

Fig. 3.16.6. Representative SEM micrograph of Alloy 16, as die cast condition (1000X).

ALLOY 16

Alloy #16	Wt.%	Si	Mg	Fe	Cu	Ni	Cr	Mn	Ti	Zn	Sr	Al
		12.86	0.41	1.63	1.21	0.06	0.14	0.44	0.01	0.46	0.024	Balance

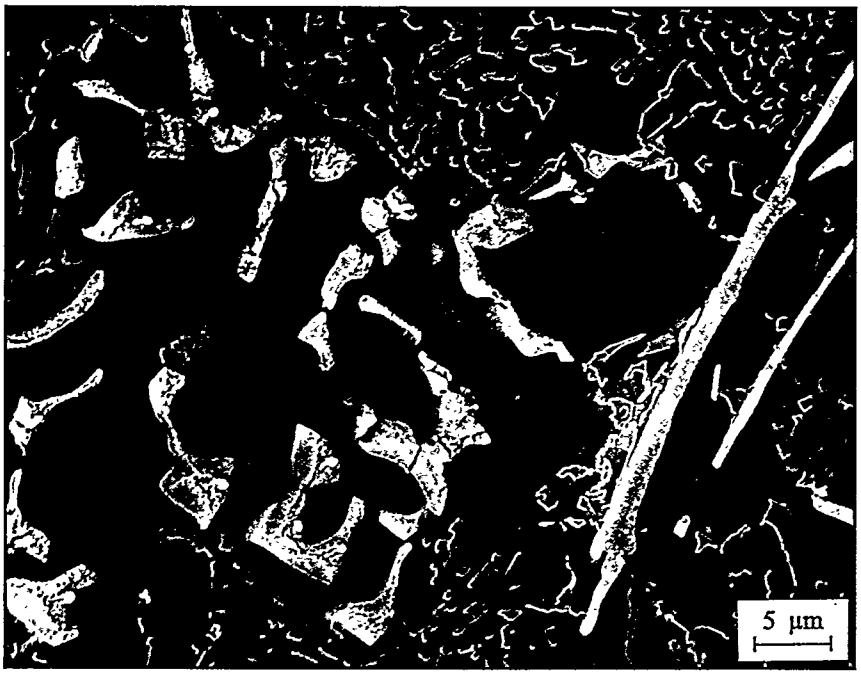

Fig. 3.16.7. SEM micrograph of Alloy 16 in the die cas condition, showing Fe bearing Chinese script and needles and the Al-Si eutectic structure (2000X).

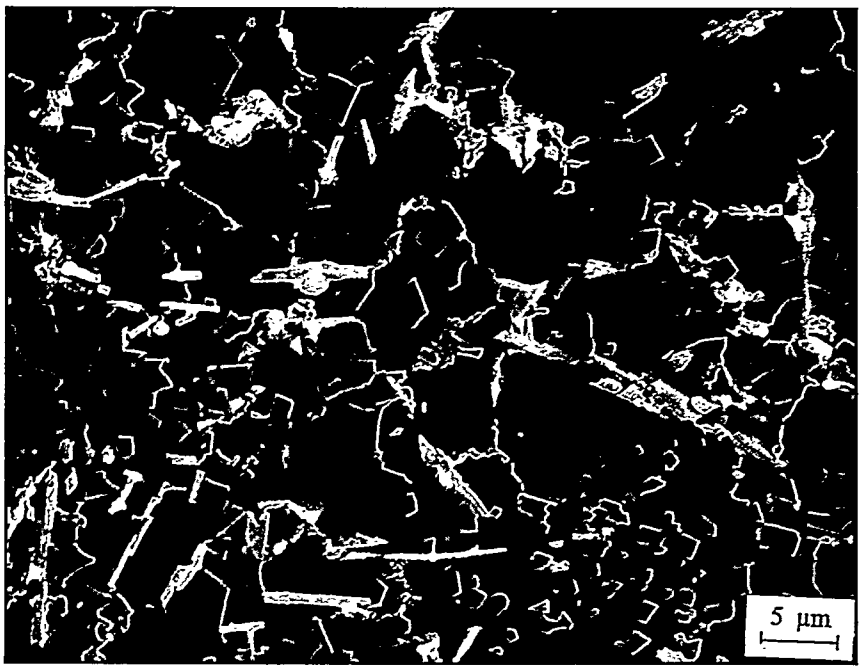

Fig. 3.16.8. SEM micrograph of Alloy 16 in the die ca condition, showing Cu bearing particles (bright phase) *wit in the Al-Si eutectic (2000X).*

ALLOY 16

Alloy #17	Wt.%	Si	Mg	Fe	Cu	Ni	Cr	Mn	Ti	Zn	Sr	Al
		8.39	0.02	0.90	2.71	0.04	0.06	0.22	0.03	1.10	--	balance

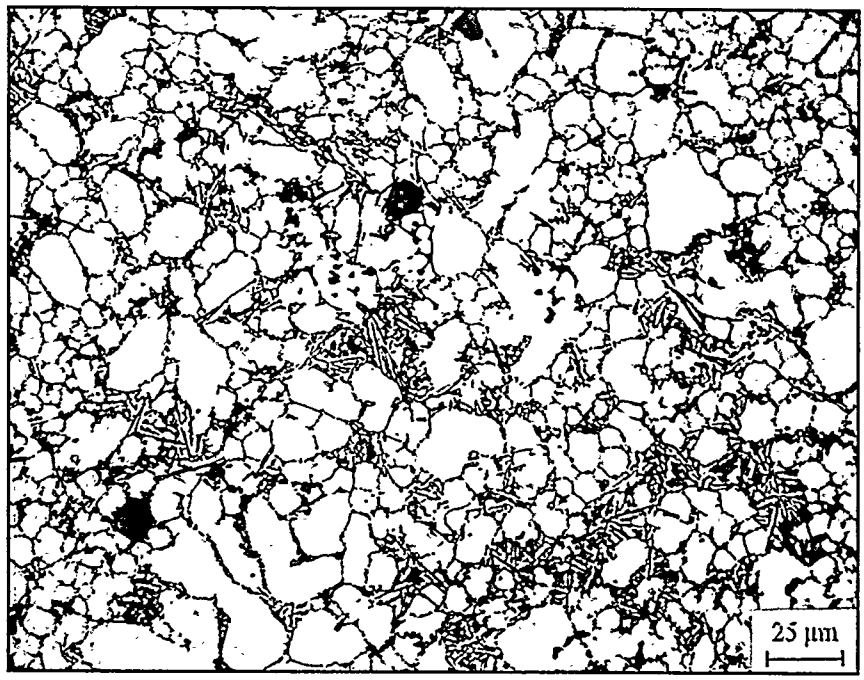

Fig. 3.17.5. Representative optical micrograph of Alloy 17, in the as die cast condition.

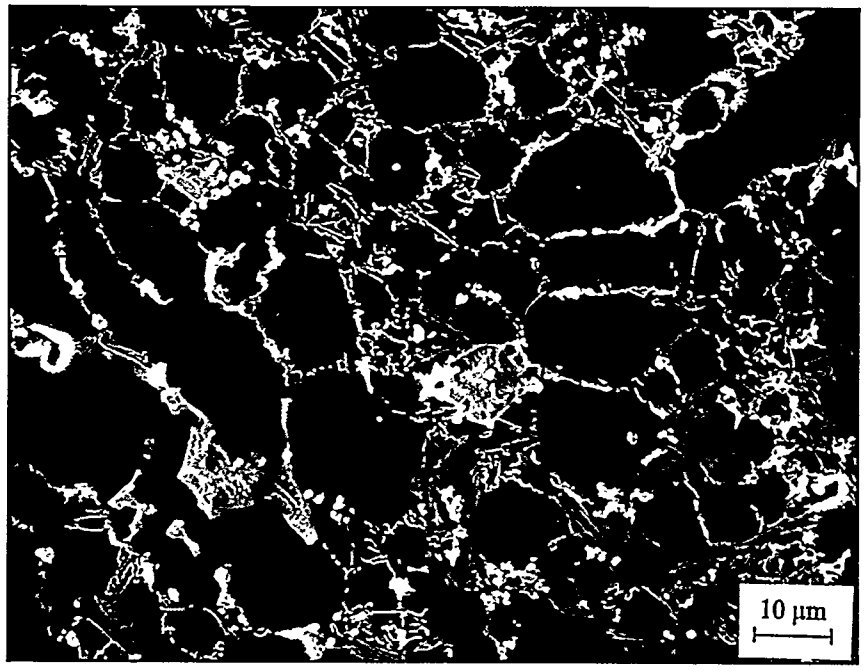

Fig. 3.17.6. Representative SEM micrograph of Alloy 17 in the as die cast condition (1000X).

ALLOY 17

Alloy #17	Wt.%	Si	Mg	Fe	Cu	Ni	Cr	Mn	Ti	Zn	Sr	Al
		8.39	0.02	0.90	2.71	0.04	0.06	0.22	0.03	1.10	–	balance

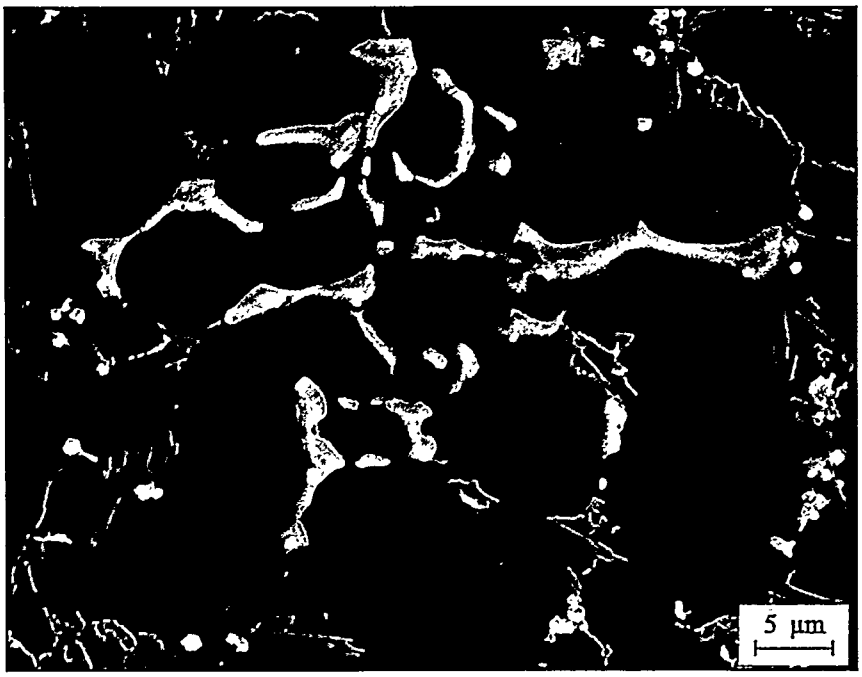

Fig. 3.17.7. SEM micrograph of Alloy 17 in the die cast condition, showing Fe bearing Chinese script and the Al-Si eutectic structure (2000X).

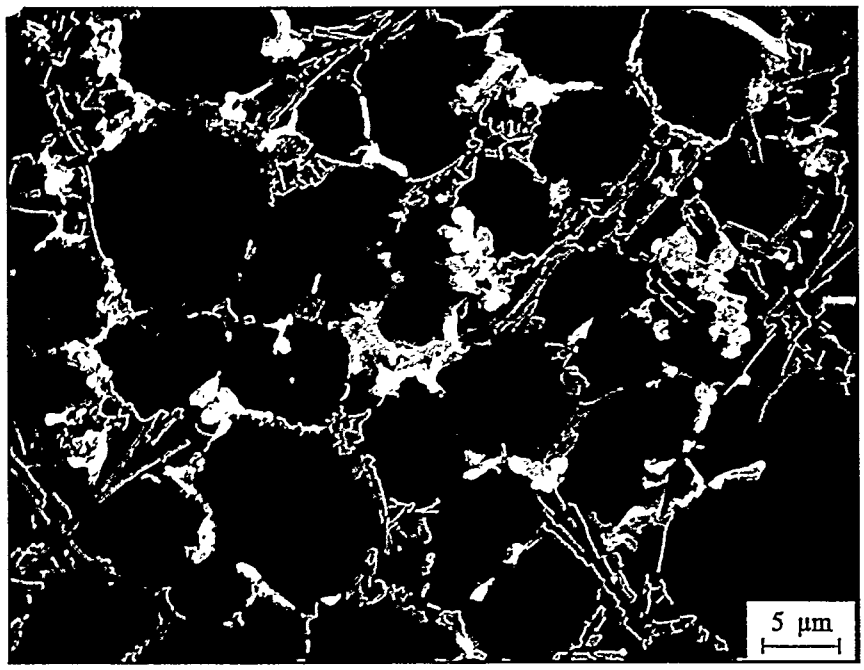

Fig. 3.17.8. SEM micrograph of Alloy 17 in the die cast condition, showing Cu bearing particles (bright phase) *in the interdendritic regions and within the Al-Si eutectic (2000X).*

ALLOY 17

Alloy #18	Wt.%	Si	Mg	Fe	Cu	Ni	Cr	Mn	Ti	Zn	Sr	Al
		8.19	0.02	0.91	3.87	0.03	0.04	0.17	0.03	2.20	--	balance

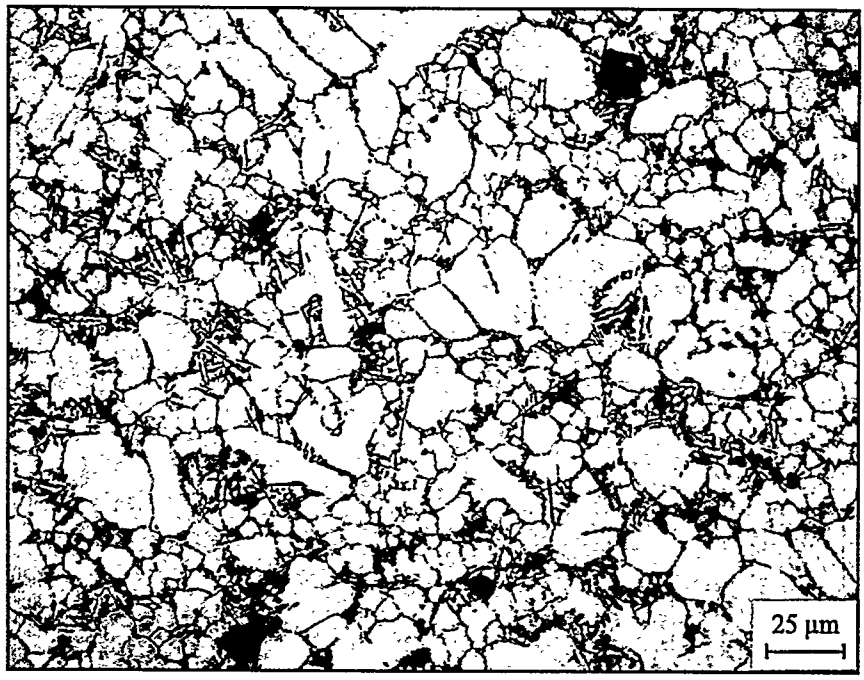

Fig. 3.18.5. Representative optical micrograph of Alloy 18, as die cast condition (400X).

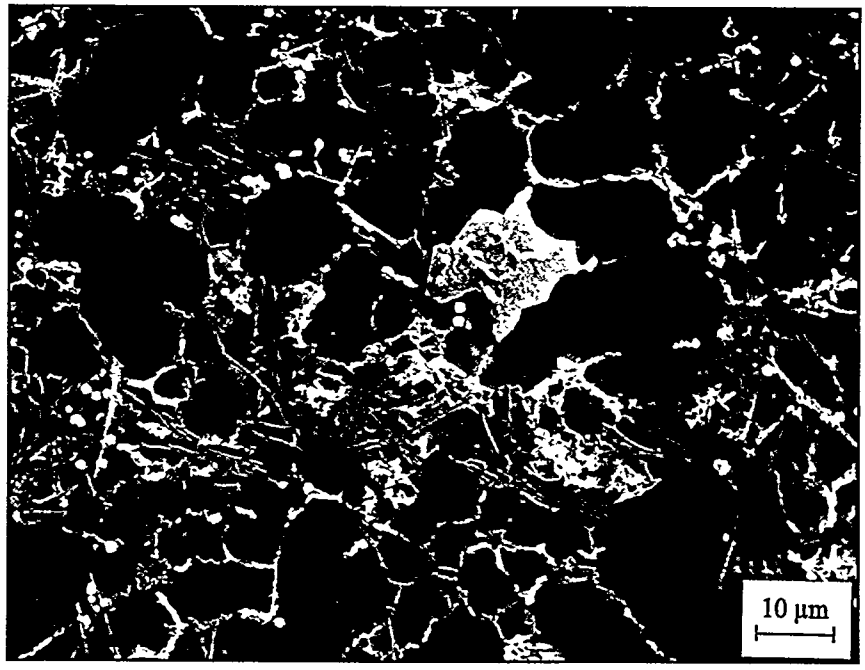

Fig. 3.18.6. Representative SEM micrograph of Alloy 18 in the die cast condition, showing Fe bearing polyhedral crystals, small particles, and needles, and the Al-Si eutectic structure (2000X).

ALLOY 18

Alloy #18	Wt.%	Si	Mg	Fe	Cu	Ni	Cr	Mn	Ti	Zn	Sr	Al
		8.19	0.02	0.91	3.87	0.03	0.04	0.17	0.03	2.20	--	balance

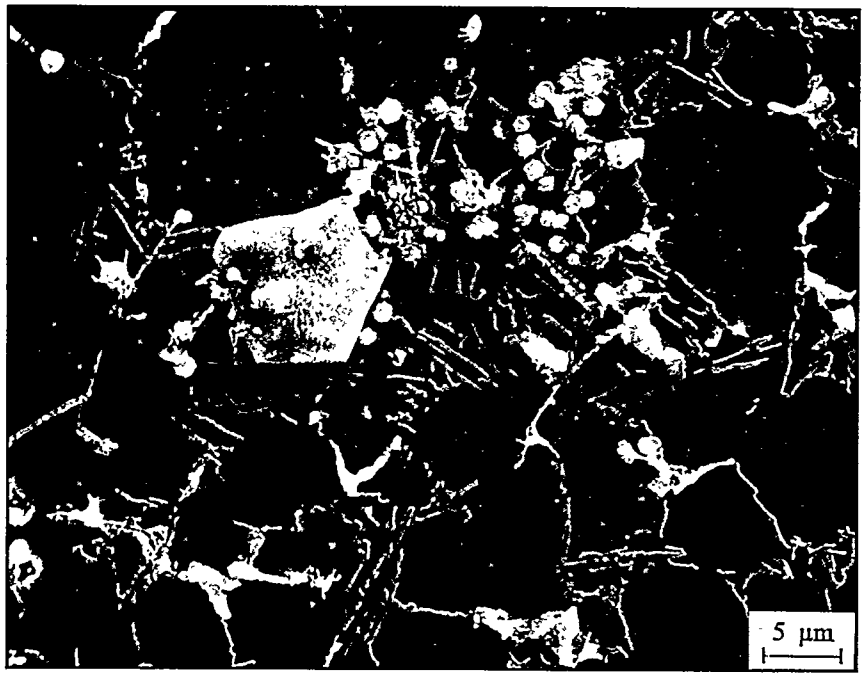

Fig. 3.18.7. SEM micrograph of Alloy 18 in the die cast condition, showing Fe bearing polyhedral crystals, small particles, and needles, and the Al-Si eutectic structure (2000X).

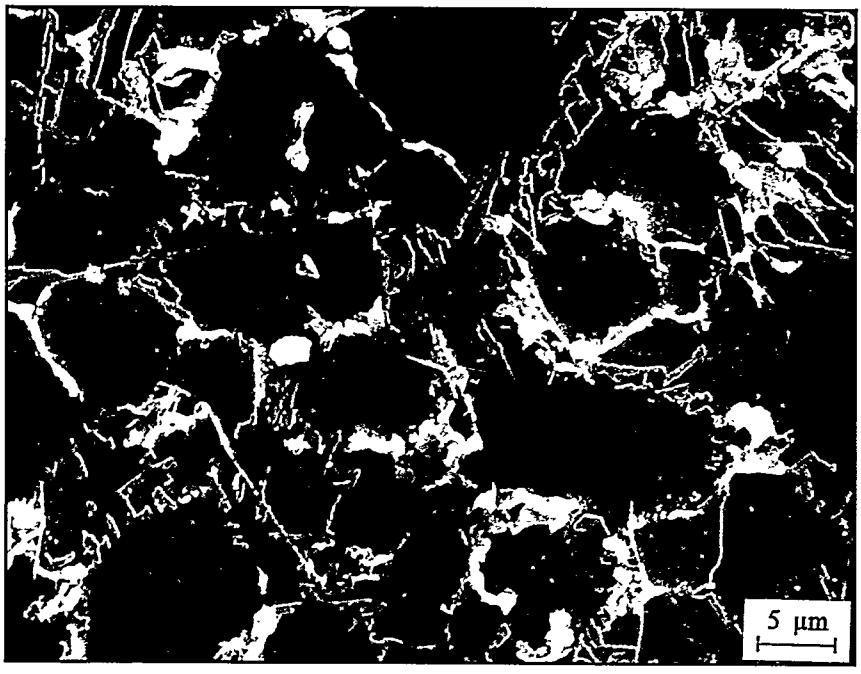

Fig. 3.18.8. SEM micrograph of Alloy 18 in the die cast condition, showing Cu bearing particles (bright phase) *in the interdendritic regions and within the Al-Si eutectic (2000X).*

ALLOY 18

Alloy #19	Wt.%	Si	Mg	Fe	Cu	Ni	Cr	Mn	Ti	Zn	Sr	Al
		9.49	0.02	0.87	2.61	0.03	0.05	0.23	0.03	2.20	--	balance

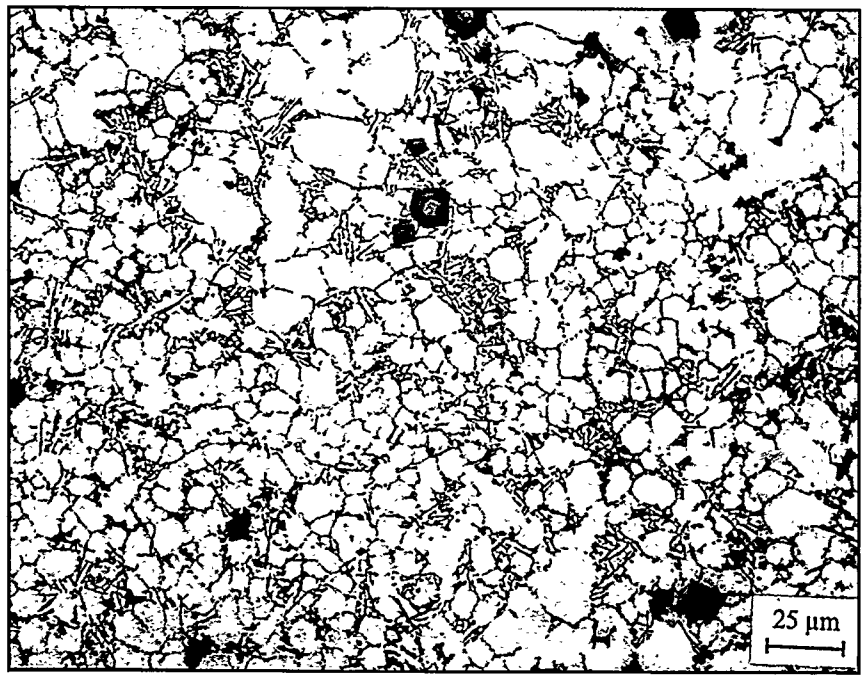

Fig. 3.19.5. Representative optical micrograph of Alloy 19, as die cast condition (400X).

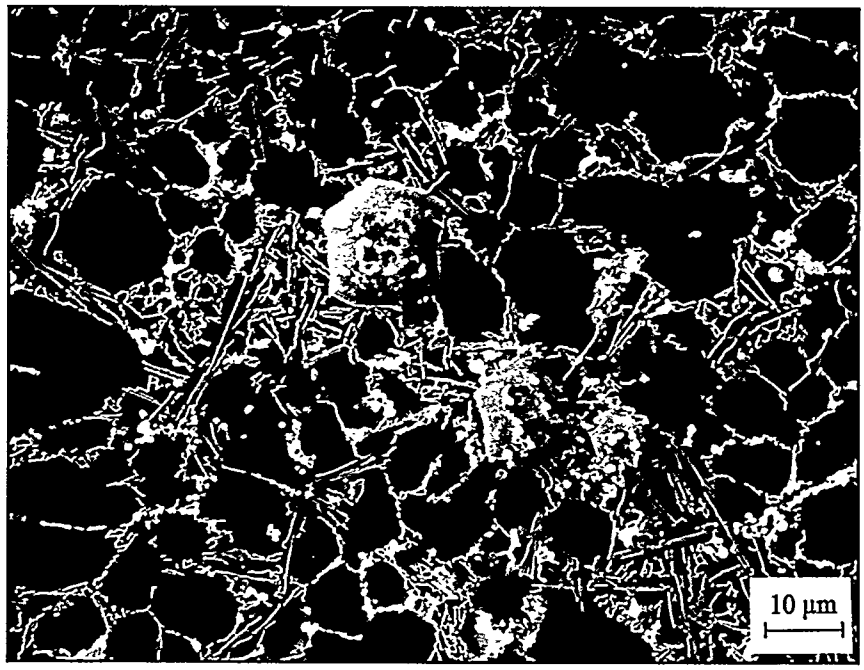

Fig. 3.19.6. Representative SEM micrograph of Alloy 19 in the die cast condition, showing Fe bearing polyhedral crystals and small particles, and the Al-Si eutectic structure (2000X).

ALLOY 19

Alloy #19	Wt.%	Si	Mg	Fe	Cu	Ni	Cr	Mn	Ti	Zn	Sr	Al
		9.49	0.02	0.87	2.61	0.03	0.05	0.23	0.03	2.20	--	balance

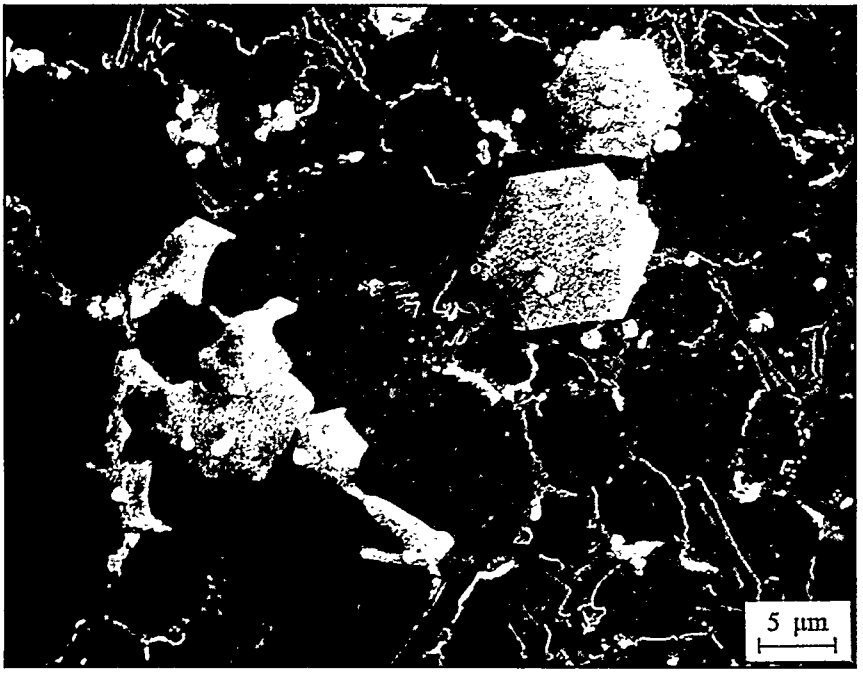

Fig. 3.19.7. SEM micrograph of Alloy 19 in the die cast condition, showing Fe bearing polyhedral crystals and small particles, and the AL-Si eutectic structure (2000X).

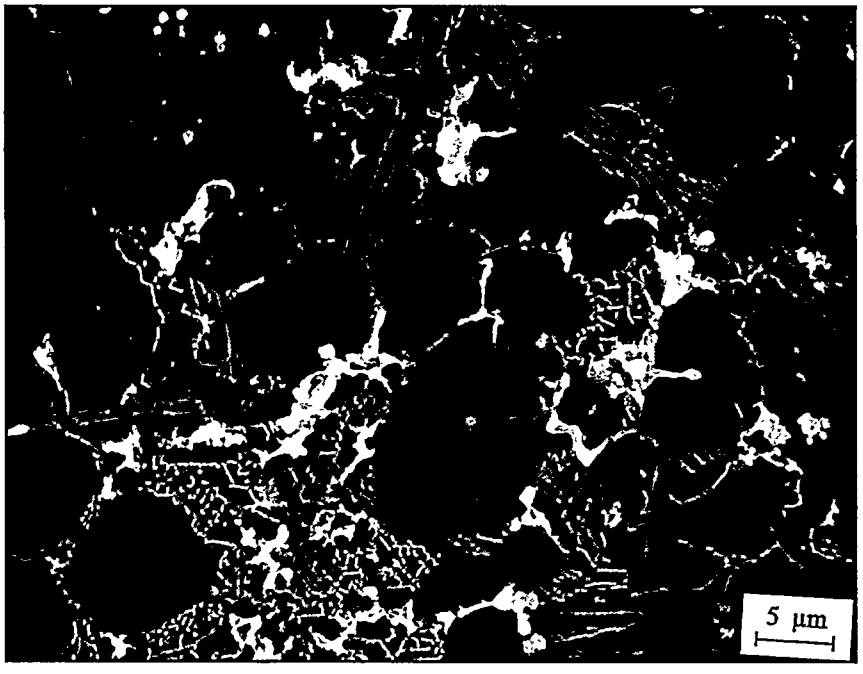

Fig. 3.19.8. SEM micrograph of Alloy 19 in the die cast condition, showing Cu bearing particles (bright phase) *in the interdendritic regions and within the Al-Si eutectic (2000X).*

ALLOY 19

Alloy #20	Wt.%	Si	Mg	Fe	Cu	Ni	Cr	Mn	Ti	Zn	Sr	Al
		9.50	0.09	1.43	4.00	0.13	0.06	0.21	0.05	1.10	--	balance

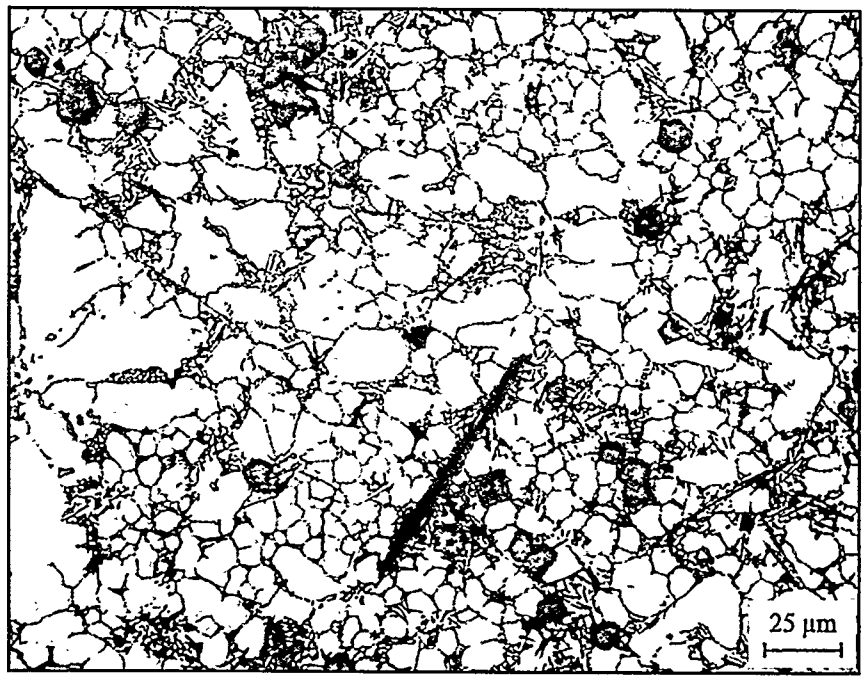

Fig. 3.20.5. Representative optical micrograph of Alloy 20, as die cast condition (400X).

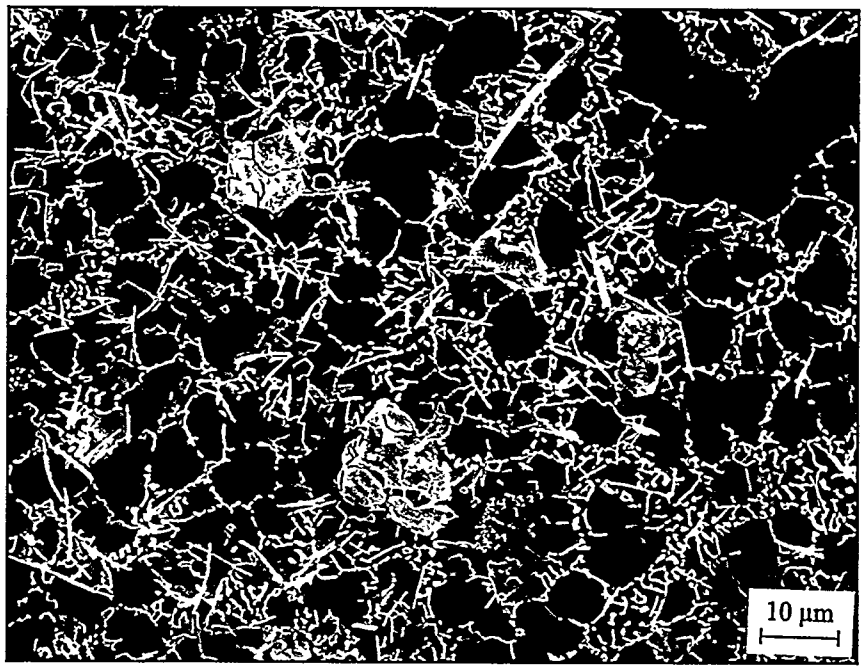

Fig. 3.20.6. Representative SEM micrograph of Alloy 20, as die cast condition (1000X).

ALLOY 20

Alloy #20	Wt.%	Si	Mg	Fe	Cu	Ni	Cr	Mn	Ti	Zn	Sr	Al
		9.50	0.09	1.43	4.00	0.13	0.06	0.21	0.05	1.10	–	balance

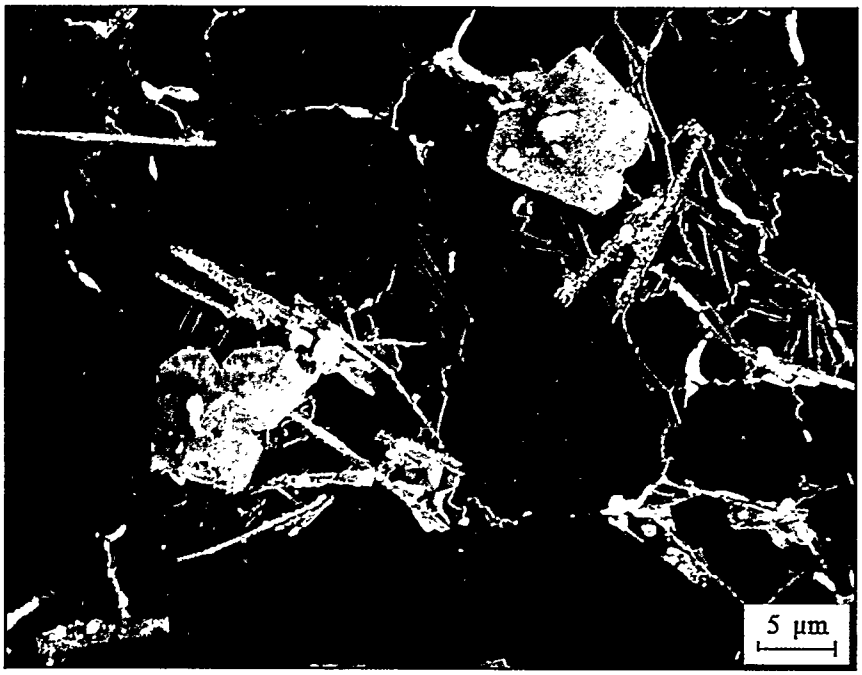

Fig. 3.20.7. SEM micrograph of Alloy 20 in the die cast condition, showing Fe bearing polyhedral crystals and needles, and the Al-Si eutectic structure (2000X).

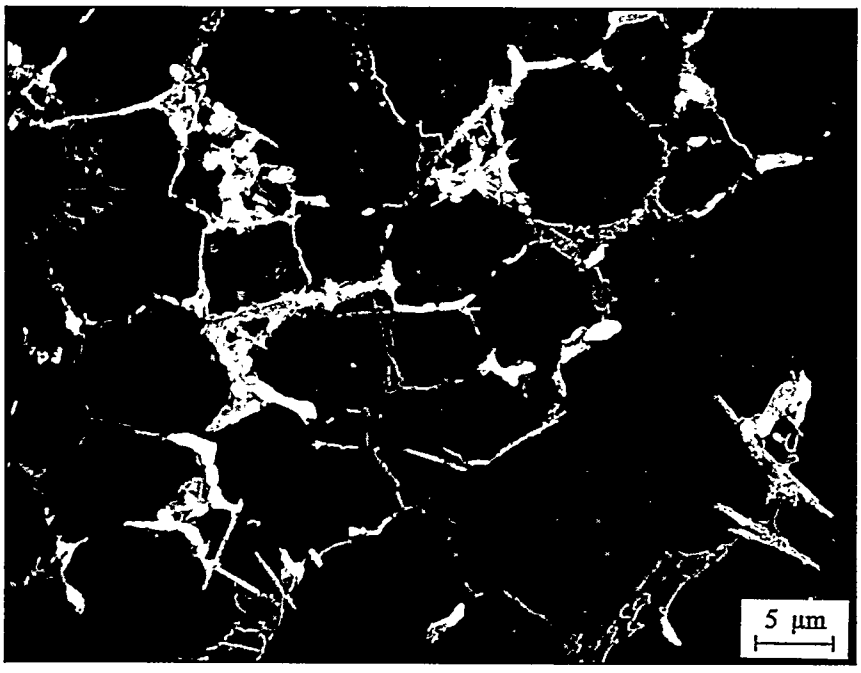

Fig. 3.20.8. SEM micrograph of Alloy 20 in the die cast condition, showing Cu bearing particles (bright phase) *in the interdendritic regions and within the Al-Si eutectic.*

ALLOY 20

Alloy #21	Wt.%	Si	Mg	Fe	Cu	Ni	Cr	Mn	Ti	Zn	Sr	Al
		9.66	0.05	1.22	2.68	0.03	0.06	0.26	0.03	2.10	--	balance

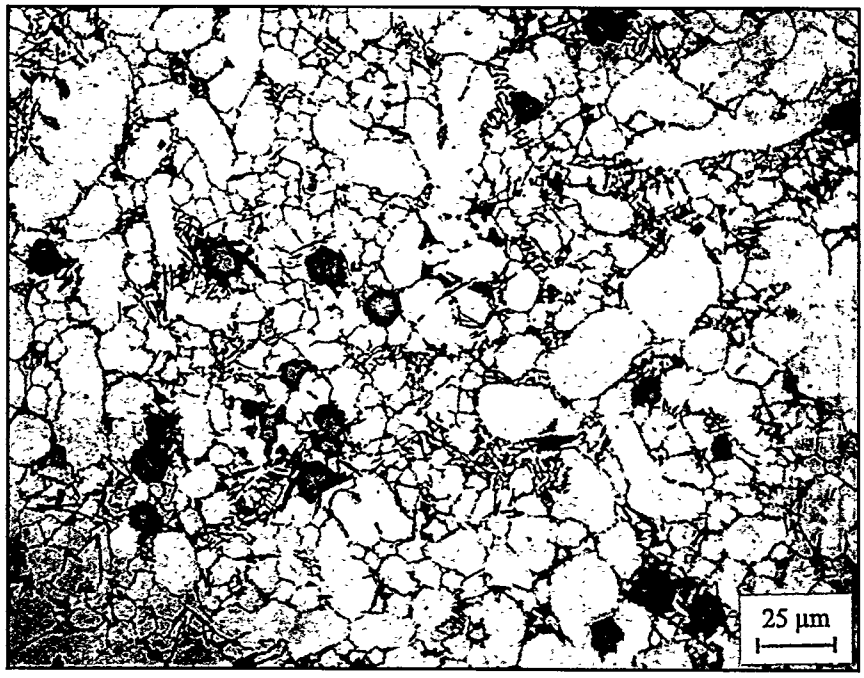

Fig. 3.21.5. Representative optical micrograph of Alloy 21, as die cast condition (400X).

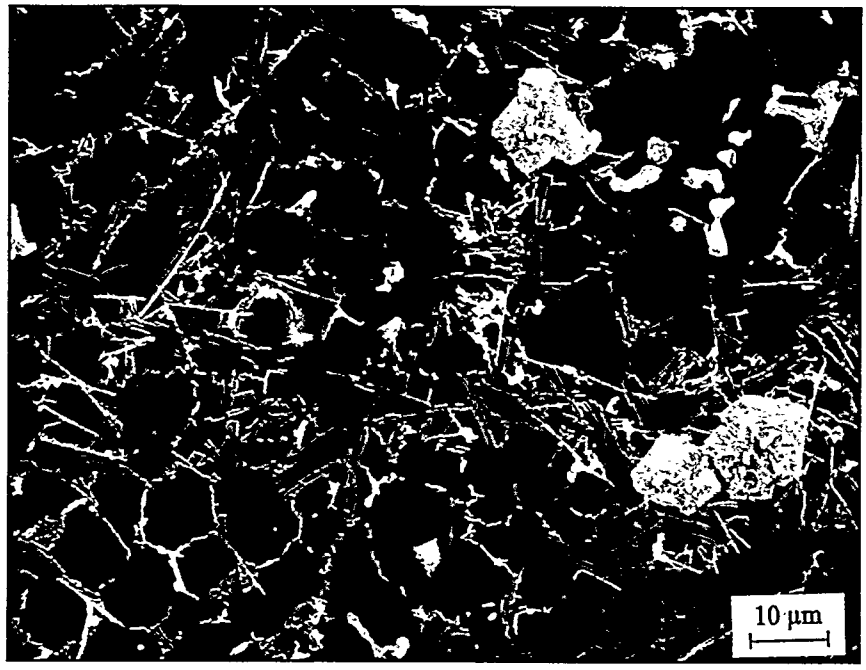

Fig. 3.21.6. Representative SEM micrograph of Alloy 21, as die cast condition (1000X).

ALLOY 21

Alloy #21	Wt.%	Si	Mg	Fe	Cu	Ni	Cr	Mn	Ti	Zn	Sr	Al
		9.66	0.05	1.22	2.68	0.03	0.06	0.26	0.03	2.10	--	balance

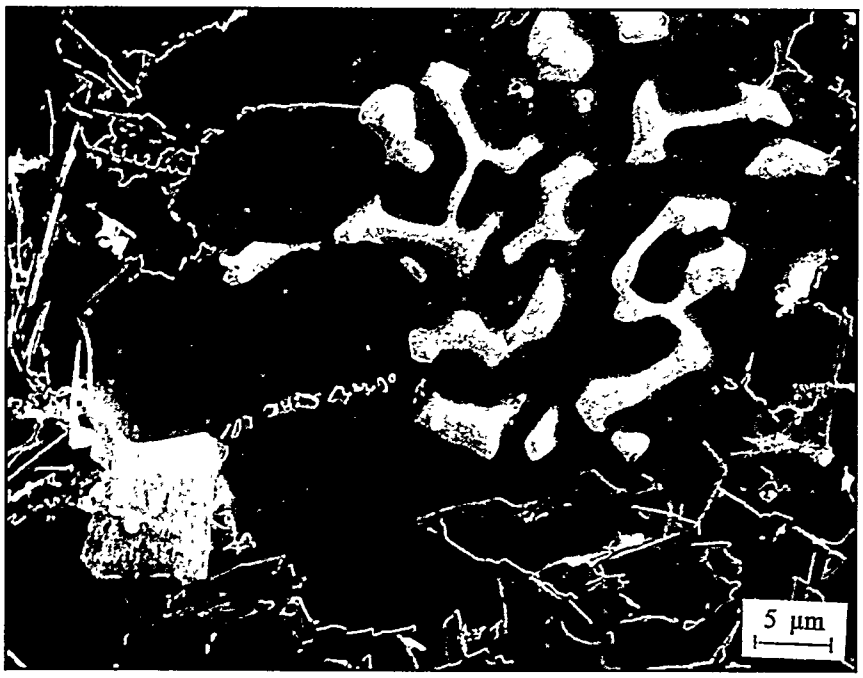

Fig. 3.21.7. SEM micrograph of Alloy 21 in the die cast condition, showing Fe bearing Chinese script, polyhedral crystals and needles, and the Al-Si eutectic structure (2000X).

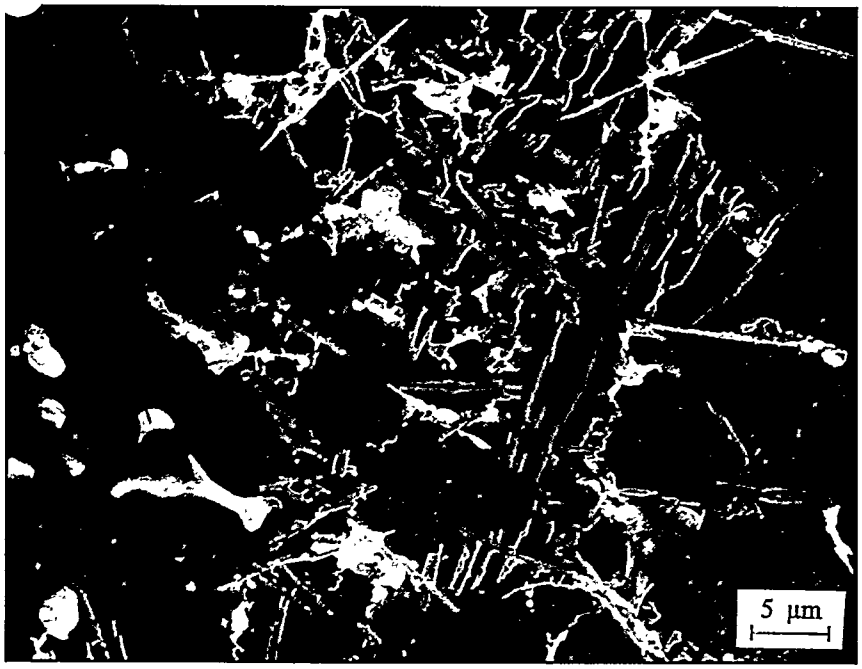

Fig. 3.21.8. SEM micrograph of Alloy 21 in the die cast condition, showing Cu bearing particles (bright phase) *within the Al-Si eutectic (2000X).*

Alloy #22	Wt.%	Si	Mg	Fe	Cu	Ni	Cr	Mn	Ti	Zn	Sr	Al
		9.69	0.05	1.05	4.54	0.04	0.06	0.27	0.03	1.20	--	balance

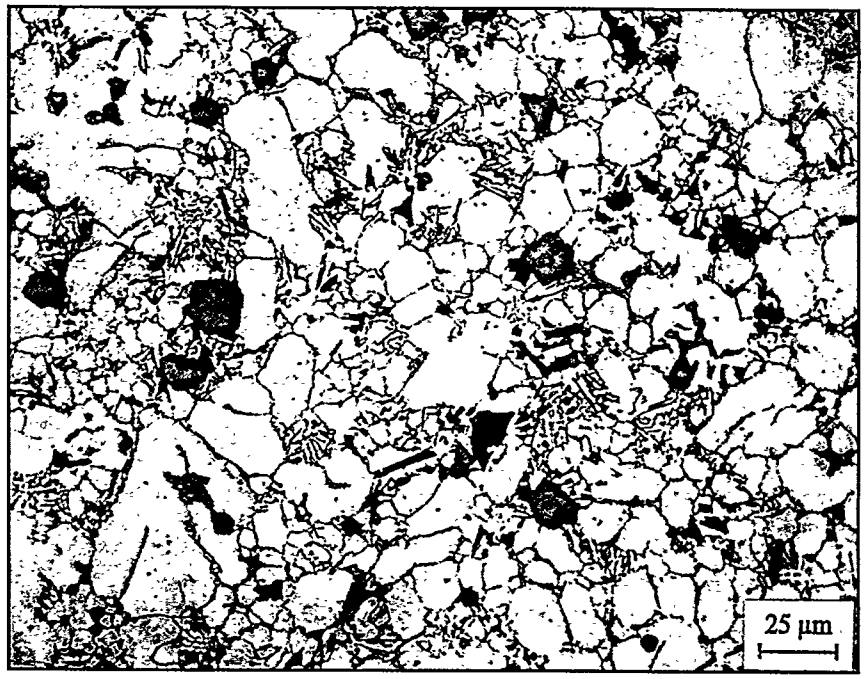

Fig. 3.22.5. Representative optical microstructure of Alloy 22, as die cast condition (400X).

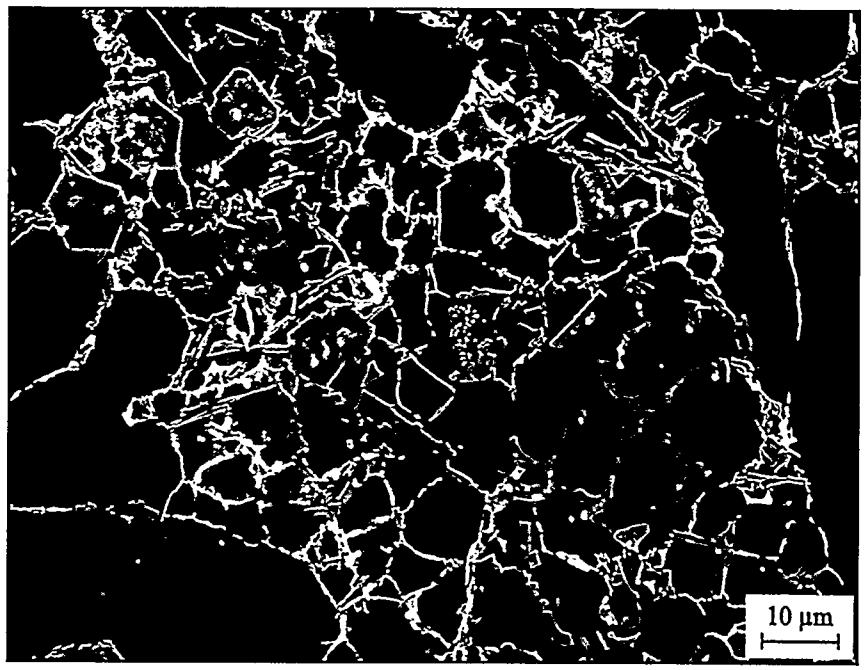

Fig. 3.22.6. Representative SEM micrograph of Alloy 22, as die cast condition (1000X).

Alloy #22	Wt.%	Si	Mg	Fe	Cu	Ni	Cr	Mn	Ti	Zn	Sr	Al
		9.69	0.05	1.05	4.54	0.04	0.06	0.27	0.03	1.20	--	balance

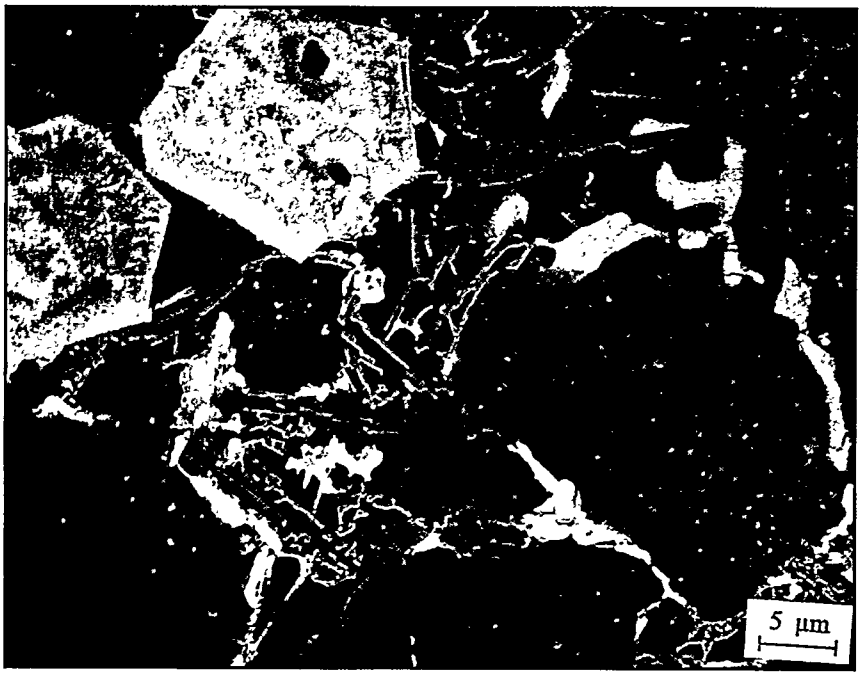

Fig. 3.22.7 SEM micrograph of Alloy 22 in the die cast condition, showing Fe bearing polyhedral crystals and Chinese script, and the Al-Si eutectic structure (2000X).

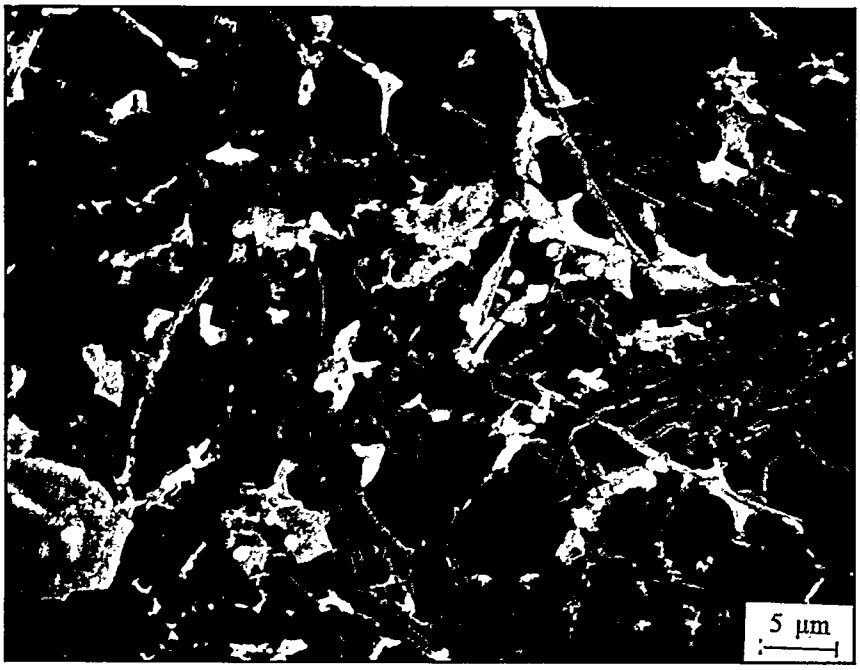

Fig. 3.22.8. SEM micrograph of Alloy 22 in the die cast condition, showing Cu bearing particles (bright phase) *within the Al-Si eutectic structure and the Fe bearing needles (2000X).*

Alloy #23	Wt.%	Si	Mg	Fe	Cu	Ni	Cr	Mn	Ti	Zn	Sr	Al
		10.88	0.05	1.27	2.62	0.04	0.06	0.26	0.03	1.20	--	balance

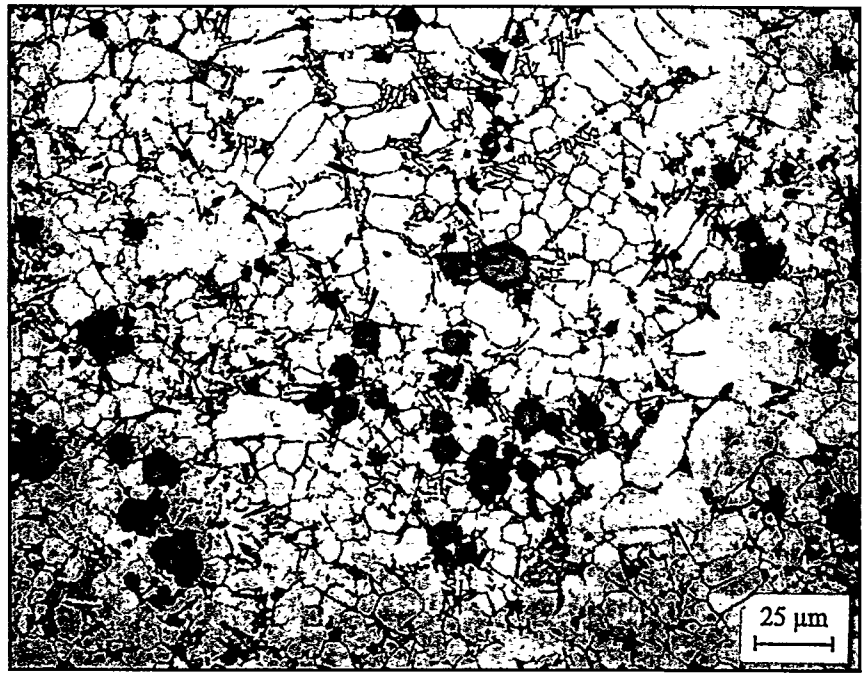

Fig. 3.23.5. Representative optical micrograph of Alloy 23, in the as die cast condition.

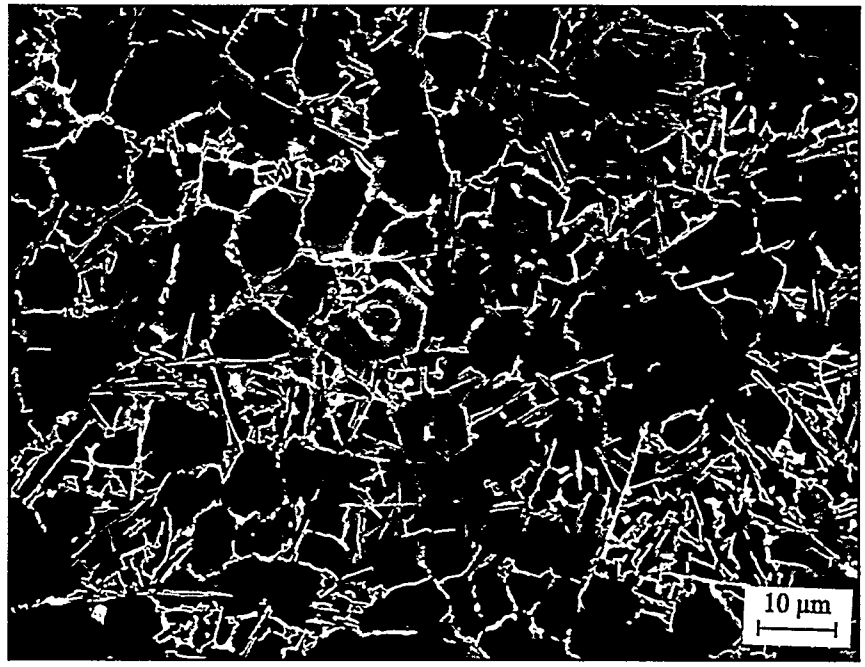

Fig. 3.23.6. Representative SEM micrograph of Alloy 23, in the as die cast condition.

ALLOY 23

Alloy #23	Wt.%	Si	Mg	Fe	Cu	Ni	Cr	Mn	Ti	Zn	Sr	Al
		10.88	0.05	1.27	2.62	0.04	0.06	0.26	0.03	1.20	--	balance

Fig. 3.23.7. SEM micrograph of Alloy 23 in the die cast condition, showing Fe bearing polyhedral crystals and needles, and the Al-Si eutectic structure (2000X).

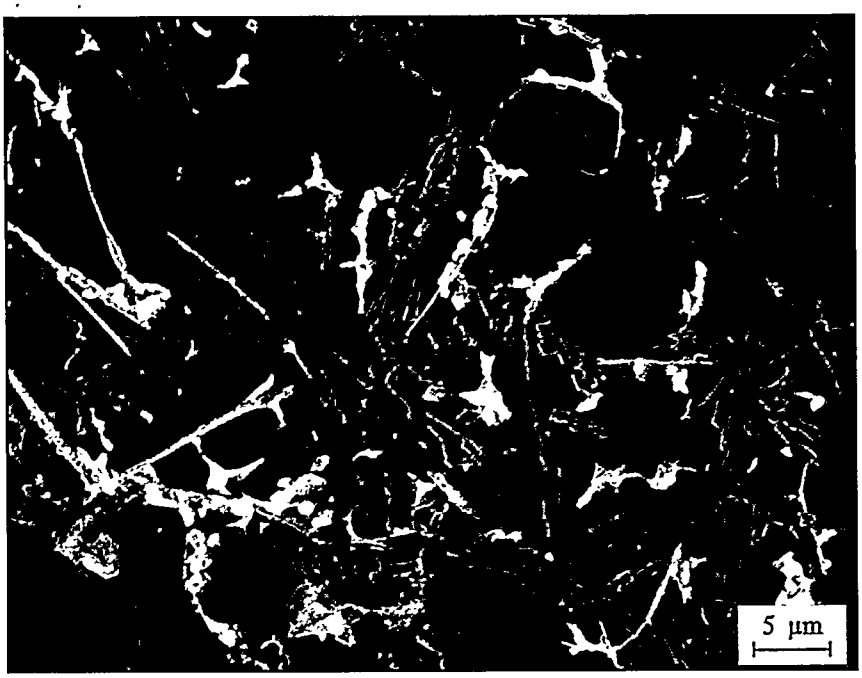

Fig. 3.23.8. SEM micrograph of Alloy 23 in the die cast condition, showing Cu bearing particles (bright phase) *within the Al-Si eutectic (2000X).*

ALLOY 23

Alloy #24	Wt.%	Si	Mg	Fe	Cu	Ni	Cr	Mn	Ti	Zn	Sr	Al
		10.93	0.05	1.02	5.06	0.12	0.06	0.24	0.05	2.20	--	balance

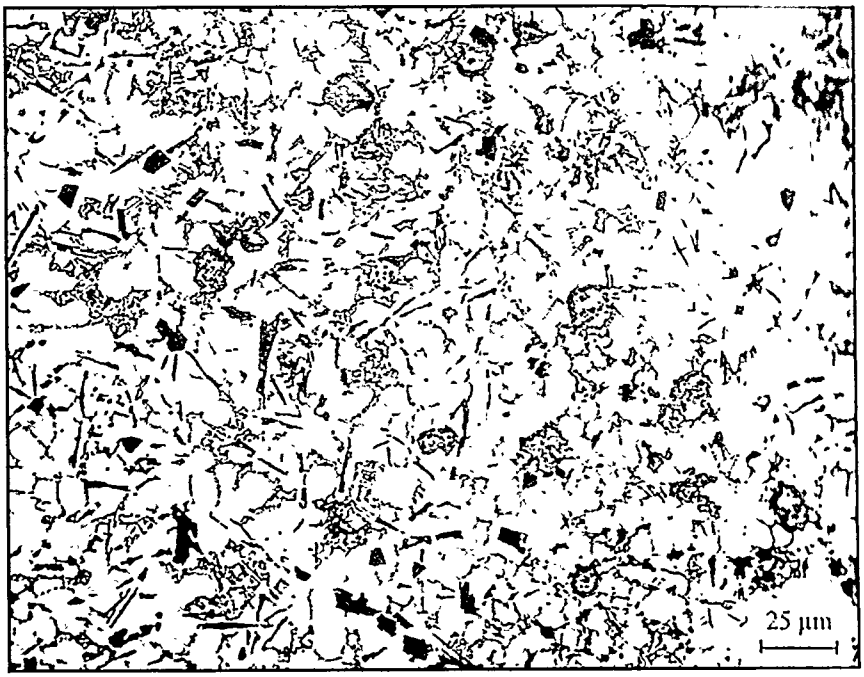

Fig. 3.24.5. Representative optical micrograph of Alloy 24, as die cast condition (400X).

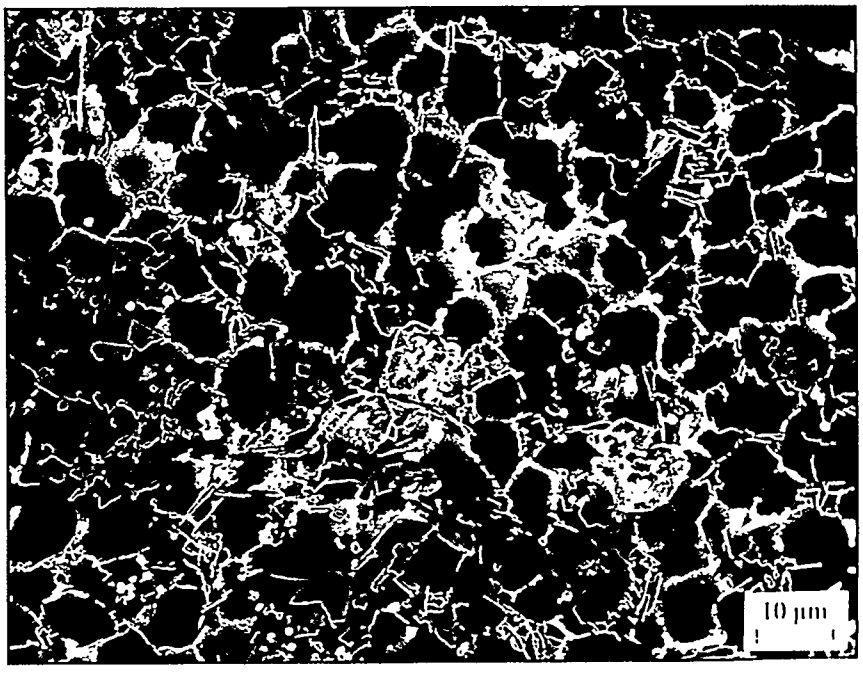

Fig. 3.24.6. Representative SEM micrograph of Alloy 24, as die cast condition (1000X).

Alloy #24	Wt.%	Si	Mg	Fe	Cu	Ni	Cr	Mn	Ti	Zn	Sr	Al
		10.93	0.05	1.02	5.06	0.12	0.06	0.24	0.05	2.20	--	balance

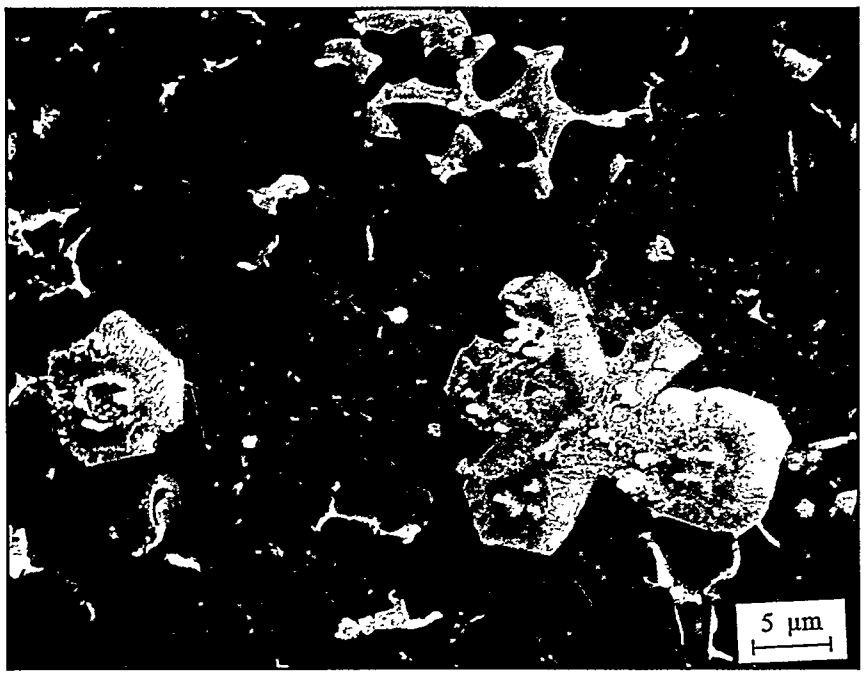

Fig. 3.24.7. SEM micrograph of Alloy 24 in the die cast condition, showing Fe bearing polyhedral crystals and Chinese script, and the Al-Si eutectic structure (2000X).

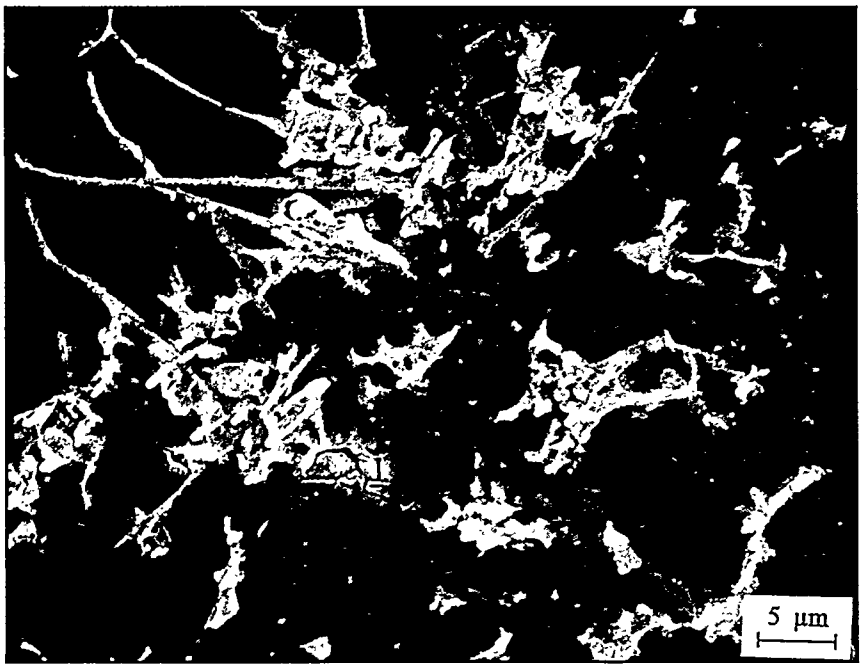

Fig. 3.24.8. SEM micrograph of Alloy 24 in the die cast condition, showing Cu bearing particles (bright phase) *within the Al-Si eutectic and the Fe bearing needles (2000X).*

CHAPTER 4:

ANALYSIS OF ALLOY CHEMISTRY, MICROSTRUCTURE AND PROPERTIES

Analysis of Alloy Chemistry, Microstructure, and Properties

The results given in Chapter 3 are analyzed with respect to the cast microstructure as well as to mechanical and physical properties. In Section 4.1, the focus is on microstructural analysis, whereas in section 4.2 the mechanical and physical properties are reviewed and discussed. Throughout the analysis, an alloy composition designated to optimize a given property is highlighted. Optimizing an alloy for a given set of properties is one of the ultimate goals of metallurgical and materials engineers.

4.1 Microstructure

Typical aluminum die casting alloys are not simple binary alloys but rather they constitute multi-element systems. The principal alloying element in aluminum die casting alloys is silicon; however, iron, copper, magnesium, manganese, titanium, strontium, chromium, nickel, and zinc, which are secondary alloying elements, play a role in influencing the evolution of the microstructure and the phases that form during solidification.

Though 24 alloys are considered in this book, the microstructure analysis presented in this chapter focuses on the first 16 alloys (Alloy1 to Alloy 16). This is because Alloys 1 to 16 represent the alloys where the levels of the primary and the secondary alloying elements were designed at two extremes—a low level, and a high level.

Analysis of the microstructures of these alloys is presented by reviewing (i) differential thermal analysis (DTA) curves, cooling curves, and cooling rates; (ii) phase analysis *via* energy disperssive x-rays (EDX), and (iii) microstructure analysis *via* optical and scanning electron microscopy (SEM).

4.1.1 DTA Curves, Cooling Curves, and Cooling Rate Analysis

By examining the DTA and cooling curves of an alloy, information about its solidification sequence can be obtained. For example, in all the alloys investigated a main peak is observed. This peak corresponds to the Al-Si eutectic reaction. See Fig. 3.1.4 for Alloy 1, Fig. 3.2.4 for Alloy 2, etc...to Fig. 3.2.24 for Alloy 24. The starting temperature for the Al-Si eutectic reaction (the main peak) ranges from 535°C to 562°C.

In Alloys 1 through 8 (alloys that contain silicon in the range 6.79 to 7.15%) a large peak, ahead of the main peak, i.e., to the right of the main peak is observed. This peak occurs at temperatures higher than the eutectic reaction temperature. This relatively large peak signifies the formation of the primary aluminum dendrites. Moreover, it can be seen that in Alloys 1 through 8, the peaks corresponding to the formation of the primary aluminum dendrites occur in the temperature range between 583°C and 597°C. During the interval from the crest of the large peak and the eutectic reaction we observe variations in the shape of the curve. This is due to the formation of Fe bearing phases.

In Alloys 9 through 16 (Figs. 3.9.4 through 3.16.4) a small convex shaped peak, ahead of the main peak, is observed. This convex starts between 563°C and 590°C, and signifies the formation of certain phases such as Fe bearing needles, Chinese script Fe phase, and/or primary silicon particles.

The DTA curves of Alloys 3, 4, 7, 8, 9, 10, 13, and 14 (Figs. 3.3.4, 3.4.4, 3.7.4 to 3.10.4, 3.13.4, and 3.14.4) all show a small distinct peak, subsequent to the Al-Si eutectic reaction between 480°C and 495°C. All of these alloys contain high levels of Cu (4.70% to 5.09%) and contain Cu bearing phases throughout their microstructures. In contrast, Alloys 1, 2, 5, 6, 11, 12, 15, and 16 have lower Cu contents (between 1.13% and 1.29%). Consequently, they have small amounts of the Cu bearing phase, and do not exhibit a distinct peak (to the left of the main peak) indicating formation of only an insignificant amount of the Cu bearing phase—see Figs. 3.1.4, 3.2.4, 3.5.4, 3.6.4, 3.11.4, 3.12.4, 3.15.4, and 3.16.4. Furthermore, we have found that Cr does influence the onset of the formation of the Cu-bearing phase. When the Cr content of the alloy is relatively high, say 0.11% to 0.15% (such as in Alloys 3, 4, 9, and 10) we note that the Cu bearing phase forms between 490°C and 495°C (Figs. 3.3.4, 3.4.4, 3.9.4, and 3.10.4). Whereas when the Cr content of the alloy is low, say 0.01% (such as in Alloys 7, 8, 13, and 14), the Cu bearing phase begins to form at 480°C (Figs. 3.7.4, 3.8.4, 3.13.4, and 3.14.4).

In certain alloys, such as Alloys 3, 4, 5, 6, 11, 13, and 14, one can observe another small peak, or convex, to the left side of the main peak and before the peak due to the copper bearing phase (Figs. 3.3.4, 3.4.4, 3.5.4, 3.6.4, 3.11.4, 3.13.4, and 3.14.4). All these alloys contain a relatively high level of nickel, and their Al-Si eutectic contains small Fe bearing needles with nickel present in this phase. Thus the alloys which contain a relatively high level of nickel (~0.5%) manifest another small peak indicative of the precipitation of the Fe-Ni bearing needles found in the Al-Si eutectic phase.

The cooling curves of the alloys listed in Table 2.5 provide fingerprints of the phase transformation sequences that take place during their solidification, even though the cooling rates in the two sets of investigations differ[1]. In general, for the Al-Si alloys listed in Table 2.5, there exist three distinct regions within the cooling curve that are of interest. As solidification proceeds, the very first fingerprint is that of the first phase(s) that form; namely:

- Primary Al dendrites
  (for hypoeutectic alloys, <12.5%Si)
- Primary silicon particles
  (for hypereutectic alloys, >12.5%Si)
- Fe bearing phases

For example, we see a distinct arrest in the cooling curves of those alloys with a high Si content (~13%) and a high Fe content (1.51% to 1.63%)—Figs. 3.11.3 (Alloy 11), 3.12.3 (Alloy 12), 3.15.3 (Alloy 15), and 3.16.3 (Alloy 16). In contrast, alloys that have a high Si content (~13%) and a low Fe content (0.58% to 0.74%)—Alloys 9, 10, 13, and 14, do not exhibit this distinct arrest, but rather they show a cooling rate change.

The second fingerprint observed is that of the Al-Si eutectic reaction which occurs between 545°C and 575°C. For alloys

containing a low level of Si (Alloys 1 – 8), this range of 545 – 475°C pertains. For alloys containing higher levels of Si (Alloys 9 – 16) the eutectic reaction range is narrower, 560°C – 575°C. A similar trend is observed in the other Alloys—Alloys 17 to 24.

The third fingerprint observed is that due to the precipitation of Cu-bearing phases, though this arrest is not as distinct because of the relatively high cooling used. In general, however, the Cu-bearing phase precipitates between 480°C and 495°C, and as discussed previously, this reaction occurs in the range 480°C – 495°C.

The effect of the cooling rate is significant in the development of the microstructure during solidification in that as the cooling rate increases a corresponding refinement in microstructural indices such as grain size, dendrite arm spacing (DAS), and the size of the second phases that precipitate out is observed. These refinements, in turn, impact, in a beneficial way, the resultant mechanical properties.

The effect of cooling rate on the resultant microstructure can clearly be seen by comparing Figs. 4.1.1 (a) and (b). Fig. 4.1.1. (A) is the structure of Alloy 1 (7.15%Si) cast in a graphite mold and experiencing a cooling rate of about 750°C/min. Fig. 4.1.1. (B) is the structure of the same alloy die cast and experiencing a cooling rate that is over 9000°C/min. The observed microstructure refinement is significant. The microstructures shown in Fig. 4.1.2 are further evidence of the refinement attained by cooling rate; the refinement in the cell spacing, DAS, and the size of the interdendritic phases can be observed by comparing Fig. 4.1.2 (a) and (b). A similar comparison may be made for Alloy 15 (12.78%Si) – Fig. 4.1.3 (a) and (b).

In addition to the overall refinement of the microstructure, as shown in Figs. 4.1.1 through 4.1.3, cooling rate also affects the size of the phases that precipitate, as well as their morphology. Fig. 4.1.4, for example, shows the microstructure of Alloy 14 (12.94%Si) cooled at two different rates; 10°C/min and 750°C/min. In Fig. 4.1.4 (a) we notice primary silicon particles at the surface and we notice that the Fe bearing phase is mainly in the form of Chinese script. In contrast, in Fig. 4.1.4 (b), we notice primary silicon particles and some primary aluminum dendrites. As the cooling rate is further increased, we notice that the primary aluminum dendrites become more distinct (see Fig. 3.14.5) and the primary silicon particles are all across the structure.

Examining the Fe phase that precipitates out prior to the Al-Si eutectic reaction, we note the effect of the cooling rate on the morphology and size of this phase. At low colling rates, the Fe phase in Alloy 4 which contains high Fe, Mn and Cr contents is mostly in the form of needles. As the cooling rate increases, we note thta the needles are replaced with mostly Chinese script and a starlike Fe bearing phase. At even higher cooling, such as in die casting, the Fe phase morphology is polyhedral and starlike. This is evidenced by the microstructures presented in Fig. 4.1.5 (a) cooled at 10°C/min, Fig. 4.1.5 (b) cooled at 750°C/min, and Figs. 3.4.5 to 3.4.7 cooled at over 9000°C/min.

Similarly, a change in the morphology of the Cu-bearing phase as a function of cooling rate has been observed. At relatively low cooling rates, the Cu-phase is in the shape of clusters of lumpy Cu bearing particles that precipitate mostly adjacent to the Fe-bearing needles and within the Al-Si eutectic (see Figs. 4.1.2 for Alloy1, and Fig. 4.1.5 for Alloy 4). Whereas in the die cast samples (cast at a higher cooling rate), the Cu bearing phase forms elongated particles along the interdendritic regions – Fig. 3.4.8 for Alloy 4.

4.1.2 Phase Analysis

Though cooling rate has an appreciable effect on the scale of the structure formed, the morphology of the phases that precipitate out during solidification is predominantly influenced by the chemistry of the alloy.

As discussed in the previous section, the Fe containing second phase has been observed in a variety of different morphologies-needles, Chinese script, star-like, and polyhedral particles. Some examples:

- A very large needle shaped Fe containing phase is observed in Alloys 7 and 11 (Figs. 3.7.7 and 3.11.7);
- A large needle shaped Fe containing phase is observed in Alloy 1 and 13 (Figs. 3.1.7 and 3.13.7);
- A small needle shaped Fe containing phase is observed in Alloys 8 and 12 (Figs. 3.6.7 and 3.12.7);
- Well-developed Chinese script is observed in Alloys 2 and 8 (Figs. 3.2.7 and 3.8.7);
- Disintegrated Chinese script is observed in Alloy 16 (Fig. 3.16.7);
- A starlike Fe-containing phase is observed in Alloy 6 (Fig. 3.6.7);
- A large polyhedral Fe-containing phase (~10 mm in size) is observed in Alloy 10 (Fig. 3.10.7);
- A small polyhedral Fe containing phase (~1 mm in size is observed in Alloys 5 and 9 (Figs. 3.5.7 and 3.9.7).

In each case, EDX spectra analysis reveals the chemical composition of the phase. EDX spectra for the phases described above are given in Figs. 4.1.6 through 4.1.13. The reason for the formation of small needles as opposed to large needles is due to the presence of Ni and Cu. Nickel and Copper favor the formation of small needles (compare Figs. 4.1.6 and 4.1.7). The Chinese script phase contains Mn and Cu (see Fig. 4.1.8) and the star-like phase contains Cr in addition to Mn and Cu. Generally speaking, when the Cr content of the alloy is low and the Mn content is high, the Fe-bearing polyhedral particles are relatively large. On the other hand, when the Cr content of the alloy is high and the Mn content is low, the Fe-bearing polyhedral particles are small. Thus the level of Mn and Cr in the alloy significantly influences the resultant microstructure. From the above analysis, it can be concluded that increasing the sludge factor favors the formation of polyhedral and Chinese script phases over the needle shaped phase. The formation of the Chinese script phase is favored when Mn is present without Cr. With increasing Cr content, the polyhedral phase is favored.

Fig. 4.1.1 (a) Graphite mold casting (cooling rate: ~ 750°C/min).

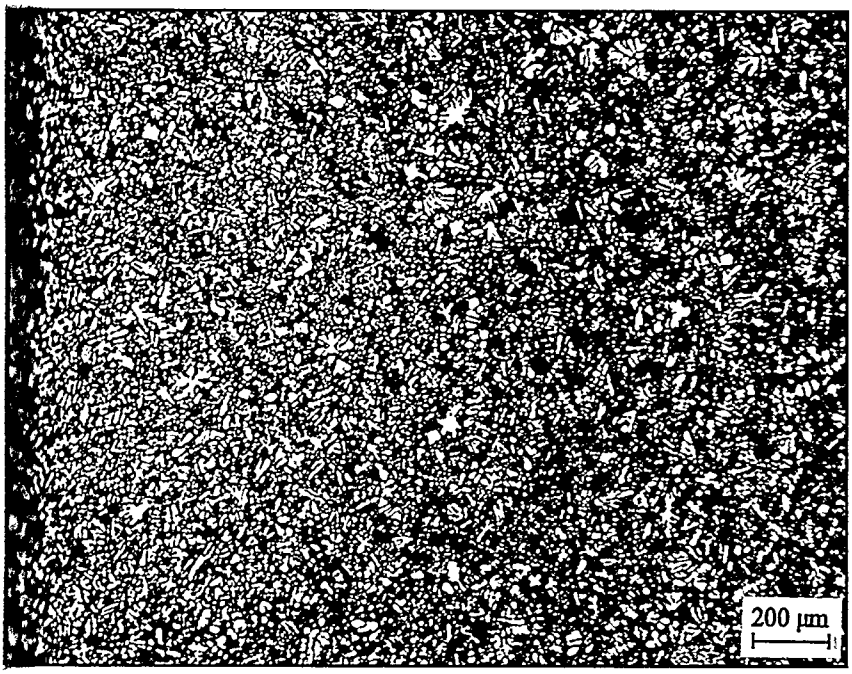

Fig. 4.1.1 (b). Die casting (cooling rate: >9000°C/min). Both photograhs show the grain structure of Alloy 1 (7.15%Si, 0.03%Mg, 0.68%Fe, 1.24%Cu, 0.01%Ni, 0.01%Cr, 0.01%Mn, 0.01%Ti, 0.44%Zn and 0.00%Sr).

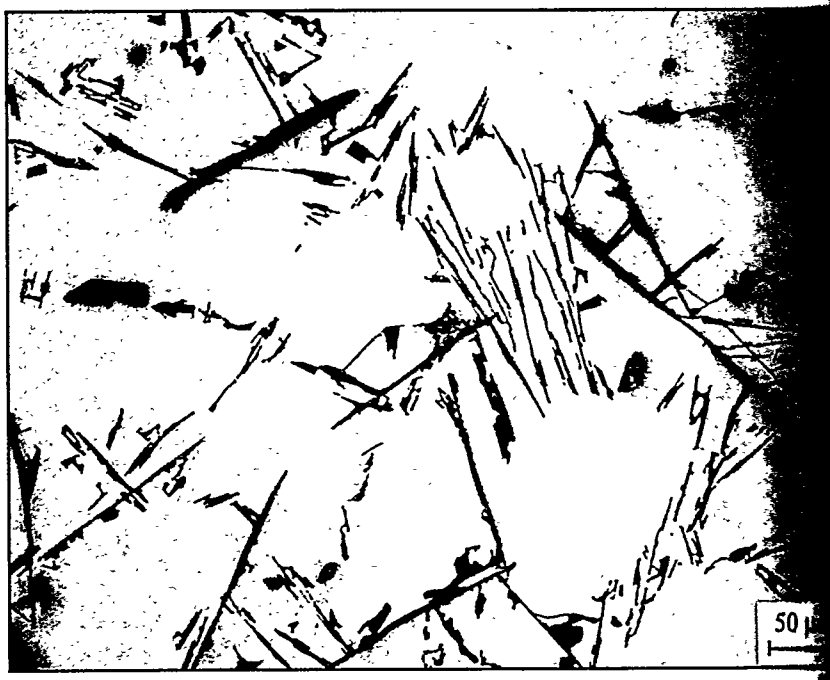

1.2 (a) Cooled at 10°C/min (DTA sample).

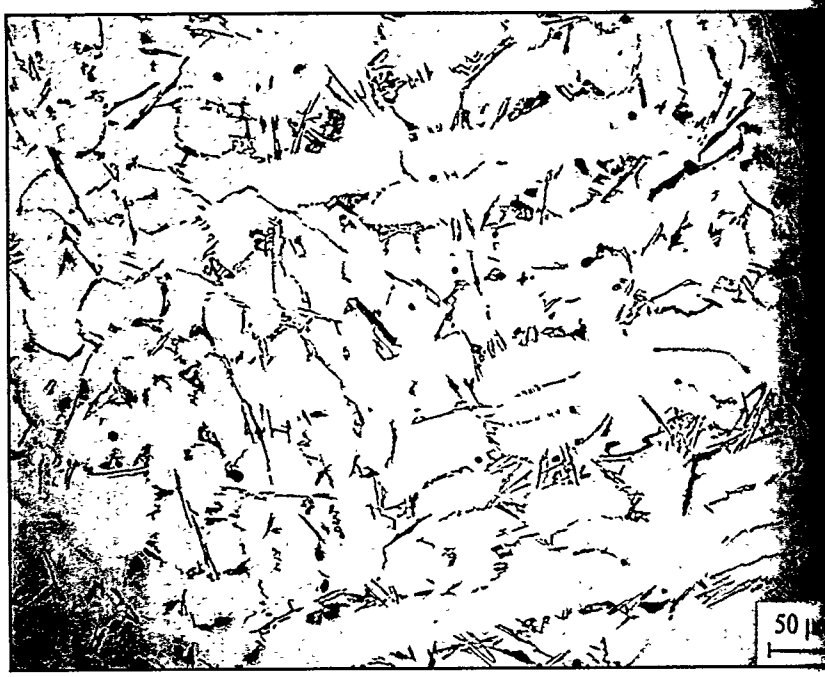

Fig. 4.1.2 (b) Graphite mold casting (cooling rate: ~750°C/min). The above photographs are microstructures of Alloy 1 (7.15%Si, %Mg, 0.68%Fe, 1.24%Cu, 0.01%Ni, 0.01%Cr, 0.01%Mn, %Ti, 0.44%Zn and 0.00%Sr) solidified at different cooling rates.

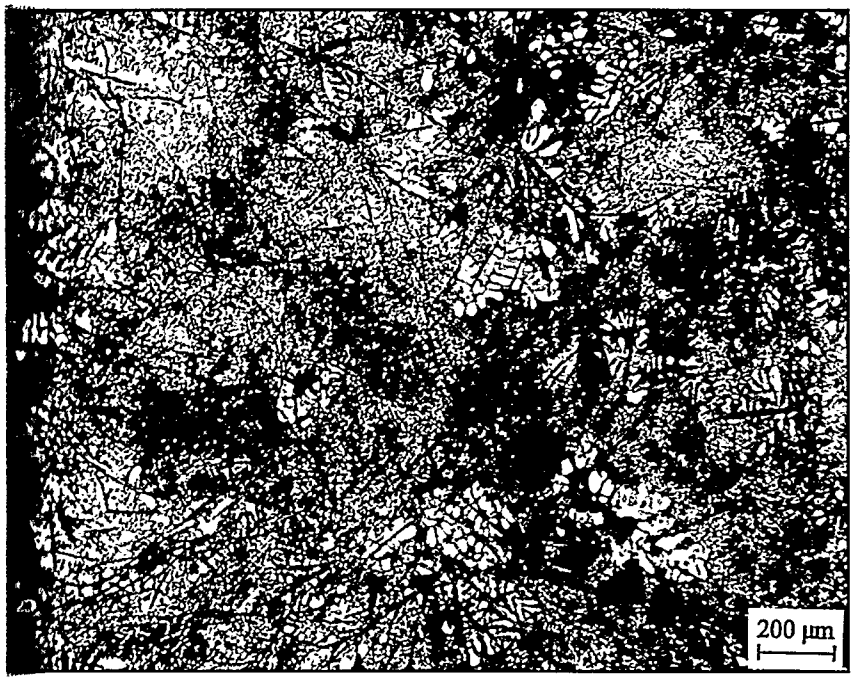

Fig. 4.1.3 (a) Graphite mold casting (cooling rate: ~750°C/min).

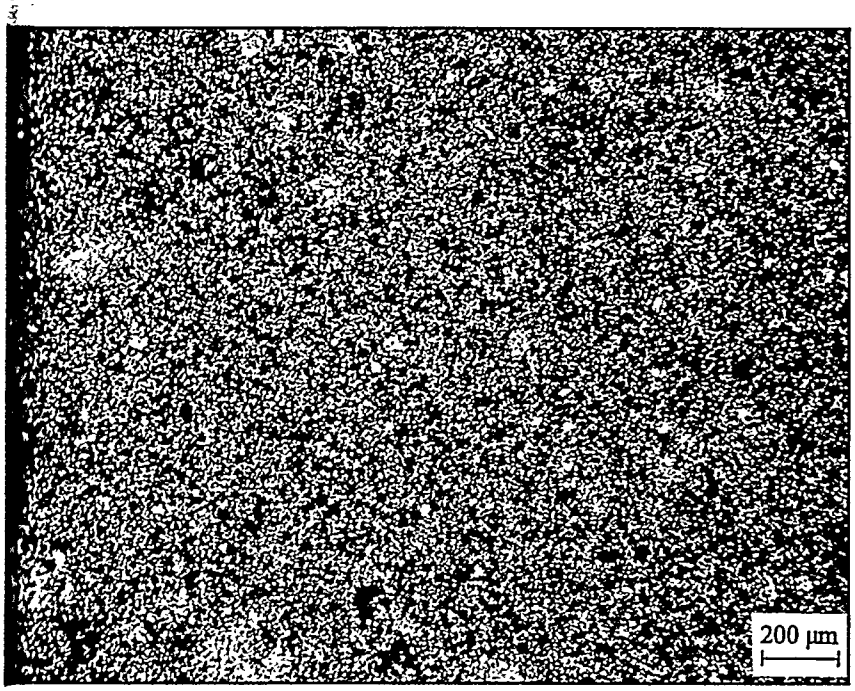

Fig. 4.1.3 (b). Die casting (cooling rate: >9000°C/min). The above micrographs show the grain structure of Alloy 15 (12.78%Si, 0.47%Mg, 1.51%Fe, 1.27%Cu, 0.06%Ni, 0.14%Cr, 0.01%Mn, 0.18%Ti, 2.94%Zn, and 0.00%Sr).

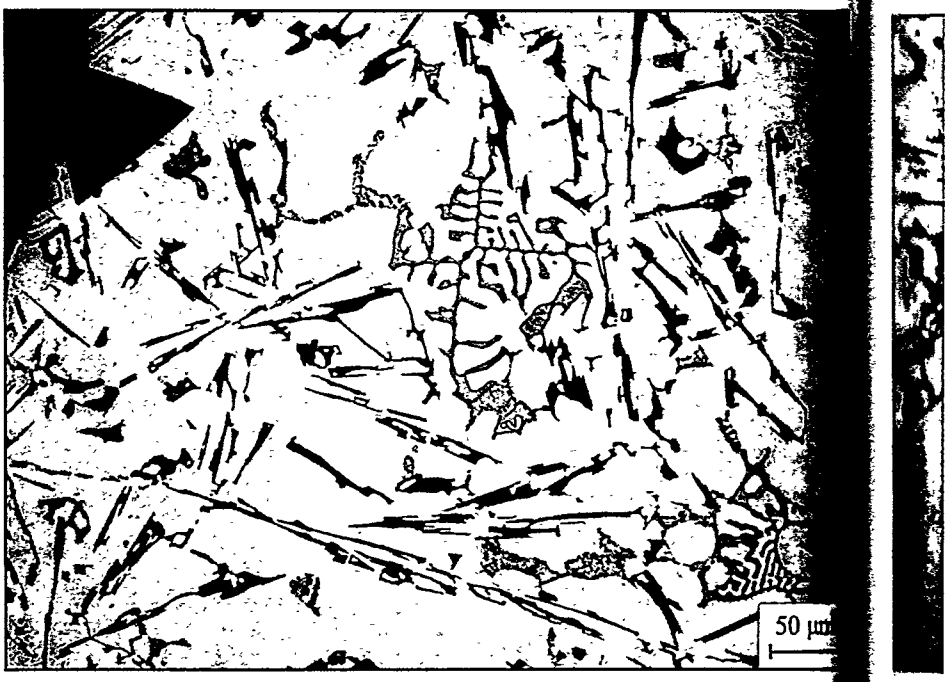

4.1.4 (a) Cooled at 10°C/min (DTA sample).

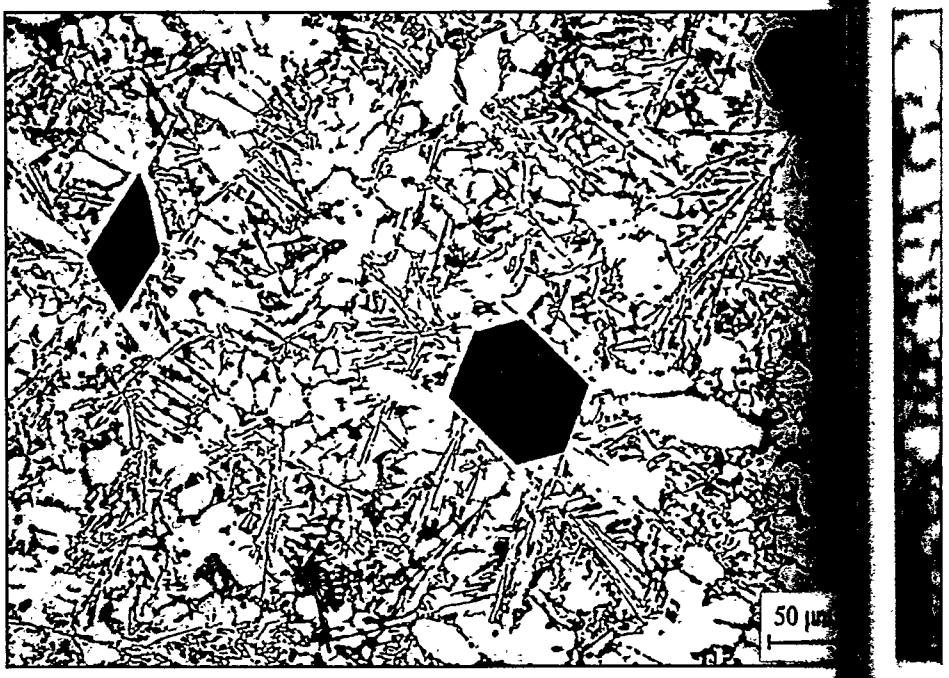

Fig. 4.1.4 (b) Graphite mold casting (cooling rate: ~750°C/min). The microstrucutres shown are of Alloy 14 (12.94%Si, 0.48%Mg, 0.%Fe, 4.77%Cu, 0.50%Ni, 0.01%Cr, 0.57%Mn, 0.01%Ti, 0.55%Zn and 0.00%Sr) solidified at different cooling rates.

Fig. 4.1.5. (a) Cooled at 10°C/min (DTA sample).

Fig. 4.1.5 (b) Graphite mold casting (cooling rate: ~750°C/min). Shown are the microstructures of Alloy 4 (6.94%Si, 0.04%Mg, 1.48%Fe, 4.74%Cu, 0.47Ni, 0.15%Cr, 0.45%Mn, 0.16%Ti, 2.69%Zn and 0.00%Sr) solidified at different cooling rates.

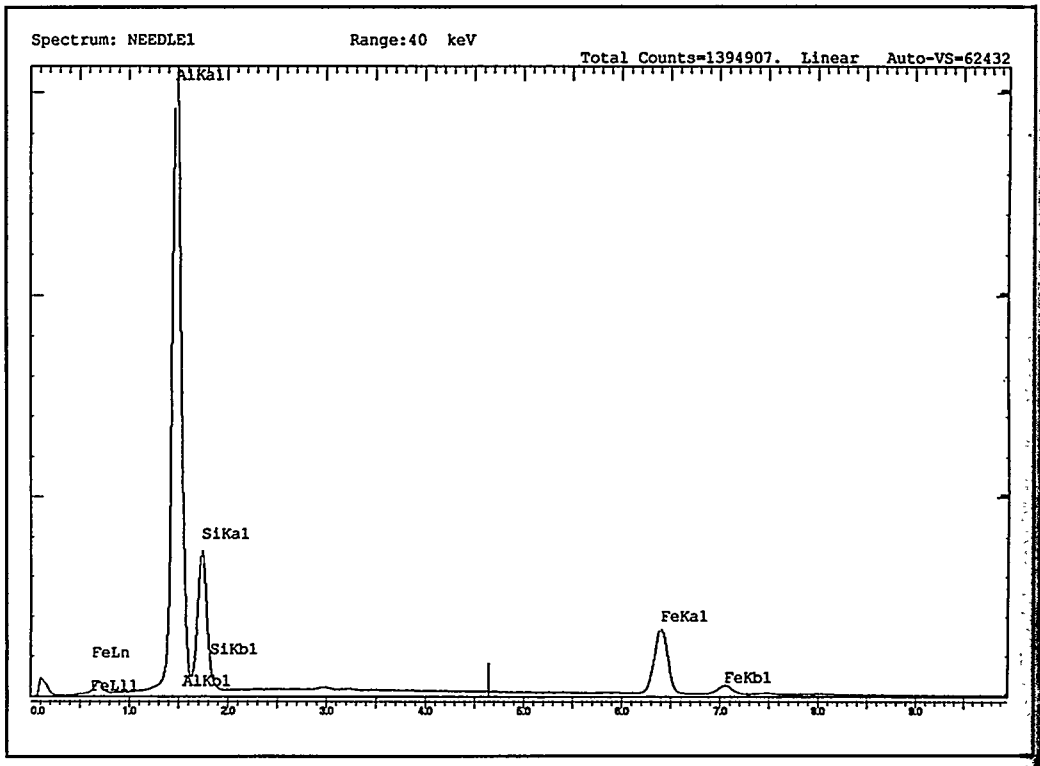

I.1.6. EDX spectrum of large Fe bearing needle in Alloy 11 (12.86%Si, 0.04%Mg, 1.59%Fe, 1.21%Cu, 0.45%Ni, 0.01%Cr, 0.01%Mn, 0.18%Ti, 0.49%Zn, and 0.00%Sr).

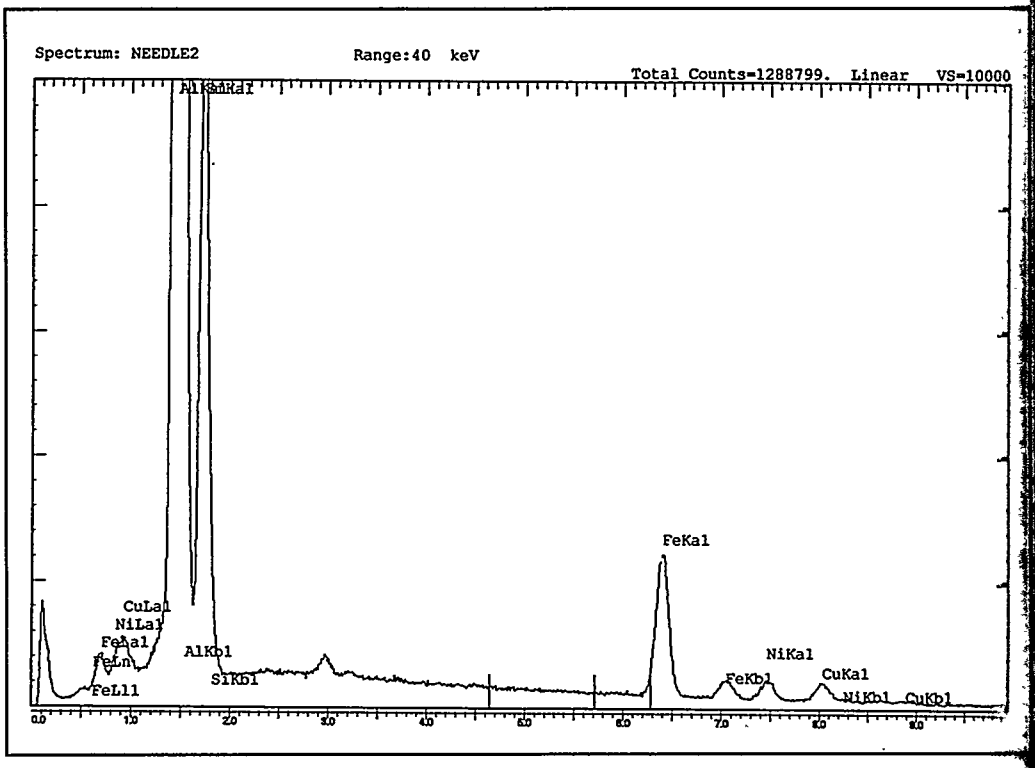

Fig. 4.1.7. EDX spectrum of small Fe bearing needle in Alloy 11 (12.86%Si, 0.04%Mg, 1.59%Fe, 1.21%Cu, 0.45%Ni, 0.01%Cr, 0.01%Mn, 0.18%Ti 0.49%Zn and 0.00%Sr).

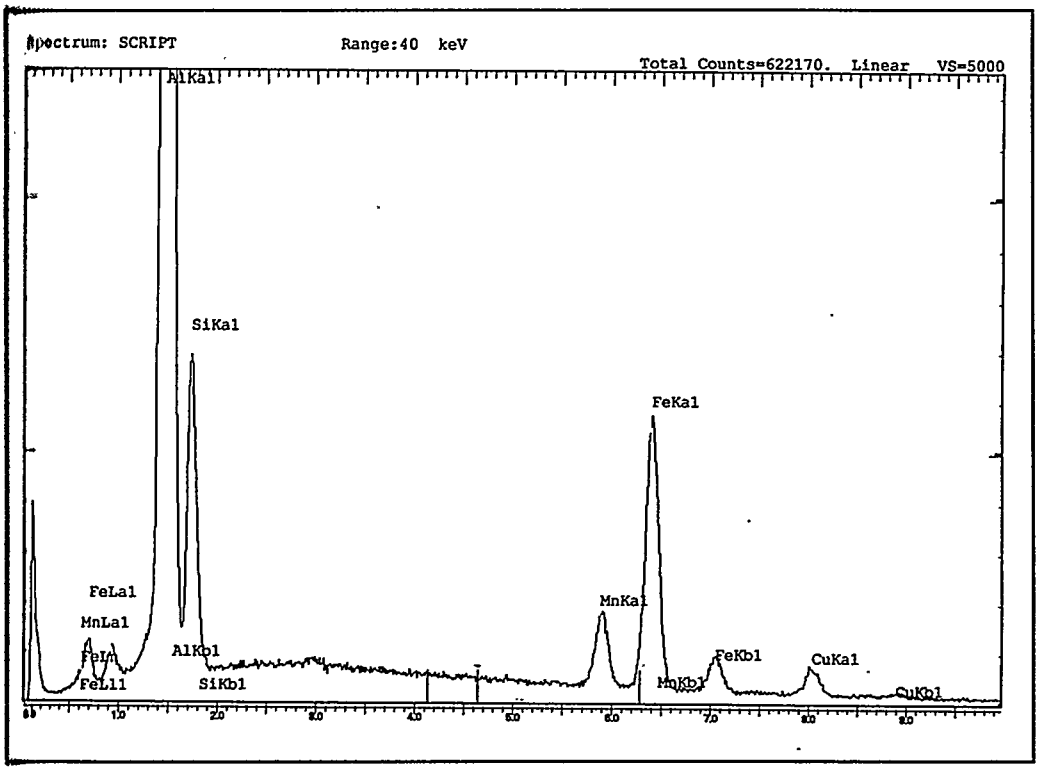

Fig. 4.1.8. EDX spectrum of Fe-bearing Chinese script in Alloy 8 (6.79%Si, 0.46%Mg, 1.49%Fe, 4.77%Cu, 0.01%Cr, 0.45%Mn, 0.20%Ti, 0.42%Zn and 0.00%Sr).

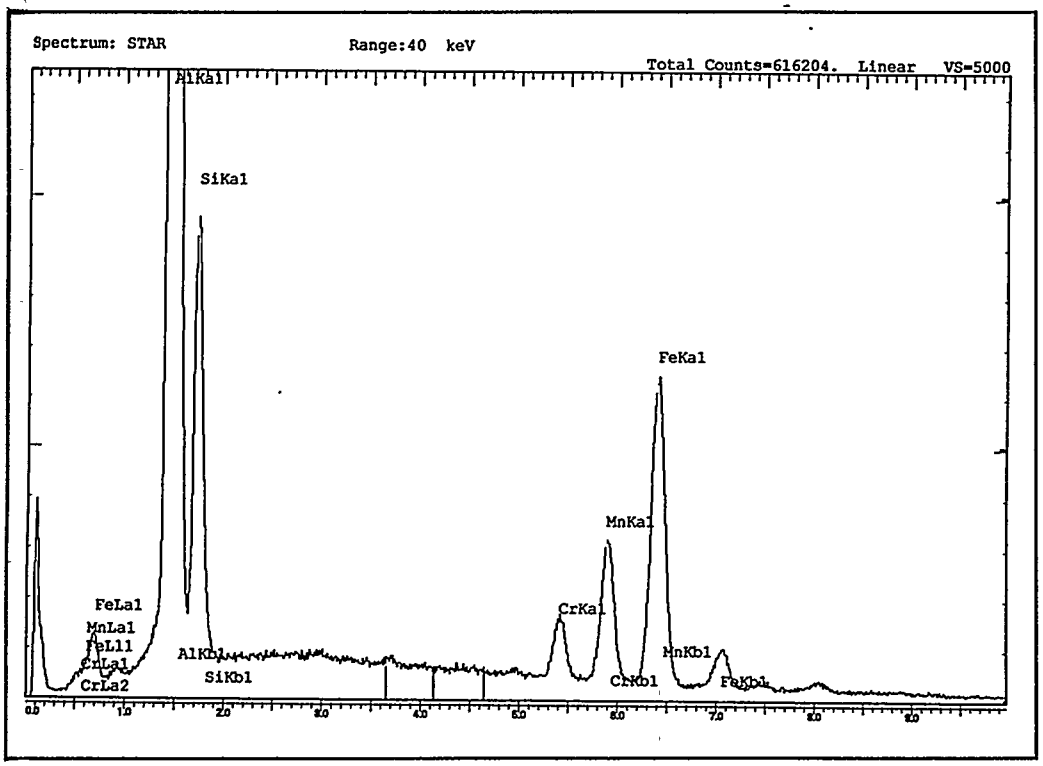

Fig. 4.1.9. EDX spectrun of Fe-bearing starlike particle in Alloy 6 (6.98%Si, 0.44%Mg, 0.57%Fe, 1.13%Cu, 0.48%Ni, 0.13%Cr, 0.45%Mn, 0.18%Ti, 0.38%Zn and 0.002%Sr).

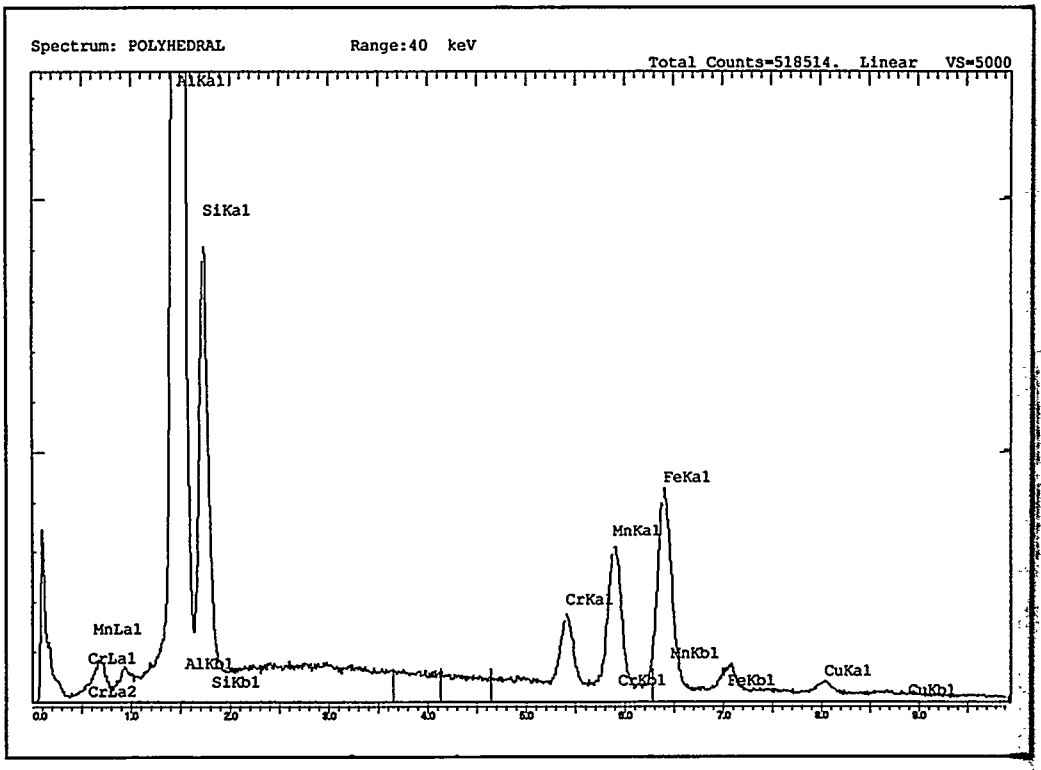

Fig. 4.1.10. EDX spectrum of Fe-bearing large polyhedral particle in Alloy 10 (12.69%Si, 0.03%Mg, 0.73%Fe, 5.09%Cu, 0.07%Ni, 0.11%Cr, 0.37%Mn, 0.01%Ti, 2.73%Zn and 0.00%Sr).

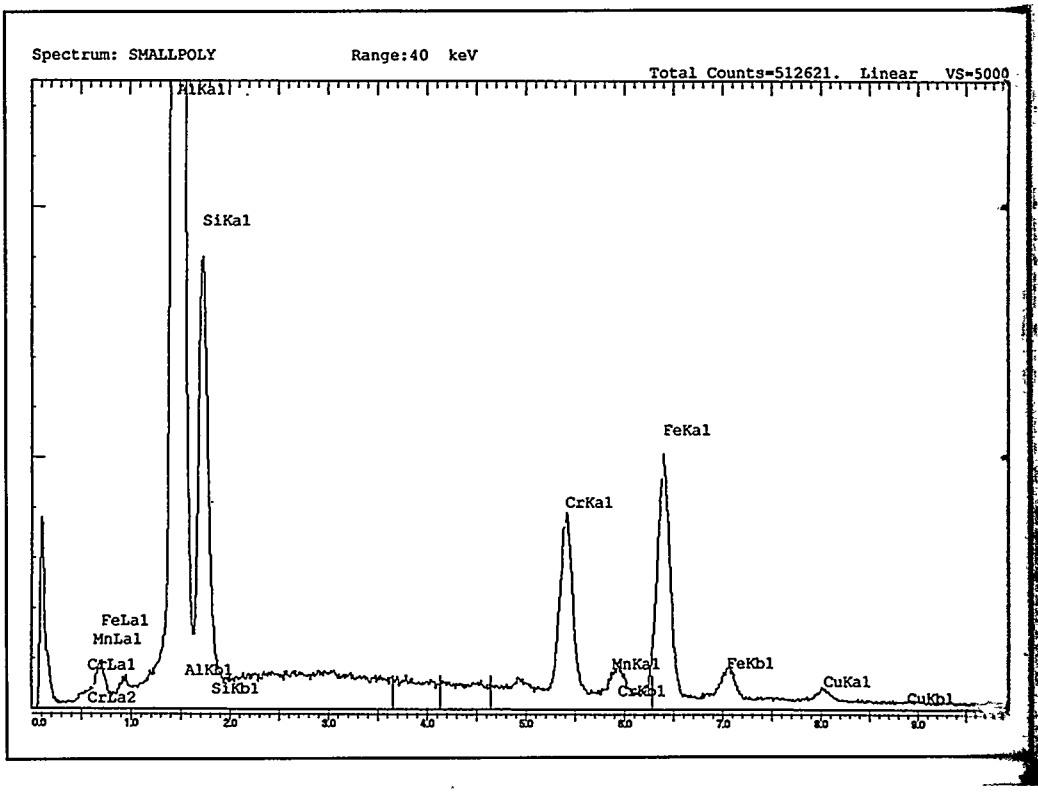

Fig. 4.1.11. EDX spectrum of Fe-bearing small polyhedral particle in Alloy 9 (12.71%Si, 0.05%Mg, 0.63%Fe, 4.96%Cu, 0.06%Ni, 0.14%Cr, 0.01%Mn, 0.20%Ti, 0.50%Zn and 0.017%Sr).

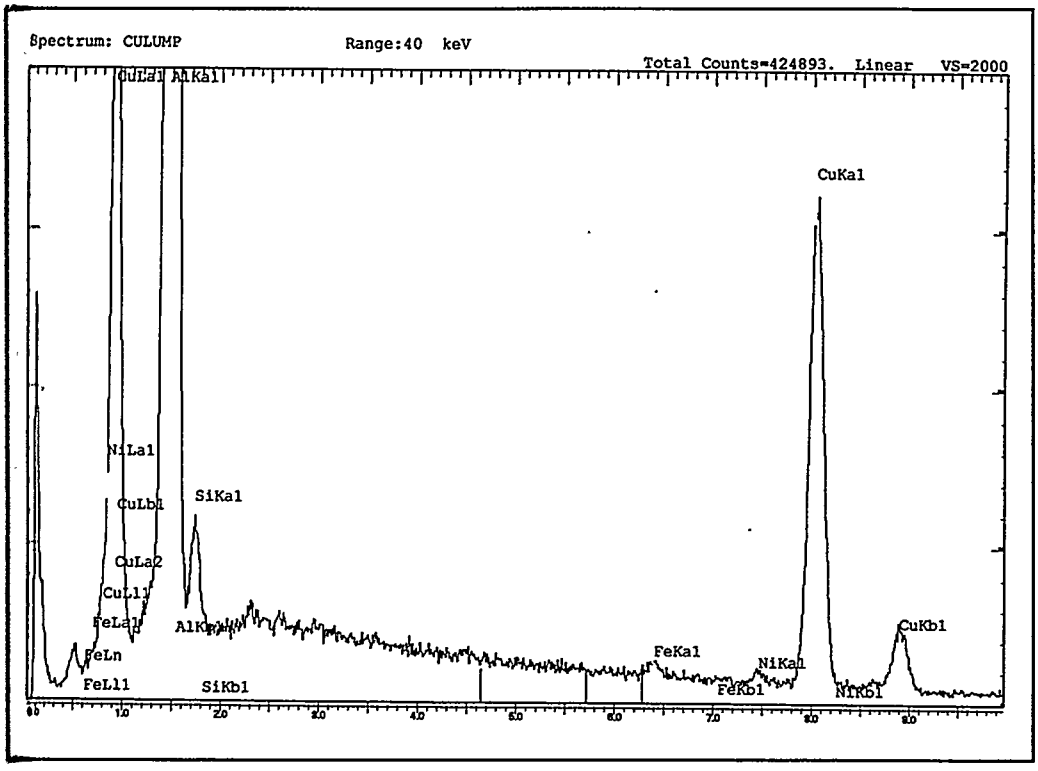

Fig. 4.1.12. EDX spectrum of Cu-bearing lumpy particle in Alloy 9 (12.71%Si, 0.05%Mg, 0.63%Fe, 4.96%Cu, 0.06%Ni, 0.14%Cr, 0.01%Mn, 0.20%Ti, 0.50%Zn and 0.017%Sr).

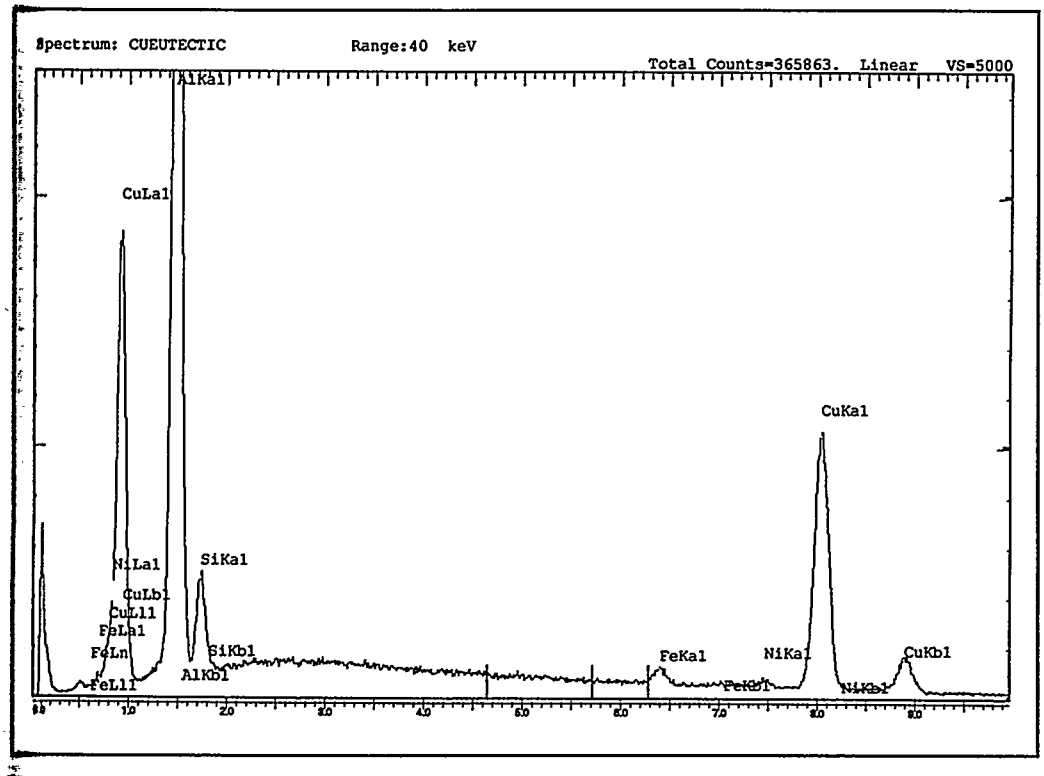

Fig. 4.1.13. EDX spectrum of Cu-bearing net-shape eutectic phase in Alloy 9 (12.71%Si, 0.05%Mg, 0.63%Fe, 4.96%Cu, 0.06%Ni, 0.14%Cr, 0.01%Mn, 0.20%Ti, 0.50%Zn and 0.017%Sr).

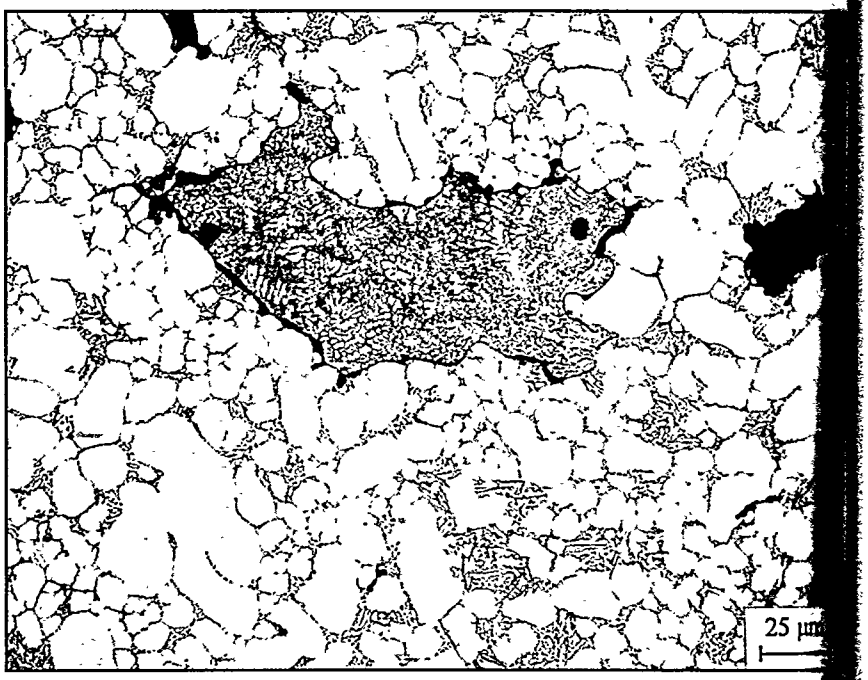

Fig. 4.1.14 (a). In Alloy 1 (7.15%Si, 0.03%Mg, 0.68%Fe, 1.24%Cu, %Ni, 0.01%Cr, 0.01%Mn, 0.01%Ti, 0.44%Zn and 0.00%Sr).

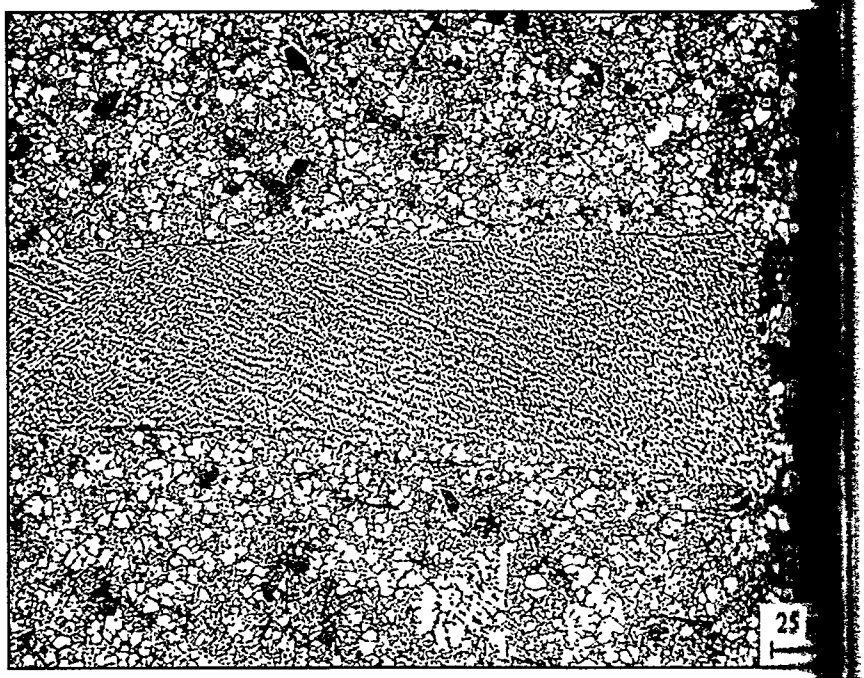

Fig. 4.1.14 (b). In Alloy 12 (12.95%Si, 0.05%Mg, 1.55%Fe, 1.29%Cu, %Ni, 0.01%Cr, 0.43%Mn, 0.01%Ti, 2.91%Zn and 0.23%Sr). The . ostructure photographs show abnormal structure in die cast tensile bars of Alloys 1 and 12.

Though both Mn and Cr play an important role in the resultant morphology of the Fe bearing phase, it should be noted that the critical element which has a predominant effect on the morphology of the Fe phase is iron. The iron content of the alloy establishes the total volume of the Fe bearing phase that will precipitate out. The presence and distribution of the different morphologies depend on the amount of Fe, Ni and Cr present in the alloy, and their ratio to one another. For illustration purposes, consider two alloys: a low Fe alloy and a high Fe alloy. At the low Fe content (~0.7%), and with Mn and Cr present, the Fe bearing phase will precipitate out as Chinese script, star-like particles, or as polyhedral particles; however, no needle shaped Fe phase will form. As to which morphology – polyhedral or Chinese script will form? That depends on the levels of Mn and Cr in the alloy. In contrast, at the high Fe content (~1.6%), the needle shaped Fe phase will always form. However, at these high levels of Fe, as the Mn and Cr contents of the alloy are increased, Chinese script, star-like particles, and polyhedral particles will form together with the needle shaped Fe phase.

4.1.3 Microstructure Characteristics

The question: *Is there a need to grain refine die casting alloys* has often been posed. It is quite clear from the microstructural analysis of this exhaustive study, that die casting, because of its inherent fast solidification rate, results in a structure that is very fine without the addition of grain refiners – see for example, Fig. 4.1.1 for Alloy 1. However, it is also clear that adding Ti as a grain refiner further refines the microstructure – see for example the additional refinement obtained in Alloy 15 versus Alloy 1 by comparing the microstructures shown in Fig. 4.1.3 (for Alloy 15) with those of Fig. 4.1.1 (for Alloy 1). Thus, to optimize refinement, and to obtain optimum strength, grain refinement of die casting alloys is recommended. The reduction in grain size will increase the strength of the alloy as described by the Hall-Petch equation:

$$s = s_o + kd^{-1/2}$$

where s is the alloy's ultimate tensile strength; s is the reference strength for a single crystal, d is the grain size, and k is a material constant.

In a similar fashion, strontium additions further refine the eutectic silicon despite the fact that the die cast eutectic structure is quite fine to start with because of the high cooling rate of the process. This is seen by comparing the microstructure of Alloy 1, which does not contain strontium (Fig. 3.1.6), to that of Alloy 2, which contains 0.018% strontium (Fig. 3.2.6). As expected, strontium does not have a significant effect on the eutectic structure of alloys that contain a high level of silicon (higher than 12.5%).

Porosity is typically present in die cast components and the pores are mostly found at the center of cross sections. Generally speaking, more pores are found in alloys with lower silicon content (Alloys 1 to 8) than in alloys with higher silicon content (Alloys 9 to 16). The alloys near the eutectic composition – the higher silicon content alloys— have a narrow freezing range (relative to the low silicon containing alloys) which explains the difference in porosity levels.

Abnormal microstructural features are often encountered within die cast components. These are typically particles that solidified at the surfaces of the shot sleeve, or at the gates, and are brought into the die-casting by the pressurized melt flow. These particles do not re-melt and may form "islands" that are well embedded in the matrix, or islands that are separated from the matrix – see Figs. 4.1.14 (a) and (b) showing these abnormal features in Alloys 1 and 12, respectively. Abnormal microstructures are a concern in that they detract from the mechanical properties of the cast part.

---

[1] *The DTA measurements were carried out at a cooling rate of 10°C/min whereas the cooling curve had a range of 600-900°C/min.*

Effect of Alloy Chemistry on Properties

4.2.1 Statistical Data Analysis

The Taguchi method of design of experiments replaces a full factorial experiment with a leaner, less expensive and faster to perform partial factorial experiment. Since this partial experiment is only a sample of the full experiment, the analysis of the partial experiments must include an analysis of the confidence that can be placed in the results. Analysis of Variance (ANOVA) is a standard statistical technique that is routinely used to provide a measure of confidence. ANOVA does not directly analyze the data, but rather determines the variability (variance) of the data. Confidence is then determined from the variance. ANOVA can also be used to establish the relative significance of the individual factors, i.e. the relative contribution of the elements and element interactions to the property being measured. Moreover, ANOVA can be used to predict an optimum condition and project the result at the optimum condition, i.e., predict an optimum alloy composition, and project the magnitude of the property at the optimum alloy composition. Instead of a detailed presentation of the procedure for performing ANOVA, the reader is referred to many texts that are available on the subject [1, 2, and 3].

ANOVA is performed on the mechanical and physical property data for the sixteen alloys listed in Table 2.5. The aim of the analysis is:

- To establish confidence levels in the data;
- To determine the percent contribution by each of the elements and element interaction that are listed in Table 2.2 towards the variation in each of the properties;
- To predict an optimum alloy composition for each property; and,
- To project the magnitude of each of the properties at the optimum alloy composition.

Stepwise multiple regression analysis is also performed on the mechanical and physical property data for the sixteen alloys listed in Table 2.5 with the aim of developing empirical equations that relate alloy chemistry to mechanical and physical properties. Results of the analysis of variance and the multiple regression analysis are presented in this chapter.

4.2.2 Effect of Alloy Chemistry on Room Temperature Tensile Properties

Tables 4.2.1 and 4.2.2 present the average tensile properties for the twenty-four alloys presented in Tables 2.5 and 2.6, respectively. For ease of visualization, the same information is presented in chart form in Figs. 4.2.1 to 4.2.8. Tables 4.2.1 and 4.2.2 also show the standard deviation and the coefficient of variance for each of the measured properties.

Table 4.2.1. Summary of average room temperature tensile properties for Alloys 1 to 16.

Alloy No.	Tensile Strength			Yield Strength			Elongation			Modulus of Elasticity		
	Average (ksi)	St. dev.* (ksi)	CV** (%)	Average (ksi)	St. dev. (ksi)	CV (%)	Average (%)	St. dev. (%)	CV (%)	Average (ksi)	St. dev. (ksi)	CV (%)
1	39.6	0.9	2.3	16.6	0.4	2.4	5.85	0.97	16.6	10,536	1,024	9.7
2	42.4	0.8	1.9	20.0	0.4	2.0	7.43	1.18	15.9	10,915	753	6.9
3	45.4	1.0	2.2	24.8	0.3	1.2	2.08	0.23	11.1	11,262	753	6.7
4	47.0	0.9	1.9	25.5	0.4	1.6	2.81	0.29	10.3	11,079	746	6.7
5	44.4	0.7	1.6	24.9	0.3	1.2	3.76	0.52	13.8	10,671	427	4.0
6	46.2	1.5	3.2	24.9	0.5	2.0	3.78	0.75	19.8	11,008	748	6.8
7	49.1	0.6	1.2	32.2	0.6	1.9	1.42	0.08	5.6	11,435	687	6.0
8	48.9	0.9	1.8	30.0	0.3	1.0	1.93	0.19	9.8	11,111	385	3.5
9	46.8	1.8	3.8	27.5	0.4	1.5	1.69	0.29	17.2	11,583	685	5.9
10	44.3	2.4	5.4	28.2	0.4	1.4	1.40	0.37	26.4	11,420	539	4.7
11	35.1	2.0	5.7	23.8	0.5	2.1	0.75	0.13	17.3	11,621	595	5.1
12	40.4	2.2	5.4	23.3	0.4	1.7	1.42	0.32	22.5	11,418	826	7.2
13	47.2	1.6	3.4	31.0	0.5	1.6	1.39	0.24	17.3	11,552	391	3.4
14	41.9	4.0	9.5	32.9	0.7	2.1	0.67	0.32	47.8	11,644	389	3.3
15	42.6	2.1	4.9	29.2	0.4	1.4	0.97	0.17	17.5	11,639	562	4.8
16	43.0	2.5	5.8	26.9	0.4	1.5	1.41	0.39	27.7	11,620	700	6.0

*St. dev. - Standard deviation **CV - Coefficient of Variation (= St. dev./Mean 100%)

Table 4.2.2. Summary of average room temperature tensile properties for alloys 17 to 24.

Alloy No.	Tensile Strength			Yield Strength			Elongation			Modulus of Elasticity		
	Average (ksi)	St. dev.* (ksi)	CV** (%)	Average (ksi)	St. dev. (ksi)	CV (%)	Average (%)	St. dev. (%)	CV (%)	Average (ksi)	St. dev. (ksi)	CV (%)
17	45.0	0.7	1.6	19.6	0.3	1.5	5.34	0.59	11.0	10,913	678	6.2
18	46.2	0.8	1.7	21.8	0.7	3.2	3.68	0.49	13.3	10,918	804	7.4
19	45.4	1.6	3.5	20.3	0.3	1.5	4.62	1.00	21.6	11,032	771	7.0
20	45.4	2.6	5.7	25.1	0.2	0.8	1.93	0.44	22.8	11,317	356	3.1
21	44.0	4.6	10.5	21.8	0.7	3.2	2.73	0.73	26.7	10,958	683	6.2
22	45.6	3.2	7.0	24.5	0.4	1.6	2.30	0.74	32.2	10,917	624	5.7
23	41.3	3.0	7.3	22.1	0.5	2.3	1.79	0.51	28.5	11,193	481	4.3
24	45.0	2.1	4.7	26.6	0.4	1.5	1.51	0.31	20.5	11,656	728	6.2

***St. dev. - Standard deviation** ****CV - Coefficient of Variation (= St. dev./Mean 100%)**

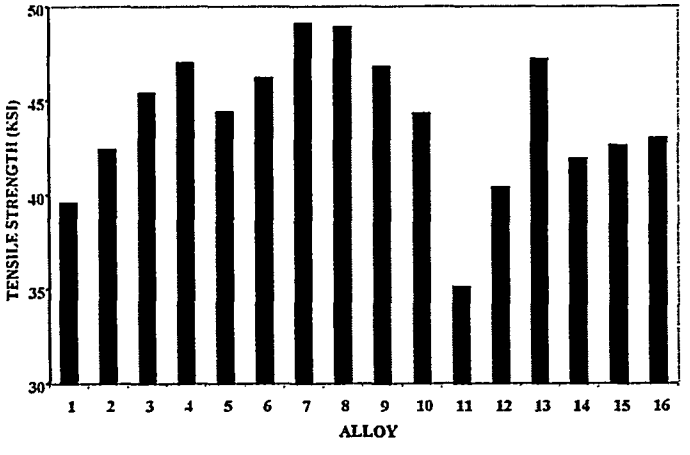

Fig. 4.2.1. Room temperature tensile strengths of Alloys 1 to 16.

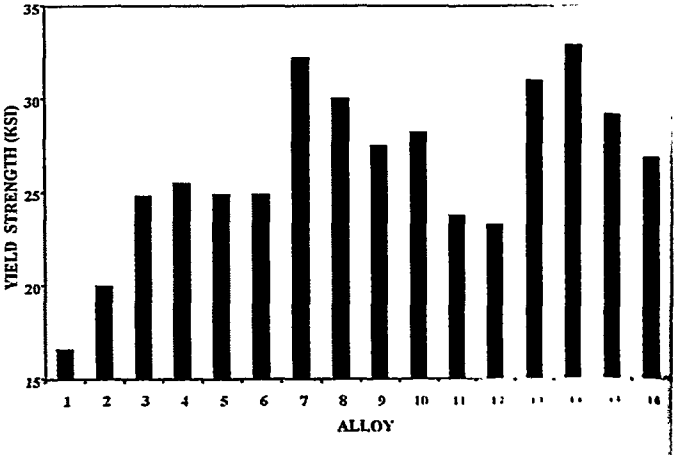

Fig. 4.2.2. Room temperature yield strengths of Alloys

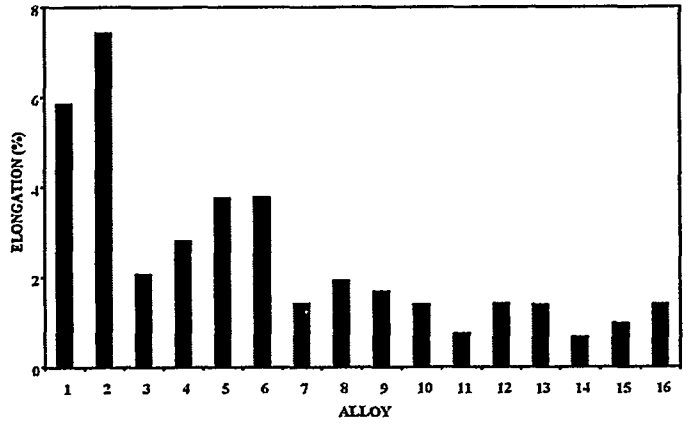

Fig. 4.2.3. Room temperature elongation of Alloys 1 to 16.

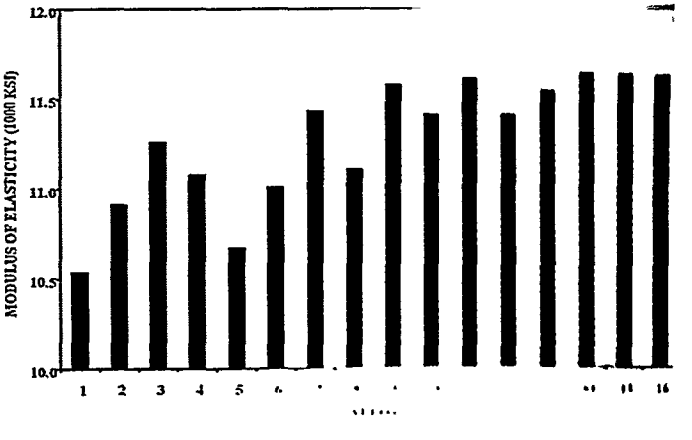

Fig. 4.2.4. Room temperature modulus of

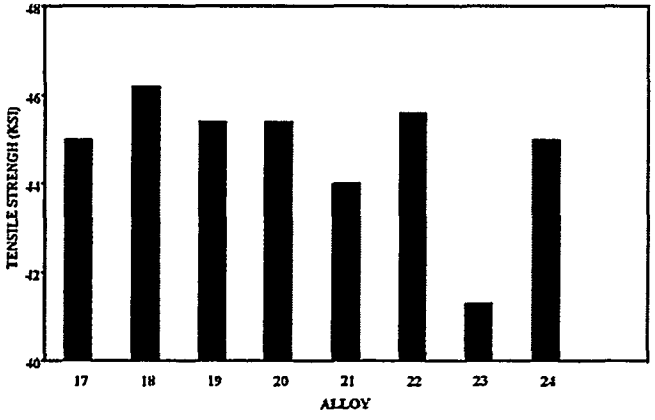

Fig. 4.2.5. Room temperature tensile strengths of Alloys 17 to 24.

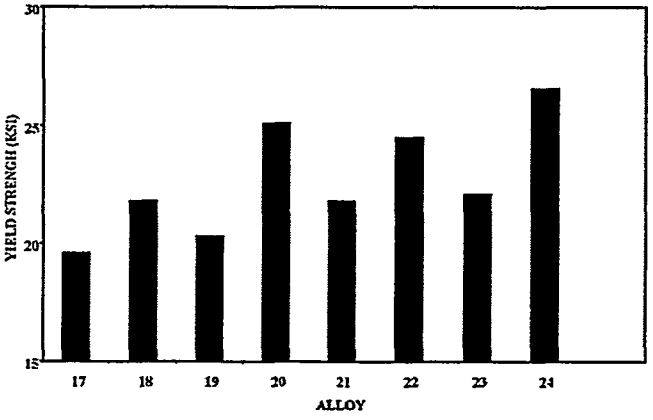

Fig. 4.2.6. Room temperature yield strengths of Alloys 17 to 24.

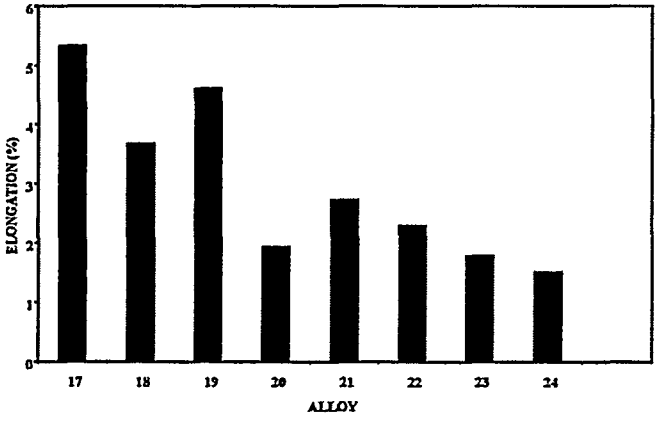

Fig. 4.2.7. Room temperature elongation of Alloys 17 to 24.

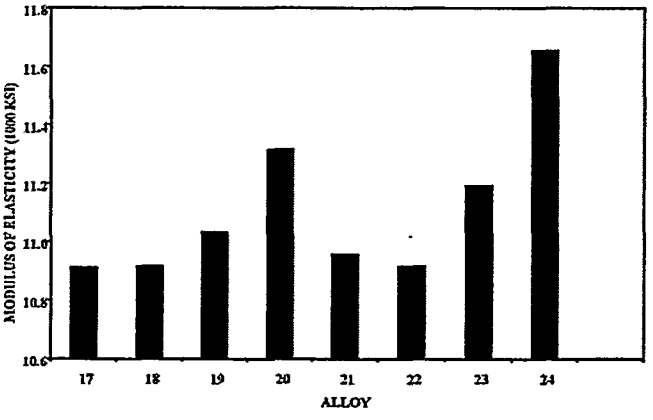

Fig. 4.2.8. Room temperature modulus of elasticity of Alloys 17 to 24.

Tensile Strength

Results of the pooled analysis of variance for tensile strength of the alloys in Table 2.5 are shown in Table 4.2.3. The procedure for performing pooled ANOVA is detailed elsewhere [3]. The Percent Contribution (P) in Table 4.2.3 is an indication of the relative power of an element, or an interaction, to affect variation in tensile strength. Table 4.2.3 indicates that, at the levels studied, the element that affects the variation in tensile strength most significantly is Cu. Its relative contribution to variation in tensile strength is about 33%. Mg and Si also have significant effects. At higher levels, Cu and Mg tend to increase the tensile strength; on the other hand, Si tends to decrease the tensile strength[1]. Other elements that have an effect on tensile strength are, in the order of decreasing effect, Sr, Cr, Zn, Ni, and Ti. Iron, at the levels studied, does not seem to affect tensile strength.

The percent contribution due to the error term provides an estimate of the adequacy of the experiment [2]. If the error term is low, say 15% or less, it is assumed that no important factors were omitted from the experiment and no measurement errors were significant. On the other hand, if the percent contribution due to the error term is high, say 50% or more, then some important factors were omitted, production conditions were not precisely controlled, or measurement errors were excessive. The percent contribution due to the error term in this ANOVA is about 21%. Given the nature of the die casting process, and the inevitability of incurring defects that can escape detection, and the sensitivity of tensile strength to defects, this error value is acceptable.

The statistical procedure for calculating the alloy composition for maximum tensile strength is outlined elsewhere [3]. Considering only the elements and interactions included in Table 2.2, the maximum tensile strength can be obtained from an alloy of the following composition:

Element	Cu	Mg	Si	Sr	Zn	Ni	Ti	Fe	Mn	Cr	Al
Wt. %	4.90	0.46	6.96	0.020	2.78	0.04	0.19	0.65	0.01	0.14	Bal.

At this composition the projected tensile strength is 53.41 ± 0.75 ksi with a confidence interval of 99.5%.

Among the sixteen alloys in Table 2.5, Alloy 7 has the highest tensile strength (49.1 ksi), and alloy 11 had the lowest tensile strength (35.1 ksi). Figs. 3.7.5 to 3.7.8 show the microstructure of alloy 7. This microstructure is characterized by a significantly large quantity of a Cu-rich phase that is present either in the interdendritic/intergrannular regions in the form of chains of particles, or within the Al-Si eutectic in the form of small individual particles. Alloy 7 is also characterized by the presence of Fe bearing needles and by a fine fibrous silicon phase. Fig. 4.2.9 (a) shows that the fracture surface of this alloy exhibits a mixture of cellular and fibrous structures, with the cellular structure showing a complicated array of small facets. This fracture surface suggests a brittle fracture. Figs. 3.11.5 to 3.11.8 show the microstructure of Alloy 11. This microstructure is characterized by the presence of very large Fe bearing needles. A small amount of a Cu bearing phase is also present, but as chains of small particles dispersed in the interdendritic areas and within the Al-Si eutectic areas. The Si particles are coarser than those in alloy 7. Fig. 4.2.9 (b) shows that the fracture surfaces of alloy 11 have a cellular structure with some needle-like cleavages. The cellular structure consists of large and small facets, and the overall fracture is brittle in nature.

Table 4.2.3. Pooled ANOVA table for room temperature tensile strength of Alloys 1 to 16.

Source of Variance	Degree of Freedom f	Sum of Squares S	Variance (Mean Squares) V	Variance Ratio F	Pure Sum of Squares S'	Percent Contribution P
Si	1	898.73	898.73	267.10	895.37	11.64
Mg	1	932.48	932.48	277.13	929.12	12.08
Si·Mg	1	70.91	70.91	21.08	67.55	0.88
Fe	Pooled					
Cu	1	2536.54	2536.54	753.85	2533.18	32.93
Ni	1	156.05	156.05	46.38	152.69	1.99
Cr	1	418.42	418.42	124.35	415.06	5.40
Mn	1	30.30	30.30	9.01	26.94	0.35
Ti	1	125.38	125.38	37.26	122.01	1.59
Zn	1	202.71	202.71	60.24	199.34	2.59
Fe·Mn·Cr	1	44.27	44.27	13.16	40.90	0.53
Fe·Mn	1	191.69	191.69	56.97	188.33	2.45
Sr	1	513.23	513.23	152.53	509.87	6.63
Cu·Zn	Pooled					
Error (e)	467	1571.35	3.3648	1.00	1611.72	20.95
Total	479	7692.07				100.00

[1] *It should be noted that Si was tested at only two levels: 7% and 13%. The difference between these two levels is quite large, and so the predicted decrease in tensile strength with increasing Si content is not necessarily a steady one, and there may be an initial increase in tensile strength, followed by a decrease.*

Yield strength

Results of the pooled analysis of variance for yield strength of the alloys in Table 2.5 are shown in Table 4.2.4. Table 4.2.4 indicates that, at the levels studied, Mg and Cu have the most significant effect on the variation in yield strength; each contributing about 39%. Silicon contributes 12.4% and is followed by Fe, Zn, and Ti in decreasing order. At higher levels, all these elements tend to increase the yield strength. The percent contribution due to the error term to this analysis is less than 1.4%, which is very acceptable.

Considering only the elements and interactions included in Table 2.2 the maximum yield strength can be obtained from an alloy of the following composition:

Element	Cu	Mg	Si	Zn	Ti	Fe	Mn	Cr	Ni	Sr
Wt. %	4.90	0.46	2.85	2.78	0.19	1.55	0.01	0.01	0.05-0.5	0-0.02

At this composition the projected yield strength is 35.33 ± 0.17 ksi with a confidence interval of 99.5%.

Among the alloys listed in Table 2.5, Alloy 14 has the highest yield strength (32.9 ksi), and Alloy 1 had the lowest yield strength (16.6 ksi). Figs. 3.14.5 to 3.14.8 show the microstructure of Alloy 14. This microstructure is characterized by a large amount of the Cu-rich phase that is present in the form of chains of particles in the interdendritic and intergranular regions and as small individual particles and net-shape eutectic within the Al-Si eutectic regions. Only a few Fe-rich particles are observed, and these are *"polyhedron"* in shape. Primary Si particles are present, and the eutectic Si is fine, but somewhat coarser than that observed in Alloy 7. Fig. 4.2.10 (a) shows that the fracture surface of this alloy exhibits a complicated array of small facets with a few fibrous and cleaved primary Si particles. The overall fracture is brittle in nature. Figs. 3.1.5 to 3.1.8 show the microstructure of Alloy 1. This microstructure is characterized by the presence of lesser amounts of intermetallic compounds in the interdendritic regions than in all the other alloys in Table 2.5. The Fe-rich phase in Alloy 1 appears as small amounts of needles. The Cu-rich phase is present in small amounts and takes the form of chains, or clusters, of lumpy particles in the interdendritic areas as well as within the Al-Si eutectic. Fig. 4.2.10 (b) shows that the fracture surface of Alloy 1 has a fibrous structure and cleaved Si facets. The overall fracture is ductile in nature.

4.2.4. Pooled ANOVA table for room temperature yield strength Alloys 1 to 16.

Source of Variance	Degree of Freedom f	Sum of Squares S	Variance (Mean Squares) V	Variance Ratio F	Pure Sum of Squares S'	Percent Contribution P
Si	1	1063.92	1063.92	4335.59	1063.67	12.39
Mg	1	3373.16	3373.16	13746.05	3372.92	39.28
Si·Mg	1	109.80	109.80	447.46	109.56	1.28
Fe	1	185.42	185.42	755.60	185.17	2.16
Cu	1	3365.36	3365.36	13714.24	3365.11	39.19
Ni	Pooled					
Cr	Pooled					
Mn	Pooled					
Ti	1	9.59	9.59	39.07	9.34	0.11
Zn	1	86.78	86.78	353.66	86.54	1.01
Fe·Mn·Cr	1	55.65	55.65	226.78	55.41	0.65
Fe·Mn	1	199.26	199.26	811.99	199.01	2.32
Sr	Pooled					
Cu·Zn	1	22.28	22.28	90.78	22.03	0.26
Error (e)	469	115.09	0.2454	1.00	117.54	1.37
Total	479	8586.30				100.00

Elongation

Results of the pooled analysis of variance for elongation of the alloys in Table 2.5 are shown in Table 4.2.5. Table 4.2.5 indicates that, at the levels studied, Si has the most significant effect on elongation variation; contributing about 40%. Fe and Cu also have significant effects contributing 18.5% and 15.4%; they are follwed by Mg, Ni, Cr, and Mn, in decreasing order. At higher levels, Si, Fe, Cu, Mg, Ni and Cr tend to decrease the elongation; on the other hand, Mn tends to increase the elongation. The interaction of Si and Mg also has a small effect. The percent contribution due to the error term to this analysis is 7.7%, which is acceptable.

Considering only the elements and interactions included in Table 2.2, the maximum elongation can be obtained from an alloy of the following composition:

Element	Si	Fe	Cu	Mg	Ni	Cr	Mn	Ti	Zn	Sr	Al
Wt. %	6.96	0.65	1.21	0.04	0.04	0.01	0.45	0.19	2.78	0.02	Bal.

At this composition the projected elongation is 7.32 ± 0.22% with a confidence interval of 99.5%.

Among the alloys listed in Table 2.5, Alloy 2 has the highest elongation (7.43%), and Alloy 14 had the lowest elongation (0.67%). Figs. 3.2.5 to 3.2.8 show the microstructure of Alloy 2. A very fine fibrous Si in the Al-Si eutectic structure and very few intermetallic compounds in the interdendritic areas characterize this microstructure. The Fe-rich phase in Alloy 2 is not too prominent and appears as a few Chinese script and as even lower lumpy particles. The Cu-rich phase is present in small amounts and takes the form of chains and clusters of particles in the interdendritic areas and within the Al-Si eutectic. The fracture surface of Alloy 2 is shown in Fig. 4.2.11 and consists of a fibrous strucutre and a large amount of broken surfaces that seem to be deformed during fracture explaining the ductile nature of this alloy. The microstructure and fracture surface of Alloy 14 was discussed earlier (Figs. 3.14.5 to 3.14.8 and 4.2.10 (a)).

Table 4.2.5. Pooled ANOVA table for room temperature elongation of Alloys 1 to 16.

Source of Variance	Degree of Freedom f	Sum of Squares S	Variance (Mean Squares) V	Variance Ratio F	Pure Sum of Squares S'	Percent Contribution P
Si	1	701.503	701.503	2503.9002	701.22	40.01
Mg	1	122.88	122.88	438.60038	122.60	7.00
Si·Mg	1	78.5191	78.5191	280.26117	78.24	4.46
Fe	1	324.005	324.005	1156.4813	323.72	18.47
Cu	1	269.336	269.336	961.35058	269.06	15.35
Ni	1	55.2862	55.2862	197.33515	55.01	3.14
Cr	1	16.6422	16.6422	59.401559	16.36	0.93
Mn	1	16.3677	16.3677	58.421996	16.09	0.92
Ti	1	13.9957	13.9957	49.955348	13.72	0.78
Zn	1	11.2048	11.2048	39.993791	10.92	0.62
Fe·Mn·Cr	Pooled					
Fe·Mn	Pooled					
Sr	1	11.7697	11.7697	42.010177	11.49	0.66
Cu·Zn	Pooled					
Error (e)	468	131.117	0.2802	1	134.20	7.66
Total	479	1752.63				100.00

Modulus of Elasticity

Results of the pooled analysis of variance for modulus of elasticity of the alloys in Table 2.5 are shown in Table 4.2.6. Table 4.2.6 shows that the percent contribution due to the error term in this analysis is quite high, about 80%. This may suggest that during the design of the experiment, some factors that significantly affect the modulus of elasticity were inadvertently omitted, the experimental conditions were not perfectly controlled, and/or errors for measuring the modulus of elasticity were excessive. However, examination of Table 4.2.7 shows that the relative difference between the highest and the lowest average modulus of elasticity is less than 10%. Also Table 4.2.7 shows that the coefficient of variance (CV) for the average modulus of elasticity over the range of the alloys in Table 2.5 is only 3.17%. The above two factors indicate that the modulus of elasticity did not have much variation over the range of alloy chemistry presented in Table 2.5.

Table 4.2.6. Pooled ANOVA table for room temperature modulus of elasticity of Alloys 1 to 16.

Source of Variance	Degree of Freedom f	Sum of Squares S	Variance (Mean Squares) V	Variance Ratio F	Pure Sum of Squares S'	Percent Contribution P
Si	1	3670598	3670598	90.6	3600786	14.83
Mg	Pooled					
Si·Mg	Pooled					
Fe	1	6034191	6034191	14.9	5628997	2.3
Cu	1	5597329	5597329	13.8	5192135	2.12
Ni	Pooled					
Cr	Pooled					
Mn	Pooled					
Ti	Pooled					
Zn	Pooled					
Fe·Mn·Cr	Pooled					
Fe·Mn	1	3893301	3893301	9.6	3488107	1.43
Sr	Pooled					
Cu·Zn	Pooled					
Error (e)	475	192467664	405195	1.0	194088440	79.32
Total	479	144698464				100.00

Table 4.2.7. Variation in the magnitude of room temperature modulus of elasticity of Alloys 1 to 16.

Property	E
max – min	1127 ksi
(max – min)/average	9.98%
St. Deviation	358 ksi
CV	3.17%

Summary

I ng the elements common in aluminum die casting alloys, both magnesium and copper seem to have the most significant effect on room temperature tensile strength and yield strength of aluminum die casting alloys. Copper dissolves in aluminum and produces significant solid solution strengthening. Copper may also precipitate out as small $CuAl_2$ particles and/or $CuAl_2$+Al eutectic in the interdendritic and intergranual regions, thus increasing the tensile strength of the alloy. Magnesium too has a substantial solid solubility in aluminum, but at the Mg levels used in this experiment, it did not show appreciable precipitation, so the increased strength is not attributed to precipitation hardening. Magnesium does, however, substantially strengthen the aluminum matrix by solid solution strengthening, and it can impart high work hardening characteristics to the alloy. An unexpected result is that Fe has a negligible effect on tensile strength; however, the interaction Fe.Mn seems to affect the tensile strength. Fe and Mn both at the high level give the highest tensile strength, but Fe at the higher level and Mn at the lower level give the lowest tensile strength. Among the elements common in die casting alloys, silicon seems to have the most significant effect on the elongation. An increase in the silicon content seems to promote a decrease in elongation, and also a decrease in tensile strength[2]. At the higher Si content, the fraction of the Al-Si eutectic phase increases and primary silicon particles form and grow; this tends to make the alloy more brittle and weak.

4.2.3 Effect of Alloy Chemistry on Elevated Temperature Tensile Properties

Tables 4.2.8 (a) to (d) and 4.2.9 (a) to (d) present the average tensile properties at 100°C and 200°C for the twenty-four alloys presented in Tables 2.5 and 2.6. For comparison the room temperature tensile properties are also presented in these tables. For ease of visualization, the same information is presented in chart form in Figs. 4.2.12 to 4.2.19. Tables 4.2.8 (a) to (d) and 4.2.9 (a) to (d) also show the standard deviation and the coefficient of variance for each of the measured properties.

Table 4.2.8. (a) Average tensile strength at different temperatures for Alloys 1 to 16.

Alloy	At 25 °C			At 100 °C			At 200 °C		
	Average (Ksi)	St.dev.* (Ksi)	CV** (%)	Average (Ksi)	St.dev.* (Ksi)	CV** (%)	Average (Ksi)	St.dev.* (Ksi)	CV** (%)
1	39.6	0.9	2.3	32.9	1.0	3.1	20.2	0.2	0.8
2	42.4	0.8	1.9	36.5	0.4	1.0	22.1	0.2	1.0
3	45.4	1.0	2.2	42.6	0.4	1.0	30.2	0.2	0.6
4	47.0	0.9	1.9	42.9	0.5	1.3	31.2	0.4	1.3
5	44.4	0.7	1.6	40.2	0.5	1.2	29.6	0.4	1.4
6	46.2	1.5	3.2	42.3	0.9	2.1	33.6	0.8	2.6
7	49.1	0.6	1.2	45.2	1.1	2.4	36.6	0.7	1.8
8	48.9	0.9	1.8	46.8	1.3	2.9	37.0	0.5	1.4
9	46.8	1.8	3.8	44.0	1.8	4.2	31.2	0.7	2.2
10	44.3	2.4	5.4	39.2	3.8	9.6	29.7	0.5	1.6
11	35.1	2.0	5.7	34.9	0.7	2.0	29.5	1.1	3.6
12	40.4	2.2	5.4	38.3	1.2	3.1	27.8	0.6	2.2
13	47.2	1.6	3.4	44.8	1.4	3.2	35.4	0.3	0.7
14	41.9	4.0	9.5	44.0	2.8	6.3	34.5	2.2	6.3
15	42.6	2.1	4.9	39.4	2.9	7.3	34.6	0.6	1.8
16	43.0	2.5	5.8	41.5	2.0	4.7	32.7	2.2	6.7

* St. dev. - Standard deviation** CV - Coefficient of Variation (= St. dev./Mean 100%)

Table 4.2.8. (b) Average yield strength at different temperatures for Alloys 1 to 16.

Alloy	At 25 °C			At 100 °C			At 200 °C		
	Average (Ksi)	St. dev.* (Ksi)	CV** (%)	Average (Ksi)	St. dev.* (Ksi)	CV** (%)	Average (Ksi)	St. dev.* (Ksi)	CV** (%)
1	16.6	0.4	2.4	16.8	0.5	2.7	14.5	0.3	2.2
2	20.0	0.4	2.0	19.7	0.4	1.9	17.3	0.3	1.6
3	24.8	0.3	1.2	24.8	0.4	1.7	21.5	0.2	0.8
4	25.5	0.4	1.6	24.9	0.4	1.5	24.0	0.2	0.7
5	24.9	0.3	1.2	24.5	0.6	2.3	24.3	0.5	2.2
6	24.9	0.5	2.0	25.0	0.7	2.8	27.6	0.5	1.9
7	32.2	0.6	1.9	30.4	0.6	2.1	30.5	0.5	1.5
8	30.0	0.3	1.0	29.5	0.4	1.5	29.9	0.3	1.1
9	27.5	0.4	1.5	27.3	0.6	2.2	23.0	0.4	1.5
10	28.2	0.4	1.4	27.9	0.4	1.5	23.2	0.3	1.3
11	23.8	0.5	2.1	24.2	0.2	0.8	21.9	0.2	0.9
12	23.3	0.4	1.7	23.3	0.3	1.4	20.4	0.2	1.2
13	31.0	0.5	1.6	30.3	0.4	1.3	29.7	0.2	0.8
14	32.9	0.7	2.1	32.7	0.4	1.3	31.5	0.8	2.4
15	29.2	0.4	1.4	29.1	0.8	2.6	28.5	0.2	0.7
16	26.9	0.4	1.5	27.2	0.3	1.0	26.4	2.5	9.6

St. dev. - Standard deviation **CV - Coefficient of Variation (= St. dev./Mean 100%)

[2] See footnote 1.

Table 4.2.8 (c). Average % elongation at different temperatures for Alloys 1 to 16.

Alloy	At 25 °C			At 100 °C			At 200 °C		
	Average (%)	St. dev.* (%)	CV** (%)	Average (%)	St. dev.* (%)	CV** (%)	Average (%)	St. dev.* (%)	CV** (%)
1	5.85	0.97	16.6	10.49	2.03	19.4	19.35	2.71	14.0
2	7.43	1.18	15.9	11.53	2.16	18.7	14.77	0.90	6.1
3	2.08	0.23	11.1	2.92	0.40	13.6	5.00	0.78	15.5
4	2.81	0.29	10.3	4.10	0.78	18.9	5.12	0.86	16.9
5	3.76	0.52	13.8	6.39	1.05	16.4	7.00	1.83	26.2
6	3.78	0.75	19.8	5.29	1.23	23.2	4.98	1.70	34.2
7	1.42	0.08	5.6	1.86	0.14	7.7	2.40	0.09	3.9
8	1.93	0.19	9.8	2.66	0.49	18.5	3.22	0.30	9.5
9	1.69	0.29	17.2	2.35	0.68	28.8	4.25	1.33	31.3
10	1.40	0.37	26.4	1.38	0.61	44.1	4.46	1.62	36.3
11	0.75	0.13	17.3	1.00	0.09	9.4	1.57	0.46	29.2
12	1.42	0.32	22.5	2.24	0.57	25.7	5.32	1.02	19.1
13	1.39	0.24	17.3	1.87	0.42	22.7	2.31	0.52	22.3
14	0.67	0.32	47.8	1.08	0.57	53.1	0.74	0.54	73.0
15	0.97	0.17	17.5	1.10	0.41	37.7	1.66	0.29	17.6
16	1.41	0.39	27.7	1.92	0.44	22.9	1.81	0.64	35.6

St. dev. - Standard deviation **CV - Coefficient of Variation (= St. dev./Mean 100%)

Table 4.2.8 (d). Average modulus of elasticity at different temperatures for Alloys 1 to 16.

Alloy	At 25 °C			At 100 °C			At 200 °C		
	Average (Ksi)	St. dev.* (Ksi)	CV** (%)	Average (Ksi)	St. dev.* (Ksi)	CV** (%)	Average (Ksi)	St. dev.* (Ksi)	CV** (%)
1	10,536	1,024	9.7	7770	875	11.3	7469	678	9.1
2	10,915	753	6.9	8926	492	5.5	7367	530	7.2
3	11,262	753	6.7	8935	316	3.5	7939	309	3.9
4	11,079	746	6.7	8717	157	1.8	8063	324	4.0
5	10,671	427	4.0	8548	229	2.7	7723	198	2.6
6	11,008	748	6.8	9009	337	3.7	8177	432	5.3
7	11,435	687	6.0	9370	1195	12.8	8436	323	3.8
8	11,111	385	3.5	8776	241	2.7	8274	285	3.4
9	11,583	685	5.9	8975	227	2.5	8445	644	7.6
10	11,420	539	4.7	9297	228	2.5	8357	272	3.2
11	11,621	595	5.1	9323	365	3.9	8643	436	5.0
12	11,418	826	7.2	8949	455	5.1	8392	385	4.6
13	11,552	391	3.4	9167	276	3.0	8399	308	3.7
14	11,644	389	3.3	9143	93	1.0	8519	328	3.9
15	11,639	562	4.8	9435	379	4.0	8275	177	2.1
16	11,620	700	6.0	8923	262	2.9	7933	1056	13.3

St. dev. - Standard deviation **CV - Coefficient of Variation (= St. dev./Mean 100%)

Table 4.2.9 (a) Average tensile strength at different temperatures for Alloy 17 to 24.

Alloy	At 25°C			At 100°C			At 200°C		
	Average (Ksi)	St. dev.* (Ksi)	CV** (%)	Average (Ksi)	St. dev.* (Ksi)	CV** (%)	Average (Ksi)	St. dev.* (Ksi)	CV** (%)
17	45.0	0.7	1.6	38.2	0.9	2.4	24.3	0.4	1.6
18	46.2	0.8	1.7	41.4	0.1	0.2	25.6	0.4	1.6
19	45.4	1.6	3.5	38.8	1.8	4.6	23.8	0.4	1.7
20	45.4	2.6	5.7	43.4	0.7	1.6	31.0	0.5	1.6
21	44.0	4.6	10.5	40.0	1.6	4.0	26.8	0.2	0.7
22	45.6	3.2	7.0	41.9	2.4	5.7	28.9	0.4	1.4
23	41.3	3.0	7.3	37.9	2.6	6.9	27.7	1.4	5.1
24	45.0	2.1	4.7	41.9	2.7	6.4	29.6	0.5	1.7

*** St. dev. - Standard deviation ** CV - Coeffiecient of Variation (= St. dev./Mean 100%)**

Table 4.2.9 (b). Average yield strength at different tempratures for Alloys 17 to 24.

Alloy	At 25°C			At 100°C			At 200°C		
	Average (Ksi)	St. dev.* (Ksi)	CV** (%)	Average (Ksi)	St. dev.* (Ksi)	CV** (%)	Average (Ksi)	St. dev.* (Ksi)	CV** (%)
17	19.6	0.3	1.5	20.1	0.3	1.5	17.6	0.3	1.7
18	21.8	0.7	3.2	22.2	0.5	2.3	18.9	0.3	1.6
19	20.3	0.3	1.5	20.5	0.3	1.5	17.4	0.3	1.7
20	25.1	0.2	0.8	25.3	0.3	1.2	23.3	0.2	0.9
21	21.8	0.7	3.2	21.8	0.1	0.5	19.4	0.3	1.5
22	24.5	0.4	1.6	25.2	0.3	1.2	21.3	0.3	1.4
23	22.1	0.5	2.3	22.2	0.5	2.3	20.3	0.4	2.0
24	26.6	0.4	1.5	26.9	0.6	2.2	22.4	0.2	0.9

*** St. dev. - Standard deviation ** CV - Coeffiecient of Variation (= St. dev./Mean 100%)**

Table 4.2.9 (c). Average % elongation at different temperatures for Alloys 17 to 24.

Alloy	At 25°C			At 100°C			At 200°C		
	Average (%)	St. dev.* (%)	CV** (%)	Average (%)	St. dev.* (%)	CV** (%)	Average (%)	St. dev.* (%)	CV** (%)
17	5.34	0.59	11.0	7.27	2.39	32.9	12.57	1.73	13.8
18	3.68	0.49	13.3	5.79	1.16	20.0	7.16	3.14	43.9
19	4.62	1.00	21.6	6.50	2.49	38.3	13.17	2.36	17.9
20	1.93	0.44	22.8	3.12	0.49	15.7	3.65	1.24	34.0
21	2.73	0.73	26.7	4.73	1.83	38.7	7.44	1.90	25.5
22	2.30	0.74	32.2	3.05	1.43	46.9	7.06	2.97	42.1
23	1.79	0.51	28.5	2.39	1.06	44.4	5.43	2.50	46.0
24	1.51	0.31	20.5	2.04	0.74	36.3	4.18	2.07	49.5

*** St. dev. - Standard deviation ** CV - Coeffiecient of Variation (= St. dev./Mean 100%)**

Table 4.2.9 (d). Average modulus of elasticity at different temperatures for Alloys 17 to 24.

Alloy	At 25°C			At 100°C			At 200°C		
	Average (Ksi)	St. dev.* (Ksi)	CV** (%)	(Ksi)	St. dev.* (Ksi)	(%)	Average (Ksi)	St. dev.* (Ksi)	CV** (%)
17	10,913	678	6.2	8,037	738	9.2	7,884	263	3.3
18	10,918	804	7.4	8,297	472	5.7	7,978	130	1.6
19	11,032	771	7.0	8,595	905	10.5	8,428	225	2.7
20	11,317	356	3.1	8,777	430	4.9	8,327	214	2.6
21	10,958	683	6.2	8,799	245	2.8	8,351	130	1.6
22	10,917	624	5.7	8,751	167	1.9	8,276	163	2.0
23	11,193	481	4.3	8,721	331	3.8	8,652	1,124	13.0
24	11,656	728	6.2	8,712	294	3.4	7,958	323	4.1

*** St. dev. - Standard deviation ** CV - Coeffiecient of Variation (= St. dev./Mean 100%)**

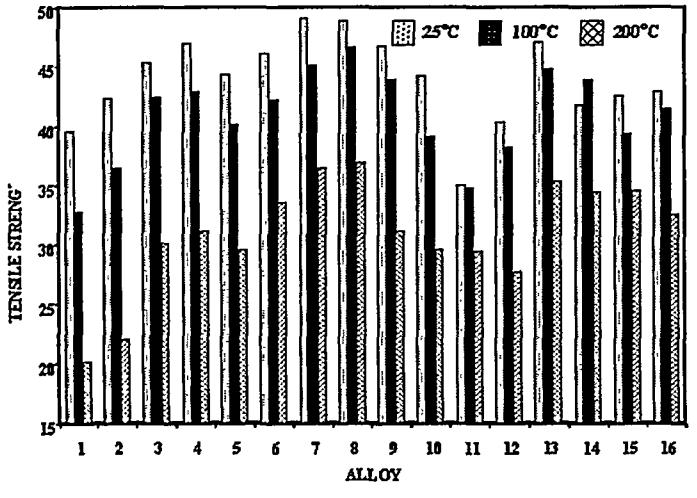

Fig. 4.2.12. Tensile strengths of Alloys 1 to 16 at 25°C, 100°C and 200°C.

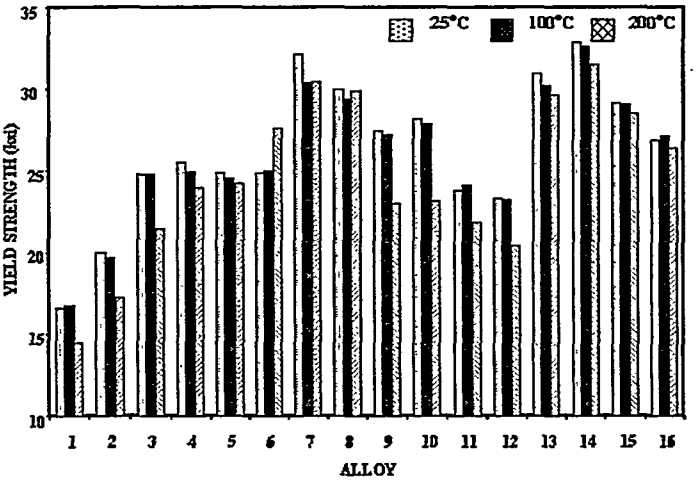

Fig. 4.2.13. Yield strengths of Alloys 1 to 16 at 25°C, 100°C and 200°C.

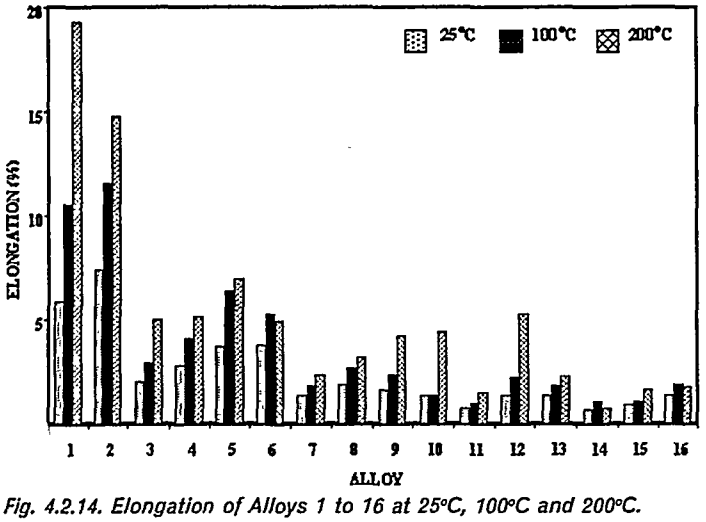

Fig. 4.2.14. Elongation of Alloys 1 to 16 at 25°C, 100°C and 200°C.

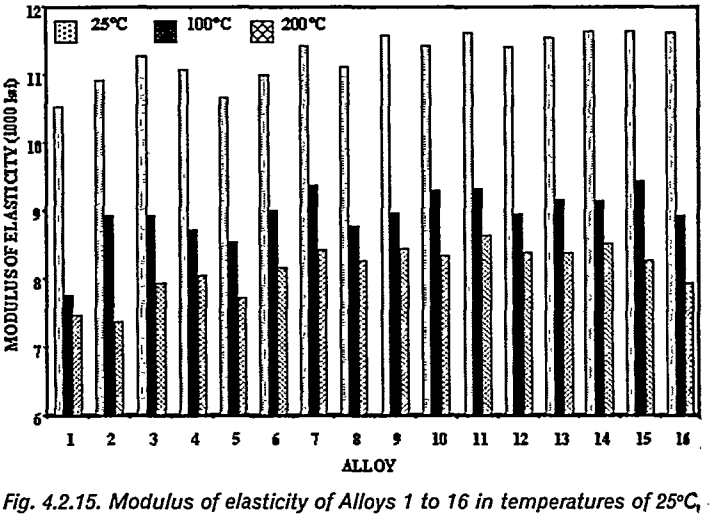

Fig. 4.2.15. Modulus of elasticity of Alloys 1 to 16 in temperatures of 25°C, 100°C and 200°C.

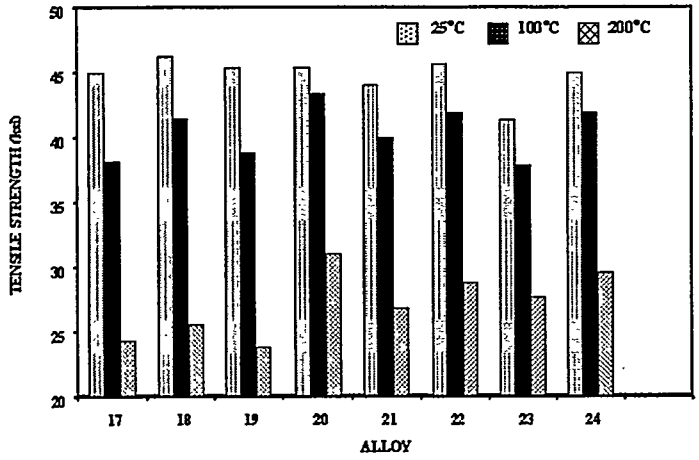

Fig. 4.2.16. Tensile strengths of Alloys 17 to 24 at 25°C, 100°C and 200°C.

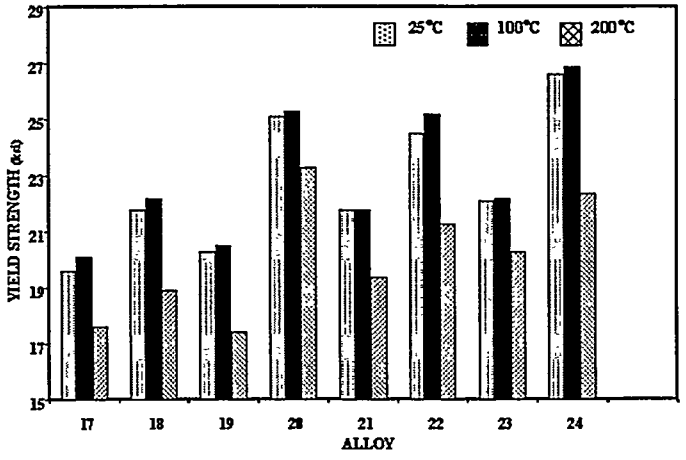

Fig. 4.2.17. Yield strengths of Alloys 17 to 24 at 25°C, 100°C and 200°C.

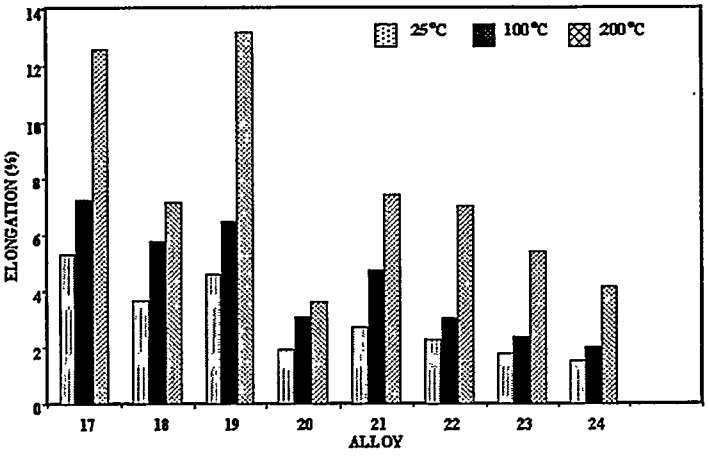

Fig. 4.2.18. Elongation of Alloys 17 to 24 at 25°C, 100°C and 200°C.

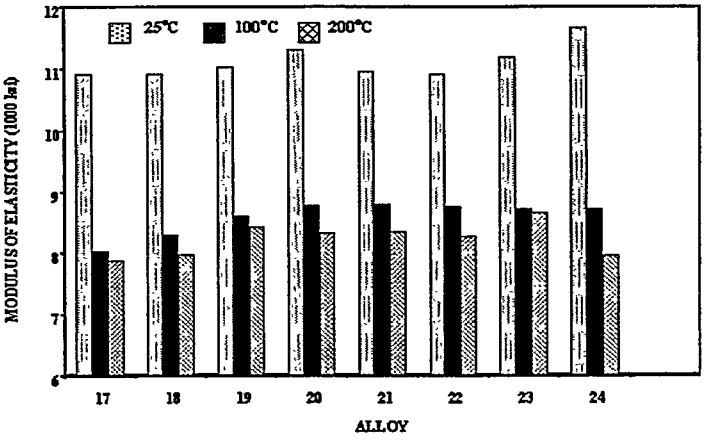

Fig. 4.2.19. Modulus of elasticity of Alloys 17 to 24 at 25°C, 100°C and 200°C.

Tensile Strength at 100°C

Results of the pooled analysis of variance for tensile strength at 100°C for the alloys in Table 2.5 are shown in Table 4.2.10. Table 4.2.10 shows that, at the levels studied, the element that affects the variation of the 100°C tensile strength most significantly is Cu. Its contribution to the variation is about 44%. Mg also has a significant effect contributing about 25% to the variance. At higher levels, Cu and Mg tend to increase the 100°C tensile strength of the alloys. All other elements seem to have comparatively insignificant effect on the 100°C tensile strength of the alloys tested. The percent contribution due to the error term in this analysis is 18.5%, which is acceptable.

Considering only the elements and interactions included in Table 2.2, the maximum tensile strength for service at 100°C can be obtained from an alloy with the following composition:

Element	Si	Fe	Cu	Mg	Ni	Cr	Mn	Ti	Zn	Sr	Al
Wt. %	6.96-12.85	1.55	4.90	0.46	0.04-0.47	0.14	0.45	0.19	0.46	0.02	Bal.

At this composition the projected tensile strength at 100°C is 50.9±0.75 ksi with a confidence interval of 95%.

Tensile Strength at 200°C

Results of the pooled analysis of variance for tensile strength at 200°C for the alloys in Table 2.5 are shown in Table 4.2.11. Table 4.2.11 shows that, at the levels studied, the element that affects the variation of the 200°C tensile strength most significantly is Mg. Its relative contribution is about 49%. Cu also has a significant effect contributing about 23% to the variance. At higher levels, Mg and Cu tend to increase the 200°C tensile strength of the alloys. All other elements seem to have comparatively insignificant effect on the 200°C tensile strength of the alloys tested. The percent contribution due to the error term in this analysis is only 4.9%, which is very acceptable.

Considering only the elements and interactions included in Table 2.2, the maximum tensile strength for service at 200°C can be obtained from an alloy with the following composition:

Element	Si	Fe	Cu	Mg	Ni	Cr	Mn	Ti	Zn	Sr	Al
Wt. %	12.85	1.55	4.90	0.46	0.47	0.14	0.01-0.45	0.19	0.46-2.78	0.02	Bal.

At this composition the projected tensile strength at 200°C is 39.9±0.6 ksi with a confidence interval of 95%.

The tensile strengths of all the alloys in Table 2.5, except Alloy 14, decrease with increasing temperature. The decrease in strength with increasing temperature seems to be more or less exponential. The average tensile strength of the 16 alloys decreased 7% as the temperature increased from 25°C to 100°C and 30% as the temperature increased from 25°C to 200°C. Alloy 1 shows the most significant decrease in strength with increasing temperature. The strength of Alloy 1 decreased 17% as the temperature increased from 25°C to 100°C and 49% as the temperature increased from 25°C to 200°C. On the other hand, Alloys 11 and 14 exhibit the least decrease in strength with increasing temperature. The strength of Alloy 11 decreased only 1% as the temperature increased from 25°C to 100°C, and 16% as the temperature increased from 25°C to 200°C. Alloy 14 shows a 5% increase in tensile strength as the temperature increases from 25°C to 100°C. However, the tensile strength decreases by 18% as the temperature is increased from 25°C to 200°C. Results of the analysis of variance for different temperatures show that the capacities of the elements to affect variation in tensile strength vary with temperature. At higher levels Cu, Mg, Cr and Ti increase the tensile strength at all the tested temperatures. At the lower temperatures, Cu has the most significant effect and at the higher temperatures Mg becomes most significant. At higher levels, Si, Fe, and Ni decrease the tensile strength at lower temperatures, but they increase the tensile strength at higher temperature.

Table 4.2.10. Pooled ANOVA table for tensile strength of Alloys 1 to 16 at 100°C.

Source of Variance	Degree of Freedom f	Sum of Squares S	Variance (Mean Squares) V	Variance Ratio F	Pure Sum of Squares S'	Percent Contribution P (%)
Si						
Mg	1	339.3	339.3	107.6	336.1	25.3
Si·Mg						
Fe	1	17.7	17.7	5.6	14.5	1.1
Cu	1	589.7	589.7	187.0	586.5	44.1
Ni						
Cr	1	25.3	25.3	8.0	22.1	1.7
Mn	1	17.7	17.7	5.6	14.6	1.1
Ti	1	17.8	17.8	5.7	14.7	1.1
Zn						
Fe·Mn·Cr						
Fe·Mn	1	16.8	16.8	5.3	13.7	1.0
Sr	1	69.2	69.2	21.9	66.0	5.0
Cu·Zn	1	19.0	19.0	6.0	15.9	1.2
Error (e)	69	217.6	3.2	1.0	246.0	18.5
Total						100.0

Table 4.2.11. Pooled ANOVA table for tensile strength of Alloys 1 to 16 at 200°C.

Source of Variance	Degree of Freedom f	Sum of Squares S	Variance (Mean Squares) V	Variance Ratio F	Pure Sum of Squares S'	Percent Contribution P (%)
Si	1	69.9	69.9	64.72	68.8	4.0
Mg	1	851.3	851.3	788.10	850.2	49.1
Si·Mg	1	61.9	61.9	57.30	60.8	3.5
Fe	1	169.2	169.2	156.63	168.1	9.7
Cu	1	397.9	397.9	368.33	396.8	22.9
Ni	1	20.1	20.1	18.61	19.0	1.1
Cr	1	29.9	29.9	27.72	28.9	1.7
Mn						
Ti	1	54.4	54.4	50.35	53.3	3.1
Zn						
Fe·Mn·Cr						
Fe·Mn						
Sr						
Cu·Zn						
Error (e)	71	76.7	1.1	1.00	85.3	4.9
Total						100.0

Alloys 7 and 8 have the highest room temperature tensile strength among the alloys shown in Table 2.5. They also have higher tensile strengths at higher temperatures. Alloy 1 has the lowest tensile strength at 100°C (32.9 ksi) and at 200°C (20.2 ksi). Both Alloys 7 and 8 contain high levels of Cu, Mg, and Fe. The major difference between these alloys is that Alloy 8 has more Mn (0.45%) than Alloy 7 (0.02%). The microstructure of Alloys 7 and 8 are show in Figs. 3.7.5 to 3.7.8 and 3.8.5 to 3.8.8, respectively. The major difference between the microstructures of the two alloys is in the mor phologies of their Fe bearing phase. The Fe bearing phas in Alloy 7 is present predominantly as needles, while a larg fraction of the Fe bearing phase in Alloy 8 is in the form c Chinese script and polyhedral particles. While the differ ence in morphology seem to have little effect on the tensil strength at all three temperatures, it affects the alloy elor gation considerably as shown in Table 4.2.8 (c) and i Fig. 4.2.14.

Yield strength at 100°C

Results of the pooled analysis of variance for yield strength at 100°C for the alloys in Table 2.5 are shown in Table 4.2.12. Table 4.2.12 shows that, at the levels studied, both Mg and Cu significantly affect the 100°C yield strength. Magnesium's relative contribution to the variance in the 100°C yield strength is about 39%, while copper's contribution is about 35%. Silicon, too has a significant positive effect on the 100°C yield strength of the die cast alloys considered in this book, contributing about 17% to the variance in 100°C yield strength of the alloys. At higher levels, Cu, Mg, and Si all tend to increase the 100°C yield strength of the alloys. The percent contribution due to the error term in this analysis is only 3.4%, which is very acceptable.

Considering only the elements and interactions included in Table 2.2, the maximum yield strength for service at 100°C can be obtained from an alloy with the following composition:

Element	Si	Cu	Fe	Mn	Mg	Ni	Cr	Zn	Ti	Sr
Wt. %	12.85	4.90	1.55	0.01	0.46	0.04-0.47	0.01-0.15	0.47-2.78	0.01-0.19	0-0.02

At this composition the projected yield strength at 100°C is 33±0.3 ksi with a confidence interval of 95%.

Yield strength at 200°C

Results of the pooled analysis of variance for yield strength at 200°C for the alloys in Table 2.5 are shown in Table 4.2.13. Table 4.2.13 shows that, at the levels studied, magnesium has an overwhelming effect on the 200°C yield strength of die casting alloys contributing about 67% of the variance. Copper is a distant second contributing about 18% of the variance. The rest of the elements seem to have an insignificant effect on the 200°C yield strength of die casting alloys. At higher levels, both Mg and Cu tend to enhance the 200°C yield strength of the alloys. The percent contribution due to the error term in this analysis is only 6.1%, which is quite acceptable.

Considering only the elements and interactions included in Table 2.2, the maximum yield strength for service at 200°C can be obtained from an alloy with the following composition:

Element	Si	Cu	Fe	Mn	Mg	Ni	Cr	Zn	Ti	Sr
Wt. %	12.85	4.9	1.55	0.01	0.46	0.04-0.47	0.01-0.15	0.46-2.78	0.19	0-0.02

At this composition the projected yield strength at 200°C is 33.1±0.7 ksi with a confidence interval of 95%.

The yield strength of all the alloys shown in Table 2.5 does not change significantly when the test temperature is increased from 25°C to 100°C, but they decrease significantly when the test temperature is raised to 200°C. The average yield strength of the sixteen alloys decreased only 1% when the test temperature was raised from 25°C to 100°C, and 7% when the test temperature was raised from 25°C to 200°C. The most significant decrease in yield strength happens in Alloy 10 (18% drop in yield strength when the test temperature was raised from 25°C to 200°C). The least significant decrease in yield strength happens in Alloy 15 (2% drop in yield strength when the test temperature was raised from 25°C to 200°C).

At higher levels Si, Cu, Fe and Mg all increase the yield strength at all three test temperatures. Among the sixteen alloys of Table 2.5, Alloy 14 has the highest yield strength and Alloy 1 has the lowest yield strength at all three test temperatures. The microstructures of Alloys 1 and 14 at 100°C and 200°C are not much different from their microstructures at 25°C. (Figs. 3.1.5 to 3.1.8 and 3.14.5 to 3.14.8.)

Table 4.2.12. Pooled ANOVA table for tensile strength of Alloys 1 to 16 at 100°C.

Source of Variance	Degree of Freedom f	Sum of Squares S	Variance (Mean Squares) V	Variance Ratio F	Pure Sum of Squares S'	Percent Contribution P (%)
Si	1	213.7	213.7	390.1	213.2	16.8
Mg	1	493.6	493.6	901.1	493.1	38.9
Si-Mg	1	14.0	14.0	25.6	13.5	1.1
Fe	1	26.5	26.5	48.4	26.0	2.0
Cu	1	449.5	449.5	820.5	448.9	35.4
Ni						
Cr						
Mn						
Ti						
Zn						
Fe-Mn-Cr						
Fe-Mn	1	31.4	31.4	57.4	30.9	2.4
Sr						
Cu-Zn						
Error (e)	73	40.0	0.5	1.0	43.3	3.4
Total						100.0

Table 4.2.13. Pooled ANOVA table for tensile strength of Alloys 1 to 16 at 200°C.

Source of Variance	Degree of Freedom f	Sum of Squares S	Variance (Mean Squares) V	Variance Ratio F	Pure Sum of Squares S'	Percent Contribution P (%)
Si	1	71.5	71.5	50.98	70.1	3.8
Mg	1	1224.2	1224.2	872.82	1222.8	66.8
Si·Mg						
Fe	1	45.3	45.3	32.29	43.9	2.4
Cu	1	327.5	327.5	233.46	326.1	17.8
Ni						
Cr						
Mn						
Ti	1	29.2	29.2	20.85	27.8	1.5
Zn						
Fe·Mn·Cr						
Fe·Mn	1	30.1	30.1	21.43	28.7	1.6
Sr						
Cu·Zn						
Error (e)	73	102.4	1.4026	1.00	110.8	6.1
Total						100.0

Elongation at 100°C

Results of the pooled analysis of variance for elongation at 100°C for the alloys in Table 2.5 are shown in Table 4.2.14. Table 4.2.14 shows that, at the levels studied, silicon, followed by iron and copper has the most significant effects on the ductility of die casting alloys at 100°C, contributing to the variance 38.2%, 18.9% and 17.2% respectively. Magnesium, on the other hand, contributes only 5% to the observed variance. At higher levels all these elements decrease the elongation at 100°C. The percent contribution due to the error term in this analysis is only 8.7%, which is quite acceptable.

Considering only the elements and interactions included in Table 2.2, the maximum elongation at 100°C can be obtained from an alloy with the following composition:

Element	Si	Cu	Fe	Mn	Mg	Ni	Cr	Zn	Ti	Sr
Wt. %	6.96	1.21	0.65	0.01	0.04	0.04	0.01	0.46-2.78	0.01-0.19	0-0.02

At this composition the projected elongation at 100°C is 11.3±0.5% with a confidence interval of 95%.

Elongation at 200°C

Results of the pooled analysis of variance for elongation at 200°C for the alloys in Table 2.5 are shown in Table 4.2.15. Table 4.2.15 shows that, at the levels studied, silicon, magnesium, iron, and copper have significant effects on the ductility of die casting alloys at 200°C, contributing to the variance 25.1%, 20.3%, 16.0%, and 13.3% respectively. At higher levels all these elements decrease the elongation at 200°C. The percent contribution due to the error term in this analysis is only 5.9%, which is quite acceptable.

Considering only the elements and interactions included in Table 2.2, the maximum elongation at 200°C can be obtained from an alloy with the following composition:

Element	Si	Cu	Fe	Mn	Mg	Ni	Cr	Zn	Ti	Sr
Wt. %	6.96	1.21	0.65	0.01	0.04	0.04	0.01	0.46-2.78	0.01-0.19	0-0.02

At this composition the projected elongation at 200°C is 18.9±0.7% with a confidence interval of 95%.

The elongation of most of the alloys shown in Table 2.5 increases with an increase in temperature. However, the extent of increase in elongation with temperature varies significantly from alloy to alloy. The average increase in elongation of the 16 alloys is about 50% when the test temperature increases from 25°C to 100°C, and 117% when the test temperature increases from 25°C to 200°C. The elongation of Alloy1 increases 79% when the temperature increases from 25°C to 100°C, and 231% when the test temperature increases from 25°C to 200°C. The elongation of Alloy 12 increases 57% when the temperature increases from 25°C to 100°C, and 274% when the temperature increases from 25°C to 200°C. On the other hand, Alloy 14 shows negligible change in ductility when the test temperature increases from 25°C (0.67%) to 200°C (0.74%).

Table 4.2.14 Pooled ANOVA table for elongation of Alloys 1 to 16 at 100 °C.

Source of Variance	Degree of Freedom f	Sum of Squares S	Variance (Mean Squares) V	Variance Ratio F	Pure Sum of Squares S'	Percent Contribution P (%)
Si	1	326.4	326.4	347.6	325.4	38.2
Mg	1	58.0	58.0	61.8	57.1	6.7
Si·Mg	1	43.8	43.8	46.7	42.9	5.0
Fe	1	162.2	162.2	172.8	161.3	18.9
Cu	1	147.2	147.2	156.8	146.3	17.2
Ni	1	21.0	21.0	22.3	20.0	2.4
Cr	1	16.6	16.6	17.6	15.6	1.8
Mn						
Ti						
Zn						
Fe·Mn·Cr						
Fe·Mn	1	10.0	10.0	10.6	9.1	1.1
Sr						
Cu·Zn						
Error (e)	71	66.7	0.9	1.0	74.2	8.7
Total						100.0

Table 4.2.15. Pooled ANOVA table for % elongation of Alloys 1 to 16 at 200°C.

Source of Variance	Degree of Freedom f	Sum of Squares S	Variance (Mean Squares) V	Variance Ratio F	Pure Sum of Squares S'	Percent Contribution P (%)
Si	1	493.2	493.2	338.16	491.7	25.1
Mg	1	398.5	398.5	273.24	397.0	20.3
Si·Mg	1	96.6	96.6	66.21	95.1	4.9
Fe	1	315.1	315.1	216.06	313.6	16.0
Cu	1	262.0	262.0	179.67	260.6	13.3
Ni	1	123.5	123.5	84.67	122.0	6.2
Cr	1	74.0	74.0	50.74	72.5	3.7
Mn						
Ti	1	21.0	21.0	14.43	19.6	1.0
Zn						
Fe·Mn·Cr	1	23.3	23.3	15.98	21.8	1.1
Fe·Mn	1	51.1	51.1	35.04	49.6	2.5
Sr						
Cu·Zn						
Error (e)	69	100.6	1.5	1.00	115.2	5.9
Total						100.0

Modulus of Elasticity at 100°C and 200°C

Results of the pooled analysis of variance for modulus of elasticity of the alloys in Table 2.5 at 100°C and 200°C are shown in Tables 4.2.16 (a) and (b), respectively. The analysis shows that the percent contribution due to the error term at the two temperatures is quite high, about 74% and 72%, respectively. This may suggest that in the experiment, some factors that significantly affect the modulus of elasticity were inadvertently omitted. The examination of the relative difference between the highest and the lowest average modulus of elasticity for the alloys also shows that its variation is not significant (18.6% at 100°C, and 15.7% at 200°C). So, as discussed earlier for the modulus of elasticity at 25°C, the alloy's chemical composition does not significantly affect the elevated temperature modulus of elasticity.

Table 4.2.16 (a). Pooled ANOVA table for modulus of elasticity of Alloys 1 to 16 at 100°C.

Source of Variance	Degree of Freedom f	Sum of Squares S	Variance (Mean Squares) V	Variance Ratio F	Pure Sum of Squares S'	Percent Contribution P (%)
Si	1	3147311	3147311	12.8	2902281	11.1
Mg						
Si·Mg						
Fe						
Cu						
Ni						
Cr						
Mn						
Ti						
Zn						
Fe·Mn·Cr						
Fe·Mn	1	4105824	4105824	16.8	3860795	14.8
Sr						
Cu·Zn						
Error (e)	77	18867303	245029	1.0	19357363	74.1
Total						100.0

Table 4.2.16 (b). Pooled ANOVA table for modulus of elasticity Alloys 1 to 16 at 200°C.

Source of Variance	Degree of Freedom f	Sum of Squares S	Variance (Mean Squares) V	Variance Ratio F	Pure Sum of Squares S'	Percent Contribution P (%)
Si	1	3854989	3854989	17.28	3631921	14.8
Mg						
Si·Mg	1	1924665	1924665	8.63	1701597	6.9
Fe						
Cu	1	1880820	1880820	8.43	1657752	6.7
Ni						
Cr						
Mn						
Ti						
Zn						
Fe·Mn·Cr						
Fe·Mn						
Sr						
Cu·Zn						
Error (e)	76	16953174	223068	1.00	17622378	71.6
Total						100.0

4.2.4 Effect of Alloy Chemistry on Fatigue Life

An equation of the form:

$$\text{Log } N = A_o + A_1 \cdot \text{Log}(S_{max} - S_o)$$

was used to represent the mean S/N curve. The equation was first re-written in the form:

$$S_{max} = \alpha \cdot N^{\beta} + S_o, \text{ where } a = 10^{-Ao/A1} \text{ and } \beta = 1/A_1$$

And then used to calculate the maximum stress at $1x10^8$ and at $5x10^8$ cycles.

The results are shown in Table 4.2.17 (a) for Alloys 1 to 16 and in Table 4.2.17 (b) for Alloys 17 to 24. Two standard measures are commonly used to show the effectiveness of the equation in representing the measured data, one is the standard error of estimate (se), and the other is the correlation coefficient (r). Both parameters are shown in Tables 4.2.17 (a) and 4.2.17 (b). The definition and calculation of these two measures are detailed elsewhere [4]. For ease of visualization, the information is presented in chart form in Figure 4.2.20 (a) for Alloys 1 to 16 and in Figure 4.2.20 (b) for Alloys 17 to 24.

The maximum stresses at $5x10^8$ cycles shown in Tables 4.2.17 (a) and (b) range between 15 ksi, (for Alloy 1) and 23 ksi (for Alloy 10). These values compare very well with documented values for standard aluminum die casting Alloys 360 (20 ksi), A360 (18 Ksi), 380 and A380 (20 ksi), 390 and A390 (20 ksi) and 413 and A413 (19 ksi) [5].

Results of the pooled analysis of variance for fatigue life at $1x10^8$ cycles for the alloys in Table 2.5 are shown in Table 4.2.18. Table 4.2.18 indicates that, at the levels studied, the element that affects fatigue life most significantly is silicon. Its relative contribution to fatigue life variance is about 55%. Copper also has significant effects on fatigue life with a percent contribution of 19.4%. At higher levels, silicon and copper tend to increase the fatigue life of the alloy. Iron, magnesium, chromium, nickel, and strontium all have minor effects on fatigue life of aluminum die casting alloys. On the other hand, the interaction of iron with manganese and chromium is significant to fatigue life as it contributes about 7% to the variance.

The percent contribution due to the error term in this analysis is less than 3.5%. Given the nature of the die casting process, and the inevitability of incurring metallurgical defects that can escape detection, and the sensitivity of fatigue life to defects, this error is quite satisfactory.

Considering only the elements and interactions included in Table 2.2, the maximum fatigue life at $1x10^8$ cycles can be obtained from an alloy of the following composition:

Element	Si	Cu	Mn	Zn	Ti	Fe	Mg	Ni	Cr	Sr
Wt. %	12.85	4.90	0.45	2.78	0.19	0.65-1.55	0.04-0.46	0.04-0.47	0.01-0.14	0-0.02

At this composition the projected maximum stress at $1x10^8$ cycles is 23.66 ± 0.59 ksi with a confidence interval of 99.5%.

The effect of silicon on the fatigue characteristics of aluminum die casting alloys can be understood by examining Figs. 3.1.2, 3.2.2, ... 3.16.2. In general, for those alloys with relatively low silicon contents (Figs. 3.1.2, 3.2.2, ... 3.8.2), it is observed that at lower cycles to failure; i.e., lower than 10^5 cycles, an increase in cycles-to-failure is attended by a rapid drop in maximum stress. On the other hand, for those alloys with relatively high silicon contents (Figs. 3.9.2, 3.10.2, 3.11.2, 3.12.2, 3.13.2, 3.14.2, 3.15.2 and 3.16.2) the drop in maximum strength with an increase in cycles to failure is not as sharp. The alloys with lower Si contents seem to have a transition region in the range of 10^5 to 10^7 cycles in their log-normal curves, after this range the mean curves become flatter. The alloys with higher Si contents do not show such a clear transition range and the slopes of their mean curves change gradually, as shown in Figs. 3.9.2, 3.10.2, ... 3.16.2. This suggests that aluminum die casting alloys with relatively low Si contents may exhibit a transformation from plastic to elastic deformation with a decrease in maximum applied stress.

The pronounced effect of Si on fatigue life of aluminum die casting alloys may be attributed to two reasons. First, generally speaking, porosity and defects are crack initiating sites for fatigue fracture. It has been observed from microscopic examination of the fractured surfaces of the specimens that most of the failures especially high cycle failures, started at pores. At high silicon contents (about 13%) the tendency of the alloy to form scattered shrinkage porosity is low. Accordingly, the probability for a crack to initiate at a pore is low and consequently fatigue life is high. On the other hand, when the Si content of the alloy is relatively low (about 7%) the tendency of the alloy to form scattered shrinkage porosity is relatively high. Hence, the probability for a crack to initiate at a pore is also relatively high and fatigue life is comparatively low. The photograph in Figure 3.1.2 shows the fracture surface of Alloy 1 (7.15% Si content). This sample failed at a maximum stress of 16.4 ksi after $6.5x10^6$ cycles and fracture initiated at a pore. The photograph in Figure 3.10.2 shows the fracture surface of Alloy 10 (12.69% Si content). This sample failed at a maximum stress of 20.3 ksi after $6.7x10^5$ cycles and here also fracture initiated at a pore. A comparison of the microstructures of Alloys 1 to 16 shows that the pore size in the low Si content alloy is considerably larger than the pore size in the high Si content alloy. Second, the study of the effect of alloying elements on tensile properties of die casting aluminum alloys shown in Section 4.2.2 has shown that the Si content of the alloy significantly affects the alloy's yield strength and its modulus of elasticity. Alloys with relatively high Si contents (about 13% Si) have higher yield strengths and moduli of elasticity than alloys with lower Si contents (about 7% Si). This difference in strength and stiffness may contribute to the observed difference in fatigue behavior between high Si content and low Si content aluminum alloys. Those alloys with the higher Si content may deform elastically under stress while alloys with low Si content may deform plastically under a comparable stress.

Table 4.2.17 (a). Stress-life equations, standard errors of estimate (se), correlation coefficients (r) and maximum stresses for Alloys 1 to 16.

Alloy	Stress-life Relationships (Equations)	se	r	Calculated S_{max} at Fatigue Life of	
				$1x10^8$	$5x10^8$
1	$LogN=8.2727-3.5100 \cdot Log(S_{max}-14.2)$ or $S_{max}= 227.48 \cdot N^{-0.2849} + 14.2$	0.3095	-0.9674	15.40	14.96
2	$LogN=6.3829-1.7752 \cdot Log(S_{max}-19.0)$ or $S_{max}= 3939.93 \cdot N^{-0.5633} + 19.0$	0.2693	-0.9822	19.12	19.05
3	$LogN=7.3787-2.6310 \cdot Log(S_{max}-16.1)$ or $S_{max}= 637.60 \cdot N^{-0.3801} + 16.1$	0.2502	-0.9781	16.68	16.41
4	$LogN=6.7769-2.1648 \cdot Log(S_{max}-20.2)$ or $S_{max}= 1350.54 \cdot N^{-0.4619} + 20.2$	0.6187	-0.8797	20.47	20.33
5	$LogN=7.0114-2.1852 \cdot Log(S_{max}-17.2)$ or $S_{max}= 1616.29 \cdot N^{-0.4576} + 17.2$	0.6692	-0.7921	17.55	17.37
6	$LogN=7.0592-2.4820 \cdot Log(S_{max}-17.1)$ or $S_{max}= 698.47 \cdot N^{-0.4029} + 17.1$	0.5401	-0.9031	17.52	17.32
7	$LogN=7.2626-2.4171 \cdot Log(S_{max}-19.0)$ or $S_{max}= 1010.75 \cdot N^{-0.4137} + 19.0$	0.5779	-0.9091	19.50	19.25
8	$LogN=6.4875-2.0230 \cdot Log(S_{max}-19.0)$ or $S_{max}= 1610.51 \cdot N^{-0.4943} + 19.0$	0.7116	-0.8457	19.18	19.08
9	$LogN=12.3030-6.5226 \cdot Log(S_{max}-18.4)$ or $S_{max}= 76.95 \cdot N^{-0.1533} + 18.4$	0.4799	-0.9720	22.97	21.97
10	$LogN=7.7694-3.4545 \cdot Log(S_{max}-22.6)$ or $S_{max}= 177.44 \cdot N^{-0.2895} + 22.6$	0.7823	-0.8698	23.46	23.14
11	$LogN=10.3048-5.4056 \cdot Log(S_{max}-18.3)$ or $S_{max}= 80.60 \cdot N^{-0.1850} + 18.3$	0.3971	-0.9707	20.97	20.28
12	$LogN=7.5163-3.2477 \cdot Log(S_{max}-19.9)$ or $S_{max}= 206.23 \cdot N^{-0.3079} + 19.9$	0.5614	-0.9379	20.61	20.33
13	$LogN=10.2573-4.9385 \cdot Log(S_{max}-18.7)$ or $S_{max}= 119.39 \cdot N^{-0.2025} + 18.7$	0.3162	-0.9815	21.56	20.77
14	$LogN=6.9253-2.4123 \cdot Log(S_{max}-21.9)$ or $S_{max}= 742.68 \cdot N^{-0.4145} + 21.9$	0.7924	-0.8660	22.26	22.08
15	$LogN=9.3530-4.3464 \cdot Log(S_{max}-17.1)$ or $S_{max}= 141.88 \cdot N^{-0.2301} + 17.1$	0.5136	-0.9544	19.15	18.51
16	$LogN=6.9562-2.6498 \cdot Log(S_{max}-19.9)$ or $S_{max}= 422.69 \cdot N^{-0.3775} + 19.9$	0.5449	-0.9442	20.30	20.12

Table 4.2.17 (b). Stress-life equations, standard errors of estimate (se), correlation coefficients (r), and maximum stresses for Alloys 17 to 24.

Alloy	Stress-life Relationships (Equations)	se	r	Calculated S_{max} at Fatigue Life of	
				$1x10^8$	$5x10^8$
17	$LogN=7.2885-2.5974 \cdot Log(S_{max}-17.95)$ or $S_{max}= 639.82 \cdot N^{-0.3850} + 17.95$	0.3666	-0.9620	18.48	18.24
18	$LogN=8.5196-3.6030 \cdot Log(S_{max}-16.14)$ or $S_{max}= 231.49 \cdot N^{-0.2775} + 16.14$	0.5331	-0.9173	17.53	17.03
19	$LogN=7.1801-2.4872 \cdot Log(S_{max}-17.95)$ or $S_{max}= 770.67 \cdot N^{-0.4021} + 17.95$	0.4483	-0.9431	18.42	18.20
20	$LogN=10.4598-4.9707 \cdot Log(S_{max}-14.82)$ or $S_{max}= 126.40 \cdot N^{-0.2009} + 14.82$	0.6590	-0.8848	17.94	17.07
21	$LogN=7.8377-3.2594 \cdot Log(S_{max}-19.53)$ or $S_{max}= 253.90 \cdot N^{-0.3068} + 19.53$	0.5056	-0.9497	20.42	20.07
22	$LogN=7.5496-2.7433 \cdot Log(S_{max}-21.72)$ or $S_{max}= 564.97 \cdot N^{-0.3645} + 21.72$	0.8862	-0.7659	22.41	22.10
23	$LogN=7.4442-2.6682 \cdot Log(S_{max}-19.43)$ or $S_{max}= 616.53 \cdot N^{-0.3748} + 19.43$	0.5394	-0.9173	20.05	19.77
24	$LogN= 8.0684-3.1791 \cdot Log(S_{max}-20.46)$ or $S_{max}= 345.14 \cdot N^{-0.3146} + 20.46$	0.5166	-0.9388	21.51	21.09

Fig. 4.2.20 (a). Fatigue life–the maximum stress at 5 x 10^8 cycles of Alloys 1-16.

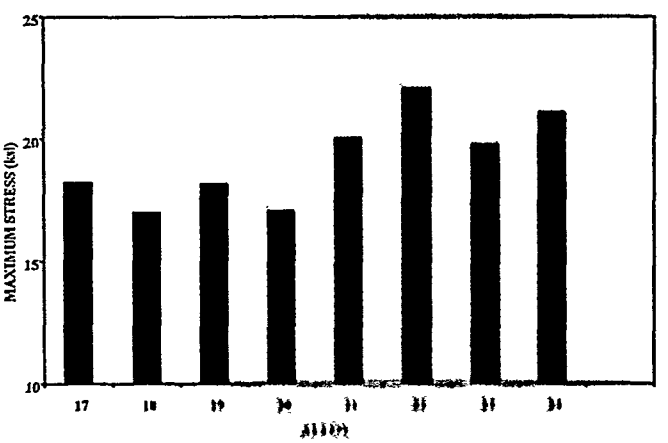

Fig. 4.2.20 (b). Fatigue life-the maximum stress of 5 x 10^8 cycles of Alloys 17-24

Table 4.2.18. Pooled ANOVA for fatigue life of Alloys 1 to 16–maximum stress for cycles-to-failure is 5 x 10^3 Cycles.

Source of Variance	Degree of Freedom (f)	Sum of Squares (S)	Variance (Mean Squares) (V)	Variance Ratio (F)	Pure Sum of Squares (S')	Percent Contribution P (%)
Si	1	41.8	41.8	238.9	41.62	54.74
Mg	Pooled					
Si·Mg	1	2.907	2.907	16.62	2.732	3.59
Fe	Pooled					
Cu	1	14.94	14.94	85.39	14.76	19.42
Ni	Pooled					
Cr	Pooled					
Mn	1	5.221	5.221	29.84	5.046	6.64
Ti	1	1.677	1.677	9.586	1.502	1.98
Zn	1	2.356	2.356	13.47	2.181	2.87
Fe·Mn·Cr	1	5.736	5.736	32.79	5.561	7.31
Fe·Mn	Pooled					
Sr	Pooled					
Cu·Zn	Pooled					
Error (e)	8	1.4	0.175	1	2.624	3.45
Total	15	76.03				100.00

4.2.5 Effect of Alloy Chemistry on Impact Resistance

Tables 4.2.19 (a) and (b) present the average absorbed energies for the twenty-four alloys presented in Tables 2.5 and 2.6, respectively. For ease of visualization, the same information is presented in chart form in Figures 4.2.21(a) and (b). Tables 4.2.19 (a) and (b) also show the standard deviation and the coefficient of variance for each of the measured properties.

Results of the pooled analysis of variance for Charpy impact resistance for the alloys in Table 2.5 are shown in Table 4.2.20. Table 4.2.20 shows that, at the levels studied, the element that affects the variation in impact resistance most significantly is Cu. Its relative contribution to the variation of the absorbed energy is about 25%. Fe, Si, and Mg also have significant effects contributing about 19%, 18%, and 11% to the variance, respectively. Other elements that have an effect on impact resistance are, in the order of decreasing effect, Ni, Cr, and Zn. The interaction of Si with Mg also has some effect contributing 5.9% to the variance in impact strength. At higher levels, all these elements, except Zn, reduce the impact resistance. Zn at its higher level has a slight positive effect on impact resistance. The percent contribution due to the error term in this analysis is 5.7%, which is quite acceptable.

Considering only the elements and interactions in Table 2.2, the maximum impact resistance would result from an alloy with the following composition:

Element	Si	Cu	Mn	Zn	Ti	Fe	Mg	Ni	Cr	Sn
Wt. %	6.96	1.21	0.01-0.45	2.78	0.01-0.19	0.65	0.04	0.04	0.01	0.00

At this composition the projected maximum absorbed energy is 6.23 ± 0.12 lbf-ft with a confidence interval of 99.5%.

The variation in impact resistance with alloy chemistry follows almost the same trend as the variation in elongation. Generally the less the total amount of added elements, the greater the impact resistance. Among the sixteen alloys in Table 2.5, Alloy 2 has the highest impact resistance with an absorbed energy of 6.43 lbf-ft. Alloy 14 has the lowest impact resistance with an absorbed energy of 1.26 lbf-ft. Figures 3.2.5 to 3.2.8 show the microstructure of Alloy 2, and Figures 3.14.5 to 3.14.8 show the microstructure of Alloy 14. Figure 4.2.22 shows the fracture surfaces of Alloys 2 and 14 at low magnification. Figures 4.2.23 (a) and (b) show the fracture surfaces of Alloys 2 and 14. It is clear that Alloy 2 underwent a ductile fracture as evidence by its fibrous structure. On the other hand, Alloy 14 underwent a brittle fracture. There is no detectable deformation around the fracture area and the fracture surface is mainly cellular structure consisting of facets of various sizes.

Table 4.2.19 (a). Summary of average absorbed energies in the Charpy Impact Test for Alloys 1 to 16.

Alloy		1	2	3	4	5	6	7	8
Absorbed Energy	lbf-ft	5.04	6.48	1.68	1.79	3.13	2.42	1.29	1.65
St. dev.**	lbt-ft	0.43	0.57	0.26	0.24	0.36	0.29	0.20	0.19
C.V.**	%	8.5	8.8	15.2	13.1	11.5	11.9	15.6	11.6
Alloy		**9**	**10**	**11**	**12**	**13**	**14**	**15**	**16**
Absorbed Energy	lbf-ft	1.95	1.83	1.64	2.03	1.47	1.26	1.65	1.97
St. dev.*	lbf-ft	0.13	0.24	0.16	0.19	0.18	0.13	0.26	0.16
C.V.**	%	6.6	12.9	9.6	9.5	12.2	10.2	15.5	8.3

***St. dev. - Standard deviation **C.V. - Coefficient of Variation (= St. dev./Mean 100%)**

Table 4.2.19 (b). Summary of average absorbed energies in the Charpy Impact Test for Alloys 17 to 24.

Alloy		17	18	19	20	21	22	23	24
Absorbed Energy	lbf-ft	3.70	2.47	3.18	1.79	2.68	2.47	2.53	2.01
St. dev.**	lbt-ft	0.29	0.37	0.19	0.22	0.20	0.27	0.30	0.21
C.V.**	%	7.8	15.0	6.0	12.3	7.5	10.9	11.9	11.1

Table 4.2.20. Pooled ANOVA table for impact resistance of Alloys 1 to 16.

Source of Variance	Degree of Freedom f	Sum of Squares S	Variance (Mean Squares) V	Variance Ratio F	Pure Sum of Squares S'	Percent Contribution P
Si	1	217.5	217.5	1779.2	217.4	18.01%
Mg	1	137.0	137.0	1120.2	136.8	11.34%
Si·Mg	1	71.4	71.4	583.8	71.3	5.90%
Fe	1	227.1	227.1	1857.5	227.0	18.80%
Cu	1	301.3	301.3	2464.1	301.1	24.95%
Ni	1	99.6	99.6	814.5	99.5	8.24%
Cr	1	49.0	49.0	400.5	48.8	4.05%
Mn	Pooled					
Ti	Pooled					
Zn	1	12.2	12.2	99.5	12.0	1.00%
Fe·Mn·Cr	1	9.3	9.3	75.7	9.1	0.76%
Fe·Mn	Pooled					
Sr	Pooled					
Cu·Zn	1	15.7	15.7	128.5	15.6	1.29%
Error (e)	549	67.1	0.1223	1.00	68.3	5.66%
Total	559	1207.0				100%

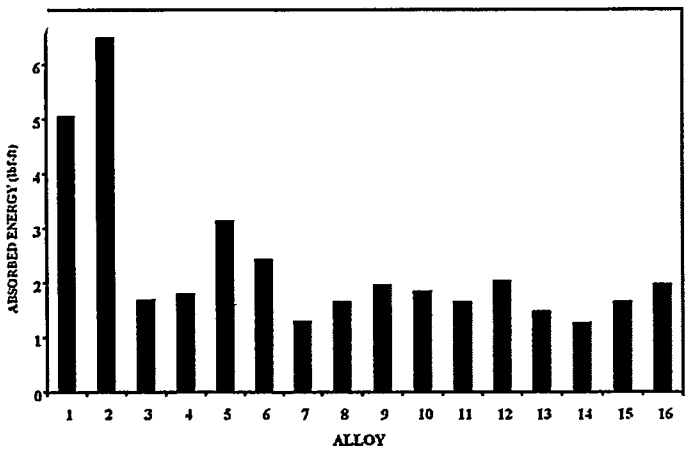

Fig. 4.2.21 (a). Absorbed energy of Alloys 1 to 16 in Charpy Impact test.

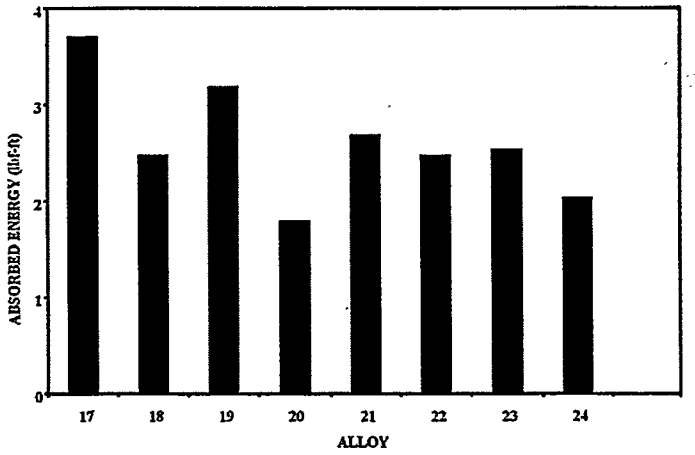

Fig. 4.2.21 (b). Absorbed energy of Alloys 17 to 24 in Charpy Impact test.

4.2.6 Effect of Alloy Chemistry on Wear Resistance

Tables 4.2.21 (a) and (b) present the average volume loss measured in the dry sand abrasive test for the twenty-four alloys presented in Tables 2.5 and 2.6. For ease of visualization, the same information is presented in chart form in Figures 4.2.24 (a) and (b). Tables 4.2.21 (a) and (b) also show the standard deviation and the coefficient of variance for each of the measured properties.

Results of the pooled analysis of variance for wear resistance measured in Dry Sand Abrasive Test for the alloys in Table 2.5 are shown in Table 4.2.22. Table 4.2.22 shows that, at the levels studied, the element that affects the variation in wear resistance most significantly is Mg. Its relative contribution to the variation in volume loss is about 47%. Si has a significant effect contributing about 14% to the variance. Fe also has some effect contributing about 6% to the variance. At higher levels, Mg, Fe, and Cr decrease the dry abrasive wear resistance, while Si increases the dry abrasive wear resistance. The effects of all the other elements are negligible. The percent contribution due to the error term in this analysis is 26%, which is acceptable given the nature of abrasive wear testing.

Considering only the elements and interactions included in Table 2.2, the maximum dry sand abrasive wear resistance can be obtained from an alloy of the following composition:

Element	Si	Cu	Mn	Zn	Ti	Fe	Mg	Ni	Cr	Sr
Wt. %	12.85	1.21-4.90	0.01-0.45	0.45-2.78	0.01-0.19	0.65	0.04	0.04-0.47	0.01	0-0.02

At this composition the projected minimum volume loss is 0.3712 ± 0.0132 cm³ with a confidence interval of 95%.

Table 4.2.21 (a). Summary of average volume loss in the dry sand abrasive test for Alloys 1 to 16.

Alloy		1	2	3	4	5	6	7	8
Volume loss	cm³	0.3883	0.4187	0.4527	0.4333	0.5256	0.4730	0.5289	0.5076
St. dev.*	cm³	0.0220	0.0288	0.0370	0.0322	0.0312	0.0171	0.0204	0.0373
C.V.**	%	5.7	6.9	8.2	7.4	5.9	3.6	3.9	7.3
Alloy		**9**	**10**	**11**	**12**	**13**	**14**	**15**	**16**
Volume loss	cm³	0.3974	0.3979	0.4190	0.3833	0.4291	0.4383	0.4683	0.4871
St. dev.*	cm³	0.0079	0.0159	0.0252	0.0119	0.0313	0.0263	0.0185	0.0210
C.V.**	%	2.0	4.0	6.0	3.1	7.3	6.0	4.0	4.3

***St. dev. - Standard deviation **C.V. - Coefficient of Variation (=St. dev./Mean 100%)**

Table 4.2.21 (b). Summary of average volume loss in the dry sand abrasive test for Alloys 17 to 24.

Alloy		17	18	19	20	21	22	23	24
Volume loss	cm³	0.4150	0.4375	0.4213	0.4516	0.4457	0.4307	0.4086	0.3992
St. dev.*	cm³	0.0330	0.0274	0.0253	0.0298	0.0301	0.0285	0.0326	0.0323
C.V.**	%	8.0	6.3	6.0	6.6	6.8	6.6	8.0	8.1

Table 4.2.22. Pooled ANOVA table for wear resistance of Alloys 1 to 16.

Source of Variance	Degree of Freedom f	Sum of Squares S	Variance (Mean Squares) V	Variance Ratio F	Pure Sum of Squares S'	Percent Contribution P
Si	1	0.0296	0.0296	42.58	0.0289	13.7
Mg	1	0.1006	0.1006	144.75	0.0999	47.4
Si-Mg	1	0.0043	0.0043	6.15	0.0036	1.7
Fe	1	0.0140	0.0140	20.17	0.0133	6.3
Cu						
Ni						
Cr	1	0.0047	0.0047	6.70	0.0040	1.9
Mn						
Ti						
Zn						
Fe-Mn-Cr	1	0.0068	0.0068	9.81	0.0061	2.9
Fe-Mn						
Sr						
Cu-Zn						
Error (e)	73	0.0507	0.0007	1	0.0549	26.1
Total	79	0.2107				100.0

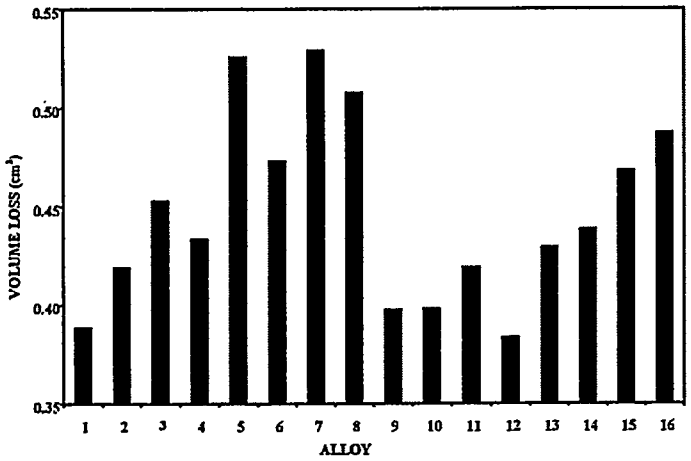

Fig. 4.2.24 (a). Volume loss from Alloys 1 to 16 in the dry sand abrasive test.

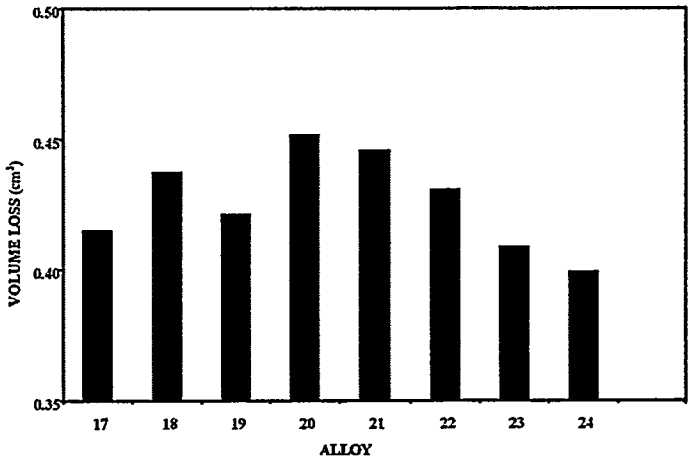

Fig. 4.2.24 (b). Volume loss from Alloys 17 to 24 in the dry sand abrasive test.

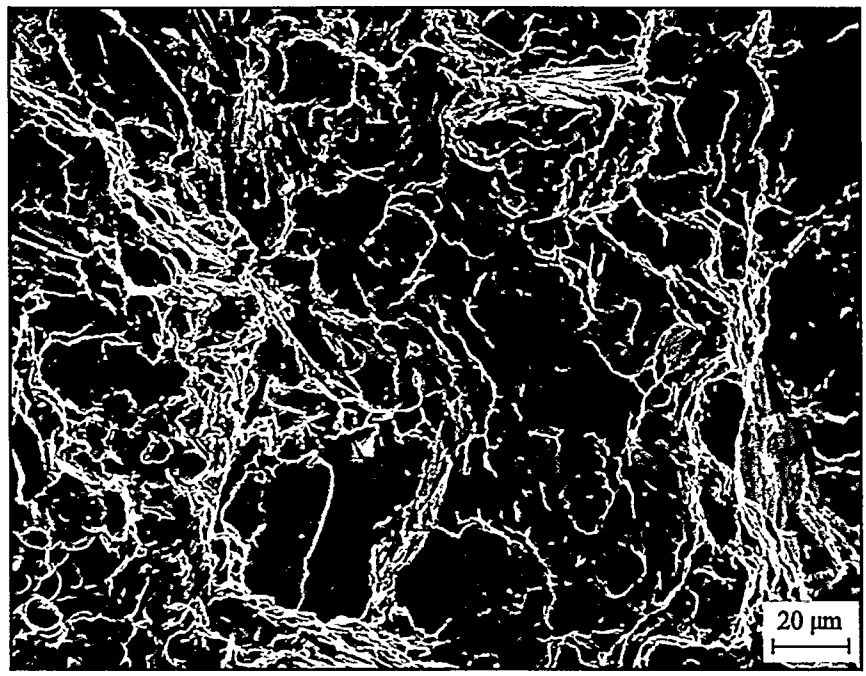

ig. 4.2.9 (a). Alloy 7 (6.92%Si, 0.50%Mg, 1.63%Fe, 4.94%Cu, .03%Ni, 0.01%Cr, 0.02%Mn, 0.01%Ti, 2.73%Zn and 0.022%Sr).

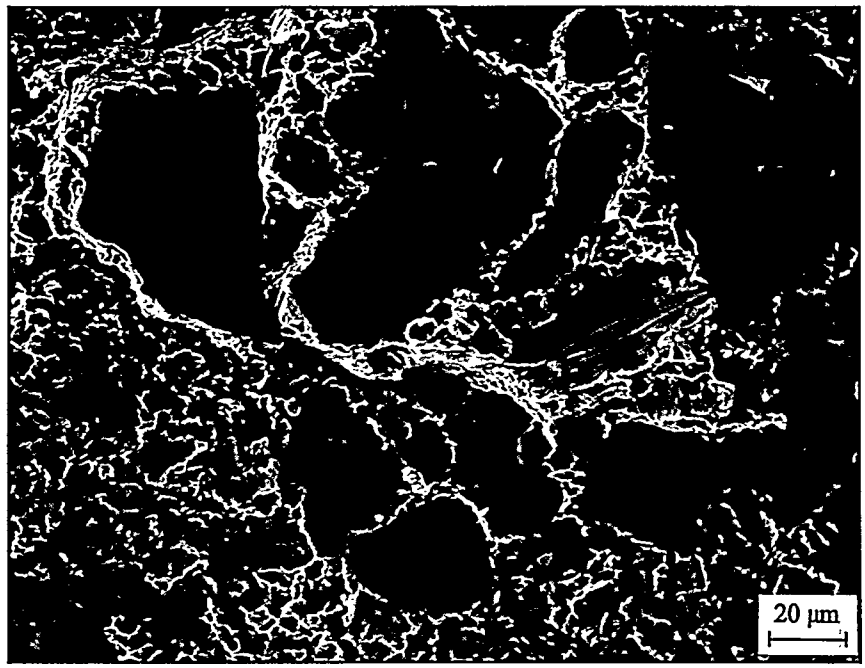

ig. 4.2.9 (b). Alloy 11 (12.86%Si, 0.04%Mg, 1.59%Fe, 1.21%Cu, .45%Ni, 0.01%Cr, 0.01%Mn, 0.18%Ti, 0.49%Zn and 0.00%Sr). The nicrographs shown are of fracture surfaces of tensile test speci- nens tested at room temperature.

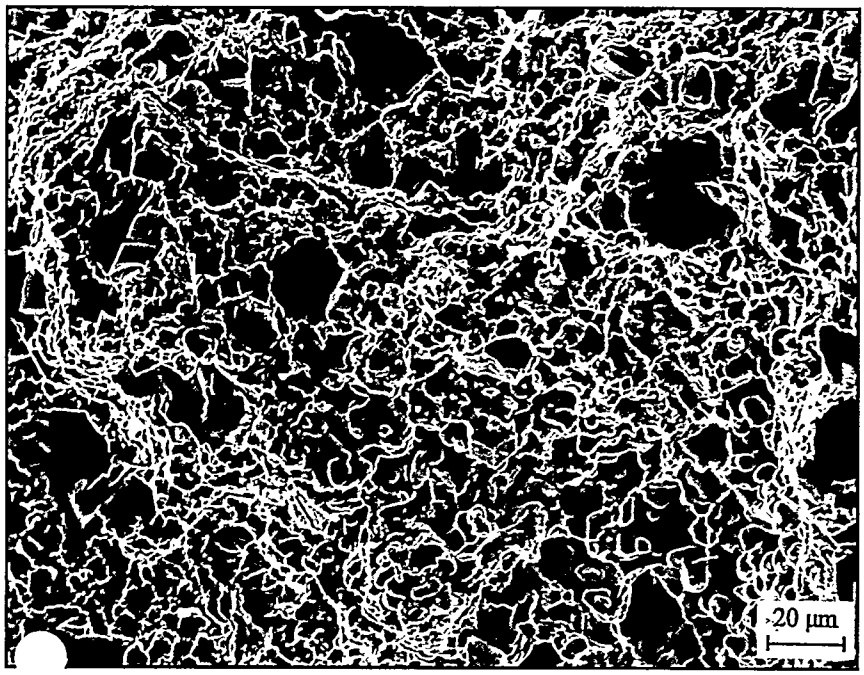

Fig. 4.2.10 (a). Alloy 14 (12.94%Si, 0.48%Mg, 0.74%Fe, 4.77%Cu, 0.50%Ni, 0.01%Cr, 0.57%Mn, 0.01%Ti, 0.55%Zn and 0.00%Sr).

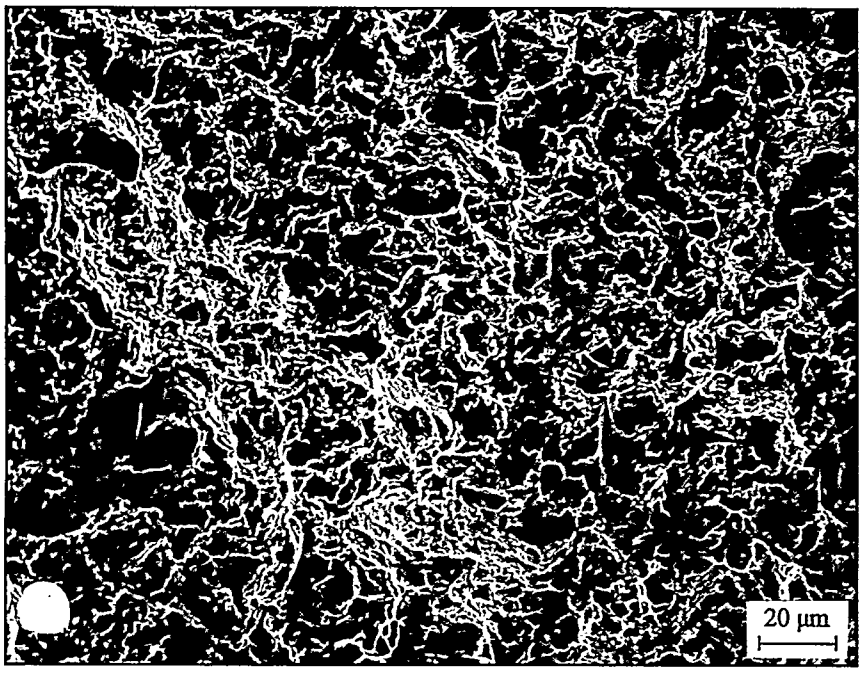

Fig. 4.2.10 (b). Alloy 1 (7.15%Si, 0.03%Mg, 0.68%Fe, 1.24%Cu, 0.01%Ni, 0.01%Cr, 0.01%Mn, 0.01%Ti, 0.44%Zn and 0.00%Sr). The micrographs shown are of fracture surfaces of tensile test specimens tested at room temperature.

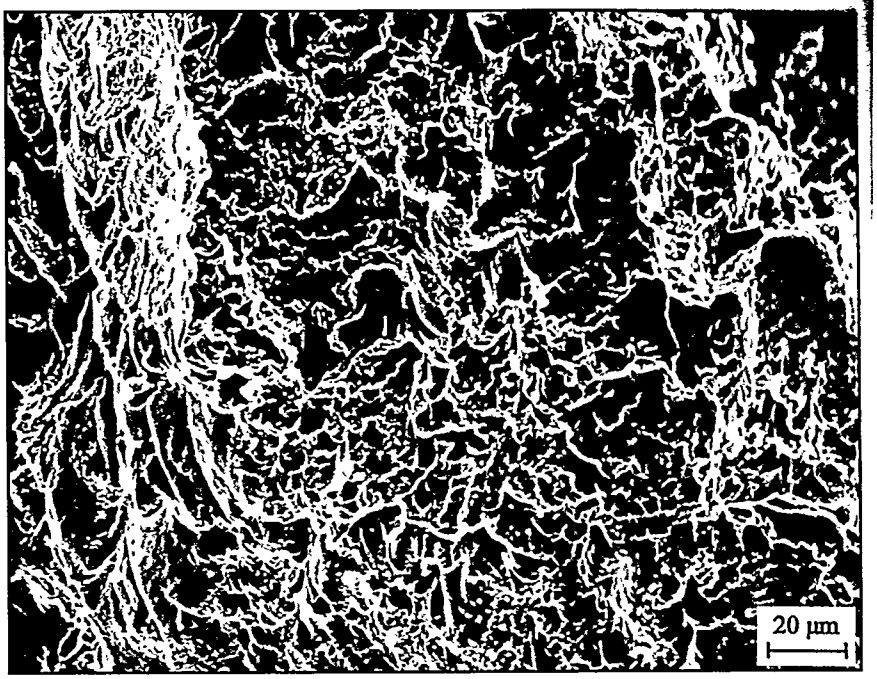

Fig. 4.2.11. Fracture surface of tensile test specimen tested at room temperature. Alloy 2 (6.99%Si, 0.01%Mg, 0.56%Fe, 1.15%Cu, 0.01%Ni, 0.01%Cr, 0.47%Mn, 0.24%Ti, 2.87%Zn and 0.018%Sr).

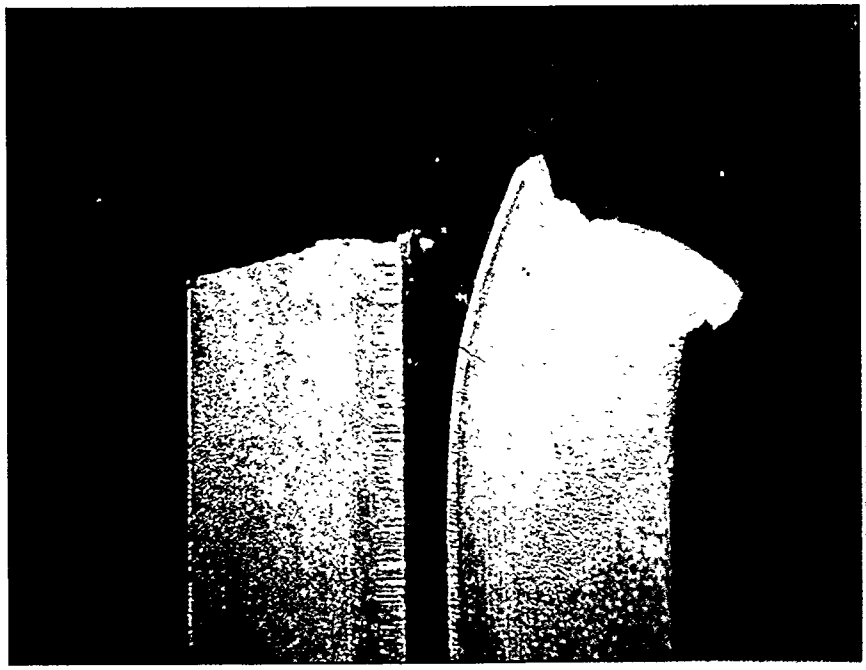

Fig. 4.2.22. Fractured impact test specimens tested at room temperature. Left: Alloy 14 (12.94%Si, 0.48%Mg, 0.74%Fe, 4.77%Cu, 0.50%Ni, 0.01%Cr, 0.57%Mn, 0.01%Ti, 0.55%Zn and 0.00%Sr). Right: Alloy 2 (6.99%Si, 0.01%Mg, 0.56%Fe, 1.15%Cu, 0.01%Ni, 0.01%Cr, 0.47%Mn, 0.24%Ti, 2.87%Zn and 0.018%Sr).

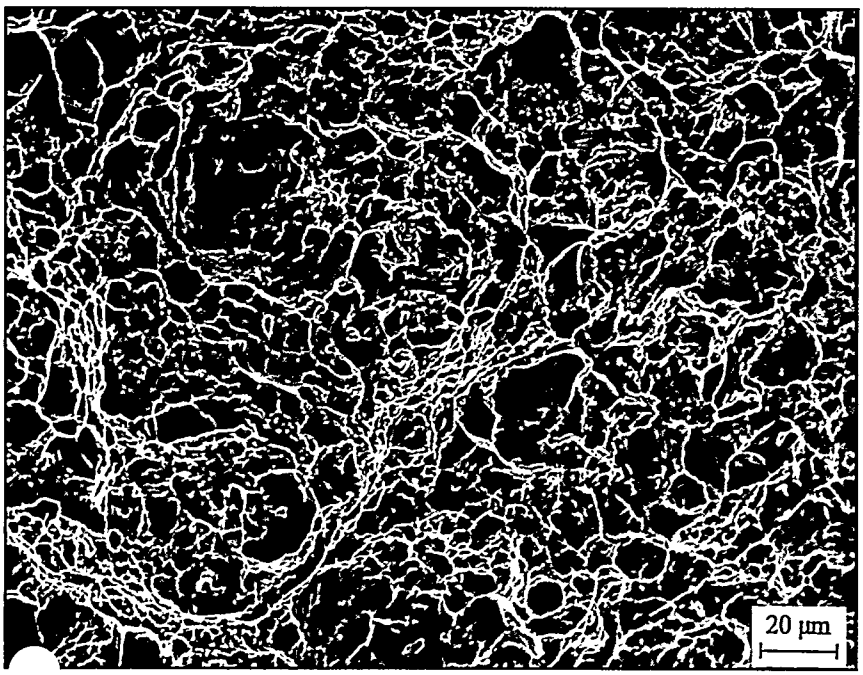

Fig. 4.2.23 (a). Alloy 2 (6.99%Si, 0.01%Mg, 0.56%Fe, 1.15%Cu, 0.01%Ni, 0.01%Cr, 0.47%Mn, 0.24%Ti, 2.87%Zn and 0.018%Sr).

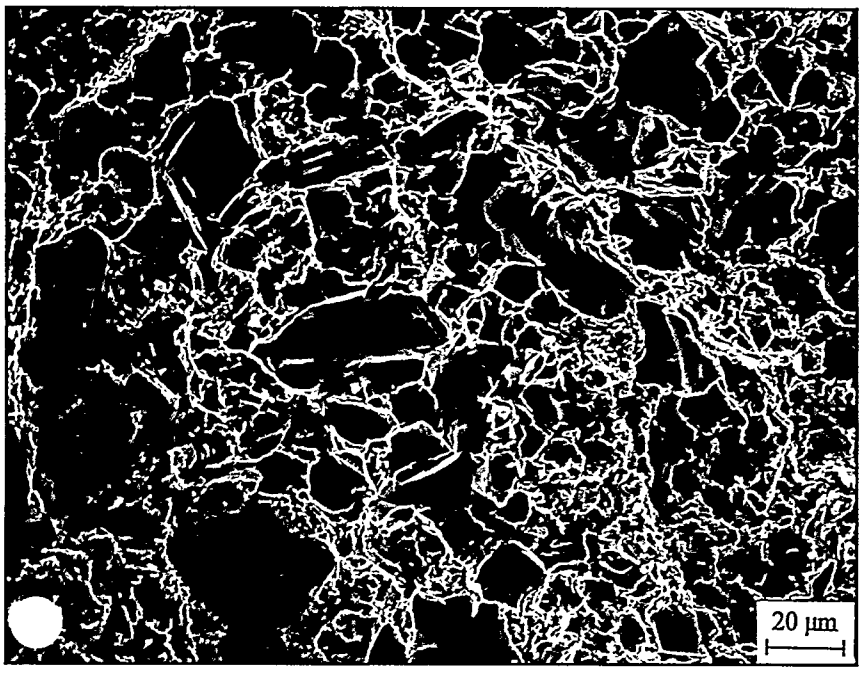

Fig. 4.2.23 (b). Alloy 14 (12.94%Si, 0.48%Mg, 0.74%Fe, 4.77%Cu, 0.50%Ni, 0.01%Cr, 0.57%Mn, 0.01%Ti, 0.55%Zn and 0.00%Sr). The micrographs shown are of fracture surfaces of impact test specimens tested at room temperature.

4.2.7 Effect of Alloy Chemistry on Hardness

Tests show that the hardness of die cast specimens increase with time. Generally speaking, the hardness increases rapidly during the first three days after casting, and then it slows down. Fig. 4.2.23 shows the change in the hardness of Alloys 1 and 14 during the first month after they were die cast. The data is obtained from specimens with a 0.25"x0.25" square cross section. The average hardness of the sixteen alloys shown in Table 2.5 as measured on the square specimens increased by about 6.5% during the first three days after casting. It is interesting to note that hardness measurements taken after six months from die-casting showed a slight increase over measurements taken one month after die casting.

Tables 4.2.23 (a) and (b) present the average hardness (RHB) for the twenty-five alloys shown in Tables 2.5 and 2.6 one month after they were die-cast. Tables 4.2.23 (a) and (b) show three groups of data representing hardness values for specimens with different shapes and dimensions. The data confirm the fact that castings that solidify at a relatively high cooling rate (specimens with 0.25"x0.25" square cross section) are, in general, harder than specimens that solidify at a lower cooling rate (specimens with 3/8" and 5/8" diameters). For ease of visualization the hardness variation with alloy composition for specimens with 0.25"x0.25" square cross section is presented in chart form in Figs. 4.2.25 (a) and (b).

Results of the pooled analysis of variance for hardness of the alloys in Table 2.5 are shown in Table 4.2.24. The data analyzed was measured from the 0.25" x 0.25" square cross section die cast specimens. The analysis indicates that, at the levels studied, the element that affects hardness most significantly is copper. Its relative contribution to hardness variance is about 34%. Also silicon has a significant effect on hardness with a percent contribution to the variance of about 29%. Mg, Fe, Cr, Ni, and Ti follow silicon, in decreasing order. At higher levels, all these elements tend to increase the hardness of the alloy. Interactions of Si with Mg and Fe with Mn also have some influence on hardness. The percent contribution due to the error term to this analysis is less than 1.8%, which is very acceptable.

Considering only the elements and interactions included in Table 2.2, the maximum hardness can be obtained from an alloy of the following composition:

Element	Si	Cu	Mn	Zn	Ti	Fe	Mg	Ni	Cr	Sr
Wt. %	12.85	4.90	0.01	0.46-2.87	0.19	1.55	0.46	0.47	0.14	0-0.02

At this composition the projected highest hardness is 87.7 ± 0.7 RHB with a confidence interval of 95%.

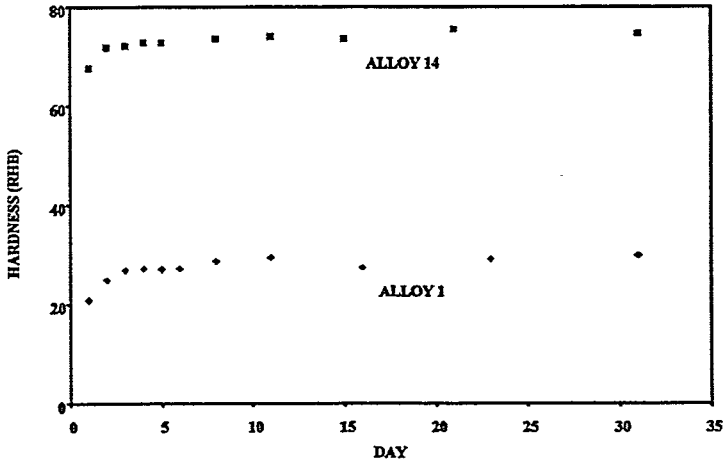

Fig. 4.2.23. Variations in hardness (RHB) with time for Alloys 1 and 14.

Table 4.2.23 (a). Summary of average hardness (RHB) for Alloys 1 to 16.

Specimen size	Alloy							
	1	2	3	4	5	6	7	8
1/4" x 1/4" flat die casting	29.9 ± 2.1	33.8 ± 2.1	60.9 ± 1.3	60.4 ± 1.3	51.0 ± 1.2	58.2 ± 1.3	71.9 ± 0.8	67.0 ± 0.7
3/8" diameter die casting	16.9 ± 3.7	22.5 ± 2.1	53.7 ± 2.9	52.7 ± 1.5	38.9 ± 1.3	47.9 ± 1.9	64.9 ± 3.2	58.9 ± 1.8
5/8" diameter die casting	19.8 ± 1.6	21.2 ± 2.1	54.1 ± 1.2	56.0 ± 0.8	46.8 ± 1.5	46.6 ± 2.2	64.3 ± 2.1	57.8 ± 1.4
Specimen size	**Alloy**							
	9	10	11	12	13	14	15	16
1/4" x 1/4" flat die casting	70.8 ± 2.0	69.5 ± 1.7	63.7 ± 1.2	58.8 ± 1.7	72.3 ± 0.7	74.6 ± 1.5	70.4 ± 1.6	63.1 ± 1.0
3/8" diameter casting	60.9 ± 2.8	63.2 ± 1.4	55.1 ± 2.3	50.0 ± 1.1	63.5 ± 1.3	66.9 ± 1.7	61.4 ± 2.6	52.8 ± 1.1
5/8" diameter die casting	60.3 ± 1.8	61.3 ± 1.7	53.7 ± 2.1	47.6 ± 1.6	64.3 ± 1.7	66.5 ± 2.3	60.7 ± 1.5	50.7 ± 1.1

Table 4.2.23 (b). Summary of average hardness (RHB) for Alloys 17 to 24.

Specimen size	Alloy							
	17	18	19	20	21	22	23	24
1/4" x 1/4" flat die casting	47.4 ± 1.0	54.9 ± 0.9	50.9 ± 1.3	64.4 ± 1.0	56.5 ± 0.9	60.8 ± 1.2	58.8 ± 1.2	67.7 ± 0.9
3/8" diameter die casting	39.9 ± 1.4	45.4 ± 1.5	43.0 ± 1.3	57.6 ± 1.4	49.1 ± 1.1	55.0 ± 1.2	50.6 ± 1.7	61.1 ± 1.1
5/8" diameter die casting	37.3 ± 2.1	45.3 ± 1.3	41.0 ± 1.7	57.0 ± 1.3	48.0 ± 1.4	52.8 ± 1.4	49.9 ± 1.9	59.1 ± 1.8

Table 4.2.24. Pooled ANOVA table for hardness (RHB) measurement of Alloys 1 to 16.

Source of Variance	Degree of Freedom f	Sum of Squares S	Variance (Mean Squares) V	Variance Ratio F	Pure Sum of Squares S'	Percent Contribution P
Si	1	7570.8	7570.8	2558.1	7567.8	29.2
Mg	1	4086.5	4086.5	1380.8	4083.5	15.8
Si·Mg	1	1293.9	1293.9	437.2	1290.9	5.0
Fe	1	1964.2	1964.2	663.7	1961.2	7.6
Cu	1	8800.1	8800.1	2973.5	8797.2	34.0
Ni	1	348.7	348.7	117.8	345.7	1.3
Cr	1	650.4	650.4	219.8	647.5	2.5
Mn						
Ti	1	180.6	180.6	61.0	177.7	0.7
Zn						
Fe·Mn·Cr						
Fe·Mn	1	555.0	555.0	187.5	552.1	2.1
Sr						
Cu·Zn						
Error (e)	150	443.9	2.9595	1.0	470.6	1.8
Total	159	25894.2				100.0

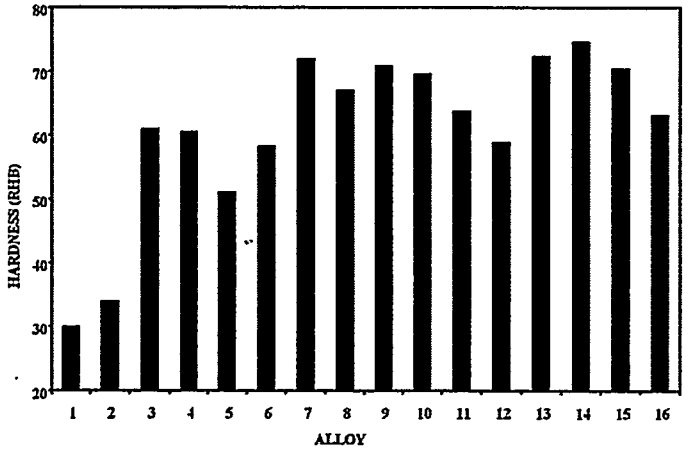

Fig. 4.2.25 (a). hardness (RHB) of Alloys 1 to 16 measured on 1/4" X 1/4" flat die cast specimen.

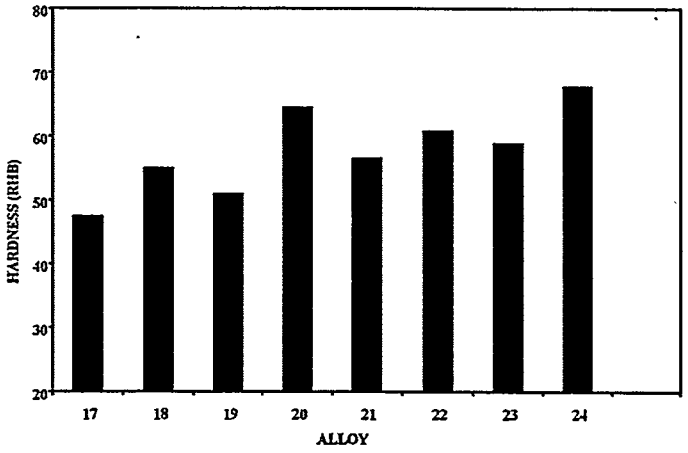

Fig. 4.2.25 (b). Hardness (RHB) of Alloys 17 to 24 measured on 1/4" x 1/4" flat die cast specimen.

4.2.8 Effect of Alloy Chemistry on Thermal Conductivity

The measured thermal conductivity of the alloys in Table 2.5 is shown in Tables 4.2.25 (a) and (b). For ease of visualization, the same information is presented in chart form in Figures 4.2.26 (a) and (b).

Results of the pooled analysis of variance for thermal conductivity of the alloys in Table 2.5 are shown in Table 4.2.26. Table 4.2.26 shows that, at the levels studied, the element that affects thermal conductivity most significantly is titanium. Its relative contribution to the variance in thermal conductivity is about 23%. Silicon, iron, copper, and zinc also have significant effects, contributing to the variance in thermal conductivity about 20%, 18%, 14%, and 9%, respectively. Mg and Cr have minor effects and the interaction of Fe×Mn has some effect. As expected, all element additions decrease the thermal conductivity, but to varying degrees, except Cr. The results showed that Cr, at higher level, slightly increased the thermal conductivity, contributing about 0.3% to the variance. The percent contribution due to the error term in this analysis is small, about 4.6%, which shows that the design of the experiment and the performance of the thermal conductivity measurements were adequate.

Considering only the elements in Table 2.2 and their interactions, the maximum room temperature thermal conductivity can be obtained from an alloy with the following composition:

Element	Si	Cu	Mn	Zn	Ti	Fe	Mg	Ni	Cr	Sr
Wt. %	6.96	1.21	0.01	0.46	0.01	0.65	0.04	0.04-0.47	0.14	0-0.002

At this composition the projected room temperature thermal conductivity is 136.3 ± 1.6 W/m.K at a confidence level of 95%. It is also useful to note that, considering only the elements in Table 2.2 and their interactions, the minimum room temperature thermal conductivity (i.e., maximum room temperature thermal resistivity) can be obtained from an alloy with the following composition:

Element	Si	Cu	Mn	Zn	Ti	Fe	Mg	Ni	Cr	Sr
Wt. %	12.85	4.90	0.01	2.87	0.19	1.55	0.46	0.04-0.47	0.01	0-0.02

At this composition the projected room temperature thermal conductivity is 89.3 ± 1.6 W/m.K at a confidence level of 95%.

Among the sixteen alloys in Table 2.5, Alloy 1 has the highest room temperature thermal conductivity (137.1 ± 1.0 W/m.K), and Alloy 15 has the lowest room temperature thermal conductivity (99.9 ± 2.2 W/m.K). Figures 4.1.1 (a) and (b) and 4.1.3 (a) and (b) show the grain structures and Figures 3.1.5 to 3.1.8 and 3.15.5 to 3.15.8 show the microstructures of Alloy 1 and Alloy 15, respectively. Comparison of these figures shows that Alloy 1 has considerably larger grain size (and therefore less grain boundary area) than Alloy 15, while Alloy 15 has much more Al-Si eutectic structure and intermetallic compounds in the interdendritic areas than Alloy 1. Since grain boundaries, intermetallics, and the complex eutectic structure all contribute to wave scattering, it is understandable that Alloy 15 has considerably lower thermal conductivity than Alloy 1.

Among the elements, titanium has the most significant effect on thermal conductivity, followed by silicon, iron, copper, and zinc. Addition of titanium refines the structure and reduces the grain size of the alloy and thus increases the grain boundary area. The amount of silicon is directly related to the fraction of the eutectic structure and the numbers of the primary silicon particles and thus the interfacial areas. Fe bearing phase can be in different morphologies in the alloys. The needle phase has the largest surface:volume ratio and therefor it has the largest interfacial area with the alloy matrix, and consequently it affects thermal conductivity more than the other morphologies. Mn and Cr additions can transform the Fe-rich needles to Chinese script or polyhedral crystals, and so, the Fe×Mn interaction plays a role in affecting the thermal conductivity. The lowest thermal conductivity should be obtained at higher level of Fe and lower level of Mn, but not both at higher levels. However, a high thermal conductivity was not obtained at the lower level of Fe and higher level of Mn. This is probably because the excess Mn goes into solid solution with aluminum and counteracts any beneficial effect that Mn may have on thermal conductivity.

Table 4.2.25 (a). Summary of average thermal conductivity for Alloys 1 to 16.

Alloy		1	2	3	4	5	6	7	8
Thermal Conductivity	W/m·K	137.1	115.5	117.1	108.4	126.0	119.9	105.6	108.6
St.dev.*	W/m·K	1.0	1.1	0.6	0.8	1.0	2.4	0.4	1.4
C.V.**	%	0.7	1.0	0.5	0.8	0.8	2.0	0.4	1.3
Alloy		**9**	**10**	**11**	**12**	**13**	**14**	**15**	**16**
Thermal Conductivity	W/m·K	111.7	110.6	103.2	115.5	102.2	113.0	99.9	116.1
St.dev.*	W/m·K	0.4	1.3	4.3	1.4	0.8	0.2	2.2	1.1
C.V.**	%	0.4	1.2	4.2	1.2	0.7	0.2	2.2	0.9

St. dev. - Standard deviation **CV - Coefficient of Variation (= St. dev./Mean 100%)

Table 4.2.25 (b). Summary of average thermal conductivity for Alloys 17 to 24.

Alloy		17	18	19	20	21	22	23	24
Thermal Conductivity	W/m-K	122.1	119.1	121.0	111.0	113.8	119.2	113.8	111.6
St. dev.**	W/m-K	1.0	1.8	0.4	0.4	2.6	0.7	2.5	1.5
C.V.**	%	0.8	1.5	0.3	0.4	2.2	0.6	2.2	1.3

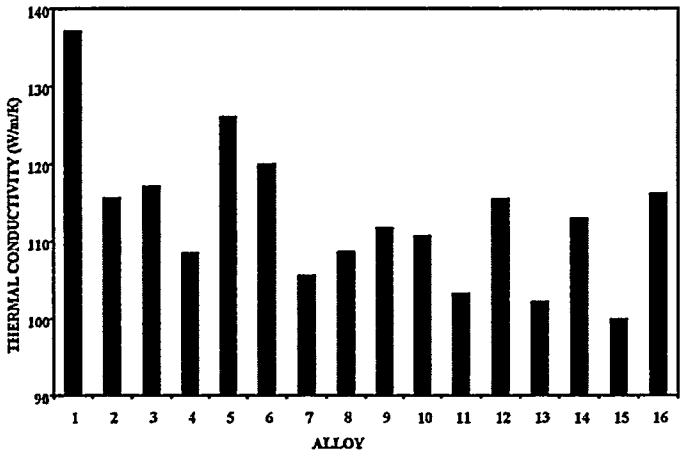

Fig. 4.2.26 (a). Thermal conductivity for Alloys 1 to 16.

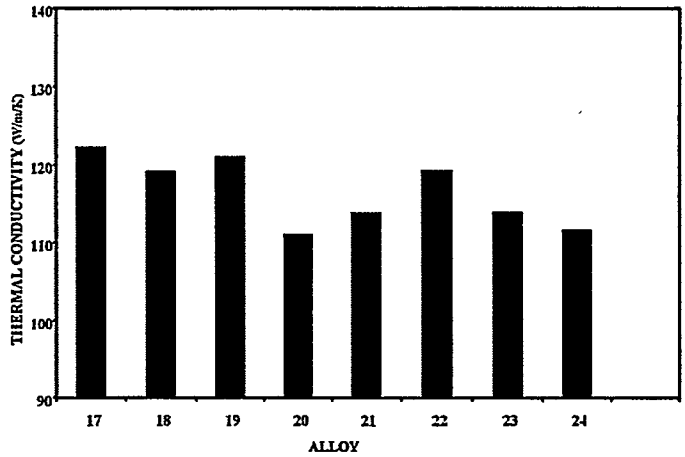

Fig. 4.2.26 (b). Thermal conductivity of Alloys 17 to 24.

Table 4.2.26. Pooled ANOVA table for thermal conductivity measurement of Alloys 1 to 16.

Source of Variance	Degree of Freedom f	Sum of Squares S	Variance (Mean Squares) V	Variance Ratio F	Pure Sum of Squares S'	Percent Contribution P
Si	1	1634.7	1634.7	408.4	1630.7	20.0
Mg	1	292.9	292.9	73.2	288.9	3.6
Si·Mg						
Fe	1	1426.6	1426.6	356.4	1422.5	17.5
Cu	1	1176.7	1176.7	294.0	1172.7	14.4
Ni						
Cr	1	31.5	31.5	7.9	27.5	0.3
Mn						
Ti	1	1909.2	1909.2	477.0	1905.2	23.4
Zn	1	694.0	694.0	173.4	690.0	8.5
Fe·Mn·Cr						
Fe·Mn	1	623.0	623.0	155.6	619.0	7.6
Sr						
Cu·Zn						
Error (e)	87	348.2	4.0028	1.0	376.3	4.6
Total	95	8136.9				100.0

4.2.9 Effect of Alloy Chemistry on Electrical Conductivity

The measured electrical conductivity of the alloys in Table 2.5 is shown in Tables 4.2.27 (a) and (b). For ease of visualization, the same information is presented in chart form in Figures 4.2.27 (a) and (b).

Results of the pooled analysis of variance for electrical conductivity of the alloys in Table 2.5 are shown in Table 4.2.28. Table 4.2.28 shows that, at the levels studied, the element that affects electrical conductivity most significantly is silicon. Its relative contribution to the variance in electrical conductivity is about 46%. Copper and titanium have significant effects, contributing to the variance in electrical conductivity about 15% and 13%, respectively, and are followed by Zn, Fe, Mg, and Sr, in decreasing order. The interactions of Fe × Mn and Si × Mg also have some effects. As expected, all element additions decrease the electrical conductivity, but to varying degrees, except Sr. The results showed that Sr, at higher level, slightly increased the electrical conductivity, contributing about 1% to the variance. The percent contribution due to the error term in this analysis is small, about 3.6%, which shows that the design of the experiment and the performance of the electrical conductivity measurements were adequate.

Considering only the elements in Table 2.5 and their interactions, the maximum room temperature electrical conductivity can be obtained from an alloy with the following composition:

Element	Si	Cu	Mn	Zn	Ti	Fe	Mg	Ni	Cr	Sr
Wt. %	6.96	1.21	0.01	0.46	0.01	0.65	0.04	0.04-0.47	0.01-0.14	0.02

At this composition the projected room temperature electrical conductivity is 31.1 ± 0.4 %IACS at a confidence level of 95%. It is also useful to note that, considering only the elements in Table 2.2 and their interactions, the minimum room temperature electrical conductivity (i.e., maximum room temperature electrical resistivity) can be obtained from an alloy with the following composition:

Element	Si	Cu	Mn	Zn	Ti	Fe	Mg	Ni	Cr	Sr
Wt. %	12.85	4.90	0.01	2.87	0.19	1.55	0.46	0.04-0.47	0.01-0.14	0.00

At this composition the projected room temperature electrical conductivity is 16.5 ± 0.4 %IACS at a confidence level of 95%.

As in heat transfer, the larger grain boundary areas and larger interfacial areas between intermetallic compounds and the alloy matrix contribute more barrier to the electron movement, and consequently reduce the electrical conductivity. So, generally, the greater amounts of elements in the alloy and the smaller the grain size, the lower the electrical conductivity. Among the sixteen alloys in Table 2.5, Alloy 1 has the least element contents and is not grain refined and so it has the highest room temperature electrical conductivity (30.71 ± 0.19 %IACS). Alloy 11 has the lowest room temperature electrical conductivity (19.42± 0.19 %IACS) among these alloys. This is because it has a high Si content, is grain refined, and it also has a high Fe and low Mn and Cr contents, which give the alloy large amounts of Fe bearing needles. The needle phase has the largest surface:volume ratio and therefor it has the largest interfacial area with the alloy matrix, and consequently it affects thermal conductivity more than the other morphologies. Alloy 15 has the same characteristics as Alloy 11, high Si content, grain refined, and high Fe and low Mn and Cr contents, so it has the room temperature electrical conductivity (20.19 ± 0.58 %IACS) as low as Alloy11. The grain structures and microstructures of Alloys 1 and 15 are shown in Figs 4.1.1 (a) and (b), 4.1.3 (a) and (b), 3.1.5 to 3.1.8 and 3.15.5 to 3.15.8, respectively, and were discussed earlier.

Table 4.2.27 (a). Summary of average electrical conductivity for Alloys 1 to 16.

Alloy		1	2	3	4	5	6	7	8
Electrical Conductivity	%IACS	30.71	26.21	26.60	22.56	26.99	25.41	22.16	23.51
St. dev.**	%IACS	0.19	1.53	0.21	0.22	0.09	0.15	0.72	0.02
C.V.**	%	0.6	5.8	0.8	1.0	0.3	0.6	3.2	0.1
Alloy		**9**	**10**	**11**	**12**	**13**	**14**	**15**	**16**
Electrical Conductivity	%IACS	21.28	20.31	19.42	23.55	20.44	21.65	20.19	24.53
St. dev.*	%IACS	0.30	0.06	0.19	0.11	0.04	0.11	0.58	0.49
C.V.**	%	1.4	0.3	1.0	0.5	0.2	0.5	2.9	2.0

***St. dev. - Standard deviation **C.V. - Coefficient of Variation (= St. dev./Mean 100%)**

Table 4.2.27 (b). Summary of average electrical conductivity for Alloys 17 to 24.

Alloy		17	18	19	20	21	22	23	24
Electrical Conductivity	%IACS	26.12	24.00	24.34	22.13	21.56	23.21	22.70	21.64
St. dev.*	%IACS	0.38	0.14	0.25	0.09	0.24	0.45	0.62	0.09
C.V.**	%	1.5	0.6	1.0	0.4	1.1	2.0	2.7	0.4

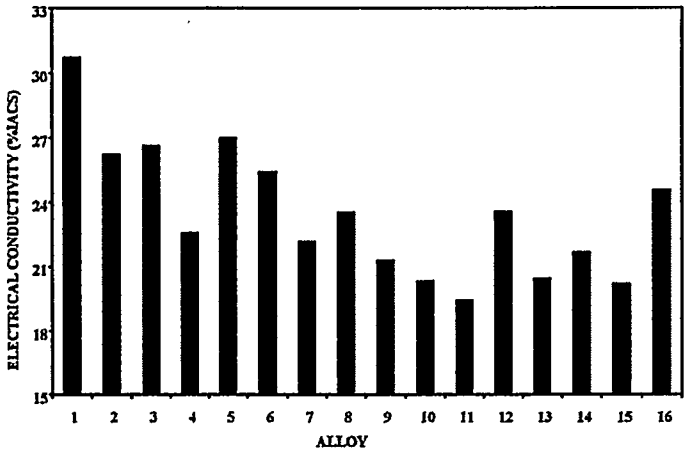

2.27 (a). Electrical conductivity of Alloys 1 to 16.

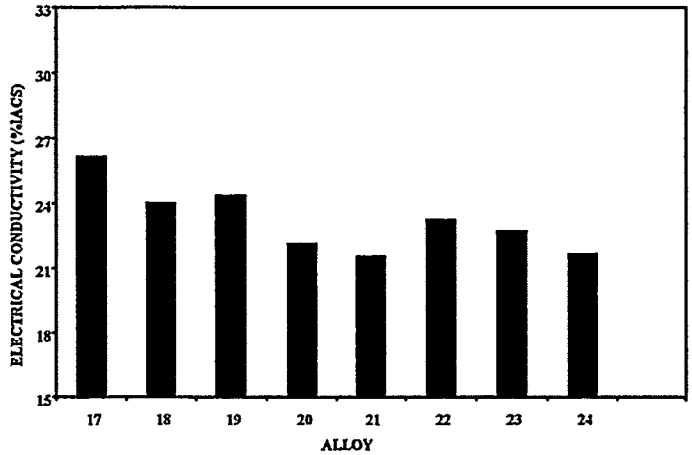

Fig. 4.2.27 (b). Electrical conductivity of Alloys 17 to 24.

Table 4.2.28. Pooled ANOVA table for electrical conductivity measurement for Alloys 1 to 16.

Source of Variance	Degree of Freedom f	Sum of Squares S	Variance (Mean Squares) V	Variance Ratio F	Pure Sum of Squares S'	Percent Contribution P
Si	1	269.7	269.7	799.2	269.3	45.8
Mg	1	8.5	8.5	25.1	8.1	1.4
Si·Mg	1	26.7	26.7	79.2	26.4	4.5
Fe	1	27.7	27.7	82.1	27.4	4.6
Cu	1	86.1	86.1	255.1	85.7	14.6
Ni						
Cr						
Mn						
Ti	1	76.0	76.0	225.1	75.6	12.8
Zn	1	28.2	28.2	83.5	27.8	4.7
Fe·Mn·Cr	1	8.5	8.5	25.2	8.2	1.4
Fe·Mn	1	33.4	33.4	98.9	33.0	5.6
Sr	1	6.1	6.1	18.0	5.7	1.0
Cu·Zn						
Error (e)	53	17.9	0.3374	1.0	21.3	3.6
Total	63	588.6				100.0

4.3 Chemistry—Property Correlation

Data on mechanical and physical properties of twenty-four die casting alloys has been presented in Chapter 3. However, one may require estimates of a particular property at chemistry points between those cited in this book. One way of providing this information is through fitting curves to the discrete data in order to obtain intermediate estimates. Multiple regression analysis is used to generate such curves. Because measured data inevitably exhibits some degree of error or "noise", multiple regression analysis techniques seek to derive a single curve that represents the general trend of the data. Because any individual data point may be inaccurate, no effort is made to intersect every point. Rather, the curve is designed to follow the pattern of the points taken as a group. The process of using the pattern of the data to make predictions is often referred to as trend analysis. Trend analysis may be used to make extrapolations beyond the limits of the observed data or interpolations within the range of the data. In both cases one must keep in mind that these are predictions based on mathematical models, and as such are always subject to inaccuracies. Therefore, predicted property values must always be verified before they are used in any design.

Table 4.3.1 lists equations that relate the various properties of aluminum die casting alloys to alloy chemistry. The equations were obtained by performing multiple regression analysis on property data for Alloys 1 through 24. In each case, the "goodness of the fit", as described by the r^2 value[1], is given. It must be well understood that these equations were obtained using a very limited number of data points (25 alloy compositions). For a robust statistical analysis where 10 factors (alloying elements) are involved, it is recommended that at least 100 observations (different alloys) be used to ensure a high degree of accuracy. Hence, these equations may not be used as property predictors in the design of die cast parts and components, but rather as trend indicators.

References

1. *G. Taguchi, System of Experimental Design, UNIPUB, Kraus International Publication, 1987.*
2. *P. Ross, Taguchi Techniques for Quality Engineering, McGraw-Hill Book Company, 1988.*
3. *R. Roy, A Primer on the Taguchi Method, Van Norstrand Reinhold Book Company, 1990.*
4. *J. B. Conway and L. H. Sjodahl, Analysis and Representation of Fatigue Data, ASM International, Materials Park, Ohio, 1991.*
5. *ASM Specialty Handbook, Aluminum and Aluminum Alloys, Edited by J. R. Davis, ASM International, 1993.*

Table 4.3.1. Trend equations for the effect of alloy chemistry on the various properties of aluminum die casting alloys.

TREND EQUATION	r	r^2
P1 = 44.93-0.46Si+0.67Cu-0.18Fe+0.76Mg-0.13Mn+0.23Ni+0.16Cr+0.33Zn+0.20Ti+0.35Sr	0.899	0.808
P2 = 34.93-0.13Si+0.88Cu+0.02Fe+0.87Mg+0.10Mn+0.16Ni+0.27Cr-0.04Zn-0.05Ti+0.31Sr	0.851	0.725
P3 = 18.07+0.16Si+0.60Cu+0.26Fe+0.60Mg+0.16Mn+0.13Ni+0.11Cr-0.42Zn-0.03Ti+0.06Sr	0.756	0.571
P4 = 12.56+0.31Si+0.75Cu+0.12Fe+0.77Mg+0.08Mn+0.04Ni+0.14Cr-0.36Zn+0.12Ti+0.03Sr	0.820	0.672
P5 = 12.62+0.37Si+0.80Cu+0.12Fe+0.75Mg+0.09Mn+0.07Ni+0.15Cr-0.42Zn+0.06Ti+0.01Sr	0.824	0.679
P6 = 12.98+0.17Si+0.59Cu+0.14Fe+0.52Mg+0.15Mn+0.05Ni+0.19Cr-0.47Zn+0.03Ti+0.03Sr	0.691	0.478
P7 = 10.62-0.61Si-0.50Cu-0.46Fe-0.57Mg-0.21Mn-0.07Ni+0.06Cr+0.25Zn+0.08Ti+0.07Sr	0.938	0.880
P8 = 17.39-0.61Si-0.53Cu-0.45Fe-0.62Mg-0.19Mn-0.09Ni+0.02Cr+0.20Zn+0.05Ti+0.08Sr	0.941	0.885
P9 = 25.34-0.44Si-0.51Cu-0.39Fe-0.52Mg-0.26Mn-0.18Ni-0.10Cr+0.22Zn+0.01Sr	0.855	0.731
P10 = 11.52+0.67Si+0.54Cu-0.04Fe+0.56Mg-0.008Ni+0.33Cr+0.06Zn+0.22Ti-0.12Sr	0.852	0.725
P11 = 7.55-0.39Si-0.44Cu-0.44Fe-0.75Mg-0.31Mn-0.14Ni+0.04Cr+ 0.02Zn+0.1Ti+0.04Sr	0.905	0.819
P12 = 10.49+0.52Si+0.63Cu+0.27Fe+0.81Mg+0.16Mn+0.13Ni+0.03Cr-0.08Zn-0.03Sr	0.901	0.812
P13 = 148.50-0.47Si-0.19Cu-0.46Fe-0.60Mg-0.02Mn+0.02Ni+0.02Cr-0.25Zn-0.38Ti+0.22Sr	0.820	0.673
P14 = 36.44-0.72Si-0.26Cu-0.32Fe-0.63Mg-0.08Mn+0.01Ni+0.02Cr-0.36Zn-0.27Ti+0.31Sr	0.890	0.792
P15 = 2.71-0.40Si+0.74Cu+0.30Fe+0.87Mg+0.09Mn+0.06Cr+0.51Zn+0.56Ti	0.980	0.961

P1 is room temperature ultimate tensile strength in ksi.
P2 is ultimate tensile strength at 100°C in ksi.
P3 is ultimate tensile sttrength at 200°C in ksi.
P4 is room temperature yield strength in ksi.
P5 is yield strength at 100°C in ksi.
P6 is yield strength at 200°C in ksi.
P7 is room temperature elongation.
P8 is elongation at 100°C.
P9 is elongation at 200°C.
P10 is maximum stress for a fatigue life of 100,000,000 cycles in ksi.
P11 is impact resistance in $lb_f \cdot ft.$
P12 is hardness (RHB).
P13 is thermal conductivity in W/mK.
P14 is electrical conductivity in %IACS.
P15 is specific gravity.

[1] *r^2 is the coefficient of determination, where r is the correlation coefficient. For a perfect fit, $r^2 = 1$, signifying that the curve explains 100% of the variability of the data. $r^2 = 0$ signifies that the curve does not represent the data.*